Investigation of ZnO nanorod solar cells with layer-by-layer deposited CdTe quantum dot absorbers

Joe Briscoe
School of Applied Science
Cranfield University
Supervisors: Dr Steve Dunn and Prof Robert Dorey

PhD Thesis
August 3, 2011

Abstract

Innovation in solar cell design is required to reduce cost and compete with traditional power generation. Current innovative solar technologies include nanostructured dye-sensitised solar cells and polymer solar cells, which both contain organic materials with limited lifetime. This project aims to combine the advantages of ZnO nanorods and quantum dot (QD) absorbers in an all-inorganic solar cell, using the layer-by-layer (LbL) process to increase light absorption in the cell.

The parameters that affect the aqueous chemical growth of ZnO nanorods were investigated on Ag-coated substrates in order to improve the density and alignment of the nanorods. Rods 3–6 μm long and 90–500 nm in diameter were grown on fluorine-doped tin oxide (FTO)-coated glass substrates for use in solar cells.

ZnO nanorods were doped with antimony (Sb) *in-situ* during their aqueous synthesis to make them p-type. Direct addition of Sb acetate to the reaction adversely affected the nanorod morphology, which was avoided by first dissolving the Sb acetate in ethylene glycol. Optical and electrical properties of the nanorods were altered with Sb-doping, but p-type behaviour was not proven conclusively.

ZnO nanorods were conformally coated with CdTe QD-polymer films using a LbL process. Increasing the number of coated layers increased the level of light absorption at wavelengths of 500-900 nm due to absorption by the QDs. Air annealing of the QD-polymer films above 200 °C led to oxidation of the film, which did not occur when annealing in vacuum. Annealing in vacuum up to 350 °C led to a slight reduction in quantum confinement effects attributed to increased interaction between the nanoparticles due to reduced separation. At 450 °C the polymer was completely removed and no quantum confinement remained in the CdTe.

To complete the solar cells CuSCN was deposited between the LbL-coated ZnO nanorods by repeatedly spreading a solution of CuSCN in propyl sulphide on the surface and allowing it to dry. This film filled between the coated nanorods, but the drying and quantity of solution used had to be carefully controlled to avoid cracking in the film. Spin-coating of CuSCN solutions was attempted, but films suitable for solar cells were not produced. Poly(styrenesulfonate)-doped poly(3,4- ethylenedioxythiophene) (PEDOT:PSS) was deposited by spin-coating as an alternative to CuSCN, but the film only penetrated ~200 nm below the nanorod tips.

Solar cells were produced with different thicknesses of LbL films, annealed components and other variations. A model was proposed whereby carriers are extracted from the LbL film through exciton transfer between QDs. Annealing of the ZnO nanorods in air and reduction of the cracks in the CuSCN film both improved the efficiency of the solar cells. Annealing of the LbL film in vacuum improved the performance of the cells by increasing the efficiency of charge transfer. In devices with annealed LbL films 50-layer devices had higher efficiency than 30-layer devices and cells using CuSCN had a higher efficiency than those with PEDOT:PSS. The best cells produced used 50 layer CdTe-polymer films annealed at 350 °C in vacuum with CuSCN. These produced an energy conversion efficiency of 0.0062 %, which compares to 1–3 % for similar cells in the literature and 10–20 % for commercial devices.

This thesis is dedicated to Paul and Monica Briscoe.

I was privileged to know them for so long and I am so glad they knew I would achieve this.

Acknowledgements

I would like to thank all those who have helped and supervised me in my PhD. Steve Dunn and Diego Gallardo who helped me to make a firm start, develop my skills as a researcher, and guided me through my PhD. Rob Dorey who stepped in to make sure I completed my work successfully and who has provided me with a mass of helpful and excellent suggestions to develop this thesis. Andy Stallard, Matt Taunt and Chris Shaw, without whom I could never have gathered all the data I needed. I would also like to thank all my colleagues in our group with whom I've chatted, discussed and brain-stormed my work on many occasions and who have made me feel very much at home and comfortable in my work.

My thanks also go out to my parents, Lyn and Bob, who have supported me through this process, and without whom I would never have made it here. My special thanks go to Jane Clubb, who has been there for me always, helped me through my troubles and provided me with a great deal of strength and support.

Publications and Presentations

Journal papers

Briscoe, J., Gallardo, D. E., Lesnyak, V. and Dunn, S., Influence of annealing on composition and optical properties of CdTe nanoparticle layer-by-layer films, *Journal of Nanoscience and Nanotechnology*. **11** (6), 5270-5273 (2011).

Briscoe, J., Gallardo, D. E., Hatch S., Lesnyak, V., Gaponik, N. and Dunn, S., Enhanced quantum dot deposition on ZnO nanorods for photovoltaics through layer-by-layer processing. *Journal of Materials Chemistry*. **21** (8), 2517-2523 (2011).

Briscoe, J., Gallardo, D. E. and Dunn, S., In situ antimony doping of solution-grown ZnO nanorods, *Chemical Communications*, **2009**, 1273-1275.

Briscoe, J. and Dunn, S., Extra thin absorber solar cells based on nanostructured semiconductors, *Materials Science and Technology*. Under review.

Conference proceedings

Briscoe, J., Gallardo, D. E. and Dunn, S., Layer-by-layer CdTe nanoparticle absorbers for ZnO nanorod solar cells - the influence of annealing on cell performance, *MRS Proceedings* **1260**, T06-02 (2010).

Briscoe, J., Gallardo, D. E. and Dunn, S., Antimony doped ZnO nanorods - a change from n to p type? *MRS Proceedings* **1256**, N16-33 (2010).

Damitha, A. A., Adikaari, T., Briscoe, J., Dunn, S., Carey, J. D. and Silva, S. R. P., Effect of transparent electrode on the performance of bulk heterojunction solar cells, *MRS Proceedings*, **1270**, HH14-23 (2010).

Oral presentations

Self-assembled CdTe nanoparticle absorbers for ZnO nanorod solar cells - the influence of annealing on cell performance. *Materials Research Symposium*, San Francisco, April 2010.

In-situ antimony doping of zinc oxide nanorods grown in aqueous solution. *Electroceramics XI*, Manchester, September 2008.

Poster presentations

Thermal annealing of layer-by-layer deposited nanoparticle composites. *MRS*, April 2010.

Antimony doped ZnO nanorods - a change from n to p type? *MRS*, April 2010.

Self-assembled CdTe nanoparticle absorbers for ZnO nanorod solar cells. *SET for Britain*, Houses of Parliament, March 2010.

Contents

List of Figures

List of Tables

Notation

b_s Incident spectral flux density
CB Conduction band
CVD Chemical vapour deposition
DSSC Dye-sensitised solar cell
EDX Energy-dispersive X-ray spectroscopy
E_g Band gap
EG Ethylene glycol
EQE External quantum efficiency
eta extra-thin absorber
FF Fill factor
FTO Fluorine-doped tin oxide
ICDD International Centre for Diffraction Data
ILGAR Ion-layer gas reaction
IQE Internal quantum efficiency
IPCE Incident photon-to-electron conversion efficiency
ITO Indium-tin oxide
J_{max} Current density at maximum power
J_{sc} Short-circuit current density
k_b Boltzmann constant
LED Light-emitting diode
LHE Light-harvesting efficiency
MBE Molecular beam epitaxy
MEH-PPV Poly(2-methoxy-5-[2'-ethyl-hexyloxy]-1,4-phenylene vinylene)
NP Nanoparticle
P3HT Poly(3-hexylthiophene)
PEDOT:PSS Poly(styrenesulfonate)-doped poly(3,4- ethylenedioxythiophene)
PLD Pulsed laser deposition
P_{max} Maximum power
QD Quantum dot
SEM Scanning-electron microscope
SILAR Successive ionic layer adsorption and reaction
spiro-OMeTAD 2,2',7,7'-tetrakis(N,N-di-p-methoxyphenylamine)-9,9'-spirobifluorene
TGA Thermo-gravimetric analysis (based on context)
TGA Thioglycolic acid (based on context)
VB Valence band
V_{max} Voltage at maximum power
V_{oc} Open-circuit voltage
XPS X-ray photoelectron spectroscopy
XRD X-ray diffraction

Chapter 1

Introduction

1.1 Background — electricity generation

Energy security and climate change are very important topics at the current time. There is an increasing consensus that we must reduce our reliance on fossil fuel-based energy production because of both security of supply and the impact of carbon dioxide emissions on the climate. A number of solutions to this problem have been proposed and are either in use or under investigation. These include three main avenues for electricity generation to reduce fossil fuel use and/or carbon dioxide emissions. The first is to continue to use fossil fuels and combine this with carbon sequestration, such as 'carbon-capture and storage' (CCS) systems. The second is to increase the use of nuclear fission to produce electricity. And the third is to use renewable energy production. It could be said that the forth possibility is to use nuclear fusion to produce electricity, however this is much further from practical implementation that the other possibilities. All of these options have advantages and disadvantages. CCS allows the use of the established system of burning fossil fuels for energy, but does not remove all of the CO_2 emitted and does nothing to address the problems with security of supply. Nuclear fission also relies on the import of a fuel in the form of uranium, which could be an issue as many of the sources of this element are in unstable regions. However, relatively small quantities of this fuel are required to produce electricity compared to fossil fuel and no CO_2 is emitted. The largest drawback of this option is that it produces radioactive nuclear waste that takes thousands or tens of thousands of years to break down. Renewable energy generation produces no CO_2 and requires no input of fuel, but the supply is intermittent due to changes in weather conditions, reliance on daylight, etc. The source of energy is also very diffuse therefore installations can have a large impact on the landscape. Additionally, many renewable energy sources are still expensive compared to more traditional means of generation. It is likely that a mixture of these solutions will be used in the future to decrease our reliance on fossil fuels.

Within the renewable option there are a number of technologies such as wind, tidal, solar photovoltaic (PV), geothermal, biomass, etc. Many of these technologies are already being used around the world, and among them solar PV has much scope for improvement in the area of materials to both improve efficiency and reduce cost; solar PV remains the most expensive renewable method to generate electricity (e.g. 15-30 USc/kWh for commercial scale solar PV compared to 5-9 USc/kWh for on-shore wind [1]). Solar PV has the advantage that it has a fairly low visual impact compared to many other renewable options: PV panels could be installed on roofs of nearly all building without being highly visible, which can be appealing compared to high visual-impact technologies such as wind turbines. Additionally, once installed solar modules need very little maintenance as they have no moving parts, and will last for at least 25 years with no more than a 10–20 % drop in output [2].

1.1.1 Challenges in photovoltaics

In the years since the first commercial installations solar PV has gradually become less expensive; PV module price has dropped by 22 % every time the global installed capacity has doubled, and is currently approximately two thirds less than 5 years ago [2]. Economies of scale have been a large factor in the cost reduction, but technological progress and increased production efficiency have also played a part [2]. This cost reduction has been assisted by a rapid acceleration of installation in recent years: in 2011 the global installed capacity reached almost 40 GW, of which nearly half (16.6 GW) was installed in 2010 [3]. A large portion of this installation was made by Germany (7.4 GW) [3], who were the first country to introduce feed-in-tariffs (FiTs), which helped to drive this increase. FiTs are schemes whereby electricity generated by PVs is sold back to the grid at a premium rate, which is guaranteed for a number of years. The costs of such schemes are taken on by the utility companies to meet their renewable obligations [2]. PV installation is increasing in a number of other European countries due to implementation of FiT schemes, and such increased demand should further reduce costs, which should drive further demand etc. With the increase in efficiency of production the energy payback time of PV systems has also decreased: a PV module will generate the same quantity of energy that was used to produce it within 1–3 years [2]. The cost of production has reduced to such a degree, and cost of energy produced by non-renewable methods (fossil-fuel and nuclear) is increasing at such a rate, that PV is expected to reach grid parity in the near future [2]. Grid parity is the point at which the generation costs of PV electricity match that of conventional generation methods. It is thought that when comparing PV to conventional generation at peak times (during the day, when PV is generating) grid parity may have already been reached in Southern Europe. The longest time predicted until grid parity is in Northern Europe when comparing PV prices to the baseline electricity price (lower than peak), where it will be reached by 2025 [2]. However, although PV electricity costs are decreasing, the rapid approach of grid parity is largely assisted by steep rises in fossil fuel cost. Therefore PV costs would ideally be driven even lower than grid parity so that they become more economical than fossil fuel generation methods, and electricity prices could begin to reduce if sufficient capacity could be installed.

The PV market is still largely dominated by crystalline silicon (c-Si) with 80 % of installed capacity [2]. Here cost reduction has largely come from economies of scale in the production of this material and associated modules. Record light-to-electrical energy conversion efficiencies for silicon solar cells are 25.0 % for single crystal and 20.4 % for polycrystalline silicon [4], with c-Si modules operating at around 12–20 % efficiency [2].

There are a number of alternative materials and designs to silicon-based cells that are either used for cells or are under development. These include thin-film solar cells, dye-sensitised solar cells (DSSCs) and polymer/organic solar cells. Thin-film solar cells use direct band gap semiconductors therefore require much thinner layers of material than silicon solar cells to absorb sufficient sunlight. The cells are highly stable and efficient, but the materials used are generally quite expensive and sometimes toxic. They have been produced commercially for some time with CdTe-based thin-film solar cells being the most well established and economical thin-film technology due to standardised and well-established manufacturing techniques [2]. However, because the cost remains higher and the production base is less established these are not as wide-spread as silicon solar cells: over 1000 companies are involved in c-Si solar cell manufacture compared to only 30 for thin-film solar cells [2]. The record efficiency for a CdTe solar cell is 16.7 %, and submodule is 12.5 % [4]. The main other type of thin-film solar cell is based on $\mathrm{CuIn}_{1-x}\mathrm{Ga}_x\mathrm{Se}_2$ (CIGS). These cells are more efficient than CdTe (cell record efficiency 19.6 %, submodule 16.7 % [4]), but due to complex, non-standard production techniques they remain more expensive and less widely used than CdTe [2].

DSSCs use porous TiO_2 sensitised with an organic dye to absorb the sunlight and are completed with a liquid electrolyte to regenerate the dye. They have very recently reached commercialisation, with around 30 MW of capacity produced in 2009, and a total of 200 MW expected by 2012 [2]. They are based on fairly affordable, non-toxic materials and are relatively simple to manufacture, therefore could be much cheaper than any currently available solar cells. DSSCs are less efficient than silicon solar cells (record 10.4 % for a cell [4], but generally <4 % for commercial modules [2], although the submodule record stands at 9.9 % [4]). The low cost means that the cost per watt of electricity should still be much lower than other solar cell types. Finally there are polymer, or organic solar cells that are made from conducting polymers and have the potential to be very cheap and easy to produce. However, they still require a large amount of research, having low efficiencies (record 8.3 % for a cell and 3.5 % for a submodule [4]).

The solar cells technologies under development that are discussed above aim to reduce the cost of producing electricity from the sun. However, they all have limitations and there is still scope for improvements to be made. One of the issues with the newer solar cell technologies is that although they are much cheaper to produce than silicon or thin-film cells the molecular, liquid-state and polymer materials used in DSSCs and organic solar cells are much less stable so are expected to last less time [2]. Thus some of the gains made due to their inexpensive production may be lost due to their short lifetime as they would need to be replaced more frequently. Therefore, there is still a need to design new types of solar cell that are cheap to produce but that are more stable than DSSCs or polymer solar cells.

One of the reasons that DSSCs and polymer solar cells can be produced so cheaply is that the materials that comprise them do not need to be extremely high quality, and generally can be produced using low energy, often chemical production techniques. It would therefore be ideal to produce solar cells using a design that means the component materials do not need to be extremely high quality, ideally being produced using inexpensive chemical techniques, but have a stability comparable to silicon or thin-film solar cell materials. This high stability is most likely to be achieved using solid-state, inorganic materials, as they are generally more stable than molecular, liquid or organic materials. An area of research that has the potential to address these requirements is that of solid-state DSSCs and extra-thin absorber (eta) solar cells. These take the basis of an inorganic nanostructured semiconductor from DSSCs, but use solid-state, inorganic absorber and/or hole-collecting materials instead of molecular and liquid materials as in the DSSC. There are a number of designs of solid-state DSSCs and eta solar cell. Some are based on porous TiO_2 and some on ZnO nanorods, as discussed in chapter 2.

Another potentially beneficial area of investigation is the use of semiconductor nanoparticles, or quantum dots (QDs) as absorber materials in this type of solar cell. These are made from inorganic semiconductors and are therefore chemically stable, but their properties can be varied by varying the size of the particles. The main variation in properties that is relevant to PVs is that the band gap of the material increases as the particles are made smaller, shifting the optical absorption maximum to shorter wavelengths (see section 2.4). This allows the absorption peak of a material to be shifted towards the optimum for solar energy conversion (see section 2.1), broadening the potential range of materials available for use in PV devices. QDs therefore have the potential to allow optimisation of the materials properties for use in a solar cell while using an inexpensive, abundant material as the absorber. However, very few solar cells use QDs as sensitisers, especially in fully solid-state designs and there are many issues with the QD-sensitised cells that require investigation. One such issue is that charge collection through porous TiO_2 and penetration of a solid-state hole collector into the pores can both limit the performance of TiO_2-based cells. Both of these limitations are reduced when using ZnO nanorods in the cell. However, using ZnO nanorods does not lead to sufficient surface-area enhancement to allow enough incident light to be absorbed by a layer of QDs. It is this challenge that is investigated in this thesis — to increase the quantity of QDs deposited onto ZnO nanorods to increase the light absorption and produce an effective QD-sensitised ZnO nanorod solar cell.

1.2 Aims and objectives

The aim of the project is to produce a QD-sensitised ZnO nanorod solar cell with enhanced light-harvesting ability achieved using the layer-by-layer (LbL) process to deposit the QDs. To make proof-of-concept devices CdTe quantum dots will be used as the LbL process has already been developed for previous work in light-emitting diodes using CdTe QDs [5]. Although bulk CdTe has a close-to-optimum band gap for solar energy conversion (see section 2.1) and the shift in band gap of these QDs therefore takes them away from this optimum value, the aim of the project is to show that the LbL process can be used to deposit QDs on ZnO nanorods for PV devices so that the methods can potentially be applied later to a broader range of QDs. For example PbS, PbSe, FeS_2 and $CuFeS_2$ have band gaps that are too small for efficient solar energy conversion, therefore QDs of such materials with band gaps closer to the optimum for solar energy conversion could potentially be used for PVs. In addition to band gap shift, another property that could benefit from quantum confinement is the shift in conduction band position to higher energies (see section 2.2.3 and figure 2.8). It is possible that using CdTe QDs could shift the conduction band to a level that allows more efficient charge transfer to ZnO, even though it shifts the band gap away from the optimum value for PVs. The potential investigation of such shift is discussed further is section 8.2.

Ideally the use of the LbL process would lead to the production of a QD-sensitised solar cell that had an energy conversion efficiency comparable with other solid-state DSSCs or QD-sensitised nanostructured solar cells currently being researched. To achieve this aim the following objectives must be met:

- Demonstrate that the layer-by-layer (LbL) process can be used to deposit multiple layers of QDs on ZnO nanorods and that adding more layers increases the light absorption of the composite.
- Show that such LbL-coated ZnO nanorods can be in-filled with a solid-state hole collector to produce a working solar cell.
- Study the properties of the cell and relate them to the component materials. Use this understanding to improve the performance of the cell so that they can compete with the efficiency of other QD-sensitised ZnO nanorod solar cells.

1.3 Thesis structure

In the thesis chapter 2 is the literature review. This explains the physics of solar cells and gives the background of the literature on eta solar cells including the original nanostructured DSSC design, cells in which one of the components was replaced with a solid-state alternative, cells where ZnO nanorods replaced porous TiO_2, and full eta solar cells where both the dye and hole collector were replaced with solid-state materials. Summaries of the methods in the literature for growth of ZnO nanorods, CdTe QDs and the LbL process are also included. Chapter 3 provides details of the experimental methods used in the project. Chapter 4 presents and discusses the results of the chemical growth of ZnO nanorods that were used in the project and how this growth was developed to improve the morphology and other properties of the nanorods. Chapter 5 describes attempts to dope ZnO nanorods with antimony, with the aim of producing p-type nanorods as opposed to undoped nanorods which are normally n-type. Chapter 6 presents the results of coating the ZnO nanorods with

CdTe QDs using the LbL process, the properties of the LbL films, and the effects of annealing the LbL films. Chapter 7 includes the details of the ZnO nanorods, LbL films, copper thiocyanate (CuSCN) hole-collecting layers and poly(styrenesulfonate)-doped poly(3,4- ethylenedioxythiophene) (PEDOT:PSS) hole collecting layers that were used in the solar cells. The results of PV characterisation of the complete solar cells are included and the PV properties of the cells are related to variations in their structure and composition. Finally, chapter 8 presents the conclusions and suggests future areas of investigation related to the thesis.

Chapter 2

Literature Review

2.1 Solar cells

2.1.1 Solar cell theory

Photovoltaic cells use materials that generate photoexcited carriers (electrons and/or holes) upon absorption of incident photons. A built-in asymmetry in the cell leads to a separation of the photoexcited carriers through the material, so that a current flows and a voltage is generated. In a traditional semiconductor solar cell, this asymmetry is provided by a p-n, or p-i-n junction, and these layers are stacked on top of each other with one or two of the layer(s) absorbing the light. The current-voltage characteristics of such a device in the dark can therefore be described by the diode equation:

$$J_{dark}(V) = J_0 \left(\exp\left(\frac{eV}{nk_BT} \right) - 1 \right), \tag{2.1}$$

where J_0 is the reverse saturation current density, e is the charge of an electron, V is the applied bias, n the diode non-ideality factor, k_B is Boltzmann's constant, and T is the temperature in Kelvin [6]. When light falls on the cell and the terminals are connected together in short-circuit, a short-circuit current flows through the circuit, and per area of the cell, the short-circuit current density is defined by [6]

$$J_{sc} = e \int b_s(E) EQE(E) dE. \tag{2.2}$$

Here the short-circuit current density is given by the integration of the product of the incident spectral flux density, b_s, with the external quantum efficiency, EQE, across the whole spectrum of incident photon energies, E. EQE is an important measure of the performance of a solar cell. It gives the probability that a photon of energy E will deliver one electron to the external circuit, and is therefore sometimes referred to as the incident photon-to-current conversion efficiency (IPCE). The EQE is dependent on the absorption coefficient of the solar cell material across the spectrum, and the efficiency of charge separation at the junction and collection through the material.

These two components of EQE can be separated, giving

$$EQE(E) = LHE(E) \times IQE(E), \tag{2.3}$$

where LHE is the light-harvesting efficiency, which expresses the portion of light absorbed by the cell, and IQE is the internal quantum efficiency, which defines the proportion of photoexcited electrons in the solar cell that contribute to the current in the external circuit. By measuring separately LHE and EQE for a cell, the losses through insufficient light absorption and recombination within the cell can be separated.

Under illumination, the current-voltage behaviour of a photovoltaic cell with an applied bias V can be approximated as a sum of the short-circuit photocurrent density and the dark current density, with the sign convention giving the dark current density as negative [6]:

$$\begin{aligned} J(V) &= J_{sc} - J_{dark}(V) \\ \Rightarrow J(V) &= J_{sc} - J_0 \left(\exp\left(\frac{eV}{nk_BT} \right) - 1 \right). \end{aligned} \tag{2.4}$$

It can be seen from figure 2.1 that as the applied bias increases the current density drops from J_{sc} at $V = 0$ to zero when $J_{dark} = J_{sc}$. This point is referred to as the open-circuit voltage, V_{oc}, as it is the voltage that is generated in the cell when the terminals are open [6]. Substituting J_{dark} from equation 2.1 gives

$$J_{sc} = J_0 \left(\exp\left(\frac{eV_{oc}}{nk_BT} \right) - 1 \right) \tag{2.5}$$

$$\Rightarrow V_{oc} = \frac{nk_BT}{e} \ln\left(\frac{J_{sc}}{J_0} + 1 \right). \tag{2.6}$$

In the range between J_{sc} and V_{oc} the cell is generating power density, P. At some current density, J_m and voltage V_m the cell is generating maximum power density, P_m (figure 2.1). The proportion of this maximum power density to the maximum theoretical power density if operating at J_{sc} and V_{oc} is defined by the fill factor [6]:

$$FF = \frac{J_m V_m}{J_{sc} V_{oc}}. \tag{2.7}$$

The overall light-to-power conversion efficiency of the cell, η, is then defined as the maximum power density as a proportion of the incident light power density, P_{in}, or irradiance [6]:

$$\eta = \frac{J_m V_m}{P_{in}} \tag{2.8}$$

$$\Rightarrow \eta = \frac{J_{sc} V_{oc} FF}{P_{in}}. \tag{2.9}$$

Equation 2.9 includes all of the characteristic parameters of a solar cell, which are generally tested under a standard air mass (AM) 1.5 spectrum (figure 2.2), corresponding

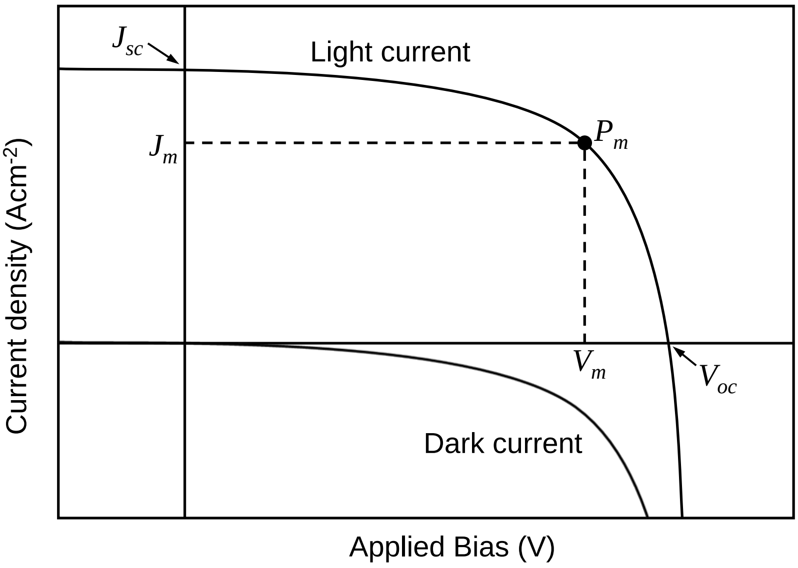

Figure 2.1: **Example J-V behaviour of a non-ideal solar cell in the dark and under illumination.** At $V = 0$ the current is equal to the short-circuit current density, J_{sc}, and at zero current the cell generates open-circuit voltage, V_{oc}. The maximum power generated, P_m is at current density J_m and voltage V_m.

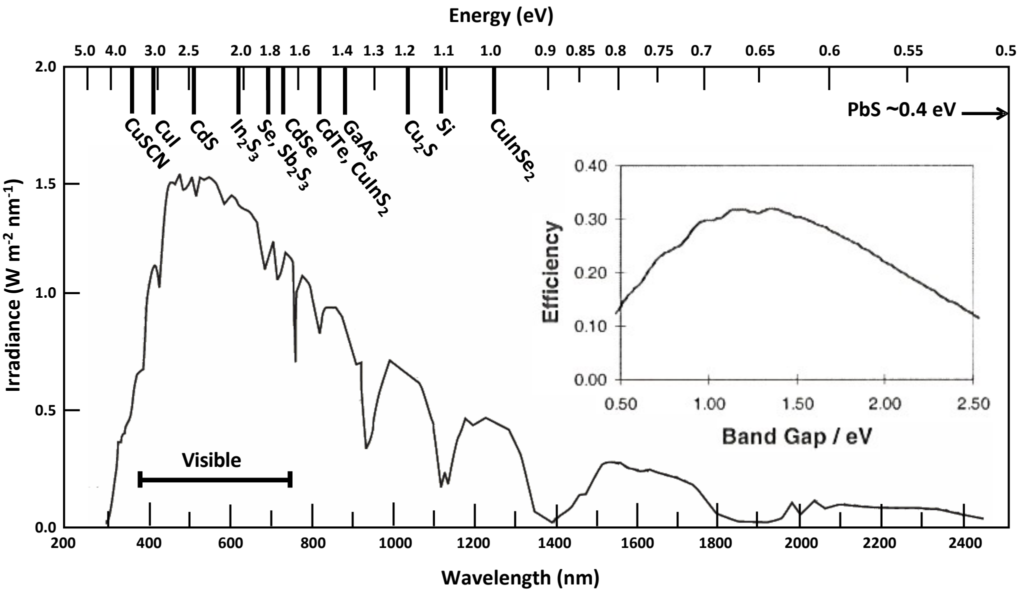

Figure 2.2: **AM 1.5 solar spectrum.** Inset shows maximum theoretical efficiency of a single band gap semiconductor solar cell under AM 1.5 illumination as a function of band gap energy. Top scale shows photon energy corresponding to wavelengths on lower scale, and is annotated with band gap energies of semiconductors used in eta solar cells, as well as common solar cell materials. Inset from figure 2.8 in Ref. 6.

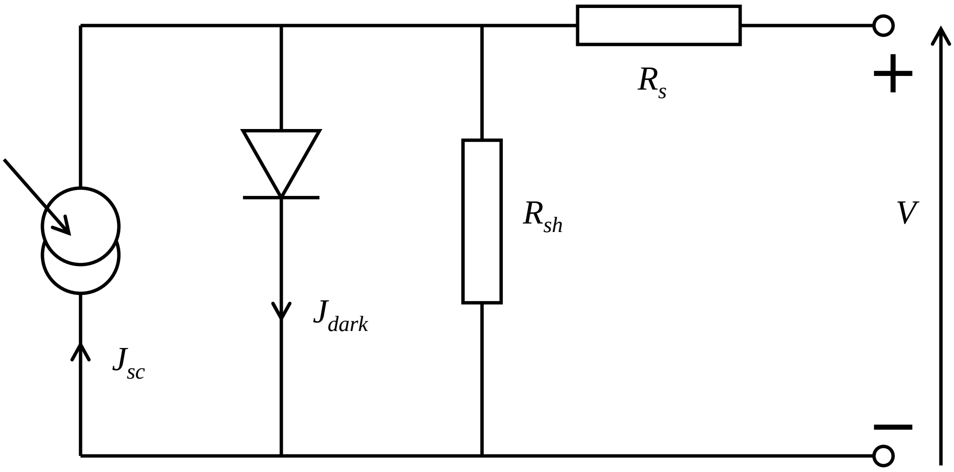

Figure 2.3: **Equivalent circuit for a solar cell.** Includes series (R_s) and shunt (R_{sh}) resistances.

to the sun being at an elevation of 42 °. The most common P_{in} used to test a cell is defined as 1 sun, corresponding to 100 mWcm^{-2}.

The reason that a solar cell does not operate at J_{sc} and V_{oc}, and therefore has $FF < 1$ is because of losses within the cell. Some of these are caused by the non-ideality of the diode, included in the non-ideality factor n. However, there are also resistances in a normal cell that must be taken into consideration. These can be separated into series resistance, R_s, and shunt resistance, R_{sh}. A diagram of an equivalent circuit of a solar cell representing these losses can be seen in figure 2.3. The series resistance of a cell is caused by resistance to current flow in the cell materials, resistance at the interface with the contacts, and resistance in the contacts [6]. The shunt resistance is caused by leakage of current through and around the cell, e.g. through short-circuits [6].

2.1.2 Solar cell materials

Early solar cells were based on a silicon p-n diode. Silicon is an indirect band gap semiconductor, which means that it has a very small absorption coefficient, therefore hundreds of microns of material are required to absorb sufficient sunlight and achieve a reasonable LHE [6]. The carriers that are generated in the silicon material must drift and diffuse to be separated at the p-n junction and then reach the contacts. This means that high quality material with low defect densities are required for the carriers to be extracted before recombining. Due to the mass production and large amount of material development in silicon from to the electronics industry such high-quality silicon is both available and reasonably affordable, therefore silicon still remains the dominant solar cell material. The highest independently confirmed efficiency for single crystal silicon solar cells is 25.0 % and for polycrystalline silicon is 20.4 % [4].

Later developments of semiconductor materials led to the production of thin-film solar cells. Thin-film solar cells use direct band gap semiconductors such as CdTe, and $\mathrm{CuInSe_2}$ or $\mathrm{CuIn_{1-x}Ga_xSe_2}$ (CIS and CIGS) with high absorption coefficients and so can absorb a large portion of the incident light in layers 2–5 μm thick [6]. Again, photogenerated carriers must drift or diffuse through these layers to reach the front and back contacts. Thus the average diffusion length of the carriers must match the thickness of the cell, i.e. a few μm, so that they do not recombine before being extracted. High quality, expensive materials must therefore be used in these cells. The highest independently confirmed efficiencies for CdTe and CIGS cells are 16.7 % and 19.6 % respectively, and for submodules are 12.5 % and 16.7 % [4].

2.2 Extra-thin absorber solar cells

The purpose of the extra-thin absorber (eta) solar cell design is to reduce the *local* thickness of absorber material while retaining the optical thickness necessary to absorb sufficient incident light. This is achieved by using a highly structured, wide band gap semiconductor as a basis for the cell onto which a narrower band gap absorber material is coated (see figure 2.4). The structured surface creates a high surface area so that with a local thickness of <100 nm [7] an effective optical thickness of >1 μm is created: sufficient to absorb most of the incident light. By using an absorber layer with a much small local thickness the material quality requirements are relaxed as the photogenerated carriers need only diffuse a few tens of nm to reach the junction with either the electron transport (n-type) or hole transport (p-type) material; a theoretical study of eta cells calculated that to achieve efficiencies of 10 % an eta cell needed an absorber with a carrier lifetime 14 times lower than a thin-film cell [8]. This low material quality requirement allows greater flexibility in both the type of material and the deposition method. Low cost chemical synthesis methods can be used as associated high defect densities have a lower impact when such low diffusion lengths are required [9, 10]. In principle the absorber material therefore need only be chosen for

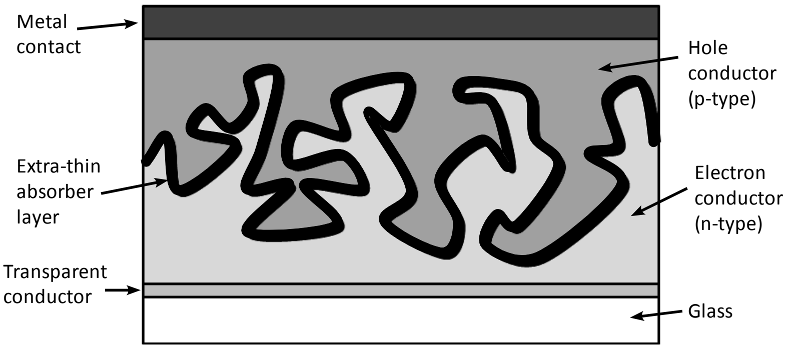

Figure 2.4: **Schematic of an extra-thin absorber solar cell.** Nanostructuring of n-type layer by using either porous $\mathrm{TiO_2}$ or ZnO nanorods allows an extra-thin absorber layer to be used. The increased surface area combined with enhanced light scattering from this structure allows a thin layer of absorber material to absorb a large portion of the incident light. The structure is filled with a p-type material to collect photogenerated holes.

properties relating to superior light absorption and ease of deposition, and the transport properties of the n- and p-type materials can be optimised separately. The aim of the eta concept is therefore to be able to produce low cost solar cells using stable materials with efficiencies approaching those of thin-film solar cells.

The following sections give a background to the development of the eta solar cell concept with examples of specific cells. Details of a number of eta cells, their methods of production and performance are given. For ease of comparison, table 2.1 gives a summary of the materials used in these cells and their key performance parameters.

Table 2.1: **Eta solar cells: materials and performance.** Summary of performance of cells discussed in following sections where sufficient data is given. Separated into cells using porous TiO_2 as a basis, and cells using ZnO nanorods.

Porous TiO_2-based cells

Buffer layer	Absorber material	Hole collector	J_{sc} /mAcm^{-2}	V_{oc} /mV	FF	η /%	Year	Ref
	Dye	Electrolyte	11.5^*	685	0.68	7.12	1991	[11]
	Dye	CuI	6^*	450	$0.53^\dagger$	1.8	1998	[12]
MgO	Dye	CuI	8.74	510	0.54	2.9	2003	[13]
	Dye	CuSCN	7.8	600	0.44	2.1	2002	[14]
	CdS QDs	Electrolyte	0.0175	395			1990	[15]
	Se	CuSCN	3^*	600		0.13	1998	[16]
	CdS	CuSCN	2.3	860	0.65	1.3	2006	[9]
	In_2S_3	CuSCN	8	475	0.58	2.3	2009	[10]
In_2S_3	Sb_2S_3	CuSCN	14.1	490	0.49	3.37	2009	[17]
In_2S_3	Cu_2S	CuSCN	0.4	310	$0.48^\dagger$	0.06	2009	[18]
In_2S_3	PbS	PEDOT:PSS	7.4	280	0.4	0.83	2006	[19]
	PbS QDs	spiro-OMeTAD	4.58	560	0.57	1.46	2009	[20]

ZnO nanorod-based cells

Absorber material	Hole collector	J_{sc} /mAcm^{-2}	V_{oc} /mV	FF	η /%	Year	Ref
CdTe	CuSCN	0.03^*	200	0.28		2005	[21]
CdSe	CuSCN	3.9^*	490	0.32	2.3	2006	[22]
In_2S_3	CuSCN	10.5	570	0.56	3.4	2008	[7]
CdSe	MEH-PPV	5^*	500	$0.31^\dagger$	0.9	2008	[23]

*These cells were tested at less than 1 sun illumination, therefore parameters, especially J_{sc}, cannot be directly compared.

†Calculated from other parameters given using $\eta = J_{sc} \cdot V_{oc} \cdot FF/P_{in}$, where P_{in} is the illumination intensity.

This table only includes the designs where a full cell has been completed and tested. Where the same group has published multiple reports on the same design of solar cell, only the results from the best performing cell are included.

2.2.1 Dye-sensitised solar cells

The concept of using a high surface area substrate to increase the light absorbed by a very thin absorber layer originated in the field of dye-sensitised solar cells (DSSCs). These cells use an organic dye material coated onto a wide band gap semiconductor to absorb the sunlight. The absorption of light by the dye promotes electrons to an excited state, which are then transferred to the semiconductor layer. An redox electrolyte is used in the cell to return the dye to the ground state (see figure 2.5 a). Due to the poor conductivity of these dyes, only photogenerated carriers from a single monolayer of dye are able to reach the semiconductor and contribute to the photocurrent. In 1991, O'Regan and Grätzel published a report of a solar cell using the wide band gap semiconductor titanium dioxide (TiO_2) sensitised with a layer of light absorbing organic dye [11]. The TiO_2 used in the cell was highly porous, and could therefore adsorb 780 times more dye than a flat electrode due to the high surface area [11] (see figure 2.5 b). This greatly increased the effective optical thickness of the dye compared to a planar cell. The optical thickness was further enhanced by scattering, which had been demonstrated previously when texturing amorphous silicon solar cells [24]. The optical thickness enhancement allowed a greater portion of the incident light to be absorbed by the cell, leading to a large increase in efficiency. This cell demonstrated light-to-electrical energy conversion efficiencies (η) of 7.12 % under simulated sunlight, which was a large improvement on previous DSSCs, which had efficiencies less than 1 % [11].

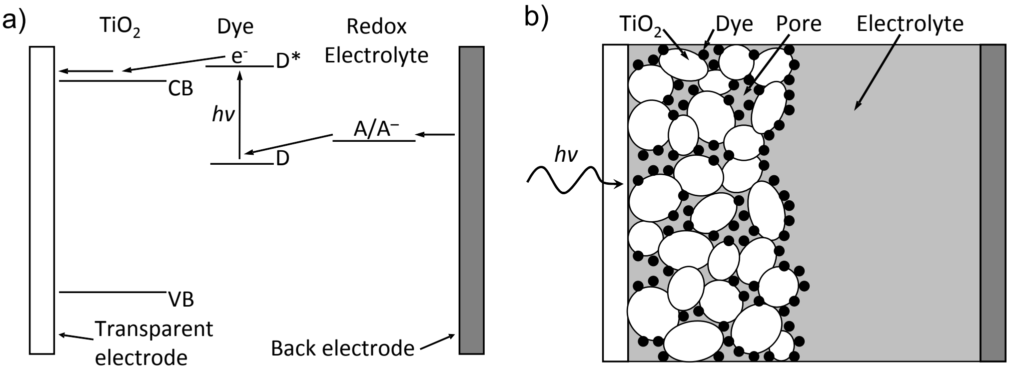

Figure 2.5: **Energy band diagram, showing operation under illumination (a) and schematic (b) of a nanostructured DSSC.** In (a) arrows show flow of electrons through cell. On absorption of a photon of energy $h\nu$ the dye is excited from the ground (D) to excited (D*) state, and transfers an excited electron to TiO_2. The dye is regenerated by an electron from the redox couple, A/A$^-$, (e.g. iodide/triiodide, I/I$_3^-$), which receives an electron from the back contact.

Despite the improvement in efficiency achieved in the DSSC by using highly porous TiO_2, there were still a number of limitations linked to stability of the liquid redox electrolyte. Problems included containment to avoid evaporation [12, 13, 25, 26] and long term stability due to the ionic conductivity, including the possibility of irreversible reactions [12]. In order to address some of these limitations, work was undertaken to replace the liquid electrolyte in the DSSCs with solid-state alternatives, while still utilising the advantages offered by a highly porous electrode.

2.2.2 Solid-state hole collectors

To replace the liquid electrolyte in a DSSC, a possible alternative was to use an appropriate p-type semiconductor. This semiconductor material had to match the valence band level for hole transfer from the dye, but not degrade it [26, 27]. In addition the material needed high transmission in the visible spectrum to allow incident light to the absorber layer (dye) [26, 27], which required a wide band gap semiconductor. In the early work on ‘solid-state DSSCs’, as they are known, copper iodide (CuI) and copper thiocyanate (CuSCN) were trialled. Their properties and deposition methods are considered below.

CuI

The first complete solid state DSSC was demonstrated in 1995 in which the electrolyte of a DSSC was replaced with the p-type semiconductor CuI [27]. CuI has a band gap of 3.1 eV [27] (transparent to wavelengths above $\sim$400 nm). It was also expected to have a band alignment to the dye and TiO_2 that was favourable for efficient charge extraction (figure 2.6). CuI was deposited from a solution in acetonitrile [27], which filled the pores, leaving CuI on drying. No high temperature or high energy steps were needed that would damage the dye. The initial TiO_2/dye/CuI cell achieved an energy conversion efficiency (η) of 0.8 % [27], and later $\eta = 1.8\,\%$ was achieved using a different dye [12]. This is significantly lower than for DSSCs using an electrolyte. In addition, the stability sought by using a solid state hole collector was not achieved; the performance of the cell degraded with time under illumination due to degradation of both the CuI film and the dye layer [27]. However, the stability of the dye was improved when UV light was filtered out of the incident radiation [27].

After this early work, CuI was used in some further solid state DSSCs. Some improvement was seen by using a buffer layer of MgO between the TiO_2 and the dye, which gave an efficiency of 2.90 % compared to 2.13 % without the buffer layer [13]. This buffer layer also limited the degradation of cell parameters: after 72 hours of illumination they were within 70 % of initial values, compared to 2 % without the buffer layer [13]. It was suggested that the MgO layer created a physical and potential barrier between the TiO_2 and CuI, suppressing the charge recombination and oxidation at the interface caused by injection of photogenerated holes from TiO_2 to either the dye or CuI [13].

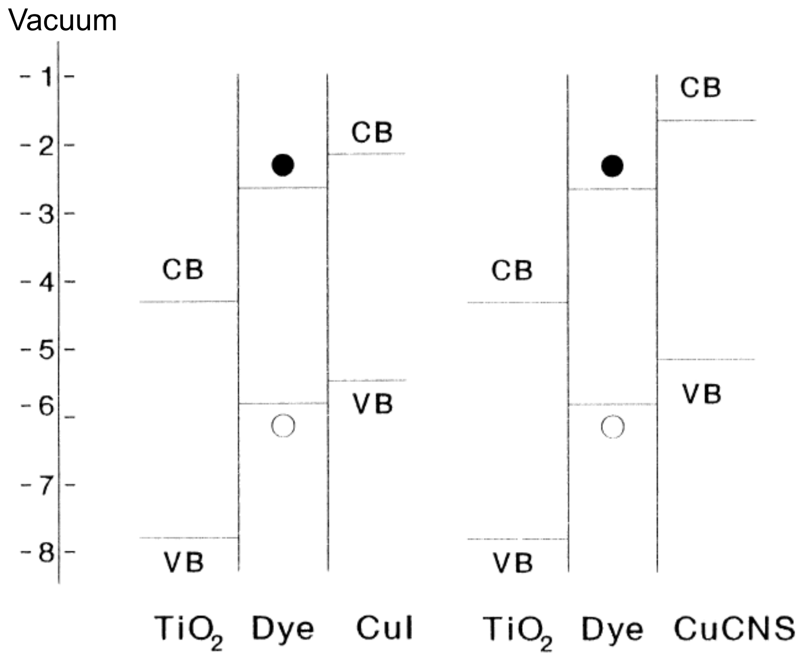

Figure 2.6: **Energy band diagram the band alignment of the TiO_2/dye/CuSCN and TiO_2/dye/CuI systems.** Shows photoexcited electrons (filled) and holes (unfilled) in the dye. Taken from figure 6 in Ref. 12.

CuSCN

CuSCN is a p-type semiconductor with a band gap of 3.6 eV [16], making it appropriate as a hole collector in a solid state DSSC. The TiO_2/CuSCN heterojunction has been studied and shown to have good rectification [28], suggesting it has potential for efficient charge separation in a solid state DSSC. The first full cell to be made using TiO_2/dye/CuSCN was produced in 1998 by O'Regan and Schwartz [29]. The dye-coated pores of the TiO_2 were filled with CuSCN using electrochemical deposition [29]. It was shown that by post treatment of the cell with KSCN and UV illumination the internal efficiency of the cell could be improved. The authors suggested that this increase in efficiency was caused by oxidation of SCN^- at the TiO_2/CuSCN interface to $(SCN)_3^-$ and/or $(SCN)_x$ (a conductive polymer, parathiocyanogen), which are able to reduce the dye more rapidly to its original state than CuSCN [29].

CuSCN has also been deposited directly from solution. This was performed by dissolving CuSCN in propyl sulphide, successively spreading the solution on the surface and allowing it to dry at 80 °C [14, 30]. The best TiO_2/dye/CuSCN cell produced by this method had $\eta = 2.1\,\%$ at $100\,\mathrm{mWcm^{-2}}$ illumination (1 sun) [14]. Again, this is lower than cells using a liquid electrolyte, but these CuSCN cells show an improvement in performance with storage. This was linked to continued evaporation of the propyl sulphide [14], which suggests that the initial drying during deposition was insufficient to allow all of the solvent to evaporate.

In 2004 both CuI and CuSCN were produced by successive ionic layer adsorption

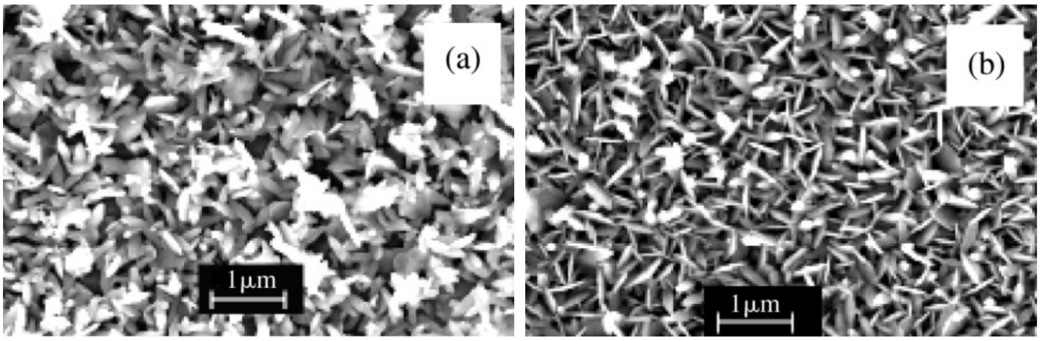

Figure 2.7: **SEM images of CuSCN produced by SILAR method.** a) on glass. b) on fluorine-doped tin oxide (FTO). Taken from figure 5 in Ref. 31.

and reaction (SILAR) methods, in which substrates are dipped in aqueous solutions containing Cu ions, followed by solutions with either iodine or thiocyanate ions [31]. These ions adhere to the substrate surface and then react with the counter ions to form the final products. SILAR was developed in 1990 by Nicolau *et al.* to deposit films of ZnS and CdS [32]. Neither CuI nor CuSCN produced by this method have been used for a complete solar cell, therefore their performance relative to different production methods cannot be compared. CuSCN produced in this way was comprised of vertical crystallites with gaps apparent between the grains in scanning electron microscope (SEM) images (see figure 2.7) [31], which could lead to pinholes when top contacts are added. Such pinholes allow short circuit current routes that reduce the overall efficiency of the cell.

Further solid state DSSCs have been reported using CuSCN and other solid state materials as hole collectors [33–36], but for the discussion to progress towards full eta solar cells it is important to look at the replacement of the light-absorbing dyes with solid-state semiconductor films, as described below.

2.2.3 Inorganic absorbers

Narrow and medium band gap (E_g) semiconductors, with E_g in the range 1–2 eV, are able to absorb a large portion of the solar spectrum (figure 2.2). They therefore have the potential to produce solar cells with the highest possible efficiencies (inset, figure 2.2). This maximum efficiency results from a balance between maximising the photocurrent and the photovoltage in the cell to achieve the maximum power point: smaller E_g semiconductors can absorb more of the solar spectrum, and therefore generate higher photocurrent, but photovoltage is always less than E_g/e, where e is the electronic charge [6]. Fulfilling the same function as molecular dyes, inorganic semiconductors have been investigated as light-sensitising materials for porous TiO_2 layers. In 1990 it was demonstrated that porous TiO_2 could be sensitised to visible light by coating with CdS [15]. CdS was grown in-situ by dipping the TiO_2 in a bath of $Cd(ClO_4)_2$, followed by a Na_2S solution, washing in water after each dip [15]. This process was repeated up to 30 times. This is essentially a SILAR method, as mentioned in section 2.2.2, although this name was not used in this study. Using this process, small particles of CdS were built up on the surface of TiO_2, which led to increased absorption of light incident on the composite [15]. The absorption onset of the CdS shifted to longer wavelengths with increasing numbers of coating cycles. This shift was ascribed to decreasing quantum confinement effects in the particles as their size increased, calculating an increase from 4 to 7 nm between 1 and 5 coating cycles [15]. An electrolytic cell was tested using a TiO_2 electrode coated with 5 cycles of CdS under monochromated light at 450 nm, giving $\eta = 6\,\%$ [15]. However, this wavelength was near to the peak in the IPCE spectrum and without characterisation under full spectrum simulated sunlight it is difficult to compare the performance to other devices. As the bulk band gap of CdS is 2.4 eV [37, 38], it is transparent to a large amount of the solar spectrum, therefore is not an ideal absorber material (see figure 2.2).

Later, successive dip coating was used to sensitise porous films with other sulphides by coating TiO_2 with nitrates of Cd, Pb, Ag, Sb and Bi, and then forming the sulphide using Na_2S [40]. It was found that only PbS and CdS coatings were stable under illumination [40]. Additionally, it was shown that the reduction in electron affinity of PbS caused by quantum confinement was required for injection of photogenerated electrons into the TiO_2 conduction band (CB); after three coatings of PbS the IPCE began to drop corresponding to the CB level of PbS dropping to lower energy than that of the TiO_2 CB [40] (see figure 2.8). This demonstrated the additional degree of flexibility that is accessible through the use of quantum confined particles: varying the particle size allows tuning of band alignment. CdS cells showed a drop in IPCE to half their original value after weeks or months of illumination, which occurred with PbS after hours. This degradation was linked to reactions with the electrolyte as well as particle growth or detachment [40].

In 1993, a porous TiO_2 film was coated with CdSe ($E_g = 1.7\,\text{eV}$) using electrochemical deposition [41]. The thickness of the deposited film was controlled between

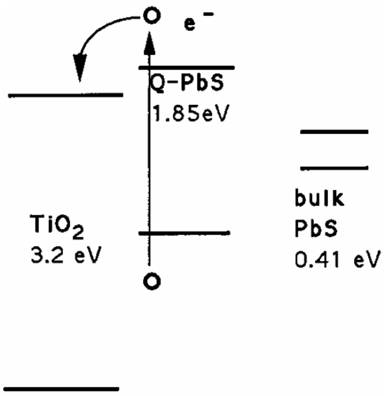

Figure 2.8: **Energy band diagram showing the change in alignment between the conduction bands of TiO_2 and PbS with and without quantum confinement effects.** From figure 1 in Ref. 39.

3 and 20 nm by varying the number of cycles in the electrochemical deposition. A blue shift was observed in the absorption onset of films <7 nm thick [41]. The onset of photocurrent in the cell changed from ~350 nm in a TiO_2 only cell, to ~700 nm in a CdSe coated cell; the coating had successfully sensitised the TiO_2 to visible light through transfer of photogenerated electrons from CdSe to TiO_2 [41]. However, the photocurrent decayed rapidly in the first 5 seconds of illumination. This was attributed to a build up of oxidised electrolyte at the interface with CdSe, limiting hole extraction and increasing recombination in CdSe [41]. Again, the short- or long-term stability of the cell suffered due to the use of a liquid electrolyte, which demonstrates why more stable, solid-state alternatives were sought as discussed in section 2.2.2.

Many other cells have been produced using inorganic absorbers coated on porous TiO_2, regenerated using an electrolyte [42–49]. However, after initial investigations into solid-state alternatives to the electrolyte or light absorbing layer in the DSSC, solar cells were produced that combined *both* modifications. These are discussed in the following sections.

2.2.4 Porous TiO_2-based eta solar cells

The first fully solid state eta solar cell was made in 1998, and comprised a 6 μm thick porous TiO_2 film coated with selenium (Se) and filled with CuSCN [16]. A 23 nm thick film of the grey, semiconducting form of Se was produced by annealing an electrochemically deposited film of Se and aging for several hours [16]. This form of Se is p-type with a band gap of 1.8 eV [16]. The Se-coated porous TiO_2 was filled and covered with CuSCN from acetonitrile solution until it protruded 10 μm above the TiO_2 [16]. The band positions of Se and CuSCN were measured by depositing these materials individually onto fluorine-doped tin oxide (FTO) glass and performing Mott-Schottky measurements (see figure 2.9). The TiO_2/Se/CuSCN solar cell had $J_{sc} = 3\,\mathrm{mAcm^{-2}}$, $V_{oc} = 600\,\mathrm{mV}$ and an efficiency of only $0.13\,\%$ at 0.8 sun, but did remain stable after prolonged illumination [16]. It was suggested that the high surface area of the Se film probably increased surface recombination, reducing the photocurrent. Also, voids in the TiO_2 film allowed contact between the Se and the FTO, which led to short-circuiting [16].

Further methods to produce eta solar cells include electrochemical deposition for CdTe [50, 51], ZnTe [51] and CuSCN [52, 53], and SILAR for CdS [50]. However, it was noted that using SILAR to coat the inside of the nanometer-sized pores of TiO_2 can lead to inhomogeneities and incomplete filling due to poor infiltration of the liquid precursors [50]. For this reason a method was developed to form the semiconductor products by reacting adsorbed precursors containing metal cations (e.g. of Cd, Cu, In) with a gas, called ion layer gas reaction (ILGAR) [50]. In this process porous TiO_2 was first dipped into a solution containing the metal chloride. Any residual solvent was then removed in an inert gas stream, and the adsorbed precursor was sulphurised with hydrogen sulphide gas, giving CdS, Cu_2S, In_2S_3 or $CuInS_2$ [50]. This process could be repeated to give controllable coating thickness, and produced a conformal and homogeneous coating of CdS [50] and $CuInS_2$ [50, 52]. ILGAR was

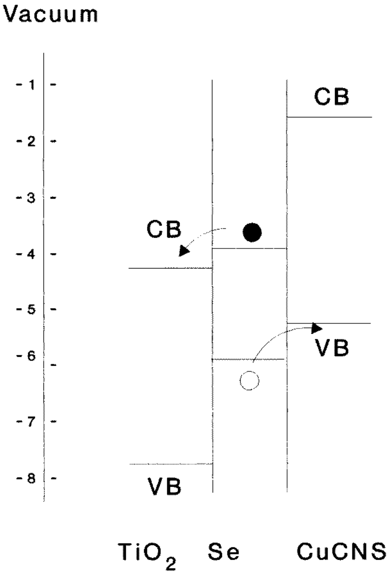

Figure 2.9: **Band alignment for the TiO_2/Se/CuSCN solar cell.** Shows transfer of photoexcited electrons and holes from Se into TiO_2 and CuSCN respectively. From figure 4 in Ref. 16.

used to coat porous TiO_2 with $CuInS_2$, which was then filled with CuSCN deposited by electrochemical deposition [53]. The J–V characteristics of this structure were tested and showed good rectification, consistent with the study discussed in section 2.2.2 [28]. This also indicates that an eta solar cell produced using this method does not suffer from the problems with short-circuiting that affected the Se-sensitised cell [16].

Following the early studies above, a number of full eta cells based on the porous TiO_2–CuSCN heterojunction and sensitised with sulphides using SILAR were produced and tested. These cells were sensitised with the sulphidic absorbers CdS [9], In_2S_3 [10], Sb_2S_3 [17] or Cu_2S [18]. The band gaps of these absorbers span almost the whole range of band gaps used in eta solar cells (see figure 2.2), and are 2.4, 2.1, 1.7-1.8, and 1.2 eV respectively. Although In_2S_3 has been used as a buffer layer with narrower band gap absorber materials deposited on top, it operates here as the sole absorber material, giving an efficiency of 2.3 % [10], which is one of the highest efficiencies currently achieved for eta cells. This demonstrates that as eta cells are currently operating well below maximum theoretical efficiency for a single band gap cell (figure 2.2 inset) they do not necessarily require the use of optimal band gap absorbers to achieve higher efficiencies. The construction of this cell also demonstrated the significance of the thickness of the TiO_2 layer for optimising the cell; it was found that the effective optical thickness of the In_2S_3 layer could be increased by increasing the thickness of the porous TiO_2 layer while using the same number of SILAR coatings [10]. This led to an increase in J_{sc} of the solar cells, but only up to ~200–300 nm of TiO_2, after which no further increase was observed. The processing of materials also has been shown to have an impact on the performance: in the CdS-sensitised cell both chemical bath deposition (CBD) and SILAR were used to deposit CdS, with CBD-produced cells showing less light absorption and poorer cell performance [9].

In both the Sb_2S_3 and Cu_2S-sensitised cells In_2S_3 was used as a buffer layer (sometimes referred to as $In(OH)_xS_y$ due to unknown variations of stoichiometry and composition of actual films produced). The use of these buffer layers improved both the performance [18] and the stability [17] of these cells. In the case of Sb_2S_3, it was noted that the In_2S_3 layer prevented oxidation of the Sb_2S_3 occurring when in contact with TiO_2 [9]. This is similar to buffer layers discussed in section 2.2.2, which prevented the transfer of high-energy, photogenerated holes from TiO_2 into the absorber material. It was found that under continuous illumination, efficiency of the Sb_2S_3 cells dropped by no more than 10 %, which was regained by standing in the dark for a few hours [17]. This indicates that with the right combination of materials and processing, such solid state eta cells can be very stable under operation.

An additional processing step that was added to some of these cells was to soak the coated TiO_2 and aqueous solution of either LiSCN [9, 17, 18] or KSCN [17], before filling with CuSCN from propyl sulphide solution. For the Sb_2S_3-sensitised cell this treatment led to an improvement of J_{sc}, V_{oc} and FF and reduced the resistance of the cell. This effect was greater for KSCN-treatment than LiSCN [17]. Post-treatment of CuSCN with KSCN was mentioned in section 2.2.2, and improvements were attributed to possible doping with SCN^- ions, increasing the conductivity of the CuSCN. Pre-treatment with LiSCN or KSCN in these cells could be explained by a similar mechanism.

This set of cells with sulphidic absorbers is useful for understanding the impact that the absorber layer, TiO_2 film and processing variations have on the efficiency of the cells. The Cu_2S-sensitised cell has the lowest efficiency of 0.06 % [18]. The exact reason for this low efficiency was not identified, but the authors suggested that there were a lot of losses at the TiO_2 interface in this cell, despite attempts to passivate with an In_2S_3 buffer layer [18]. The Sb_2S_3-sensitised cell had the highest efficiency of 3.37 % [17], which could result from the particular combination of materials in this device, but also could be because a large amount of optimisation of film thicknesses and processing was performed in this study. The large difference in photo-harvesting ability between these cells can be seen when comparing the IPCE, or external quantum efficiency (EQE), which is shown in figure 2.10.

Other examples of porous TiO_2-based eta cells also utilised chemical methods to deposit the absorber layer, but used the conducting polymer polystyrene sulfonic acid-doped poly(3,4- ethylenedioxythiophene) (PEDOT:PSS) as the hole collecting layer. All of these cells used a porous TiO_2 layer coated with an $In(OH)_xS_y$ buffer layer and PbS (or $Pb(OH)_xS_y$) absorber produced by either CBD [19, 54] or SILAR [55]. PEDOT:PSS was deposited into the coated pores of TiO_2 by spin coating from aqueous solution [19, 54, 55]. The band gap of the $In(OH)_xS_y$ buffer layer varied between 2.4 and 3.4 eV depending on the pH of the CBD solution [19]; as the composition became more S-rich or more O-rich the band gap was closer to that of In_2S_3 (2.1 eV), or In_2O_3 (3.7 eV) [19]. $In(OH)_xS_y$ in tested cells had a band gap of 2.4 eV [19]. The $Pb(OH)_xS_y$ that was deposited had a band gap of 0.85 eV, larger than bulk PbS (0.37 eV), attributed

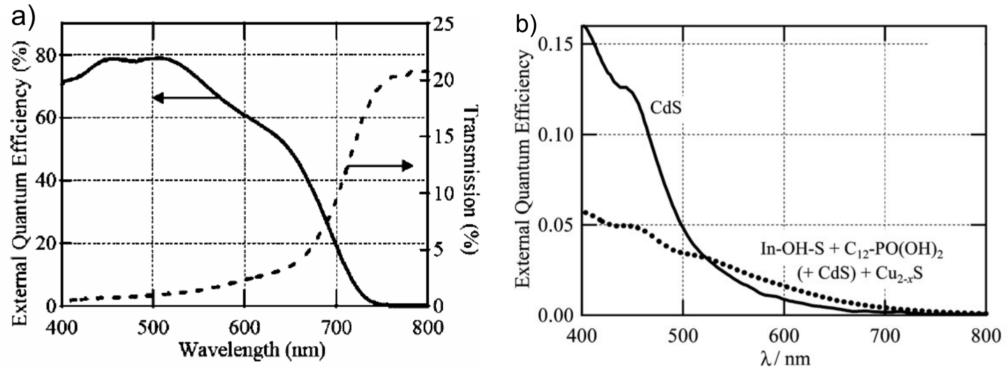

Figure 2.10: **a) EQE and transmission spectra of a TiO_2/In(OH)S/Sb_2S_3/CuSCN solar cell. b) EQE spectra of TiO_2/CdS/CuSCN and TiO_2/In(OH)S/Cu_2S/CuSCN solar cells.** a) Absorption onset and photocurrent generation onset begins at ∼750 nm, due to photon absorption by the Sb_2S_3 layer. From figure 1 in Ref. 17. b) Solid line is for CdS-sensitised cell, and dotted line is for Cu_2S-sensitised cell using In(OH)$_x$S$_y$ and dodecylphosphonate buffer layers. From figure 3 in Ref. 18.

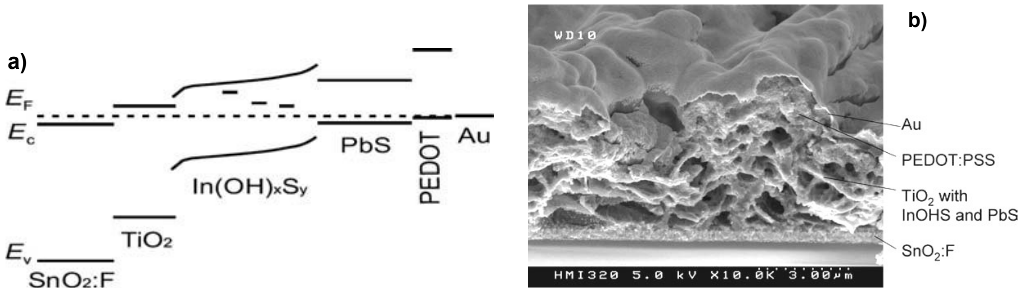

Figure 2.11: **Band diagram (a) and SEM image (b) of a TiO_2/In(OH)$_x$S$_y$/Pb(OH)$_x$S$_y$/PEDOT:PSS solar cell structure.** From figure 6 in Ref. [54] (a) and figure 4 in Ref. [19] (b).

to the same alloying process as for In(OH)$_x$S$_y$ [19]. It was found that the In(OH)$_x$S$_y$, not the Pb(OH)$_x$S$_y$, was generating the photocurrent in the cell. A later study found that the low contribution by Pb(OH)$_x$S$_y$ was due to high charge recombination at the In(OH)$_x$S$_y$/Pb(OH)$_x$S$_y$ interface because of an barrier for electrons (see figure 2.11 a) [54]. However, the solar cell performance was severely degraded if the Pb(OH)$_x$S$_y$ layer was removed [55]. The performance of the cell was also limited because it was not completely opaque, therefore not all of the incident light was absorbed. Also, the absorber layers did not completely fill the TiO_2 pores (see figure 2.11 b) [19, 55]. The authors identified that these structural issues must be addressed in order to improve the performance of the cells [19, 55].

Following early porous TiO_2 solar cells sensitised with inorganic absorbers, cells were reported using inorganic nanoparticles, or quantum dots (QDs) as absorber materials. QDs are promising absorbers for eta solar cells, because the absorption coefficient and band gap increases as the particles are made smaller [42]. Many cells used electrolytes as hole collectors, and can be thought of as similar to a DSSC, with QDs replacing the dye. However, in some cells the electrolyte was replaced with a solid state material. The first such cell was produced by Plass *et al.* in 2002, and used the hole conductor 2,2',7,7'-tetrakis(N,N-di-p-methoxyphenylamine)-9,9'-spirobifluorene (spiro-OMeTAD) [56]. Porous TiO_2 was sensitised using PbS QDs grown *in-situ* on the surface by dipping it into a lead nitrate solution, followed by a Na_2S solution [56]. This process was repeated a number of times, producing different sized QDs (6 nm after 7 cycles). PbS absorption was blue shifted due to quantum confinement, which reduced with increasing dipping cycles [56]. Plass *et al.* note that the change in position of the PbS conduction band is beneficial to electron injection into TiO_2 [56] (discussed in section 2.2.3).

In 2009, Lee *et al.* also produced a PbS QD-sensitised porous TiO_2 solar cell using spiro-OMeTAD as a hole collector [20]. They also coated the TiO_2 with PbS using lead nitrate and Na_2S solutions, but in methanol rather than water [20]. This produced superior performance compared to aqueous solutions, attributed to better wetting and faster drying [20]. The coverage of TiO_2 by PbS was found to be 30–40 %. Attempts to improve efficiency by increasing coverage were not successful as subsequent reduction in quantum confinement reduced the efficiency of electron transfer [20].

2.2.5 Zinc oxide nanorod-based solar cells

ZnO nanorods have been used in both DSSCs and eta solar cells instead of porous TiO_2 layers to create a highly structured substrate. The motivation behind this substitution was to enhance the efficiency of charge transport: ZnO nanorods offer a direct conduction path to the contact [57] and have high electron mobility (200 cm^2/Vs for ZnO compared to 10 cm^2/Vs for TiO_2 [33]). The open structure of the ZnO nanorods allows flexibility for coating procedures as the precursors can readily reach the entire surface [58]. ZnO nanorods also produce an increase in optical path through light scattering similarly to porous TiO_2 [59]. Further details of the properties of ZnO are given in section 2.3.

Dye-based absorbers

A small number of groups have produced DSSCs based on ZnO nanostructures. Studies have suggested that charge injection from dye to ZnO can occur at a rate comparable to dye-TiO_2 injection rates [61], making it a potentially successful substitution. However, when using ZnO nanorods or nanowires for DSSCs the limited surface area compared to porous TiO_2 has proved an issue, as lower dye loading can lead to poor light absorption [60, 62]. Therefore, workers have attempted to adapt the ZnO nanorods to increase the surface area. Once such adaptation was to add secondary rods to the side of the nanorods (see figure 2.12) [60]. These rods were grown by metal-organic chemical vapour deposition (MOCVD), nucleated on a thin compact ZnO film [60]. Despite this attempt at surface area enhancement, a light-harvesting efficiency

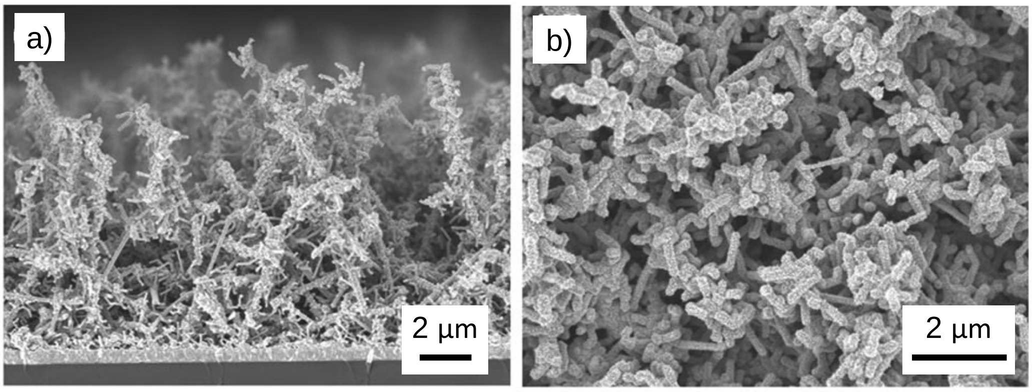

Figure 2.12: **SEM images of ZnO nanorods produced by MOCVD with secondary rods growing from the surface.** a) Side view. b) Top down. Taken from figure 2 in Ref. 60.

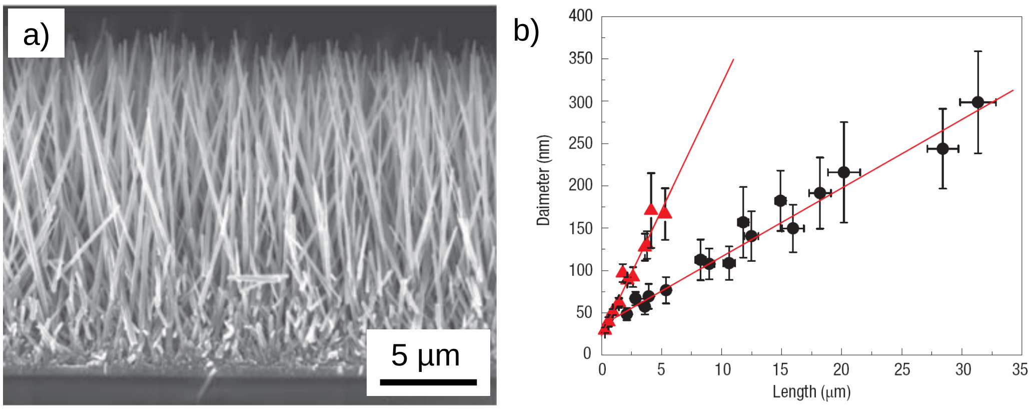

Figure 2.13: **Effect of adding PEI to the chemical synthesis of ZnO nanorods.** a) SEM image of elongated ZnO nanorods produced by chemical bath method with PEI added. b) Plot showing difference in nanorod length versus diameter without (triangles) and with (circles) PEI added to the synthesis. Taken from figure 1 in Ref. 62.

(LHE) of only 8 % at the dye absorption maximum was achieved, meaning that over 90 % of incident light was passing through the cell.

Better results for a ZnO nanorod DSSC were achieved by Law *et al.* when increasing nanorod surface area to increase dye loading and therefore light absorption [62]. In this study, nanorods were grown in a chemical bath of zinc nitrate and hexamethylenetetramine (HMT), which was heated at 92 °C for 2.5 hours, repeating the growth to produce longer nanorods [62]. With these repeated growths, the nanorod width increased as well as the length, and so the surface area did not increase sufficiently with increased growth stages to absorb enough dye. The growth method was therefore adapted by adding poly(ethylenimine) (PEI) to the synthesis, which led to growth of much more elongated rods over time with a roughness factor of up to 200, compared to 20 without PEI (see figure 2.13) [62]. This surface area enhancement was successful and an EQE of 40 % at the dye absorption peak was achieved [62], compared to only 6 % in the ZnO nanorod DSSC mentioned above [60]. With this increased light absorption achieved using higher aspect ratio nanorods an efficiency of 1.5 % was recorded [62]. However, this is still below the efficiency of porous TiO_2-based DSSCs, which have achieve efficiencies closer to 10 %. Although an improvement on previous nanorods, the surface roughness of 200 is still below that of 780 achieved in the Grätzel cell [11]. This demonstrates that despite efforts to increase the surface enhancement, the low surface area of ZnO nanorods compared to porous TiO_2 still limits the efficiency of ZnO-based devices, despite the superior charge collection capabilities of ZnO nanorods.

Apart from elongating or adapting the ZnO nanorods to increase surface area, another possibility for increasing the light absorption in ZnO nanorod-based cells is to increase the thickness of the absorber layer. Although this is not possible with dye-based absorbers due to their poor charge transport properties, it is a possibility for inorganic semiconductor absorbers. Examples of cells based on ZnO nanorods coated with such absorbers are explored in the next section.

Inorganic absorbers

The first demonstration of a semiconductor coating on ZnO nanorods was made in 2000 by depositing amorphous silicon (a-Si) onto the rods using chemical vapour deposition (CVD) [57]. ZnO nanorods in this study were deposited by electrochemical deposition $\sim 2\,\mu$m long and 100–200 nm across (see figure 2.14 a). The a-Si coating was uniform and conformal (figure 2.14 b) [57]. It was noted that ZnO nanorods are more easily coated than porous TiO_2 due to their open morphology [57]. No performance results from ZnO/a-Si solar cells were given.

In 2005 solar cells were produced based on both CdTe and CdSe-coated ZnO nanorods [21, 22, 63]. In these studies ZnO nanorods were deposited electrochemically, as were the CdSe films (see figure 2.15) [22, 63]. CdTe was deposited by metal-organic chemical vapour deposition (MOCVD) [21], and CuSCN was deposited

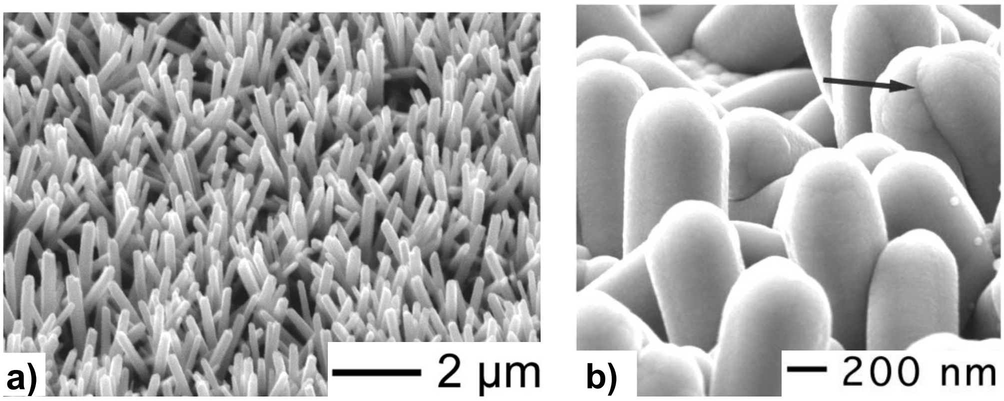

Figure 2.14: **a) ZnO nanorods grown by electrochemical deposition, and b) coated with a-Si by chemical vapour deposition.** Arrow indicates joining of coating between two rods. From figures 1 (a) and 3 (b) in Ref. 57.

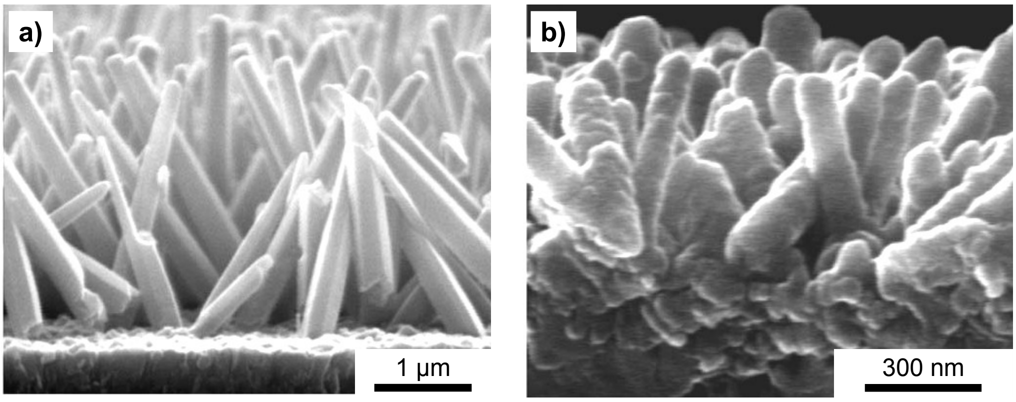

Figure 2.15: **Uncoated (a) and CdSe-coated (b) ZnO nanorods grown by electrochemical deposition.** From figures 3 (a) and 6 (b) in Ref. 22.

from propyl sulfide solution. CdTe and CdSe were chosen as their narrower band gaps enhanced absorption in the visible region, and band alignment was predicted to favour charge extraction (see figure 2.16). The best cells used a CdSe absorber layer, which was annealed after deposition to improve crystallinity and reduce trap states [22]. This cell gave $J_{sc} = 3.9\,\mathrm{mAcm^{-2}}$, $V_{oc} = 490\,\mathrm{mV}$, $FF = 0.32$ and $\eta = 2.3\,\%$ at ~1/3 sun after 1 week of storage [22]. However the efficiency dropped back to 1.5 % after further months of storage [22]. It was found that vacuum storage enhanced the performance of the cell, attributed to continued evaporation of the propyl sulfide [22], as found previously with CuSCN deposited by this method (section 2.2.2). The performance of CdTe-based cells was poorer than CdSe-based cells, with $J_{sc} = 0.03\,\mathrm{mAcm^{-2}}$, $V_{oc} = 200\,\mathrm{mV}$ and $FF = 0.28$ at ~1/3 sun [21]. The authors suggested that low J_{sc} and FF resulted from the small difference between the predicted conduction band levels of ZnO and CdTe (figure 2.16 a) [21].

Eta cells have also been produced by coating ZnO nanorods with 10–75 nm thick In_2S_3 absorber layers using ILGAR (see section 2.2.4) [7, 58, 64–66]. 1.5 μm long nanorods were produced by placing substrates in a chemical bath of NaOH and zinc nitrate at 80 °C for 90 minutes. To complete the cells the coated nanorods were filled with CuSCN from propyl sulfide solution. A cross section of this solar cell can be seen in figure 2.17 a. ILGAR produced a conformal coating of In_2S_3 on ZnO nanorods with controllable thickness (see figure 2.17 b–d) [7]. When the local thickness of the In_2S_3 layer was varied from 10 to 75 nm, J_{sc} decreased and V_{oc} increased (see figure 2.18 a) [7]. It was concluded that the diffusion length of carriers in the In_2S_3 layer was ~10 nm. Therefore, increasing the local thickness led to increased recombination and the observed reduction in J_{sc} [7]. Conversely, the increase in V_{oc} with In_2S_3 thickness was due to a reduction in tunnelling recombination through the absorber layer [7]. The optimum solar cell performance was achieved with an In_2S_3 thickness of 25 nm [7]. The influence of ZnO nanorod length on the performance of this cell structure was also studied [58]. The rod length was varied between 0 (planar cell) and 3 μm by varying the deposition time between 0 and 150 min, while the local In_2S_3 thickness

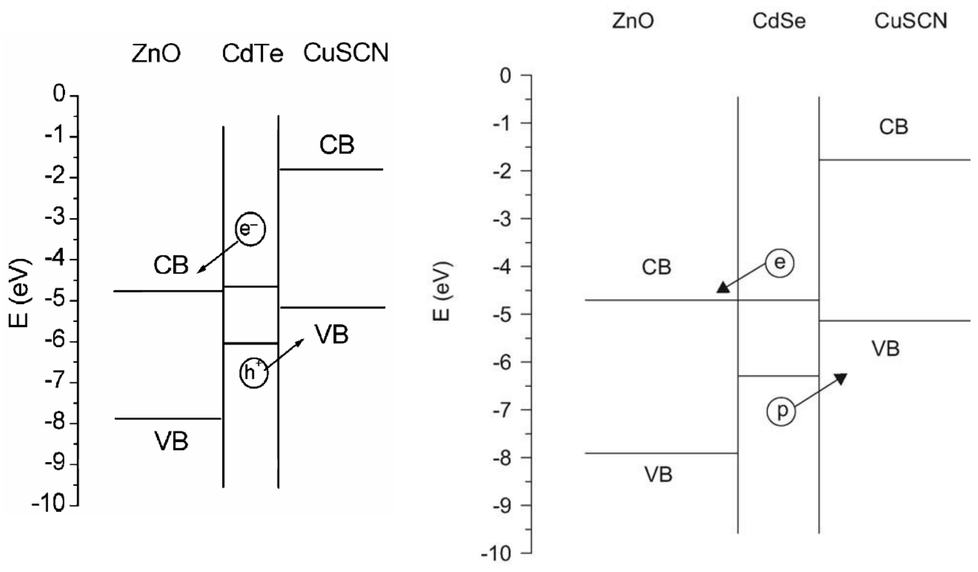

Figure 2.16: **Predicted band alignment for ZnO/CdTe/CuSCN and ZnO/CdSe/CuSCN.** From figure 1 in Ref. 21 and figure 2 in Ref. 22.

was maintained at 20 nm [58]. As the rod length increased it was found that J_{sc} increased while V_{oc} and FF decreased [58]. The decrease in V_{oc} and FF resulted from a drop in the shunt resistance, attributed to an increase in surface recombination due to increased surface area of the longer rods [58]. The optimum rod length was found to be 800 nm [58]. Further studies of ZnO nanorod/In_2S_3/CuSCN solar cells focussed on annealing the complete structure, and the effect on the In_2S_3/CuSCN interface. It was found that annealing the cell at 200 °C for 2 min produced optimal improvement in J_{sc}, V_{oc} and FF [65]. Annealing the In_2S_3/CuSCN layers caused Cu to diffuse towards the interface where it reacted with In_2S_3 giving additional sub-band gap states and a shift in the In_2S_3 band gap (see figure 2.18 b and c) [65, 66]. This reduced recombination, increasing V_{oc} [66], and shifted absorption to longer wavelengths, increasing J_{sc} [65]. The best performing ZnO/In_2S_3/CuSCN solar cell gave $J_{sc} = 10.5\,\mathrm{mAcm^{-2}}$, $V_{oc} = 570\,\mathrm{mV}$, $FF = 0.56$ and $\eta = 3.4\,\%$ at 1 sun [7].

ZnO nanorod/semiconductor/polymer solar cells were made using a novel coating method to deposit CdSe films onto ZnO nanorods [23]. The films were produced by drop-casting solutions of octadecyl amine-capped CdSe QDs in toluene onto electrochemically deposited ZnO nanorods [23]. Once deposited, the QD-coated nanorods were annealed in an air-$CdCl_2$ mix at 380 °C to form a continuous film of CdSe on the ZnO [23]. Annealing led to a large increase in the quantum efficiency of the cell and a red-shift in the absorption onset due to loss of quantum confinement (see figure 2.19) [23]. The solar cell was completed by filling the rods with the conductive polymer poly(2-methoxy-5-[2'-ethyl-hexyloxy]-1,4-phenylene vinylene) (MEH-PPV) [23]. The best ZnO nanorod/CdSe/MEH-PPV cell gave $J_{sc} = 5\,\mathrm{mAcm^{-2}}$, $V_{oc} = 500\,\mathrm{mV}$, and $\eta = 0.9\,\%$ at 0.85 sun [23]. Replacement of MEH-PPV with poly(3-hexylthiophene) (P3HT) gave an efficiency of 1.5 % [23].

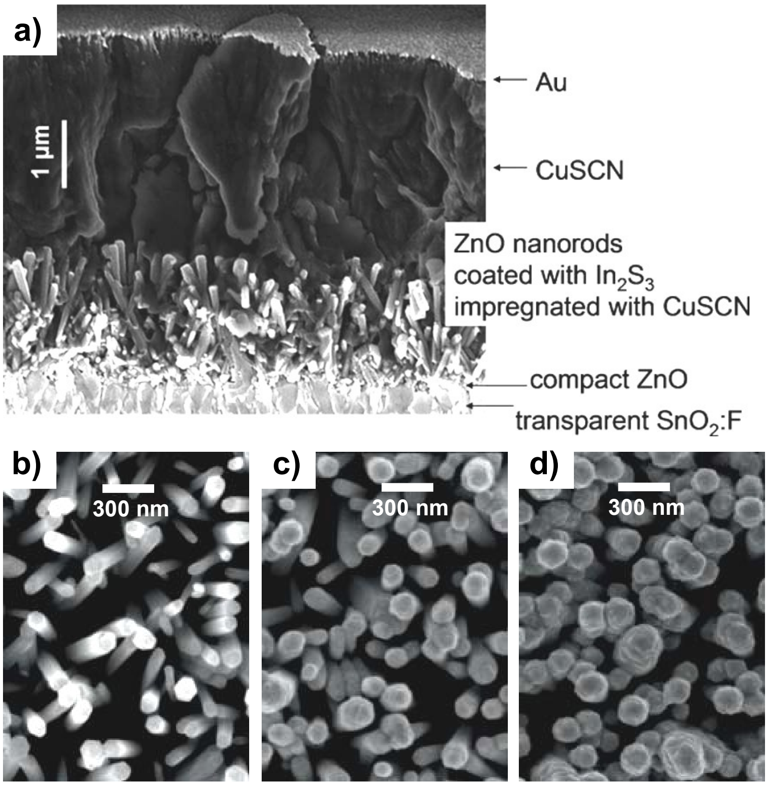

Figure 2.17: **SEM images of the cross-section of a ZnO nanorod/In_2S_3/CuSCN solar cell (a), and top-view of ZnO nanorods with 0 (b) 15 (c) and 45 nm (d) of In_2S_3 coating.** From figure 1 (a) in Ref. 64 and figure 1 in Ref. 7 (b–d).

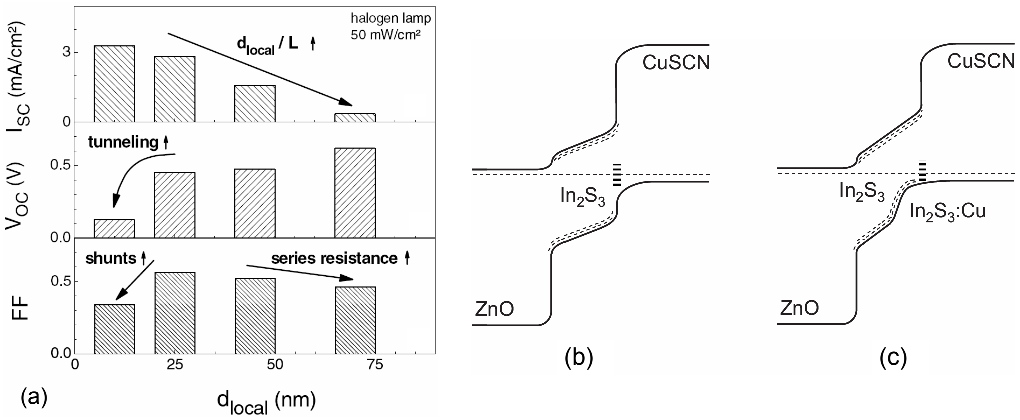

Figure 2.18: **(a) change in J_{sc}, V_{oc} and FF in the ZnO nanorod/In_2S_3/CuSCN solar cell as local thickness of In_2S_3 layer is increased. (b) and (c) proposed band structure of the In_2S_3–CuSCN interface before (b) and after (c) annealing.** From figure 3 in Ref. 7 (a) and figure 10 in Ref. 66 (b) and (c).

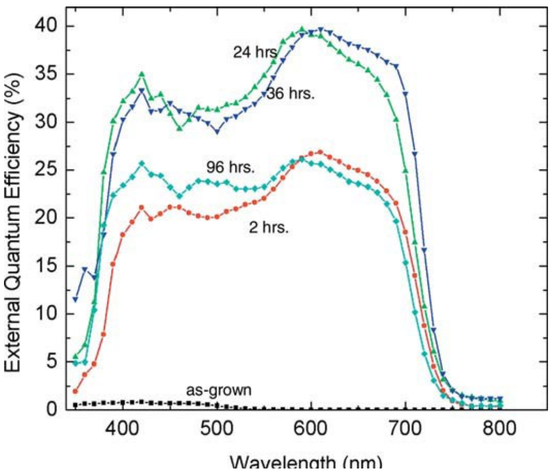

Figure 2.19: **Increase in quantum efficiency of the ZnO nanorod/CdSe/MEH-PPV solar cell with different annealing times in air/$CdCl_2$ at 380 °C.** From figure 3 in Ref. 23.

Nanoparticle absorbers

Solar cells have been produced by coating ZnO nanorods with a variety of semiconductor nanoparticles to sensitise them to visible light. Nanoparticles used include CdSe [67, 68], CdTe [69], CdS [38, 70] and $CuInS_2$ [71]. These cells have been completed or tested in electrochemical apparatus, or using electrolytes similar to DSSCs and therefore cannot be considered as eta solar cells. However, the use of nanoparticles to sensitise ZnO nanorods is important for the development of ZnO nanorod solar cells, and details of these cells are given below.

Some nanoparticle coatings have been made by immersing nanorod-coated substrates into a chemical bath of nanoparticle precursors and heating to induce nucleation of the nanoparticles directly on the surface [68, 70]. Although the structures grown in these studies are referred to as nanoparticles or nanocrystals, they are too large to display quantum confinement. These coatings are more accurately considered incomplete thin-film coatings, and in the case of CdSe-coated nanorods, the coatings are annealed after deposition at 400 °C to produce a polycrystalline thin film layer [68]. The best performing cell was obtained with a complete covering of the nanorods that appears approximately 100 nm thick, giving $\eta = 0.34\,\%$ at 1 sun [68].

Other studies using semiconductor nanoparticles to sensitise ZnO nanorods have retained the quantum confinement of the nanoparticles, thus can be referred to as quantum dots (QDs). These QDs have been grown before deposition on the nanorods, using capping molecules or shells to improve stability and prevent agglomeration in solution. The QDs have then been attached to the nanorods by soaking nanorod-coated substrates in the QD solution for up to several days [67, 69, 71]. Using this method led to a limited coverage of QDs in the case of CdSe [67] and $CuInS_2$ [71], forming less than a monolayer on the surface. These cells thus suffer similarly to ZnO DSSCs as the lower surface area of ZnO nanorods compared to porous TiO_2 means that a monolayer of absorber cannot absorb sufficient incident light, and the efficiencies of these cells remain below 1 %. For example, the CdSe nanoparticle-sensitised cell had a LHE of only around 30 % at the CdSe nanoparticle absorption peak [67], which means around 70 % if the incident light at this wavelength was passing through the cell. As a consequence the maximum EQE was ∼20 % [67] compared to ∼90 % for a cell using a 25 nm thick film of In_2S_3 as the absorber [7]. In the case of CdTe nanoparticle-sensitised nanorods, soaking in the nanoparticle solution produced a much thicker coating, estimated to be 10 nm thick [69]. The particles appeared to retain quantum confinement as the photocurrent onset occurs around 550 nm [69]: well above the bulk band gap of CdTe, which is 1.5 eV [72] (≅ 830 nm). The reason for the increased coverage in this case was not investigated, and efficiency was not given so the impact of this increased coverage cannot be compared with other cells. However, it was shown that by increasing the nanoparticle coating thickness the incident light absorption was increased [69], which should lead to increased photocurrent in the cell compared to those only using a monolayer of nanoparticles.

It has thus been shown that the efficiency of nanoparticle-coated ZnO nanorod solar cells is often limited by insufficient light absorption resulting from low nanoparticle coverage. Although higher nanoparticle coverage has been achieved in one case, the reasons for this enhancement of coverage are not understood. It is for this reason that the layer-by-layer (LbL) method for deposition of semiconductor nanoparticles is investigated in this project. It is hoped that by building up many layers of nanoparticles the LHE of the cell can be enhanced leading to improved photovoltaic performance. More details of the LbL process and its potential benefit for the coating of a nanoparticle absorber layer are given in section 2.4.1.

2.3 Zinc oxide

ZnO is a semiconductor with a direct band gap of 3.2–3.4 eV [73–75]. It has a wurzite structure, strong piezoelectric and pyroelectric properties [76], and intrinsic n-type conductivity due to native defects [77]. Previously, it has found applications in piezoelectric transducers, varistors, actuators and phosphors [75, 76]. It has also been used as a transparent conductor due to a doped resistivity as low as 10^{-4}–10^{-3} Ωcm [78]. In recent years, ZnO has received increased interest for a variety of device applications. These include optoelectronic applications, as ZnO has a high exciton binding energy of 60 meV, which allows efficient room temperature excitonic emission [76]. More recently, the variety of nanoscale morphologies demonstrated for ZnO [76] have led to further development of device designs, including suggested applications in transparent electronics and nanoscale UV optoelectronics [79]. The most common morphology studied is the 1D structure, which ZnO forms due to preferential growth along its c-axis, leading to elongated hexagonal nanorods or wires. This morphology has been achieved through vapour-phase, electrochemical, and aqueous solution-based methods [80], which are explored below.

2.3.1 Zinc oxide nanorod growth methods

Numerous reviews have considered the growth methods and mechanisms of ZnO nanorods, nanowires and other nanostructures, including Refs. 74, 80 and 81. These can be consulted for extensive detail and references on the growth of these structures. The sections below give a brief summary of the main growth methods, focussing on techniques that are most relevant to this thesis.

Vapour-phase growth

The most common method for the vapour-phase growth of ZnO nanorods and wires is chemical vapour deposition. In this method vapour species are generated by the evaporation and/or chemical reduction of precursors in a reactor such as a tube furnace. These gaseous species are then transported to a solid substrate which is at a lower temperature than the precursors where they nucleate [81], generally by the vapour-liquid-solid (VLS) or vapour-solid (VS) mechanism. The VLS mechanism requires the substrate surface to be coated with a metal catalyst, generally Au in the case of ZnO growth [74]. The vapourised ZnO dissolves into the liquid Au droplets until they become supersaturated, at which point the ZnO nucleates and begins to grow outwards [74]. By control of the initial metal particle size [80], oxygen partial pressure, and overall gas pressure [74] the nucleation of ZnO is controlled to form nanostructures of the desired dimensions. VS mechanisms do not use a metal catalyst. Instead the substrate is coated with a ZnO thin film using a method such as pulsed-laser deposition (PLD). In the VS mechanism the gaseous precursors nucleate directly onto this seed layer, producing ZnO nanorods or wires through controlled temperatures and gas pressures. This method may be preferable for device applications, as it does not leave metal impurities in, or on, the tip of the nanowires [82].

VS growth of ZnO nanorods and wires often uses the carbothermal reduction of precursors to produce gaseous Zn, which is then transported to the substrate where it reacts to form the ZnO nanostructures [81]. For this method, a 1:1 mix of commercial ZnO powder and graphite powder is used as the precursor [74, 82–85], which is heated to between 700 and 900 °C [82–85]. A gas flow of either argon [83, 84], dry air [82] or nitrogen containing trace oxygen [85] is passed through the furnace. Si [82–84], sapphire [85] or porous Al_2O_3 [86] substrates, coated with ZnO thin films by PLD, have been used. The substrate is placed downstream at a slightly lower temperature point. Depending on the conditions and position of the substrate, ZnO nanowires with a good density (average spacing of only a few nanowire diameters), and excellent alignment (almost all 90 °) can be produced. Other VS mechanisms have nucleated ZnO nanorods onto ZnO thin film-coated substrates, but not used the carbothermal method. In these cases the precursor used is Zn powder [87], which can also be mixed with dopants such as Al powder to produce doped nanorods [88]. These reactions have been performed at temperatures of 700–750 °C, using a gas flow of argon [87] or nitrogen-oxygen mixture [88]. An example of ZnO nanorods grown by the VS method are shown in figure 2.20.

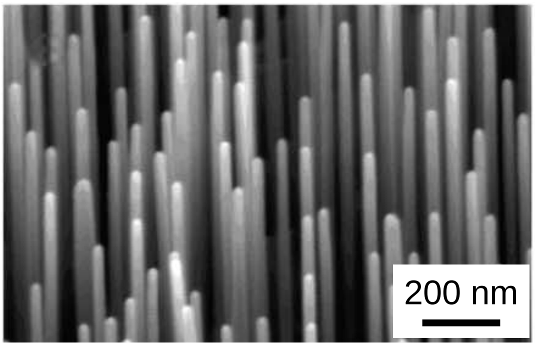

Figure 2.20: **ZnO nanorods grown by the vapour-solid mechanism.** Rods grown by the carbothermal reduction of ZnO using graphite, nucleated on Si substrates coated in a ZnO thin film by PLD. Taken from figure 3 in Ref. 84.

Nanostructures grown by these methods have not been applied widely for use in photovoltaic devices, despite sometimes achieving high aspect ratios and well-aligned growth. This is most likely because the majority of growth is performed on crystalline substrates such as sapphire or silicon, seeded with either Au catalysts of ZnO thin films. Relatively little work has been undertaken to grow ZnO nanorods on transparent conductors such as FTO or ITO, which would be suitable for photovoltaic applications.

Electrochemical deposition

ZnO nanorods have also been grown by electrochemical deposition [21, 22, 57, 63, 89, 90]. In this process a substrate is placed into a chemical bath as one electrode of a three electrode arrangement [57]. A potential is then applied between the electrodes and ZnO grows on the substrate. For the growth of ZnO nanorods a solution of 0.5 mM $ZnCl_2$ and 0.1 M KCl in water is generally used [21, 22, 63, 89, 90]. The bath is heated to 80 °C, and a potential of -1 V versus the saturated calomel electrode is applied, using Pt as a counter electrode. Oxygen is bubbled through the solution to keep it saturated. The time taken for the reaction to be completed has not been provided in the literature. Using this process ZnO nanorods of $\sim 2\,\mu$m in length with an average diameter of 150 nm are produced, and can be seen in figure 2.15 (section 2.2.5). These nanorods therefore have an aspect ratio of approximately 15, and grow at an angle of at least 45 ° from the substrate. Such electrochemically deposited nanorods have been coated in narrow band gap semiconductors and used for photovoltaic cells, as described in section 2.2.5.

The process for formation of ZnO nanorods on the surface has been described as occurring in two steps [90]. First, oxygen is electro-reduced at the surface of the substrate, increasing the OH^- concentration. This then reacts with zinc ions to deposit either amorphous $Zn(OH)_2$ or crystalline ZnO on the surface, and the conditions are controlled to produce the latter.

Chemical bath deposition

A variety of chemical bath methods have been used to grow ZnO nanostructures, using varied precursors and conditions. Here, chemical bath deposition (CBD) should be distinguished from hydrothermal growth. In hydrothermal growth the aqueous precursor solution is treated with both heat and pressure, usually by heating in a sealed vessel to above the solvent boiling point. Whereas in CBD heat but not pressure is applied, generally because the reaction is not carried out in a sealed vessel and the temperature is kept below the boiling point of the solvent. ZnO nanorod aqueous chemical synthesis methods do not use hydrothermal conditions as the temperature is always kept below 100 °C.

The CBD methods for ZnO nanorod synthesis can be separated into two main categories: thermal decomposition of zinc precursors using a ligand to control morphology, and thermal decomposition of zinc precursors using a base to control pH and produce nanorods. The former method is dominated by the thermal decomposition of zinc nitrate using hexamethylenetetramine (HMT) to control the morphology [62, 67, 71, 79, 91–100]. In this method a substrate seeded with a thin layer of ZnO is placed face down into a solution of zinc nitrate and HMT. Concentration of reactants is generally equimolar, and varies between 0.01 and 0.1 M. Some later studies use a slightly lower concentration of zinc nitrate (0.016 M) than HMT (0.025 M) [67, 71]. This solution is then heated to between 75 and 90 °C and kept at this temperature for between 0.5 and 12 hours. Upon heating, both homogeneous (in the solution) and heterogeneous (on the surface) precipitation of ZnO nanorods occurs, and at some stage, depending on the concentration and temperature, the reactants are depleted and the reaction ceases. For a 0.025 M equimolar solution this occurs after about 2.5 hours at 90 °C [62]. The size of the nanorods produced depends mainly on the initial concentration of the reactants, and varies between approximately $3 \times 1\ \mu$m at 0.1 M [94], to $1\ \mu$m × 100 nm at 0.01 M. However, both the length and the diameter of the rods can be increased by placing the substrate in fresh chemical bath solutions when the reactants have been depleted [62, 91]. A plot showing the increase in both length and diameter of nanorods grown in a 0.025 M solution at 90 °C can be seen in figure 2.21, along with an image of rods produced after 1.5 hours. As described in section 2.2.5, increasing the reaction time increases the length and diameter of the rods at similar rates, so that little increase in aspect ratio is achieved, which remains around 10. It is for this reason that Law *et al.* added PEI to the reaction to preferentially increase the length of the rods to achieve aspect ratios of up to 200 (see section 2.2.5 and figure 2.13) [62]. It is also possible that using a lower concentration of zinc nitrate than HMT can achieve higher aspect ratios of around 100 [67, 71], but direct comparison of rods grown using equimolar and non equimolar conditions is required to confirm this.

ZnO nanorods are produced in this reaction by the controlled precipitation of ZnO from Zn precursors via hydrolysis [95]. Although HMT can act as a ligand, it is reportedly a poor ligand for Zn, and its main role is to provide a controlled supply of hydroxide ions [95]. This occurs because HMT gradually decomposes to form

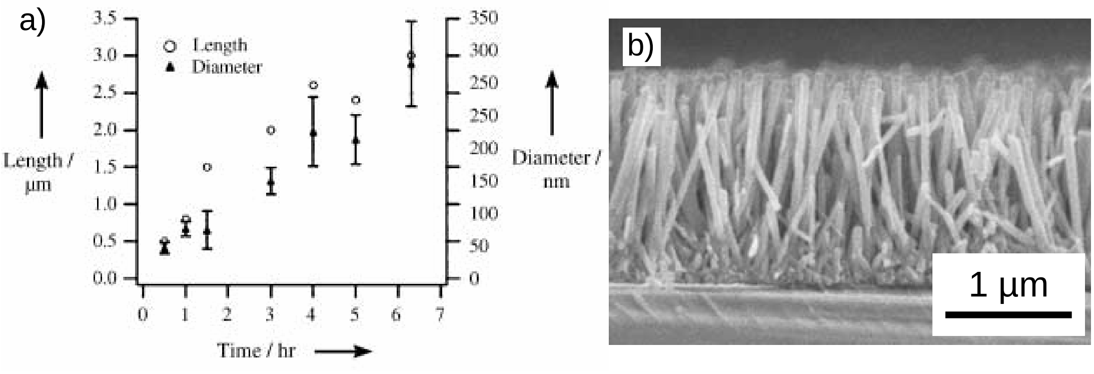

Figure 2.21: **ZnO nanorods grown using zinc nitrate and HMT.** a) Length and diameter of rods grown in 0.025 M solutions at 90 °C as a function of time. b) SEM image of rods, grown for 1.5 hours. Taken from figure 2 in Ref. 91.

ammonia and formaldehyde on heating [95]. In this reaction it is important that OH^- ions are supplied gradually, as $[Zn^{2+}]$ needs to be relatively high compared to $[OH^-]$ for rods to be formed [95]. A suggested reaction scheme for the synthesis is [74]:

$$C_2H_{12}N_4 + 6H_2O \rightleftharpoons 6HCHO + 4NH_3 \tag{2.10}$$
$$NH_3 + H_2O \rightleftharpoons NH_4^+ + OH^- \tag{2.11}$$
$$2OH^- + Zn^{2+} \rightarrow ZnO(s) + H_2O. \tag{2.12}$$

Here the HMT first decomposes (step 2.10), then the OH^- ions resulting from the formation of ammonium (step 2.11) react with dissolved zinc ions to form ZnO, which is non-soluble and therefore precipitates homogeneously, and heterogeneously if a suitable substrate is present. It has been suggested that $Zn(OH)_2$ forms before the growth of ZnO, which then grows via a dissolution-reprecipitation mechanism, where $Zn(OH)_2$ acts as a reservoir of zinc [95]. ZnO, not $Zn(OH)_2$ forms as the final precipitate because of the pH of the solution, which is buffered by HMT [95].

The most common base used for the formation of ZnO nanorods in the second growth category is ammonium hydroxide (NH_4OH). The use of NH_4OH to control the decomposition of zinc nitrate and form ZnO nanorods was studied in detail in 2005 by Tak *et al.* [101]. Zinc nitrate concentrations of 0.01–0.04 M were used, and the pH was adjusted to 10.1-10.5 by adding NH_4OH. Si substrates seeded with a layer of zinc metal were suspended in this solution, which was then heated to between 60 and 90 °C for 6 hours. This produced nanorods 2.5 μm long and 50 nm across, which were very well aligned due to the uniformity of the Si substrate. It was also found that when the reaction was repeated the length of the nanorods increased by $\sim$1 μm per synthesis, while the diameter only increased by $\sim$15 nm [101] (figure 2.22). This is very useful, as it allows the aspect ratio to be increased with increasing syntheses. Nanorods of up to 5.5 μm × 100 nm (aspect ratio 55) were produced [101]. In later work, Tak *et al.* produced further ZnO nanorods on Si substrates, using a sputtered ZnO seed layer [102, 103]. In these studies zinc nitrate concentrations of 0.01 M and

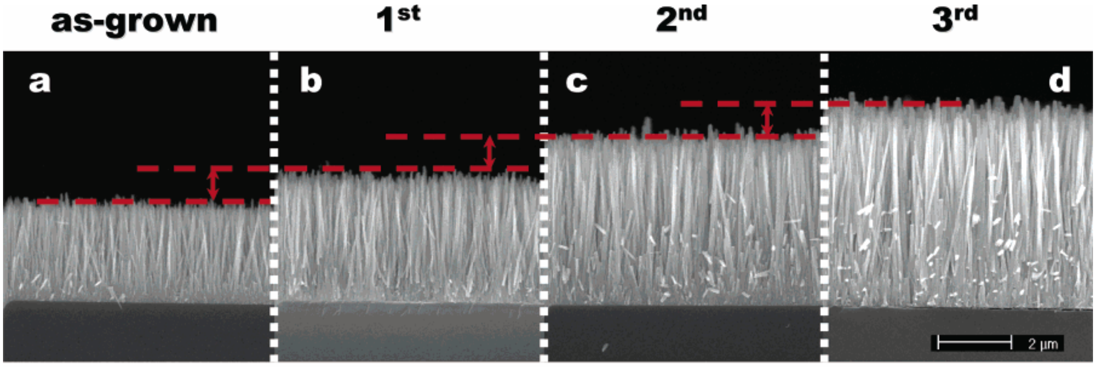

Figure 2.22: **ZnO nanorods grown using zinc nitrate and ammonium hydroxide.** a) Single growth with 0.02 M zinc nitrate at pH 10.4 b)-d) 1st-3rd additional growth steps using solutions of 0.01 M zinc nitrate at pH 10.4. All steps carried out at 90 °C for 6 hours. Taken from figure 7 in Ref. 101.

pH 11 were used, and the reaction was carried out at 95 °C for 6 hours. The ability to produce rods with increasing aspect ratio by repeating the synthesis makes this method attractive for use in eta solar cells. However, the method has not been used to grow nanorods on transparent conducting substrates such as FTO. This must be achieved for it to be used in a complete solar cell structure.

Of the synthesis methods described above, chemical synthesis using zinc nitrate and HMT was chosen to grow the nanorods studied in this thesis. This method was chosen for numerous reasons. Firstly, the method is well established in the literature, and it has been demonstrated repeatedly on transparent substrates. Thus a large volume of data on the details of the method are available. The use of a low temperature, aqueous chemical method is attractive for future scale-up as it requires relatively low energy inputs, and can be performed in large quantities. Finally, this method had previously been used in our laboratory to grow ZnO nanostructures and the equipment and chemicals were readily available, which allowed the method to be more quickly developed at the start of the project.

2.3.2 ZnO Photoluminescence

Photoluminescence (PL) is often used to understand the properties of zinc oxide bulk, thin films, and nanostructures. The room temperature emission spectrum of ZnO normally comprises a sharp peak around 370–390 nm and a broad emission between 450 and 700 nm (see figure 2.23). The sharper peak in the PL spectrum of ZnO is generally referred to as the bound exciton, or simply exciton emission as it has been attributed to the recombination of excitons bound to neutral donors or acceptors [104] and thus has an energy just below the band gap. Most studies focus on the broad band as it is attributed to recombinations in deep levels caused by intrinsic defects in ZnO and therefore can be used as a measure of crystalline quality. The exact form and location of this emission depends on the samples studied and their preparation condition as it

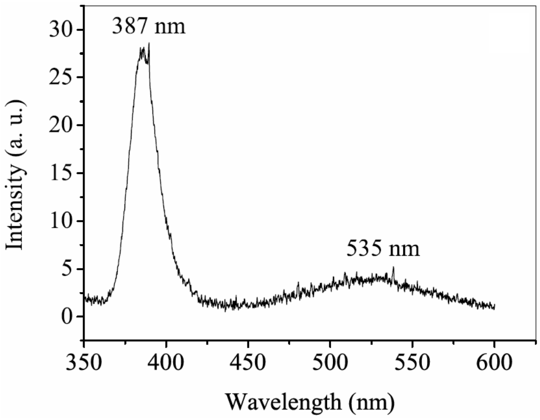

Figure 2.23: **Photoluminescence spectrum of chemically grown ZnO nanorods.** Typical emission peaks can be seen, comprising a narrow UV exciton emission, and broad defect-related green emission. Taken from figure 6 in Ref. 109.

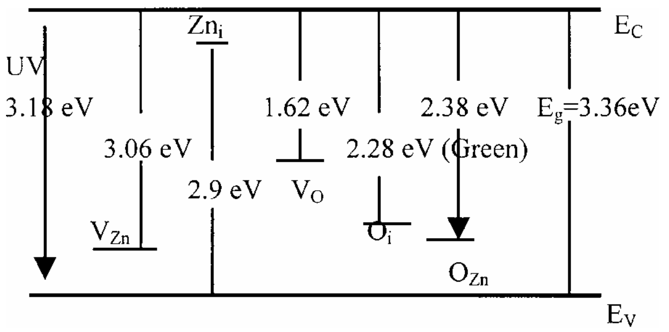

Figure 2.24: **Proposed energy levels for common defects occurring in ZnO.** Taken from figure 4 in Ref. 110.

is likely that a variety of deep defect states contribute to this emission. These defect states, along with their possible energy levels as calculated by Lin *et al.* are shown in figure 2.24. The defects most commonly attributed to the broad, green emission are oxygen vacancies (V_O) [105–107] resulting from the loss of oxygen during high temperature processing. However, as can be seen from the scheme in figure 2.24, other defects such as the O antisite (O_{Zn}) have also been attributed to this green (2.2–2.5 eV) emission. The very broad nature of the emission suggests a number of defects may be responsible in any one sample. This has been confirmed by selectively enhancing or suppressing components of this emission by treatments at different temperatures in different atmospheres [108]. In one case, such a treatment has led to the deconvolution of the broad emission into a green peak (centred 520–540 nm), attributed to V_O as in many studies, and a yellow peak (centred 580–600 nm), attributed to interstitial oxygen, O_I [106].

The remaining states occurring in ZnO are the shallow donors or acceptors, such as the zinc interstitial (Zn_I) and zinc vacancy (V_{Zn}) respectively [74, 110]. As a shallow donor, Zn_I can be attributed to the relatively high intrinsic n-type conductivity of ZnO.

The emissions due to these states are not often seen or discussed in ZnO PL as they are very close to the exciton emission and not generally strong enough to be resolved. However, some have deconvoluted the near band-edge peak to show contributions just below the excitonic energy [111]. In some cases the near band-edge emission has been strong enough to be resolved separately, and linked to surface zinc vacancies [106, 112], which are found mainly in the surface depletion region of ZnO.

2.3.3 P-type ZnO

For some time, the reliable production of p-type ZnO has proved a challenge. This is because, as mentioned above, as-grown ZnO is nominally n-type due to intrinsic defects [77]. Thus, most holes introduced by acceptor dopants are compensated by the high intrinsic free electron density. Despite this, there have been increasing examples in recent years of p-type ZnO thin films and nanostructures.

P-type doping of ZnO has most commonly been achieved with the group V elements N, P, As and Sb. Acceptor doping by N and P occurs through oxygen substitution, leading to the introduction of a shallow acceptor level. Acceptor doping with As and Sb in ZnO is slightly more complicated, as their larger ionic radii makes oxygen substitution energetically unfavourable. However, it has been shown that doping ZnO with As and Sb can produce p-type thin films [77]. P-type behaviour in As and Sb-doped ZnO was explained by Limpijumnong *et al.* to result from the formation of the complex $\mathrm{As/Sb_{Zn}\text{-}2V_{Zn}}$ (As or Sb on a zinc site coupled to two zinc vacancies), which was shown to be a shallow acceptor [113]. Early experimental success coupled with theoretical explanation of the behaviour led to the production of many more p-type ZnO thin films [114–116], including those doped with As or Sb [117–126]. The majority of these films were produced by high energy, high vacuum growth methods such as molecular-beam epitaxy (MBE) or pulsed laser deposition where the dopant was introduced to the growth source(s) [117–124, 126]. However, some acceptor-doped films have also been produced using sol-gel methods [114, 125].

P-type ZnO nanostructures

There is significant interest in producing p-type ZnO nanostructures for a variety of potential device applications. For example, transistors or diodes based on ZnO nano-homojunctions could be used for transparent electronics, UV optoelectronics and photonics. Group V acceptor dopants are added during vapour-phase synthesis of ZnO nanorods by introducing either gaseous (N or P) [85], or vaporised (As or Sb) [127, 128] materials to the gas stream. Doping of chemically grown ZnO nanorods has not been performed during the chemical synthesis. Instead, p-type dopants have been added using post-growth steps such as annealing in the presence of N-containing gases [99], or sources of As [129, 130]. In many cases p-type behaviour in such doped ZnO nanostructures has been confirmed through electrical measurements, such as rectification through a diode constructed using the doped ZnO and an n-type material [85, 99, 129, 130].

2.4 CdTe nanoparticles

CdTe is a semiconductor with a band gap of 1.4–1.5 eV [6, 131, 132], which adopts either the wurzite [6] or zinc blende structure [131]. It has a high absorption coefficient in the visible region, making it a useful material for thin-film solar cells [6, 132] (see section 2.1.2). Thin films can be produced by a number of methods including vacuum evaporation, electrochemical deposition, MBE, MOCVD, screen printing and spray pyrolysis, with the best films reportedly produced by closed space sublimation/vapour transport [6, 131]. Thin-film solar cells using n-CdS/p-CdTe heterojunctions have achieved efficiencies up to 16.7 % [4].

When all three dimensions of a material measure less than ~100 nm, it can be referred to as a nanoparticle [133]. If the dimensions are small enough to lead to quantum confinement, the particles are referred to as quantum dots [133]. Quantum confinement is the confinement of the wavefunctions of the carriers in the material; when the size of a particle approaches the order of the size of the carrier wavefunction the wavefunction is localised, and the carriers are confined [133, 134]. The wavefunction can therefore no longer be modelled based on an infinite crystal, and the subsequent density of states (DOS, the number of carrier states per unit energy and volume [134]), is altered [133, 134]. As the dimensions of the confinement are decreased, the energy levels of the material (described by the DOS) change from continuous bands to discrete, quantised levels, and the separation between levels increases [133]. In a semiconductor, this means that the fundamental energy gap, E_g, increases with decreasing particle size [133]. This is the origin of the 'tunability' of quantum dots discussed in earlier sections. Depending on the number of dimensions that are confined (one, two or three) the material is described as a 2D, 1D or 0D material, and the DOS is affected in different ways. The resulting DOS are represented in figure 2.25. The size of the carrier wavefunction is described by the de Broglie wavelength (λ_{dB}), which is a function of the effective mass of the carrier, m^*, and the carrier energy, E:

$$\lambda_{dB} = \frac{h}{\sqrt{2m^*E}} \tag{2.13}$$

where h is Plank's constant. In a typical semiconductor the de Broglie wavelength is approximately 10 nm [134], thus the dimensions of a nanoparticle must be of this order or less to be quantum confined.

CdTe nanoparticles display quantum size effects as described above when <10 nm in size. As the particles are made smaller the band gap increases from the bulk value. As a consequence the absorption and PL emission shift to shorter wavelengths as the particles get smaller. This can be seen in CdTe quantum dots capped with thioglycolic acid (TGA) as the particles grow with increasing synthesis time (figure 2.26) [135]. At the shortest synthesis time the particles are very small and the PL peak is at ~540 nm, whereas after approximately 26 hours the particles have grown larger, reducing quantum confinement, decreasing the band gap, and giving a PL peak at ~620 nm. It can also be seen that the absorption and PL peaks broaden as the synthesis time increases, which results from the greater size distribution of the particles after a longer growth

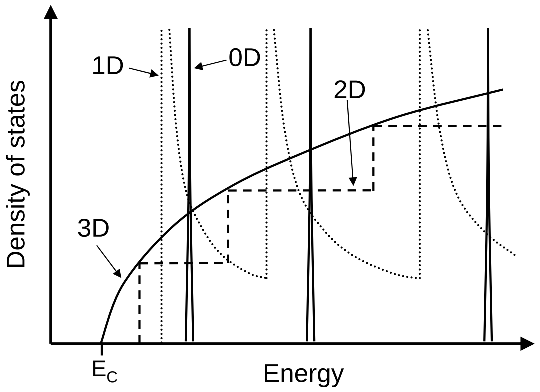

Figure 2.25: **Density of states (DOS) for electrons in the conduction band of quantum confined materials.** DOS for 3D (bulk) 2D (quantum well), 1D (quantum wire) and 0D (quantum dot) are shown. The energy of the conduction band edge (E_C) in the bulk material is indicated. This energy increases as the materials become more confined (and the valence band edge (E_V) decreases in energy), leading to the increase in band gap in quantum confined semiconductors.

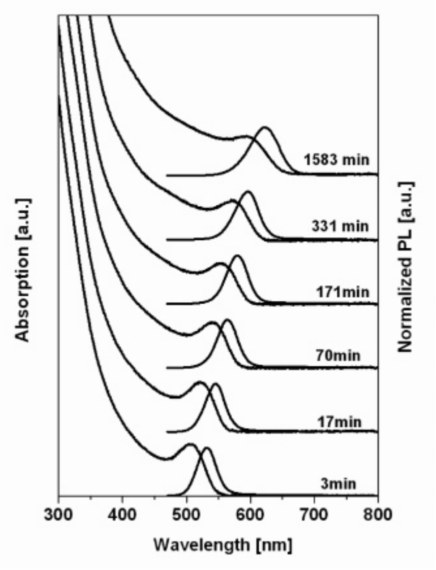

Figure 2.26: **Absorption and photoluminescence (PL) spectra of TGA-capped CdTe nanoparticles grow at times indicated.** Absorption and emission shift to longer wavelengths as the particles become larger over time due to decreasing quantum confinement and increasing the band gap. Taken from figure 1 in Ref. 135.

time.

Nanoparticles can be produced by both top-down and bottom-up techniques, with bottom-up, solution-based methods being the most popular [133]. Most solution methods for the synthesis of nanoparticles proceed by the generation of supersaturation, which leads to either homo- or heterogeneous precipitation, followed by subsequent growth of the particles [133]. For the produced nanoparticles to have a uniform size distribution, the supersaturation and therefore nucleation is carefully controlled to occur over only a short time period [133]. This is generally performed by injecting room-temperature reagents into a hot reaction vessel, which leads to rapid supersaturation coupled with a drop in the temperature. The drop in reagent concentration caused by the rapid nucleation prevents further nucleation continuing, and therefore most of the particles have nucleated at the same time and grow to a similar size [133]. The solution is then reheated gently, which leads to the gradual growth of the initial nuclei to the required size [133]. The size uniformity of the particles is further enhanced by Otswald ripening, which is the growth of larger particles at the expense of smaller ones [133]. Capping molecules (often organic) are added to the solution to avoid the particles agglomerating in the solution, bonding to the surface through either covalent or dative bonds [133] and repel other particles which are capped with the same molecules.

A bottom-up method for synthesizing CdTe nanoparticles in organic solvents that is commonly followed was reported by Talapin *et al.* in 2001 [136]. In this method CdTe nanoparticles were synthesised in a mixture of tri-*n*-octylphosphine (TOP) and dodecylamine (DDA). The nanoparticles were produced by two slightly different methods, which both approximately follow the process of supersaturation followed by gradual growth described above. The two methods vary mainly by the order that the reactants (TOP, DDA, dimethyl cadmium and tellurium powder) were dissolved and mixed together and the temperatures at which the various stages of the reaction took place. In general the rection was performed between 100 and 200 °C and lasted for up to 20 hours. By this method nanoparticles of 2.5–6 nm were produced, emitting light in the range 550–650 nm (green to red). At the end of the reaction toluene was added, in which the nanoparticles were soluble, and the mixture was filtered and isolated by precipitation using methanol.

Nanoparticles produced by the above method have been made water soluble by exchanging the capping molecules for amino-ethanethiol·HCl (AET) or mercapto-propanoic acid (MPA), which gave positive or negative surface charge respectively [137]. In this report a simplified version of the synthesis of CdTe nanoparticles in TOP/DDA was used that closely resembles the supersaturation and gradual growth model described above: dimethylcadmium and tellurim powder were added to a TOP/DDA mixture at 50 °C (leading to supersaturation), which was then heated to 145–180 °C and held at that temperature to allow the particles to grow [137]. This led to particles that emitted green, yellow or orange light depending on the growth temperature. To transfer the particles to water-soluble capping molecules they were first dissolved in chloroform. MPA mixed with KOH or AET were dissolved in methanol and then added to the nanoparticle solution, which led to flocculation and precipitation (as methanol addition did in Ref. 136). Water was then added to the suspension, giving a two-phase system, and shaking caused the nanoparticles to be transferred to the water fraction.

Water soluble nanoparticles can also be synthesised directly, as demonstrated by Gaponik *et al.* in 2002 [138]. These nanoparticles were grown by a supersaturation method in an aqueous solution [138]. However, the control of the nucleation and subsequent growth is slightly different to that described in general above; the Te precursor was added in gaseous form, and the nucleation occured at room temperature [138]. The nucleation was ceased by removing the Te precursor, and formation and growth of the final CdTe nanoparticles was induced by heating and stirring the solution [138]. This ensured a controlled period of nucleation and therefore a narrow size distribution. Such CdTe nanoparticles were used in the solar cell fabricated for this thesis and the full method is described in section 3.2.

2.4.1 Layer-by-layer deposition

Layer-by-layer (LbL) deposition is a method for producing films of materials by depositing alternating monolayers of components with opposite charges [139]. After the deposition of each layer the surface charge of the film is reversed [140] and the subsequent monolayer adheres by electrostatic forces [139]. This allows the build-up of any number of layers of material that are held together by strong electrostatic bonds, which creates stable, uniform and long-lasting films that are often resistant to dissolution by solvents [141]. LbL films can be deposited on structured as well as planar surfaces [139, 140]. LbL deposition was originally developed for deposition of composite polymer films [139] by using polymers with oppositely charged functional groups, but can be used to deposit any water-soluble, dispersible material that has surface charges [140]. This includes charged nanoparticles (metal, semiconducting or insulating), nanoplatelets (e.g. clays), proteins, pigments many other materials [141].

In this thesis, the deposition of semiconductor (CdTe) nanoparticles by the LbL process is utilised. The LbL process is used to build-up a film of semiconductor nanoparticles of any desired thickness on a surface. A schematic of the process can be seen in figure 2.27. The build-up of material is controlled through a balance between adsorption and desorption of dissolved species [141]. When the substrate is immersed in a solution, the charged species (polyelectrolyte or nanoparticle) adsorb onto the

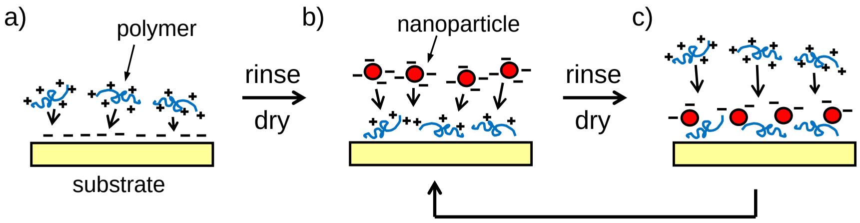

Figure 2.27: **Schematic of the layer-by-layer (LbL) deposition process for depositing nanoparticle-polymer films.** a) Substrate is immersed in solution containing a polymer electrolyte with a positive surface charge, adhering to the negatively charged substrate surface. b) Substrate is immersed in a solution containing a dispersion of nanoparticles with negative surface charge, which adhere to the polymer-coated surface. c) The process is repeated as many times as desired to build up a number of polymer-nanoparticle layers. Between each coating step the substrate is rinsed in water and dried to remove any excess material that is weakly adhered to the surface.

surface, preferably until a monolayer is formed (figure 2.27 a) [141]. The rinse stage then allows any material that is not strongly bonded to the surface to desorb, leaving a monolayer of adsorbed material [141]. This careful control of the layers leads to very uniform coatings of material [139]. When the process has been completed for both species (polymer and nanoparticle, figure 2.27 b) a composite bilayer of nanoparticle and polymer has been formed [139]. The films are very controllable, as both the thickness and the optical absorption depends linearly on the number of bilayers [139]. Because the polymer component of the films puts a lower limit on the inter-particle spacing, and therefore limits the inter-particle interactions, LbL films containing only nanoparticles have been attempted [139]. To form these layers nanoparticles with opposite surface charges (achieved with different capping molecules) were used alternately, instead of nanoparticles and a polyelectrolyte [139]. Unfortunately, the nanoparticles did not adhere well, and no more than a single bilayer could be reliably produced [139]. A full description of the LbL process used to produce the solar cells described in this thesis is given in section 3.3.

2.5 Summary

Solar cells work by generating and separating excited carriers upon the absorption of incident light. In traditional solar cells the separation is achieved across a p-n or p-i-n junction, and the cells are therefore modelled as diodes that generate current when illuminated. Solar cells can be characterised by a number parameters including the short-circuit current density, J_{sc}, open-circuit voltage, V_{oc}, exteral quantum efficiency (EQE) also known as the incident photon-to-electron conversion efficiency (IPCE), fill factor, *FF*, and overall light-to-electrical energy conversion efficiency, η. J_{sc} is determined by the incident flux density of light falling on the cell and EQE. EQE in turn is determined by the light-harvesting efficiency (LHE) and inernal quantum efficiency (IQE). Respectively, these are the proportion of incident photons that are absorbed by the cell at a given energy, and the proportion of these photons that lead to an electron contributing to the current in the external circuit. V_{oc} is the voltage that is generated in the cell under illumination when the terminals are open, and is determined mainly by the built-in bias in the diode. Because of resistive losses in the cell (both series and shunt) and non-ideal diode behaviour the cell does not operate at both J_{sc} and V_{oc}, but instead operates at the maximum power point, generating power density $P_{max} = J_m \times V_m$. The proportion of the actual power density generated, P_{max}, to the maximum theoretical power ($J_{sc} \times V_{oc}$) is the fill factor. The efficiency of the device is given by the ratio of the power density generated by the cell to the incident irradiance on the cell. Most commercial terrestrial solar cells in use today are made from either silicon (single- or poly-crystalline, or amorphous), or the thin-film materials CdTe, $\mathrm{CuInSe_2}$ or $\mathrm{CuIn_{1-x}Ga_xSe_2}$. Thinner layers of thin-film materials can be used because they have higher absorption coefficients than silicon, therefore absorb more light in a smaller quantity of material. These cells generally have efficiencies of 15–25 %.

The effectiveness of high surface area nanostructured substrates in increasing dye-sensitised solar cell (DSSC) efficiency was first demonstrated in 1991 by O'Regan and Grätzel who produced cells with 7.12 % efficiency with porous TiO_2, compared to less than 1 % without. Problems with stability led to replacement of both the dye and the electrolyte. The wide band gap p-type semiconductors CuI and CuSCN were used to replace the electrolyte in such cells. CuSCN, produced by electrochemical deposition or from propyl sulphide solution, became dominant due to its superior stability. Later the hole conducting polymers PEDOT:PSS, spiro-OMeTAD and MEH-PPV were also used for this function. The dyes were replaced with inorganic narrow band gap semiconductors, some as nanoparticles (or quantum dots, QDs). Initially, these innovations were used separately, but later solid hole conductors and inorganic absorbers were combined to produce extra-thin absorber (eta) solar cells. Porous TiO_2 eta cells were produced using absorbers such as Se, CdS, $CuInS_2$, In_2S_3, Sb_2S_3, Cu_2S and PbS thin films and QDs. Later, cells were also made using ZnO nanorods as an alternative to porous TiO_2 with CdTe, CdSe or In_2S_3 absorbers. Absorber layers were produced using MOCVD, electrochemical deposition, SILAR, ILGAR and CBD. For eta cells, porous TiO_2 and ZnO nanorods offer different advantages. Porous TiO_2 has a higher surface area, which is beneficial for very thin absorber layers such as monolayers of dyes or QDs. ZnO nanorods provide a more direct conduction path to the back contact, and are more easily penetrated by absorber layer precursors. Thus either material may be more appropriate for each absorber layer and deposition method. To date the maximum efficiency achieved by eta solar cells is 3.4 %.

ZnO is a semiconductor with a band gap of 3.2 eV. It is generally n-type with a low doped resistivity. ZnO can easily form 1D structures such as nanorods or wires due to preferential growth along the c-axis of its wurzite structure. These nanostructures have been grown by vapour-phase, electrochemical and chemical methods. Vapour-phase methods heat precursors of Zn or ZnO at 700–900 °C in controlled atmospheres. 1D nanostructures are formed on Au or ZnO-seeded substrates by vapour-liquid-solid or vapour-solid mechanisms respectively. Electrochemical deposition of ZnO nanorods has been achieved using three-electrode cells in aqueous chemical baths of $ZnCl_2$ and KCl at 80 °C. ZnO nanorods are grown chemically by decomposing Zn precursor salts in aqueous baths using either a ligand or elevated pH to create 1D structures. The most common method using a ligand is the decomposition of zinc nitrate using hexamethylenetetramine (HMT). Generally, equimolar solutions of these reactants are heated at 75–90 °C for 0.5–12 hours. Rods grown using high pH to control the morphology generally also use zinc nitrate as a precursor, and raise the pH to 10–11 using ammonium hydroxide. The reaction is performed at 60–90 °C for 6 hours. In both chemical methods nanorods can be grown directly from substrates by seeding them with a layer of ZnO and placing them face-down in the solution. ZnO photoluminescence (PL) generally displays a sharp exciton peak around 370–390 nm and a broad defect-related emission around 450–700 nm. The intensity ratio of these peaks depends on the density of defects in the ZnO sample. The defect emission has been related to emission from deep intrinsic defects in the ZnO. Shallow donors and acceptors can also lead to emission shoulders close to the main exciton emission. Efforts have been made to produce p-type ZnO, which is generally difficult due to compensation by intrinsic donor defects. P-type doping of ZnO has been achieved using the group V elements N, P, As and Sb. P-type doping by N and P occurs through oxygen substitution, and doping by As and Sb has been explained through the creation of an acceptor complex that combines As or Sb on a zinc site with two zinc vacancies. P-type ZnO nanostructures have been formed by adding these elements to gas stream in vapour-phase methods, or annealing in the presence of the elements where nanostructures were grown by chemical methods.

CdTe is a semiconductor with a 1.4–1.5 eV band gap and high absorption coefficient. Thin films of CdTe have been produced by a number of methods, and CdTe/CdS thin-film solar cells have achieved efficiencies up to 16.7 %. CdTe displays quantum confinement when the material is less than 10 nm in size. Quantum confinement refers to the confinement of the electron wavefunction in the crystal leading to an increase in the band gap of the semiconductor. The absorption and PL emissions therefore shift to shorter wavelength, and can be 'tuned' by varying the particle size. Nanoparticles (NPs) can be produced by either top-down or bottom-up methods, with the latter being more common. NPs are generally produced in chemical reactions (bottom-up) by generating a supersaturation in a precursor solution, which leads to rapid homo- or heterogeneous nucleation, followed by gradual growth. The NPs can be capped with molecules such as long-chain organic molecules or those with charged functional groups to prevent agglomeration. CdTe NPs have been produced by such a process using both organic and aqueous reactions. CdTe NPs have been synthesised in organic solvents by adding CdTe and Te precursors to tri-*n*-octylphosphine-dodecylamine solutions and heating to between 100 and 200 °C to grow the NPs. CdTe NPs have been produced in water by introducing Te gas to a dissolved Cd precursor, and then refluxing to grow the CdTe NPs. The layer-by-layer deposition method can be used to produce films of NPs while retaining their quantum confinement. This method uses dispersions of NPs with a positive or negative surface charge and a soluble polymer with the opposite charge. Substrates are dipped alternately in these solutions and the NPs and polymer build up in layers by electrostatic attraction. This method leads to uniform, stable films of NPs being produced with controllable thickness.

Chapter 3

Experimental

3.1 ZnO nanorod synthesis

3.1.1 ZnO seed layer

In order to grow ZnO nanorods on conductive substrates such as indium-tin oxide (ITO) and fluorine-doped tin oxide (FTO) it has been reported that a seed layer is required. The seed layer that was chosen for this project was developed by Greene *et al.* [92] and involves the deposition of zinc acetate on the substrate surface from a solution in ethanol and subsequent *in-situ* thermal decomposition to form a thin layer of ZnO crystallites on the surface. The method was undertaken as follows. First, all substrates were washed with soap, and ultrasonically cleaned in acetone and isopropanol for 10 minutes each. The substrates were then placed conductive side-up onto a cleanroom wipe. The zinc acetate solution was dripped onto the substrate surface using a thin glass pipette and allowed to wet the surface. One drip of solution was needed to cover approximately 1 cm^2 of the substrate. This was left for 10–15 seconds and then rinsed off with pure solvent and dried with nitrogen. The wet-rinse-dry steps were repeated 5 times for each substrate. The substrates were then placed onto a hotplate, which was set to achieve a substrate surface temperature of 350 °C, and left for 25 minutes before being switched off and allowed to cool naturally. The whole process was repeated three times.

In initial trials both deionised water and isopropanol (Fisher Scientific, 99.5+ %) were used as a solvent for the zinc acetate (Sigma-Aldrich, $\geq$98 %), to make a 5 mM solution. The zinc acetate was added to the liquid and placed in the ultrasonic bath to aid dissolution. When the solution was deposited using the above method no ZnO nanorods could be grown on the substrate, suggesting a seed layer had not been formed. It is possible that the solubility of zinc acetate in these solvent meant that it was not left on the surface but instead washed away. Alternatively ZnO may have formed in the solution, leading to deposition of ZnO crystals; the original source of this method identifies that the ZnO should be formed in-situ on the substrate surface, requiring zinc acetate, not ZnO, to be deposited from the solution [92]. Thus, for subsequent trials absolute ethanol (Fisher Scientific, 99+ %, anhydrous) was used as the solvent and for rinsing for all seed layer syntheses. Zinc acetate was dissolved in the ethanol by placing it in the ultrasonic bath for 10 minutes, shaking, and leaving for at least 4 hours before use to ensure that it was fully dissolved.

In early trials ITO was used as a substrate material. Repeated attempts to deposit a seed layer onto ITO using both 5 and 10 mM solution of zinc acetate in ethanol by the above method were not successful; some structures were observed on the substrate surface, but ZnO nanorods could not be reliably grown on the surface (see section 4.1.2). In the original paper on this synthesis method FTO, not ITO, was used as a substrate material [92]. Therefore FTO-coated glass (Pilkington USA TEC-15, 12–14 $\Omega/\Box$) was trialled as a substrate material. When using FTO substrates ZnO seed layers could clearly be seen on the surface (see section 4.1.3). ZnO nanorods could be successfully grown from these seed layers, indicating FTO was a more suitable substrate than ITO for deposition of a ZnO seed layer by this method. FTO glass was therefore used for all further work requiring conductive glass substrates. The final method that was used to deposit ZnO seed layers used cleaned FTO substrates and a 5 mM solution of zinc acetate in absolute ethanol. The zinc acetate was deposited and heated as described above. To ensure good wetting of the substrate an additional rinse and dry step with ethanol was added before the 5 wet-rinse-dry steps (before starting, and after each anneal step). Rinsing the surface with a large quantity of ethanol and drying before depositing the small amount of zinc acetate solution ensured that it wetted the surface evenly.

3.1.2 FTO etching

For the solar cells, substrates had some of the FTO removed by chemical etching before depositing the seed layer to avoid short-circuits. The area that was not to be etched was masked with Kapton tape. The etch solution was prepared by dissolving Cr pellets in HCl (32 %, Fisher). 1 g Cr was added for every 150 ml HCl. The solution was stirred slowly while heating to 90 °C. The Cr dissolved much more quickly as the solution heated up. When the Cr was fully dissolved (solution takes on a dark green colour) and the solution was at 90 °C, the substrates were added face-up. The substrates were left in the solution for 4 minutes, which was kept at $\sim$90 °C. A Zn pellet was added at the start and half way through the etching to ensure the Cr ions remained active in the solution. The solution was then emptied into a bottle through a funnel, catching the substrates, which were then rinsed thoroughly in distilled water. The Kapton tape was then removed and the substrates rinsed again. A small amount of under-cutting had occured under the tape, but this was minimal ($<$1 mm).

3.1.3 Aqueous chemical nanorod growth

Initially, synthesis of ZnO nanorods was performed on Ag-coated ITO substrates. These substrates were used because previous work in our laboratory had indicated that ZnO nanorods would nucleate on Ag-coated substrates from chemical solution.

Ag was coated onto ITO-coated glass substrates under vacuum by thermal evaporation of Ag wire. A mask with round holes, diameter $\sim$1 mm was often used so that nucleation on both Ag and bare ITO sections could be studied on the same substrate. ITO-coated glass was used to ensure conductivity across the whole substrate to improve SEM analysis, and because Ag adhered better to ITO than bare glass. Later, ZnO seeded substrates as described above were used. ZnO seed layers were also deposited onto Ag-coated ITO glass for use in some reactions.

ZnO nanorods were grown using the zinc nitrate hexahydrate (Aldrich, 98 %) — hexamethylenetetramine (HMT, Sigma-Aldrich, 99.5 %) method described in section 2.3.1. Reactant concentrations used were between 0.01 and 0.1 M, with the zinc nitrate and HMT concentrations always equal to each other in the solution. Reactants were added to the solution by first dissolving at higher concentration (0.25 or 0.1 M) in water to make batch solutions, and then adding these to the required quantity of water using a plastic syringe to mix and dilute. In some experiments this extra water and/or the batch solutions were pre-heated to 90 °C before being mixed so that the reaction started instantly on mixing, and in some cases the reactants were mixed cold and then heated to 90 °C. However, it is stated in Ref. 95 that HMT decomposes on heating, so in later experiments this batch solution was not pre-heated.

The substrates used in the reaction were placed face-down in the reaction solution. The substrates were held by being placed on a rectangular stand of a design shown in figure 3.1. By being placed face-down, ZnO nanorods could nucleate heterogeneously on the seeded or Ag-coated surface of the substrate, but the homogeneously nucleated precipitate that formed in the solution would not cover the surface as it settled to the bottom. Initially thin copper sheeting was used to make the stand (figure 3.1 a), as this did not seem to disrupt the nanorod growth. Later, PTFE stands of a similar design were made by cutting the required shape from a block of PTFE (figure 3.1 b). This limited the quantity of impurities in the reaction, as some of the Cu could potentially become soluble in the reaction and be incorporated in the ZnO, even if below detectible limits. No obvious morphological differences could be observed in the ZnO nanorods when changing the stand material. Once held on the stand

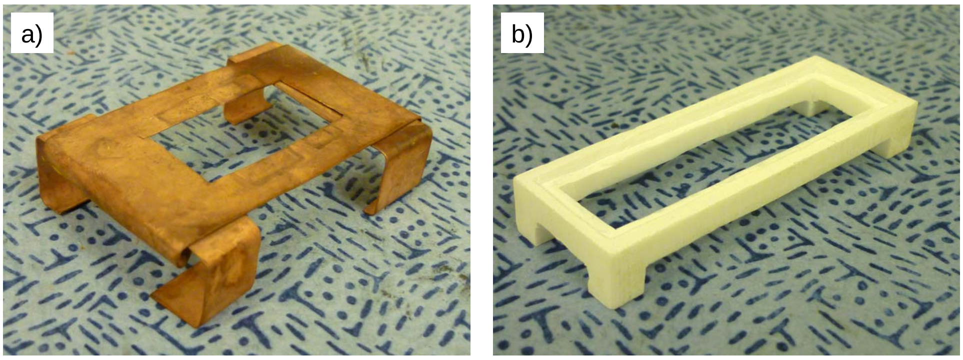

Figure 3.1: **Stands used to hold substrates during aqueous chemical synthesis of ZnO nanorods.** a) Copper stand. b) PTFE stand.

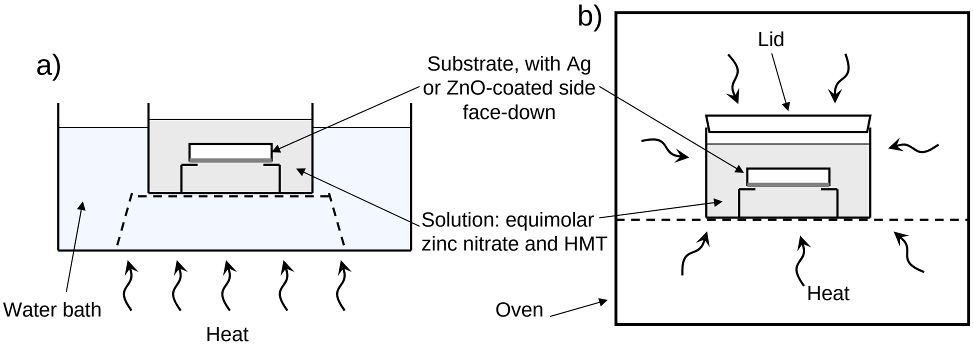

Figure 3.2: **Schematic of the apparatus for aqueous chemical synthesis of ZnO nanorods.** a) Growth of nanorods in open vessel using water bath. Closed vessel was also used in water bath. b) Growth in closed vessel in oven.

the substrates were placed into the reaction solution. This was performed at different stages of the reaction. In some cases the substrates were added as soon as the reactants were mixed, while they were still cold. When the reactants were added to pre-heated water, the substrates were added just before the reactants. Some reactions were performed in an open-topped reaction vessel, some with a covered vessel (figure 3.2). When performed in an open reaction vessel the solution level would decrease as the solution evaporated, so in some cases a small quantity of pre-heated water was added to the solution to ensure the level stayed above the substrates. Initially, the solution was heated by placing the vessel in a water bath on a hotplate (figure 3.2 a), but later, when the reactions were consistently performed in a closed vessel, the solution was heated using an oven (figure 3.2 b).

Each single reaction was performed for 2–2.5 hours, as after this time all of the reactants were depleted and the reaction had ceased. This could be observed because the homogeneous precipitate was no longer forming, and all that had formed had settled to the bottom of the vessel. After this time the substrates were taken out of the solution, the backs of the substrates were wiped and then placed face-up on a clean-room wipe. The surface was gently rinsed with distilled water to remove any loose precipitates, and the substrates were left to dry naturally or dried with a nitrogen flow. The reaction solution was left to cool and then the supernatant was removed and replaced with fresh distilled water, the precipitate shaken up and left to re-settle. This was performed three times to clean the precipitate. The majority of the water was then removed and the precipitate was removed and stored with a small quantity of water for later analysis. In some cases the substrates were taken out of the solution and placed directly into a fresh, cold solution before being returned to the oven for subsequent nanorod synthesis.

In some reactions, poly(ethylenimine) (PEI) was added with 0.025 M zinc nitrate and HMT as described in section 2.2.5. PEI was added by first diluting the supplied solution (Sigma Aldrich, 50 wt.% in water, M_w 1300) to reduce the viscosity and make it more manageable. This diluted solution was added to the reaction mixture after the zinc nitrate and HMT to make a final concentration of 5–7 mM.

The final method that was used for growing ZnO nanorods involved diluting and mixing zinc nitrate and HMT while cold to 0.025 M and adding the substrates on a PTFE stand to the solution, also while cold. PEI was not used. These were sealed in a close-lidded vessel and placed into an oven that had been pre-heated to 90 °C. The solution was left for 2.5 hours before being removed from the oven and the substrates removed and cleaned as described above. Multiple syntheses were performed using the same substrates if required. For solar cells, syntheses were repeated 20 times for earlier cells (total 50 hours), and 6 times for later cells (total 15 hours). Before CdTe coating, nanorods used in the solar cells were annealed at 400 °C for 1 hour in air to increase conductivity, as performed by Law *et al.* [62].

3.1.4 Sb-doped nanorods

ZnO nanorods were doped with Sb by adding Sb precursors to the solution of zinc nitrate and HMT and using the method described in the previous section to grow the nanorods with Ag-coated ITO substrates. Doped nanorods were grown in 0.01, 0.025 and 0.1 M solutions of zinc nitrate and HMT. Sb acetate was added to the reaction to achieve the Sb doping. The concentration of Sb acetate in the reaction was such that the concentration of Sb ions was either 5, 1 or 0.1 % that of the Zn ions. Sb acetate was either dissolved in water and added directly to the reaction bath immediately after the other reactants, or dissolved in ethylene glycol (EG) first, and then added to the aqueous solution. Sb acetate in EG solutions were made up to either 0.1 or 0.05 M, and then the required quantity of this solution was added to give the correct Sb concentration in the final solution. Sb acetate remained stable in EG solutions for many weeks. For comparison, ZnO nanorod syntheses were performed with the equivalent volume of EG added, but no Sb acetate.

3.2 Synthesis of CdTe nanoparticles

CdTe nanoparticles were obtained from project partners and the synthesis is explained in Refs. 135 and 138. The method used was as follows. CdTe precursors were first made by dissolving 0.985g (2.35 mM) of $Cd(ClO_4)_2{\cdot}6H_2O$ in 125 mL of water, stirring in 5.7 mM of thioglycolic acid (TGA) and adjusting the pH to 11.2-11.8 by dropwise NaOH addition. This solution was placed into a three necked flask fitted with a septum and valves and deaerated for 30 minutes by bubbling nitrogen through the solution. H_2Te gas, generated by reacting Al_2Te_3 with H_2SO_4, was then bubbled through the solution under nitrogen for $\sim$20 minutes while stirring (figure 3.3 a). At this stage the solution changed to an orange colour, indicating the formation of CdTe precursors. This solution was then refluxed at 100 °C with a condenser in air to form the thiol-capped CdTe nanoparticles (figure 3.3 b). After 5–10 minutes of refluxing CdTe nanoparticles of $<$2 nm in size had formed, with an absorption maximum of $\sim$420 nm. The reaction could be continued to allow the nanoparticles to grow, which

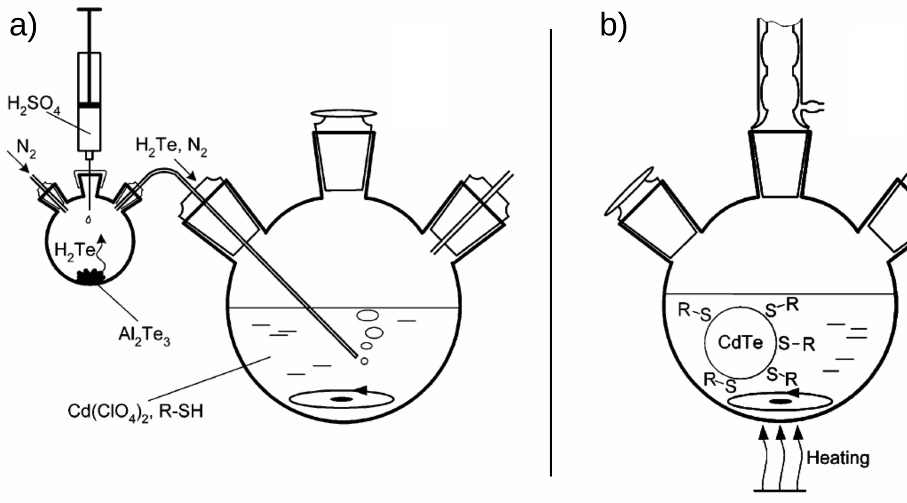

Figure 3.3: **Schematic of the procedure for synthesising thiol-capped CdTe nanoparticles.** a) Formation of CdTe precursors by reaction between dissolved cadmium chloride and H_2Te gas. Thiol capping molecule, R-SH, is also dissolved in the solution. Thioglycolic acid ($HSCH_2COOH$) is used as the capping molecule in this project. b) CdTe nanoparticles are formed by refluxing the precursor solution in the presence of air. Taken from figure 1 in Ref. 138.

led to a gradual red-shift in the absorption maximum (see figure 2.26). CdTe nanoparticles used in this project had an absorption maximum of ∼600 nm (see section 2.4), which required a growth time of ∼25 hours and corresponds to ∼3.2 nm in size.

3.3 Layer-by-layer deposition of CdTe nanoparticles

The layer-by-layer (LbL) process was used to deposit films of CdTe nanoparticles used in this project. A robot was used to move between the different stages and dip into the solutions used in the LbL process. The substrates were attached to a holder that holds them perpendicular to the substrate surface. The main stages of the process involve dipping the substrates into a solution of 20 mM poly-(diallyldimethylammonium chloride) (PDDA, Sigma Aldrich, medium molecular weight, M_w 200,000-350,000) and 0.2 M NaCl (Sigma Aldrich, 99.5 %), followed by dipping into a suspension of TGA-capped CdTe nanoparticles. This suspension was a 7:1 mix of distilled water and the original CdTe nanoparticle suspension that was supplied by our partners, giving a nanoparticle concentration of $\sim 0.7 \mu$M. Before each dip step (PDDA and CdTe) the substrates were washed by dipping into a bath of flowing distilled water, followed by drying in an air flow. The substrates were dipped and withdrawn into all solutions at 0.15 mm/sec, taking approximately 3.5 minutes to withdraw. After one complete cycle as shown in figure 3.4 a complete bilayer was formed on the surface. This was repeated from 10–50 times to form the required number of bilayers. This automated process was developed by Dr D. E. Gallardo for the deposition of LbL films of CdTe

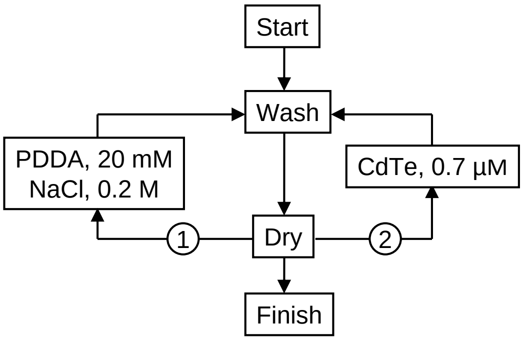

Figure 3.4: **Flow diagram showing the layer-by-layer (LbL) process for depositing films of CdTe nanoparticles embedded in PDDA.** Cycle is repeated until required number of bilayers is deposited, when cycle ceases after the final dry stage.

nanoparticles for LED devices [5, 142].

3.3.1 Annealing of layer-by-layer films

Some LbL films of CdTe nanoparticles in PDDA were annealed for 1 hour at 150–450 °C, either in air or in vacuum. In air, the substrates were placed face-up on a hotplate, which was then set to achieve the surface temperature required. The samples were heated to the required temperature, held for 1 hour, and then the hotplate was turned off and the samples were allowed to cool. The films were annealed in vacuum by attaching vertically to a metal sheet (∼2 mm thick) and placing in a vacuum chamber, which was pumped to 10^{-7} mbar. A heat lamp was used to heat the back of the sheet, where a thermocouple was attached to measure the temperature of the sheet. Again, the samples were heated to the required temperature, held for 1 hour, and then turned off and allowed to cool. Once cool the samples were removed from the vacuum chamber.

3.4 Copper thiocyanate deposition

Copper thiocyanate (CuSCN) was used as a transparent p-type material in the solar cells produced in this project. CuSCN was deposited from a propyl sulphide solution as described in section 2.2.2. Initially, ethyl sulphide (Aldrich, 98 %) was used as the solvent, but later propyl sulphide (Aldrich, 97 %) was used, as it has been found that ethyl sulphide forms complexes with CuSCN that cannot be fully removed on heating, whereas propyl sulphide can be fully removed on heating [30]. Solutions of 0.01–0.4 M were made by placing CuSCN powder (Aldrich, 99 %) in the solvent and stirring overnight. When using propyl sulphide the solution concentration was always below 0.32 M, as this is the solubility limit of CuSCN in propyl sulphide [30]. After stirring, the solution was allowed to settle as there was sometimes some undissolved material in the solution, even when working below the solubility limit. With this

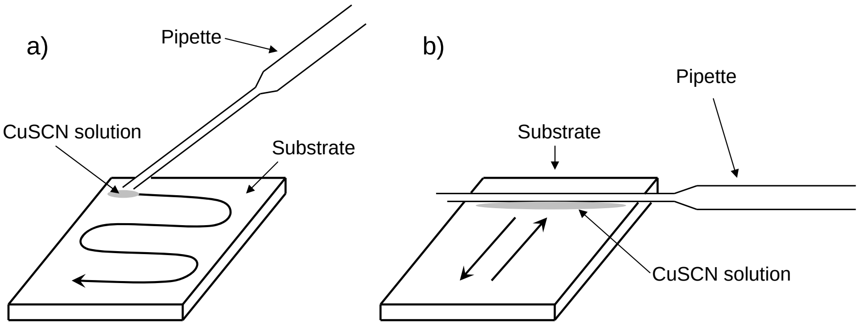

Figure 3.5: **Schematic of the methods for depositing CuSCN films.** a) CuSCN solution in propyl sulphide is dispensed from end of pipette, which is rastered holding slightly above the surface, leaving a small quantity of solution behind, which is left to dry. b) Alternative method, where solution is dispensed from pipette and then run down edge. The solution is then touched to the surface to form a meniscus, which is dragged back and forth across the surface until the solvent has all evaporated.

precipitate settled at the bottom, clean solution was taken from the top portion for use.

Substrates used included glass, ITO and FTO-coated glass, ZnO nanorods on FTO, and CdTe-coated ZnO nanorods on FTO. Coating any more than a single layer onto planar (glass, ITO, FTO) substrates was unsuccessful as the film peeled off, presumably because the surface was too smooth. The solution was coated onto the substrates by either spreading on as in the literature or by spin-coating. When spread on the substrates were placed onto a hotplate st to 70–90 °C, and solution was spread thinly over the surface by passing a narrow glass pipette over the surface while releasing small quantities of solution (see figure 3.5 a). When the surface was covered the solvent was allowed to visibly dry and the next layer was then applied. It was found to be imperative that as small a quantity of solvent as possible was applied to the surface to avoid inhomogeneities and cracking (discussed in section 7.3). To allow smaller quantities to be dispensed the spreading method was adapted towards the end of the project; a small drop of solution was dispensed from the pipette, which was then turned flat so that the drop ran along the side of the pipette. The pipette was then lowered until the drop touched the surface of the substrate, forming a meniscus between the pipette and the surface. The pipette was then passed backward and forward across the surface, maintaining the meniscus, until all of the solvent had dried (figure 3.5 b). This way, only the tiny quantity of solution that dried behind the pipette was coated at one time. The method was also adapted during the project to ensure the solvent fully evaporated: every ten layers the hotplate temperature was increased to 150 °C, which is above the boiling point of propyl sulphide (142°C), held for 5 minutes, and then returned to the previous temperature. This ensured that any remaining solvent would evaporate. Spin-coating was also trialled as an alternative for depositing CuSCN layers. The solution was dripped onto the substrate, which was then spun at 1000–2000 rpm for 10–30 seconds. These trials were performed when using ethyl sulphide as a solvent.

In the final method for depositing CuSCN (Aldrich, 99 %), propyl sulphide was used as the solvent (Aldrich, 97 %) to make a 0.1 M solution. This solution was spread repeatedly over the nanorod-coated FTO substrates, which were heated at 80 °C. The solvent was allowed to evaporate between each coating [14, 30]. The coating was repeated 50 times, increasing the temperature to 150 °C for 5 minutes every 10 coatings to allow excess solvent to evaporate.

3.5 PEDOT:PSS deposition

Poly(styrenesulfonate)-doped poly(3,4- ethylenedioxythiophene) (PEDOT:PSS) was trialled as an alternative hole conductor for use in the solar cells. Aqueous PEDOT:PSS solution was used either as-supplied (Aldrich, 1.3 wt.%, conductive grade), or diluted to 25 % of the supplied concentration in absolute ethanol. The solution was applied to the substrate by dripping on 10 drops while spinning at 2000 rpm. The substrate was spun for a further 20 s. After spinning, the substrate was placed onto a hotplate at 120 °C for two minutes for the films to dry [143]. This process was repeated up to 6 times. In some cases, the first two layers were deposited using a diluted solution, and the last 2–4 with a concentrated solution.

3.6 Device completion

After deposition of the hole collecting layer onto uncoated or CdTe-coated ZnO nanorods, gold contacts were added for electrical testing using an Edwards E480 evaporator. Substrates were covered using a mask to separate 6 individual contacts with 4×4 mm

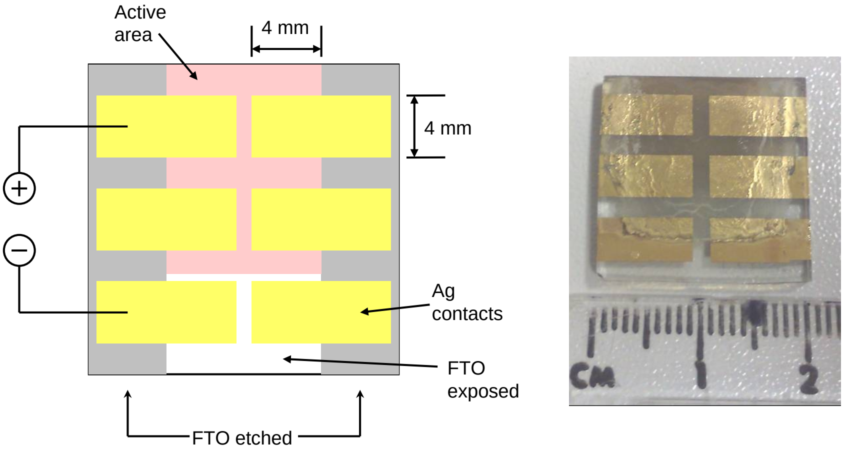

Figure 3.6: **Schematic of the layout of contacts on the substrate with corresponding photograph.** Active area, where ZnO-CdTe-CuSCN structures are grown and coated. Edges have FTO removed by etching to avoid short-circuits when contacts are made. Each of the four devices is tested in turn by connecting to the Keithley SMU with positive and negative poles as indicated.

active area on the surface (figure 3.6). The masked substrates were placed into the evaporator, pumped to $\sim 3\times10^{-6}$ mbar, and coated with 40–60 nm of gold by thermal evaporation.

3.7 Analysis

3.7.1 Scanning-electron microscopy

The morphology of the nanorods was studied using a Philips XL30 SFEG scanning electron microscope (SEM) and elemental analysis was performed using an attached energy-dispersive x-ray spectrometer (EDX, Oxford Instruments). Samples were mounted at either 90 or 45 ° to the electron beam. Most samples were conductive enough that charging was not an issue, however in some cases (e.g. cross-sectional analysis of CdTe LbL films) silver-DAG was added around the analysis area to allow excess charge to be conducted away.

3.7.2 X-ray diffraction

X-ray diffraction measurements were performed using a Siemens D5005 diffractometer. Scans were performed from 5–90 ° using Cu K_α radiation. Crystal peaks were identified using the International Centre for Diffraction Data (ICDD) database.

3.7.3 X-ray photoelectron spectroscopy

X-ray photoelectron spectroscopy (XPS) measurements were performed using a VG Instruments Escalab with a magnesium source and 20 eV pass energy. ITO-coated glass pieces were used as substrates to avoid excessive charging. A small piece of carbon tape was placed on the samples and the resulting spectra were aligned by taking the C 1s peak as a charge reference (284.6 eV). XPS measurements were performed and calibrated by Dr D. E. Gallardo.

3.7.4 Optical absorption

UV-Vis absorption spectra were measured using either a Perkin-Elmer Lambda 7 spectrophotometer or a Lambda 950 spectrophotometer with attached integrating sphere. The integrating sphere was used to capture the maximum quantity of light that passed through the substrates including scattered light, which was not captured when using the Lambda 7. Materials in solution were diluted and placed into a quartz cuvette for analysis. Analysis of CdTe LbL films were performed on glass substrates where possible, as these gave the clearest absorption measurements compared to ITO or FTO substrates. ZnO nanorods were analysed as-grown on FTO substrates or dispersed in water in a quartz cuvette. Dispersion was performed by taking the collected homogeneous precipitate and dripping 1–5 drops into 10 ml water in the cuvette. Most dispersions remained mixed for long enough to take the measurements before the nanorods settled to the bottom.

3.7.5 Photoluminescence

Photoluminescence measurements were taken by mounting the solid samples at a fixed angle to the beam of a frequency quadrupled Nd:YAG laser with an output wavelength of 266 nm. The laser was set to a repetition rate of 10 Hz and an output power of $\sim$94 mJ/pulse·cm^2. The spectra were collected using a collimator connected via a fibre-optic cable to an Ocean Optics SD2000 spectrometer. Theoretical fits were made to the measured spectra by plotting the sum of multiple gaussians, and then minimising the difference between the model and the data using the solver package in Microsoft Excel. The peak center, amplitude, and full width at half maximum were used as parameters in the fit. Additional gaussians were added or subtracted until the fit was optimised.

3.7.6 Electrical and photovoltaic characterisation

All current-voltage measurements were performed using a Kiethley 2400 SMU controlled using Labview 8.0 software. Contacts to solar cells were made using gold sprung probes built into a device holder. Cells were illuminated with a non-collimated Xe lamp, which was calibrated using a Newport reference cell to give 1 sun (100 mWcm^{-2}) output. Reference measurements of some cells were made using a Newport Oriel solar simulator with an AM 1.5 filter, also at 1 sun illumination. Each cell on each substrate (nominally four on each — see figure 3.6) was tested in turn by applying a voltage sweep both in the dark and under illumination. Multiple cells were used on the same substrate in case one cell had short-circuited or behaved anomalously. As long as three of the devices gave similar J–V characteristics it was assumed to be the standard performance for that type of device. Current values for the set of devices were not averaged, as this may have distorted the shape of the curve. Instead, the characteristics of a reprasentative device was chosen to be included for comparison in chapter 7.

Chapter 4

ZnO nanorod synthesis

The first stage of solar cells production was to produce nanorods of suitable morphology, density of growth and on suitable substrates for use in these solar cells. This chapter describes the development of the growth of these nanorods, and describes the outcomes of the variations in the growth method that were described in section 3.1.3. This includes initial trials of growing nanorods on Ag-coated substrates, the deposition of thin ZnO seed layers on transparent substrates, and subsequent growth of ZnO nanorods on these substrates. The development of the morphology, size and nucleation density of the nanorods is described, as well as the optical properties of the nanorods that were produced.

4.1 Nanorod morphology and nucleation

4.1.1 Nanorod growth on Ag

As described in section 3.1.3, nanorods were grown on Ag-coated ITO substrates using a variety of conditions. Initially, growth of nanorods was performed in an open dish, pre-heating the water and reactant batch solutions before mixing. Although in some cases this method produced rods with relatively good alignment and density (figure 4.1), it was found that the result was very unpredictable. In some cases the rods nucleated with poor density and/or alignment (figure 4.2 a), or grew with non-standard morphology (figure 4.2 b). Even if the HMT was not pre-heated (avoiding early decomposition: see section 3.1.3), or both reactants were not, the results still varied largely between syntheses. Adding the reactants to a pre-heated solution and performing the reaction in an open bath both made the conditions of the reaction hard to control. When the reactants were added hot the reaction initiated very quickly, so nucleation and growth on the substrate were sensitive to the exact temperature at which this was performed and the way the reactants were added. Also, with no lid on the reaction vessel the evaporation of the solution had to be monitored and varied depending on the air flow and ambient temperature of the room. Although every effort was made to keep these conditions controlled, it was difficult to keep them exactly the same every time.

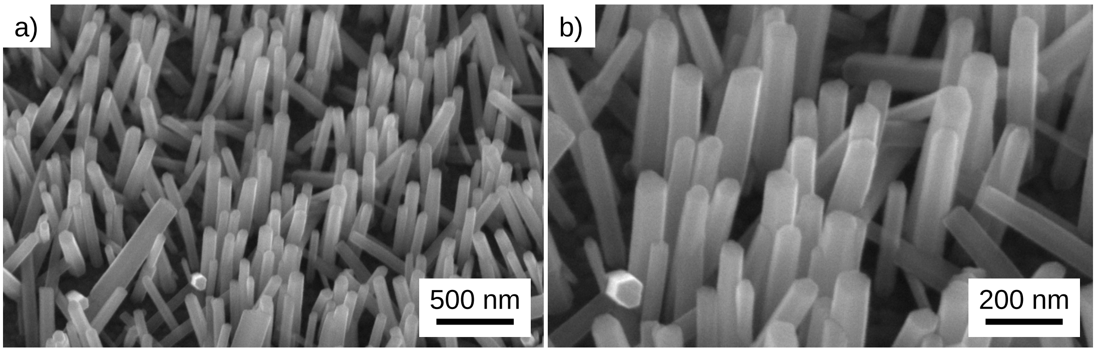

Figure 4.1: **SEM images of ZnO nanorods grown on Ag substrates in aqueous 0.01 M solution of zinc nitrate and HMT.** a) Wide view. b) Close-up image. Nanorods grown in an open bath for 2 hours. Reactants were added after heating water to 90 °C. Images taken at 45°.

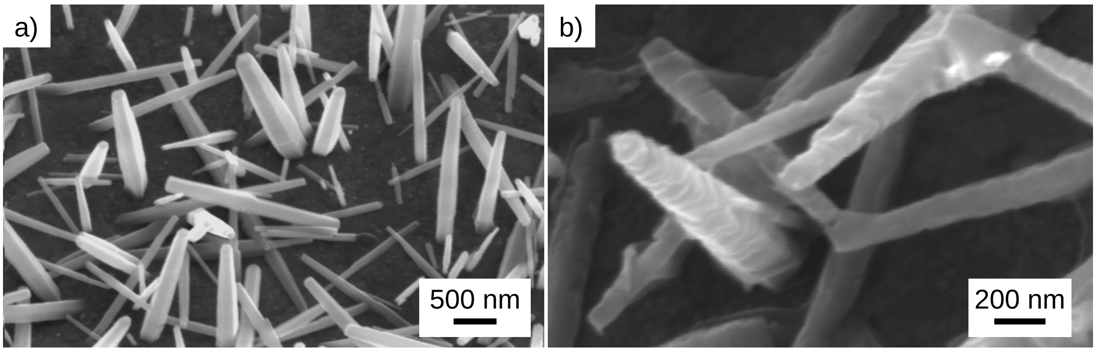

Figure 4.2: **SEM images of poor ZnO nanorods grown on Ag substrates in aqueous 0.01 M solution of zinc nitrate and HMT.** a) Poor alignment and nucleation of rods. b) Non-standard morphology. Nanorods grown in an open bath for 2 hours. Reactants were added after heating water to 90 °C. Images taken at 45°.

Heating the reactants from cold with the substrates present from the start and sealing the reaction vessel allowed conditions to be kept more constant; the reaction began gradually as the solution was heated and evaporating liquid could not escape from the reaction vessel. This method produced much more consistent results (figure 4.3). The nanorods produced in this way were consistently well-aligned and grew with good density on the substrate. It was also found that using a final solution concentration of 0.025 M of reactants also led to more dense nucleation. These rods were $\sim$2 μm long and 200 nm wide. The main benefit of this method was that it was more consistent: rods could be reliably grown on Ag substrates giving similar density, size and shape of rods.

Rods were also grown by this method using 0.1 M solutions. The solutions were heated for 6 hours to ensure the reactants were fully depleted. These rods, as expected from the literature [79], were much larger: approximately 1 μm in diameter, and 2–4 μm long (figure 4.4 a). They also nucleated very densely on the substrate so that in some area they almost fused to form a continuous film (figure 4.4 b).

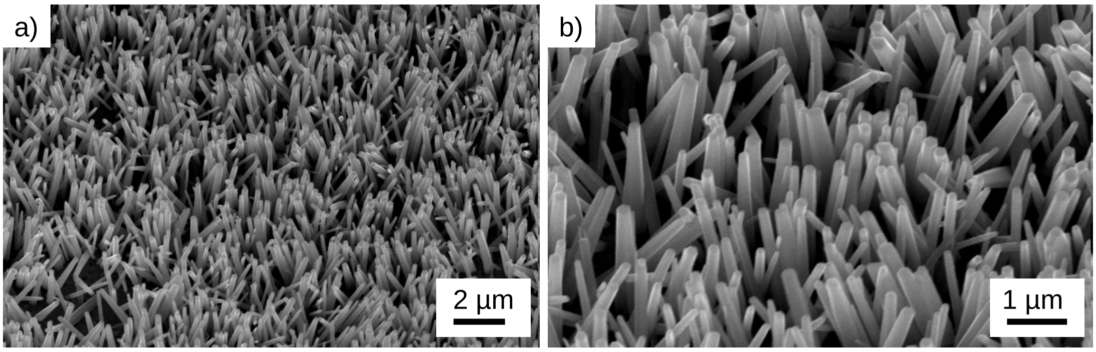

Figure 4.3: **SEM images of ZnO nanorods grown on Ag substrates in aqueous 0.025 M solution of zinc nitrate and HMT.** a) Wide view. b) Close-up image. Nanorods grown in a sealed vessel for 2.5 hours. Reactants were added before heating the solution. Images taken at 45°.

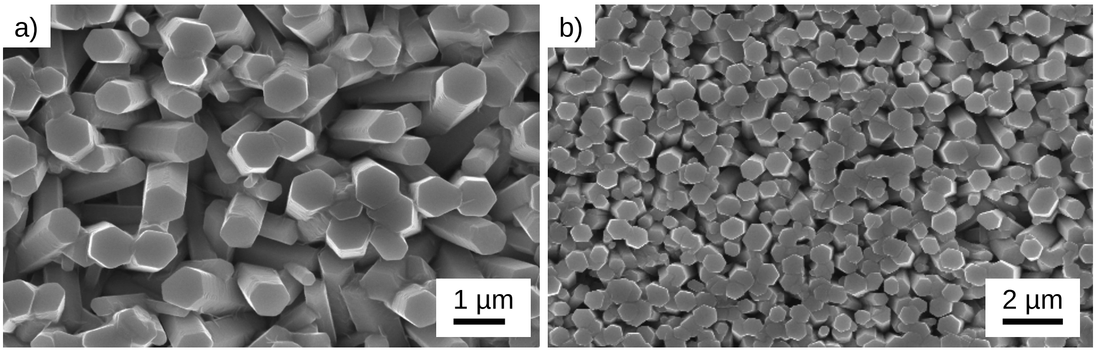

Figure 4.4: **SEM images of ZnO nanorods grown on Ag substrates in aqueous 0.1 M solution of zinc nitrate and HMT.** a) Close-up image. b) Wide view showing high density of nucleation. Nanorods grown in a sealed vessel for 6 hours. Reactants were added before heating the solution. Images taken at 90°.

4.1.2 Seed layer

Early attempts to deposit seed layers from solutions of zinc acetate in water, isopropanol, or in ethanol onto ITO-coated glass substrates by the method described in section 3.1.1 were not successful. It was difficult to ascertain whether seed layers had been formed from direct measurements as they should only be tens of nm thick. However, no nanorods grew from seed layers deposited onto ITO substrates, suggesting the seed layers had not formed, or had not adhered sufficiently

Attempts to deposit seed layers onto FTO-coated glass substrates were more successful. Because of the textured nature of the FTO substrates, the ZnO seeds could be directly imaged on the surface (figure 4.5). This allowed the successful growth of ZnO nanorods onto these seeded FTO substrates, which is discussed below.

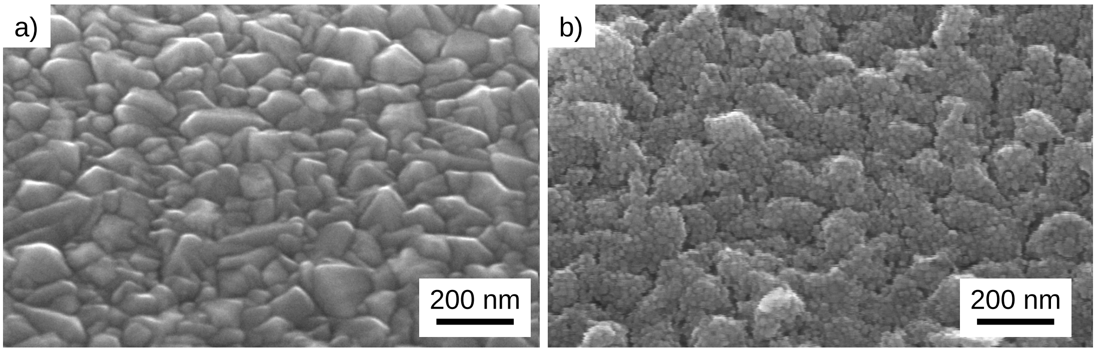

Figure 4.5: **SEM images of FTO substrates without (a) and with (b) ZnO seed layer.** Seed layer deposited from zinc acetate in ethanol solution by method described in section 3.1.1. Images taken at 45°.

4.1.3 Nanorod growth on seed layer

As with the growth on Ag-coated substrates, growth of ZnO nanorods onto seeded FTO substrates in open baths with reactants added to a hot solution was sometimes successful (figure 4.6 a). However, in this case it was more clear that adding the reactants at the start of the reaction produced more well-defined nanorods than when added hot, even in an open bath (figure 4.6 b). Again, this likely occurred because of the controlled initiation of the reaction as the temperature increased. However, as with growth on Ag-coated substrates, performing the reaction in a closed vessel allowed further control of the reaction conditions and meant that no solution was lost through evaporation. Thus the chosen method for growth of ZnO nanorods on seeded FTO substrates was to mix the reactants when cold, add the substrates from the start, and heat inside a closed vessel. This consistently led to very dense, reasonably well-aligned ZnO nanorods ~500 nm long and ~40 nm wide (figure 4.7 a). The rods were not as well aligned as those grown on Ag, which was attributed to the high roughness of the FTO surface (figure 4.5 a), which correlates with the variation in growth angle of the nanorods. This method was also be used to grow larger (1 μm × 100 nm) nanorods by introducing the substrates to multiple reaction baths, as seen in figure 4.7 b.

4.1.4 Growth with PEI

Growth of nanorods was trialled with PEI to try to increase the aspect ratio of the rods, as discussed in section 3.1.3. Images of such rods grown at 90 °C in three 2.5 hour syntheses with fresh solutions of 0.025 M zinc nitrate and HMT and ~6 mM PEI are shown in figure 4.8 a. Rods grown without PEI, but with other conditions the same are shown in figure 4.8 b. There is little difference in the morphology of the rods and the aspect ratios of both sets of rods were around 10. The aspect ratio of the rods did not increase when grown in a greater number of syntheses, up to 20 times. This indicated that for an unknown reason the use of PEI in the synthesis did not give the increased aspect ratio reported in Ref. 62. Therefore PEI was not used for further syntheses.

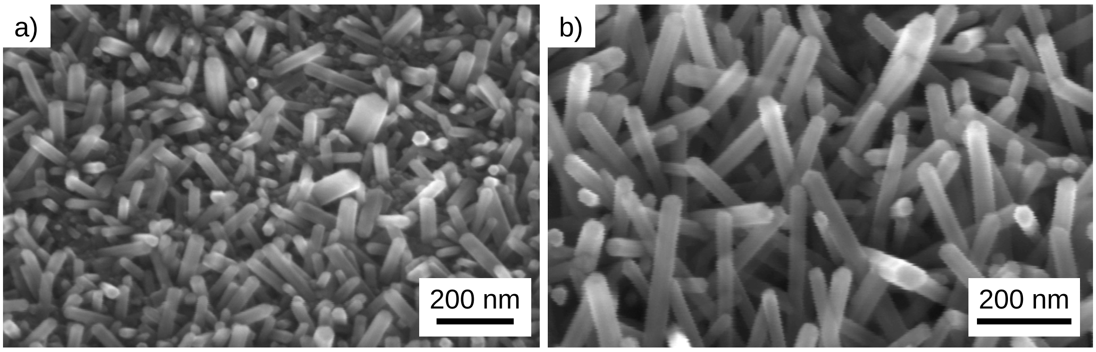

Figure 4.6: **SEM images of ZnO nanorods grown on seeded FTO substrates in aqueous 0.025 M solution of zinc nitrate and HMT.** a) Reactants added hot. b) Reactants added at start, and then heated. Both reactions performed in open bath for 2 hours. Images taken at 45°.

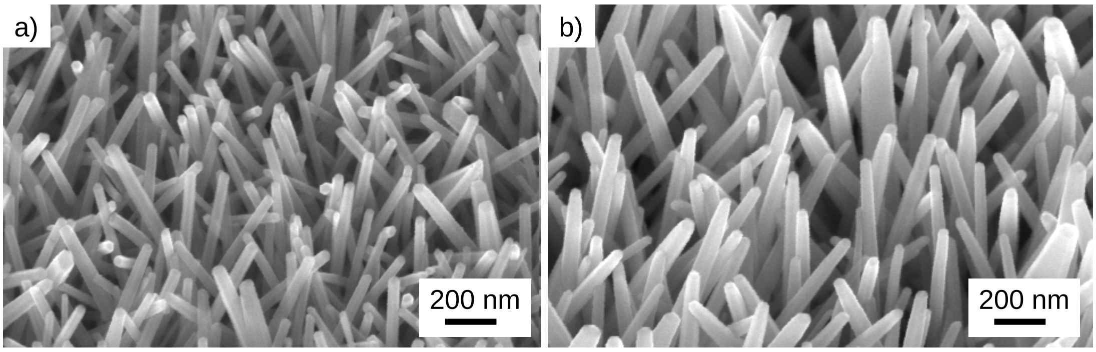

Figure 4.7: **SEM images of ZnO nanorods grown on seeded FTO substrates in aqueous 0.025 M solution of zinc nitrate and HMT.** a) Single synthesis of 2.5 hours. b) Substrates placed in three consecutive syntheses of 2.5 hours with fresh solutions each time. Both reactions performed in a sealed vessel. Images taken at 45°.

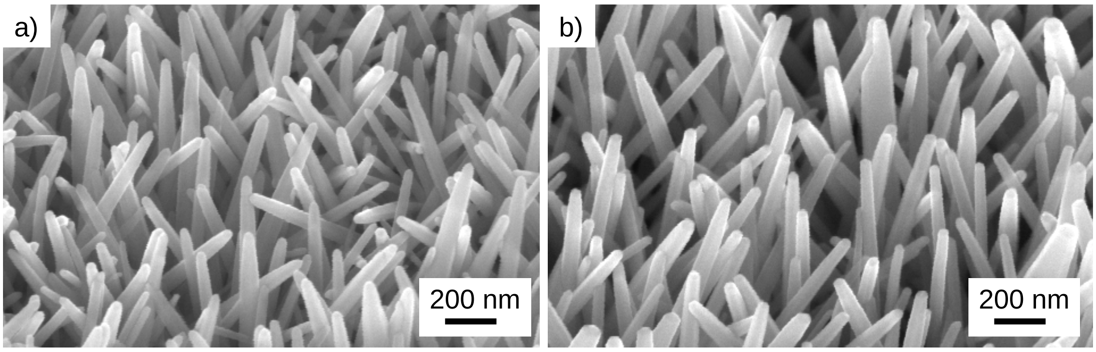

Figure 4.8: **SEM images of ZnO nanorods grown on seeded FTO substrates in aqueous 0.025 M solution of zinc nitrate and HMT.** a) Rods grown with ∼6 mM PEI added to reaction. b) Nanorods grown in same conditions, but without PEI. In both reactions substrates were placed in three consecutive syntheses of 2.5 hours in a sealed vessel with fresh solutions each time. Images taken at 45°.

4.2 Optical properties

4.2.1 Absorption

Optical absorption spectra of ZnO nanorods dispersed in water measured in the Lambda 7 spectrophotometer can be seen in figure 4.9. These nanorods were synthesised in open baths containing 0.01 M solutions of zinc nitrate and HMT. The nanorods that nucleated homogeneously in the solution were collected, washed as described in section 3.1.3, and dispersed in water for measurement. The nanorods display a sharp absorption peak around 370–380 nm (3.36–3.27 eV), which corresponds to the band gap absorption of ZnO (section 2.3). The sample marked by a dashed line displays a more gradual increase in absorption from higher wavelengths to the absorption peak, which is a result of scattering from the nanorods. The Tauc plot [144] of the spectrum with the solid line is shown in the inset. The intercept of the tangent taken near the absorption peak gives the optical gap of 2.8–3.1 eV, depending on where the tangent is taken. This is slightly below the band gap of ZnO, which is normally expected due to band tailing [145]. The optical gap may also appear slightly smaller due to the scattering mentioned above, which will reduce the gradient of the line near to the absorption peak and also makes it difficult to fit a tangent to the line.

Absorption spectra of short ZnO nanorods that have grown on the seeded FTO substrate have a less well-defined peak (figure 4.10 a). This is most likely due to the absorption of the FTO substrate, which increases rapidly below ∼350 nm, and has some absorption below 400 nm. However, for these nanorods, which have been grown in only one synthesis and are therefore only 200–500 nm long, an absorption edge can still be seen at ∼370 nm. Also, the Tauc plot (figure 4.10 b) gives an optical gap of

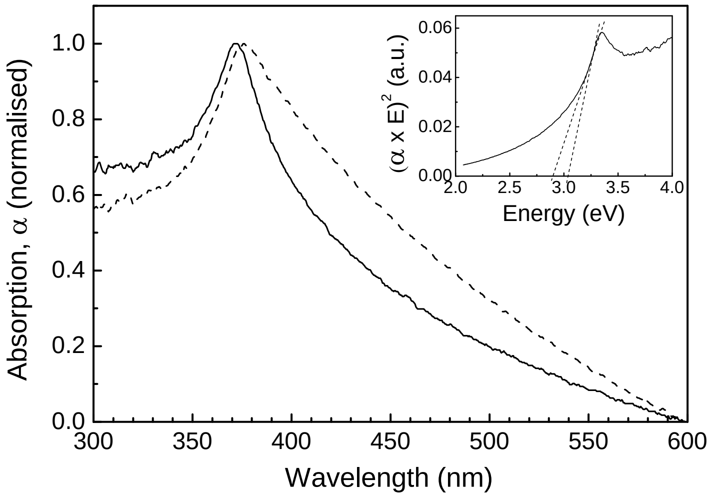

Figure 4.9: **Absorption spectra of ZnO nanorods dispersed in water. Inset shows Tauc plot for one spectrum.** A sharp absorption peak around 370–380 nm (3.36–3.27 eV) can be seen for both samples. Range of possible tangents indicated by two lines on the Tauc plot. Spectra recorded in a Perkin-Elmer Lambda 7 spectraphotometer.

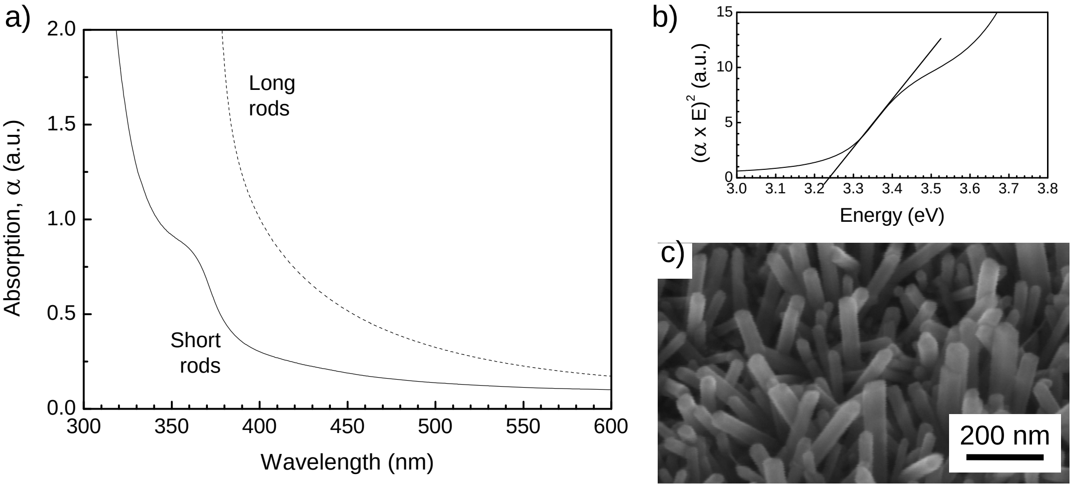

Figure 4.10: **Absorption spectrum (a), Tauc plot (b) and SEM image (c) of short ZnO nanorods grown on seeded FTO substrates. Absorption of longer rods also shown in (a).** Nanorods grown for 2.5 hours at 90 °C, three times in the case of long rods. Spectra recorded in a Perkin-Elmer Lambda 7 spectraphotometer.

3.24±0.02 eV — much closer to the expected band gap, suggesting scattering is less significant from these small rods. For longer rods, as seen in figures 4.7 b and 4.8, an absorption edge cannot be seen (figure 4.10 a). Instead the absorption increases gradually below ~600 nm, and rapidly below ~400 nm. This is both because of increased scattering and because there is much more ZnO in the path of the spectrometer leading to a much higher optical density.

4.2.2 Photoluminescence

The results of PL measurements of ZnO nanorods are presented in figure 4.11. The spectra are normalised to the exciton maximum. The spectrum for ZnO nanorods grown on Ag (figure 4.11 a) contains the common features of ZnO PL, as discussed in section 2.3.2. There is a sharp excitonic peak at ~385 nm and a broad defect-related emission between ~450 nm and ~700 nm. The defect-related emission is quite small compared to the excitonic peak, demonstrating a low level of defects, and that the rods are of good crystalline quality (see section 2.3.2). There is also a large spurious peak at 532 nm, which is a harmonic of the 266 nm excitation. For ZnO nanorods grown on FTO (figure 4.11 b) the deep defect emission at 450–700 nm is even smaller compared to the exciton emission, which implies a better crystallinity than when grown on Ag. This may result from the fact that the nanorods grown on FTO nucleate on ZnO seeds, so will have a good lattice match to the substrate. In the nanorods grown on FTO shoulders to the exciton emission at ~400 and ~420 nm can clearly be seen. The shoulder at ~420 nm can be seen slightly for the nanorods grown on Ag, but is much smaller. These shoulders are discussed in section 2.3.2 as being linked to surface zinc vacancies. This correlates with the fact that the shoulders are more pronounced in the

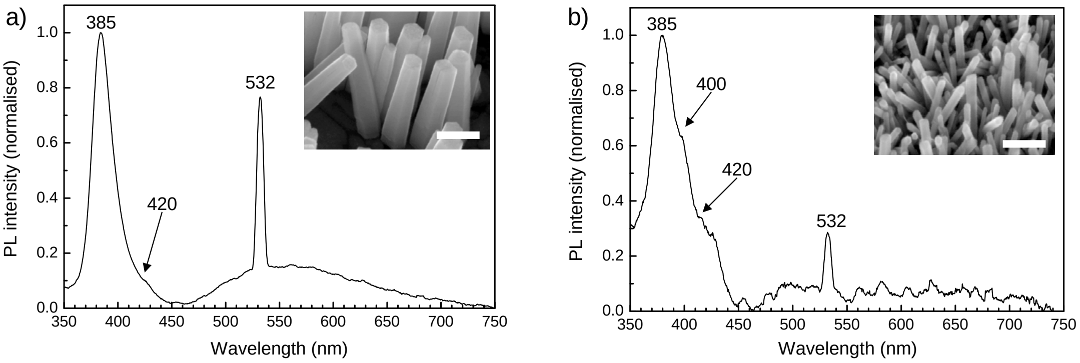

Figure 4.11: **Photoluminescence (PL) spectra of ZnO nanorods grown on Ag (a) and seeded FTO (b) substrates. Insets show corresponding rods, scale bars 200 nm.** ZnO exciton peak (385 nm), laser harmonic (532 nm) and ZnO peak shoulders around 400 and 420 nm are indicated.

nanorods grown on FTO as these rods are smaller so have a higher surface-to-volume ratio, which enhances the luminescence from surface states.

4.3 Summary

Early attempts to grow ZnO nanorods were made on Ag-coated glass substrates using 0.01 M equimolar solutions of zinc nitrate and HMT. When the reactants were added to the reaction bath after it had been heated and the reaction was performed in an open bath the subsequent nanorod growth was unpredictable. Conversely, if the reactants were mixed cold and then gradually heated up and the reaction was performed in a closed vessel the nanorods grew more reliably. It was also found that increasing the reactant concentration to 0.025 M increased the density of nucleation, as well as slightly increasing the size of the rods. Rods grown in this way were $\sim$2 μm long and $\sim$200 nm wide.

ZnO seed layers were deposited onto FTO-coated glass substrates using solutions of zinc acetate in ethanol. Other solvent such as water and isopropanol could not be used to deposit this seed layer, nor could ITO-coated glass substrates. ZnO nanorods were grown on these substrates using 0.025 M equimolar solutions of zinc nitrate and HMT, heated from cold in a closed vessel. After 2.5 hours at 90 °C the rods were $\sim$500 nm long and $\sim$40 nm wide. Substrates were also placed in three consecutive 2.5-hour reactions with fresh solutions, which produced rods $\sim$1 μm long and $\sim$100 nm wide. Absorption spectra of the shorter nanorods showed an absorption peak around 370 nm, and a Tauc plot gave an optical gap of 3.24±0.02 eV. The longer rods did not show a distinct absorption peak, instead the absorption increased gradually below $\sim$600 nm, and rapidly below $\sim$400 nm. 6 mM PEI was used as an additive to the reaction on seeded FTO substrates in an attempt to increase the aspect ratio of the rods. This was not successful, as the aspect ratio was $\sim$10 after 2.5 hours whether or not PEI was used.

Photoluminescence analysis of ZnO nanorods grown on both Ag and FTO-coated substrates showed an the expected exciton emission at ∼385 nm. There was also a defect-related emission at 450–700 nm, which was higher in the rods grown on the Ag-coated substrate. Rods grown on the FTO-coated glass substrate had enhanced shoulders at ∼400 and ∼420 nm to the 385 nm emission, which have been linked to surface zinc vacancies in ZnO and reflect the higher surface-to-volume ratio of the smaller rods grown on FTO.

This chapter has shown that the process to grown ZnO nanorods on transparent conductive substrates using zinc nitrate and HMT solutions was successful. This process was reproducible and could be repeated multiple times on the same substrates to produce longer rods. These rods were therefore suitable for use in the proposed solar cells.

Chapter 5

Sb-doped ZnO nanorods

The aim of the growth methods for Sb-doped ZnO nanorods studied here and described in section 3.1.4 was to achieve successful doping of ZnO nanorods where the dopant source was introduced during the aqueous chemical synthesis of the nanorods, rather than in post-growth, high temperature steps as demonstrated previously (section 2.3.3). The motivation for achieving this doping was the production of p-type ZnO nanorods. These could then be used in the solar cell structure to produce a new type of eta solar cell where the nanostructured basis was formed of a p-type, rather than n-type material. The layer coated on top of the absorber-coated nanorods would then need to be n-type rather than p-type to form a p-n junction. The choice of materials for this layer would therefore be much larger than the limited choice of p-type materials described in section 2.2.2, as there are a large range of possible wide band-gap n-type materials that could be deposited onto the LbL-coated ZnO nanorods. It also raises the possibility of using n-type ZnO on top of the p-type nanorods, forming a cell based on a p-n ZnO homojunction.

As explained in section 3.1.4, Sb was added to the reaction such that the concentration of Sb ions was either 5, 1 or 0.1 $\%$ that of the Zn ions. In this chapter the convention for doping of semiconductors is followed such that these are referred to as 5, 1 and 0.1 at.$\%$. This makes the assumption that Sb substitutes for Zn, so that the formula of the doped material is $\mathrm{Zn}_{(1-x)}\mathrm{Sb}_x\mathrm{O}$ and the Sb content is referred to as $(x \times 100)$ at.$\%$. Whether this refers to the added ratio of Sb and Zn or the measured ratio of Sb and Zn is specified in the text. The properties of the rods that were produced by these methods are explored in this chapter through their structure, composition, optical and electrical properties.

5.1 Morphology and composition

When Sb acetate dissolved in water was added directly to the reaction it strongly affected the crystal quality of the rods, giving ovoid rather than hexagonal structures (figure 5.1). The rods shown formed as homogeneous precipitate in the solution, as the addition of Sb acetate in this way led to very little nucleation on Ag substrates. It

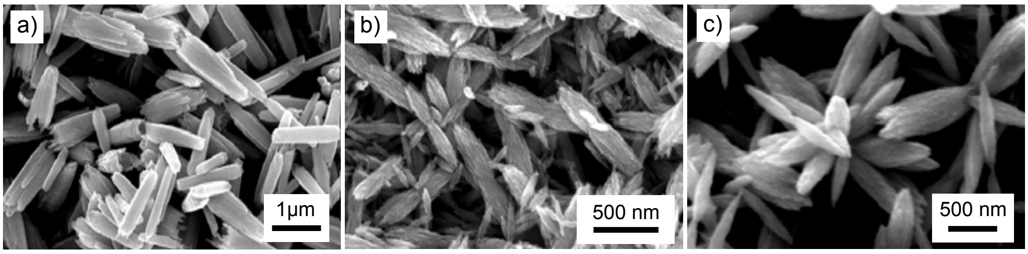

Figure 5.1: **SEM images of ZnO nanorods grown in aqueous 0.01 M solution of zinc nitrate and HMT with Sb added from aqueous solutions of Sb acetate.** a) 0.1 at.% Sb added. b) 1 at.% Sb added c) 5 at.% Sb added. Ag substrates were placed in solution but few nanorods nucleated on substrates so nanorods shown grew homogeneously in solution and were deposited for imaging.

is likely that the addition of Sb disrupts the growth of ZnO nanorods due to formation of a secondary phase rather than the desired incorporation of Sb ions into the ZnO lattice. When dissolved in water, Sb acetate hydrolyses readily to form Sb_2O_3 [146]. If this reaction occurs more rapidly than the formation of ZnO then it is likely that separate crystals of Sb_2O_3, which has an orthorhombic structure [146], will form in the solution, beginning before the nucleation of ZnO. These Sb_2O_3 particles could then act as nucleation points for what appears to be homogeneously nucleated ZnO (i.e. ZnO forming as a precipitate in the solution, rather than nucleating on the substrate). Due to the difference in crystal structure ZnO nucleated on these crystals will not have the recognised clear hexagonal structure of ZnO nanorods, but instead have a less crystalline structure such as that seen in figure 5.1. When adding increasing quantities of Sb to the reaction the growth of ZnO would be more disrupted by the presence of larger quantities of Sb_2O_3 and the structure would be more altered, as observed. In order to prevent this disruption to the growth of ZnO the synthesis was adapted to limit the formation of Sb_2O_3 by controlling the supply of free Sb ions in the aqueous solution in a similar way that the supply of Zn ions is controlled to form nanorods (see section 2.3.1). Ethylene glycol (EG) was used as a solvent for Sb acetate to try and achieve this control. Sb acetate could be successfully dissolved in EG and it was thought that EG would act as a chelating ligand for Sb, limiting the concentration of free Sb ions in the solution.

When Sb acetate was dissolved in EG before adding to the reaction solution there was a much less marked effect on the nanorod growth, as can be seen in figure 5.2. For all doping levels trialled the rods retained the hexagonal structure of ZnO and nucleated densely on the substrate. The addition of Sb to the reaction also had a size-limiting effect on the ZnO nanorod growth: all rods shown in figure 5.2 were grown in 0.1 M solutions of zinc nitrate and HMT, and it can be seen that as more Sb was added to the reaction the final size of the rods was reduced and aspect ratio increased.

Control experiments were performed by adding only EG to the reaction without Sb acetate. This showed that the EG did not have a noticeable effect on the reaction when added on its own, as can be seen in figure 5.3. Here rods grown with 1 at.% Sb added

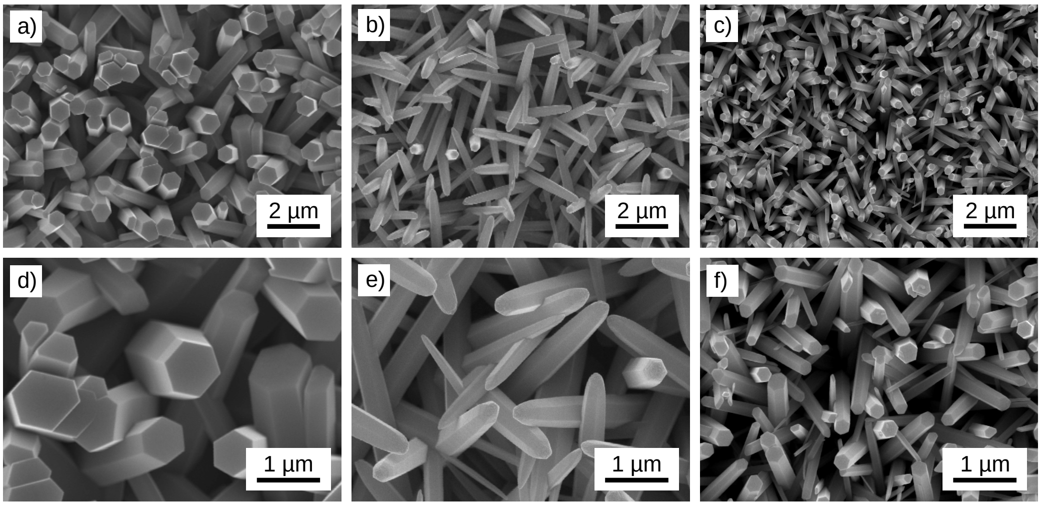

Figure 5.2: **a)–c) Wide, and d)–f) close-up SEM images of ZnO nanorods grown in aqueous 0.1 M solution of zinc nitrate and HMT, doped with Sb by adding Sb acetate dissolved in EG.** a), d) 0.1 at.% Sb added. b), e) 1 at.% Sb added. c), f) 5 at.% Sb added. Nanorods grown on Ag-coated substrates.

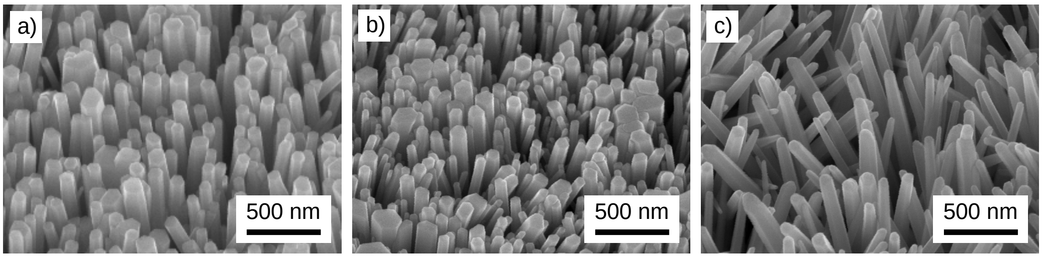

Figure 5.3: **Comparison of SEM images of ZnO nanorods grown in aqueous solutions of zinc nitrate and HMT with different additives.** a) 0.025 M zinc nitrate and HMT, with no additives. b) 0.025 M zinc nitrate and HMT with EG added. c) 0.1 M zinc nitrate and HMT with EG and 1 at.% Sb added. Nanorods grown on Ag-coated substrates seeded using Zn acetate in ethanol method.

are also shown, demonstrating that the doped rods grow with a higher aspect ratio, and less well-aligned on the substrate. These rods were grown on Ag-coated substrates that had been seeded with a layer of ZnO derived from zinc acetate in ethanol solutions (section 3.1.1), hence the high density of nucleation. The size difference due to the doping is also apparent, as the concentration of zinc nitrate and HMT had to be increased to produce doped rods (figure 5.3 c) of a similar size to the undoped ones (figure 5.3 a and b). The rods grown with only EG (figure 5.3 b) were the same size as those grown without EG (figure 5.3 a) when using the same reaction concentration. This confirms that it was the presence of Sb, not EG that limited the size of the nanorods and increased the aspect ratio. The smaller overall size, and especially diameter of the rods grown with Sb added to the reaction could result from Sb limiting the rate of growth of the rods so that they grow smaller in the reaction time. However, the reaction still ended after ∼2 hours irrespective of the Sb concentration, implying that the reactants were still depleted in the same time. If the overall rate of rod growth were limited by the addition of Sb, it would be expected that it would take longer for the reactants to be used up. However, if the *overall* rate of growth was not affected, but instead only the rate of growth on the substrate, this could produce smaller rods on the substrate while the reactants were still used up in a similar time by the production of homogeneously nucleated precipitate. This is supported by the quantity of precipitate produced in the reaction: the quantity of precipitate produced in a 0.1 M reaction with Sb added was greater than that produced in a 0.1 M reaction without Sb, implying that a larger proportion of the reactants were used up producing homogeneously nucleated precipitate and less in the heterogeneously nucleated rods on the substrate. A reduction in the rate of growth of the rods on the substrate could also account for the higher aspect ratio: the high aspect ratio of the rods in this reaction is caused by the limited OH^- ion supply slowing the formation of ZnO [95]. Therefore if the presence of Sb slowed the rate of ZnO formation on the substrate even further it would be expected that the rod aspect ratio would be greater. The larger aspect ratio of the Sb-doped rods could also be caused by a change in the nucleation on the substrate; if the Sb-doped ZnO produced a larger number of smaller nuclei than the undoped ZnO the rod diameter would be limited while the length would be more similar.

The more hexagonal morphology and higher nucleation density compared to preliminary trials implied that the desired control of Sb supply had been achieved by using EG. The change in size of rods with Sb doping indicated that the presence of Sb had an effect on the growth. However, to confirm that this effect was accompanied by the inclusion of Sb in the nanorods, and that the Sb supply was not reduced too much by the EG, EDX measurements were performed to ascertain the Sb content of the rods. Both when adding Sb from aqueous solution and EG solution the Sb content was confirmed by EDX, an example of which is shown in figure 5.4 a. The average

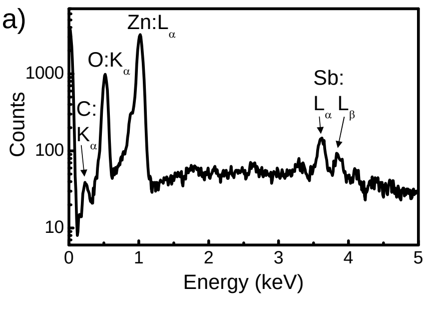

b)

Sb added	Sb measured (homogeneous)	Sb measured (heterogeneous)
5 at.%	3.1±0.8 at.%	1.06±0.09 at.%
1 at.%	0.66±0.08 at.%	0.75±0.07 at.%
0.1 at.%	0.52±0.09 at.%	Not detected

Figure 5.4: **a) Energy-dispersive X-ray (EDX) spectrum of Sb-doped ZnO nanorods with 5 at.% Sb added (nucleated homogeneously). b) Table of average measured vs. added quantities of Sb in the samples.** ‘Homogeneous’ in measured refers to homogeneously nucleated rods that had been deposited onto substrates for survey, and ‘heterogeneous’ refers to heterogeneously nucleated rods that were surveyed in-situ on the substrates. All rods surveyed were doped with Sb from EG solutions.

quantities of Sb measured in samples doped using EG are shown in the table in figure 5.4 b. The quantities were measured separately for nanorods that had nucleated homogeneously in the solution, which were then deposited onto a substrate for EDX survey, and nanorods that nucleated heterogeneously on the substrate. Both types of rods were surveyed to determine if there were any differences in the Sb-content of rods nucleated by these two different mechanisms. The values are averages of a number of EDX scans of different areas and different samples prepared by the same method and the errors given are the standard errors of these averages. Each doping content added (0.1, 1 and 5 at.% Sb) will be discussed separately, as the implications of each are different.

When 5 at.% Sb was added to the reaction the measured quantities of Sb in both the homogeneously and heterogeneously nucleated rods were lower than that added. However, the quantity measured in the heterogeneously nucleated rods was around three times lower than in homogeneously grown rods. When taking scans of more detailed areas of the homogeneously nucleated rods it was found that there were structures with irregular morphology that had much higher levels of Sb — up to 13 at.%. Such structures are shown in figure 5.5 b. The presence of these phases accounts both for the higher level of Sb measured in homogeneously nucleated rods than in heterogeneously nucleated rods, and the lower measured Sb content in the rods than the added Sb content: some of the excess Sb that was added formed Sb-rich phases such as those seen in figure 5.5 b in the homogeneously precipitated rods, but not in the rods grown

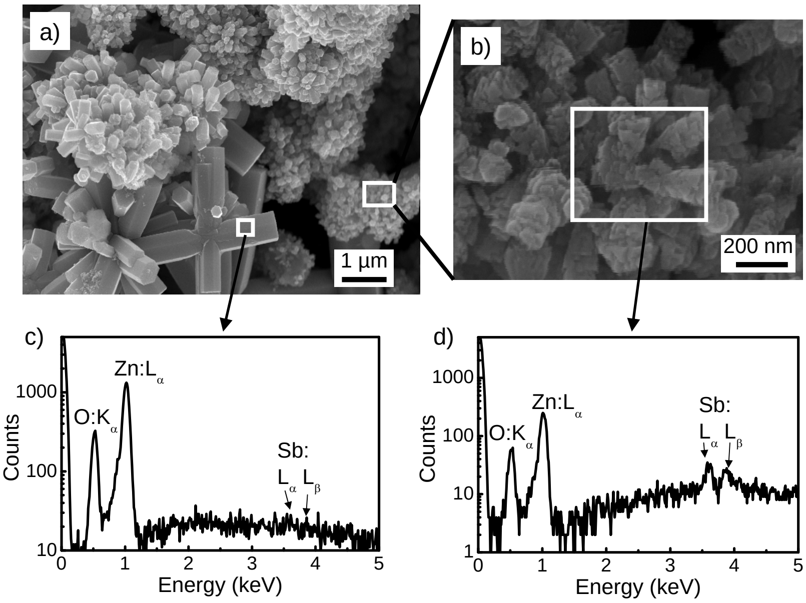

Figure 5.5: **EDX spectra of Sb-doped ZnO nanorods nucleated homogeneously with 5 at.% Sb added (c and d) corresponding to the indicated areas on the SEM images (a and b).** c) Spectrum of the hexagonal rod indicated, measuring 0.75 at.% Sb, which is close to the limit of detection above the noise. d) spectrum of the less well-defined phase, as seen in the corresponding SEM image and measured 13 at.% Sb.

on the substrate (when no such structures were seen). Hence, when surveying large areas of the precipitate the inclusion of some of this phase increased the average measured Sb content, but no such effect would occur with the surveys of rods nucleated on the substrates. The higher error in the measurement of the homogeneously nucleated rods reflects the fact that the Sb content was less consistent across the different areas surveyed. It is possible that some of the Sb-rich phases were washed away in the process of washing the precipitate as they are generally smaller and so more easily dispersed. This could account for the measured value of Sb in the homogeneously nucleated rods still being lower than the amount added. It is also possible that some of the Sb remained dissolved in the solution and did not form a solid precipitate at all, therefore was washed away immediately. It is most likely that a combination of these factors reduced the final measured Sb content of the rods.

To measure the Sb content only of the homogeneously nucleated nanorods with standard morphology and not include excess Sb that was present in different phases EDX scans were performed on isolated rods which had been suspended in solution and repeatedly washed to remove possible traces of synthesis chemicals and soluble phases. This was performed for rods with 1 at.% Sb added, which were dispersed in water and deposited on C-coated glass sparsely so single rods could be isolated. C-coated glass was used as a conductive substrate instead of Ag or ITO because the C peak lies well away from the Sb peak in the spectrum, whereas both Ag and In are close to Sb on the spectrum. An example EDX spectrum from one of these scans is shown in figure 5.6 a, and figure 5.6 b shows the rod that was surveyed for this scan. The high level of C and Si come from the substrate. A survey of 45 points detected an average of 0.66±0.08 % Sb. This value of Sb-content is an average of the entire volume of the rod. This is because the thickness of the rod (<500 nm) means that X-rays will be generated from the full cross-section (and below, as demonstrated by the high level of signals from the substrate), and surveys were taken along the whole length. Performing the survey of homogeneously precipitated rods in this way led to much more similar values being measured for homo-and heterogeneously nucleated rods, as can be seen in figure 5.4 b. The measured Sb-content is below that added, similarly to when 5 at.% Sb was added, but not by as much as the heterogeneously

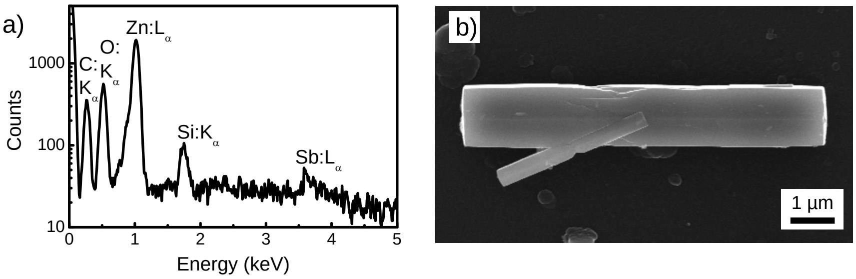

Figure 5.6: **a) EDX spectrum of isolated Sb-doped ZnO nanorod with 1 at.% Sb added, measured from a point on rod shown in (b).** Rod washed repeatedly and dispersed on C-coated glass substrate.

nucleated rods when 5 at.% Sb was added. This supports the suggestion that some of the Sb was incorporated in secondary phases that had a different morphology and that some may have been washed away in the solution. The fact that a lower proportion of the Sb added was incorporated when 5 at.% Sb was added implies that the Sb-content in ZnO could be approaching the solid solubility limit, leading to a saturation of the Sb content. It could also be that the duration of the reaction was not sufficient for the full quantity of Sb to become available from the EG at the higher doping levels; it may be that a fine-tuning of the Sb acetate concentration in EG is required to achieve the right balance of slow Sb supply to retain the ZnO morphology, but high enough Sb supply that the full quantity of Sb added is incorporated in the ZnO by the end of the reaction. Investigations into adding the same quantity of Sb to the reaction, but dissolved in different amounts of EG would ascertain whether this has an effect on the quantity of Sb included. The fact that surveying the isolated rods in the way described led to much more consistent Sb measurements between homo- and heterogeneously nucleated rods suggests that the heterogeneously nucleated rods and the standard morphology homogeneously nucleated rods do have a very similar Sb content, and there is not a fundamental difference in the incorporation of Sb in these two types of rods

Where 0.1 at.% Sb was added the measurement of Sb content in homogeneously nucleated rods was higher than the amount of Sb added, and in heterogeneously nucleated rods no Sb was detected. The inconsistency in these measurements can be attributed to the limit of the accuracy of the quantitative EDX measurements when detecting at this level: 0.1 at.% is close to the minimum level that can be resolved, so although the random error in the sampling suggests the value of Sb lie above that added, the measurement of 0.52±0.09 at.% Sb at least confirms the presence of Sb, and indicates that it is within the order of magnitude of the quantity added. This implies that the heterogeneously nucleated rods may contain some Sb despite none being detected, especially when considering the above findings that standard morphology homo- and heterogeneously nucleated rods contain approximately the same Sb content. However this would have to be confirmed by other means, such as EDX measurements in a TEM system which can give a much more accurate indication of the presence of small quantities of dopant.

The successful growth of Sb-doped ZnO nanorods with a hexagonal morphology suggests that the use of EG as a solvent and chelating ligand for Sb facilitated the desired control of Sb-ion supply in the reaction, while still providing a sufficient supply of Sb to be included in the rods. To ascertain whether the doping of the ZnO nanorods in this way had any effect on the crystal structure of the rods, X-ray diffraction measurements were performed. The resulting spectra can be seen in figure 5.7. It can be seen that the peak positions do not change within the precision of the measurement as different quantities of Sb were added to the nanorods, indicating that the crystal structure and lattice spacing were not affected by the addition of Sb. The spectrum corresponds to the ICDD spectrum 35-1451 for wurzite ZnO, as expected. The high (002) peak is indicative of nanorods that are aligned along the c-axis. There is a slight change in the ratio of the (002) to the other peaks with Sb doping, which is

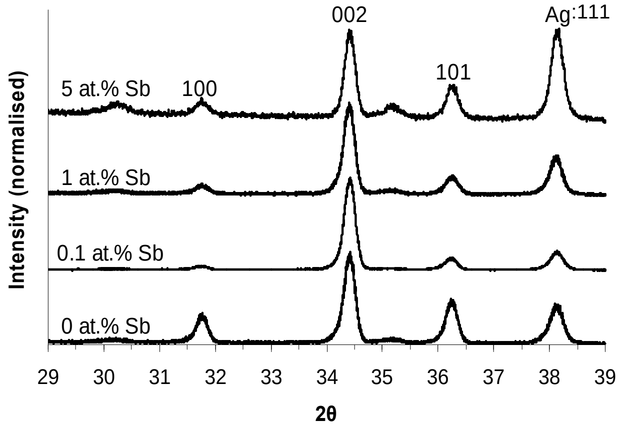

Figure 5.7: **XRD spectra of ZnO nanorods doped with Sb, with Sb quantities added as indicated.** Indices are annotated for the wurzite ZnO structure from ICDD 36-1451, as well as the peak corresponding to the Ag substrate.

indicative of the different aspect ratios and alignment with different doping levels. If any secondary phases were present, they were not detectable above the level of noise. These XRD spectra support the observations from the SEM images that when doping ZnO nanorods with Sb and controlling the Sb ion supply with EG the structure of the nanorods is not adversely affected, retaining the hexagonal wurzite structure of ZnO. Further analysis such as high resolution transmission electron microscope (HR-TEM) studies of the doped nanorods would help to ascertain any lattice changes in the ZnO resulting from Sb doping that could not be detected with XRD.

5.2 Optical properties

5.2.1 Absorption

Figure 5.8 shows absorption spectra of ZnO nanorods both undoped, and doped with 0.1 or 1 at.% Sb. 5 at.%-doped rods could not be surveyed due to high levels of scattering. These spectra were recorded for nanorods that grew as a homogeneous precipitate in solution, as absorption could not be measured for heterogeneously nucleated nanorods on Ag substrates, which are opaque. The rods surveyed were grown using Sb in EG solutions as the Sb source in the reaction. It can be seen that the absorption peak shifts towards shorter wavelengths with higher Sb content. The absorption peaks occur at approximately 375 nm (3.31 eV), 367 nm (3.38 eV) and 350 nm (3.55 eV) for 0, 0.1 and 1 at.% Sb-doped rods. Tauc plots were not made of this absorption data as high scattering made them unreliable. The increasing energy of the exciton-related absorption peak with increasing Sb-doping implies the inclusion of Sb in the ZnO nanorods led to a widening of the band gap. This implies that the inclusion of Sb into the ZnO leads to a change in band structure of the material, which could be caused by changes in the electronic environment due to the presence of the Sb orbitals and

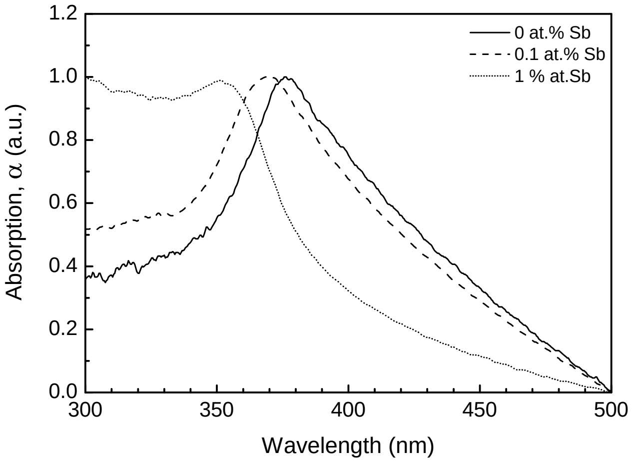

Figure 5.8: **Absorption spectra of ZnO nanorods undoped and with 0.1 and 1 at.% Sb added.** Sb added to reaction in EG solution. Nanorods surveyed grew homogeneously in solution and were diluted and dispersed in water for analysis.

also lattice strain due to the different size of the Sb ions or Sb-vacancy complex. It is possible that as the homogeneously nucleated rods were used for the absorption measurements some of the Sb-rich phases discussed above were included in the material surveyed. This could account for the large shift in absorption peak observed despite relatively small quantities of Sb being added, as some of the Sb-rich phases may have had Sb content as high as 10 at.%.

5.2.2 Photoluminescence

The photoluminescence spectra of undoped ZnO nanorods and 1 at.% Sb-doped ZnO nanorods on Ag substrates are shown in figure 5.9. The spectrum for undoped ZnO clearly shows the exciton peak, at ∼390 nm in this case, slightly shifted from that observed in section 4.2.2. The doped nanorods also show an exciton peak in this region, but which is much more broadened and possibly shifted slightly to the blue, consistent with, but not as pronounced as, the shift in the absorption measurements. It is possible that the blue shift is not as pronounced as that seen in the absorption measurements because the heterogeneously nucleated rods used for the PL measurements did not contain any of the Sb-rich phases: all of the rods surveyed would have less than 1 at.% Sb content based on section 5.1, so they would only be expected to have a very small shift. The ∼400 and ∼420 nm shoulders discussed in section 4.2.2 are also more pronounced, and the 400 nm shoulder is nearly visible as a separate peak. It is unlikely that these enhanced shoulders can be solely attributed to the slightly higher aspect ratio of the doped rods compared to undoped. These enhanced shoulders suggest that there is a higher density of zinc vacancies (V_{Zn}) in the doped rods, which could suggest the successful formation of the Sb_{Zn}-$2V_{Zn}$ complex, which is required for p-type doping using Sb. The introduction of Sb into the nanorods has also led to

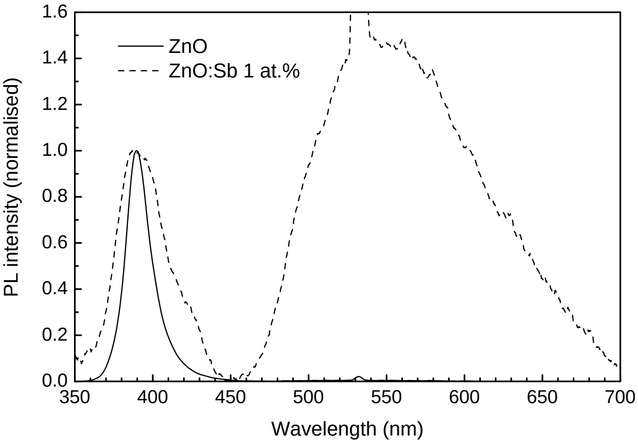

Figure 5.9: **Photoluminescence spectra of ZnO nanorods undoped and with 1 at.% Sb added.** Sb added to reaction in EG solution. Surveys were performed on nanorods grown on Ag substrates. Normalised to exciton peaks.

a significant increase in the level of deep defects: the broad defect band, absent in the undoped rods, is higher than the exciton peak in the doped rods. The defect band is a similar shape, i.e. spans the same wavelengths as that observed in undoped rods in section 4.2.2. This suggests that the deep defects present in undoped rods also occur in Sb-doped rods, but at a higher level, rather than different deep defects occurring in the doped rods.

5.3 Electrical properties

To further investigate the impact of the Sb doping on the carrier content and type within the rods, electrical measurements were performed. These were taken using an atomic force microscope (AFM) fitted with a Pt/Ir tip. The tip of the AFM was lowered onto the top of a nanorod, a voltage was applied between the AFM tip and the Ag substrate, and the resultant current was measured (figure 5.10 c). The applied voltage range was ±5 V. The resulting current vs. field data are shown in figure 5.10 a, with a close-up of the data in figure 5.10 b. As the range of voltages surveyed for each rod was the same but the length different the range of *fields* across each rod was different. Hence the data for undoped rods only spans approximately $\pm 1.2\,\mathrm{V}/\mu\mathrm{m}$ on the chart. On the plot the forward current (positive voltages) corresponds to positive Pt and negative Ag. I-V measurements could be taken only once for each rod as the measurement was performed in the short period that the tip remained on the top of a rod, and the same rod could not be re-contacted reliably.

In the undoped case the I-V curve shows no current in the reverse direction. The forward current switches on at about 1 V/μm, and grows exponentially. This behaviour indicates the existence of Schottky diodes at the interfaces of the nanorod with each metal contact, acting in opposite directions. The absence of any reverse current indi-

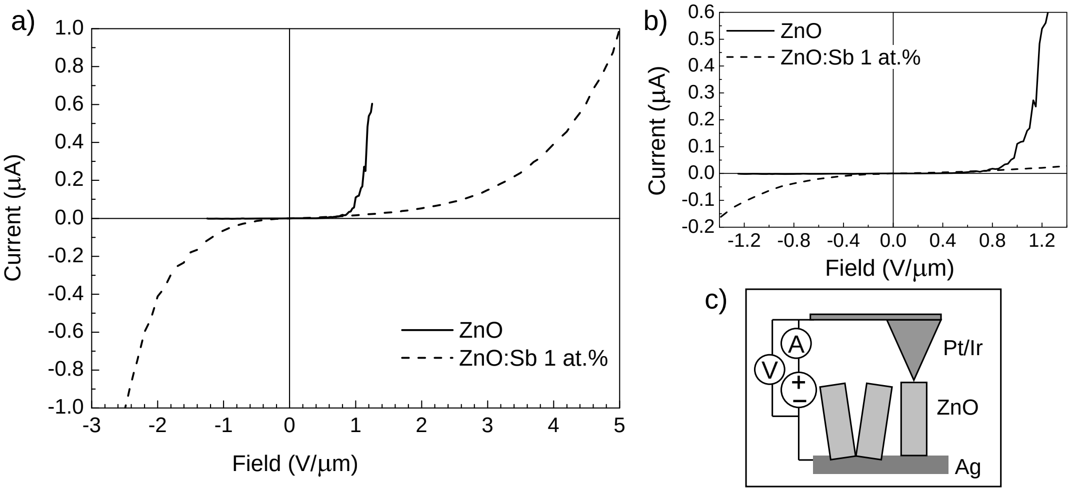

Figure 5.10: **a) Current-voltage measurements of ZnO nanorods undoped and with 1 at.% Sb added. b) Close-up of $\pm$1.2 V/μm region. c) Schematic of method for obtaining measurements using tip of AFM.** Sb added to reaction in EG solution. Applied voltage has been converted to field by dividing by the length of the nanorod surveyed.

cates that the potential barrier for electrons is larger for the Pt contact, which can be explained by its higher work function compared to Ag; when a voltage is applied in the negative direction, the Ag contact is under forward bias for electrons, so current can flow through it easily. However, the Pt contact is under reverse bias and current cannot flow through it, so no overall current results. In the opposite situation (positive field on the graph) the Pt contact is under forward bias, so current can flow through it easily, but the Ag contact is under reverse bias. Because the barrier is small at the Ag contact due to Ag having a lower work function, the diode breaks down easily, and the overall current increases exponentially following reverse breakdown behaviour. This behaviour is therefore consistent with the expected band configuration of n-type nanorods where the current is due exclusively to electrons.

In the Sb-doped case, the forward current switches on around +2 V/μm and grows exponentially, but more slowly than for undoped rods. The reverse current switches on around -1 V/μm and shows non-linear behaviour that does not fit a single model. A model for the overall behaviour could not be produced, as it is likely that a combination of forward and reverse breakdown currents for both barriers were contributing to the behaviour in both directions of applied voltage. However, similar behaviour has been observed previously when taking I-V measurements on acceptor doped ZnO [147], suggesting that the overall behaviour in the Sb-doped case may be consistent with a model based on p-type nanorods with a Fermi level near the valence band. However, this behaviour could also be explained by electron currents assisted by defect states, or mixed conduction. Further analysis is necessary for a more complete understanding, such as the construction of field-effect transistors using the nanorods.

5.4 Summary

It was shown that in-situ Sb-doping of ZnO nanorods could not be performed by adding Sb acetate directly to the reaction. This produced ovoid structures that did not have the hexagonal structure of ZnO nanorods, and very few rods nucleated on the Ag-coated substrates. By dissolving the Sb acetate in ethylene glycol (EG) before adding to the aqueous solution nanorods with the desired hexagonal morphology and high density of nucleation were produced. These rods had a very similar morphology to those without Sb-doping, although the more Sb that was added the smaller the rods grew overall (length and diameter) and the higher their aspect ratio (diameter reduced more than length). This change was due solely to the Sb, as addition of EG alone did not affect the morphology. It is possible that the addition of Sb slowed the growth of ZnO nanorods leading to the final formation of smaller, higher aspect ratio rods. The successful growth of hexagonal rods in the presence of Sb may be due to the chelating effect of EG: the supply of free Sb ions in the solution is slowed by the EG, which limits the formation of secondary phases such as Sb_2O_3 which may disrupt the nanorod growth. The inclusion of Sb into the ZnO lattice is therefore achieved with minimal disruption.

The inclusion of Sb into the ZnO nanorods was confirmed using EDX. Both homo- and heterogeneously nucleated rods had a lower measured Sb content than was added. The Sb content of homogeneously nucleated rods appeared to be higher in EDX scans, but this was attributed to the presence of Sb-rich phases in the precipitate. When individual homogeneously nucleated rods with 1 at.% Sb added were isolated and surveyed they measured 0.66±0.08 at.% Sb. This was very close to 0.75±0.07 at.% Sb, which was measured for heterogeneously nucleated rods also with 1 at.% Sb added. This indicated that the Sb content of homo- and heterogeneously nucleated rods was most likely very similar when Sb-rich phases were not included. Heterogeneously nucleated rods with 5 at.% Sb added contained 1.06±0.09 at.% Sb. Measurement of the Sb content of rods with 0.1 at.% Sb added was difficult as this was close to the detection limit of the EDX system. However, some Sb was detected in homogeneously nucleated rods, although higher than the level added, suggesting there may have been Sb in the rods. It was also shown that there were no significant changes in the crystal structure of the rods when the Sb was added, as XRD scans showed standard peaks for wurzite ZnO aligned along the c-axis, with no detectable shift due to Sb doping.

Optical absorption measurements of the doped nanorods showed a shift in the absorption peak to shorter wavelengths with increasing Sb content. This suggested that the inclusion of Sb into the nanorods was causing a change in the band structure in the ZnO so that the optical gap was increased as Sb was added. Photoluminesce measurements also showed a significant change with Sb doping. There was a significantly higher level of deep defect emissions from the doped nanorods, suggesting the addition of Sb had led to a higher level of structural defects in the nanorods. This defect emission occurred in the same range of wavelengths as the undoped rods, but was more intense, suggesting that Sb doping did not induce different deep defects, only the same ones at higher levels. In the region of the exciton peak there were much more pronounced shoulders in the doped rods, which have been linked to zinc vacancies. These zinc vacancies are present in the complex formed when Sb or As are doped in ZnO, which has been used to explain the p-type behaviour of such materials. This evidence suggests that the Sb may have been included in the ZnO lattice in structures that lead to an increased acceptor concentration.

Electrical measurements performed on the nanorods could not conclusively show that p-type nanorods had been produced with Sb-doping. However, it was confirmed that undoped rods behaved as an n-type semiconductor. The doped nanorods did show significantly different electrical behaviour, similar to that seen previously in p-type ZnO, but a model could not be fitted that definitively proved p-type behaviour.

It has been shown that Sb can be successfully incorporated into ZnO nanorods during the chemical synthesis without significantly altering the morphology by adding Sb acetate from a solution in EG to control the supply of Sb ions to the reaction. Both optical and electrical measurements demonstrated changes that could be linked with p-type behaviour. However, this could not be conclusively proven with the data obtained thus far. These Sb-doped nanorods will therefore not be used in solar cells in the way described in the introduction to this chapter, as it cannot be assumed that they are p-type, and therefore a cell with the structure p-ZnO/CdTe-PDDA/n-type cannot be produced. Further investigation of the electrical properties of the nanorods would show whether p-type rods have been produced by this method.

Chapter 6

CdTe nanoparticle layer-by-layer films

The layer-by-layer (LbL) process used in this project had been developed previously by Dr D. E. Gallardo for the deposition of CdTe-PDDA films for use in LEDs [5, 142]. The parameters for the deposition as described in section 3.3 were optimised to produce smooth films with a high volume fraction of nanoparticles ($\sim$30 %). The aim of this chapter, rather than further altering the parameters to produce any further optimisation, was to ascertain whether the LbL process could be used to coat a structured substrate such as the ZnO nanorods and to study the subsequent morphology and properties of the coating, as well as any interactions between the ZnO and CdTe. Later, studies were also made into the effects of annealing the LbL films, both when deposited on planar substrates such as glass or ITO, and on ZnO nanorods. The results of these studies are described in this chapter.

6.1 Morphology and composition

A high resolution transmission electron microscope (HR-TEM) image of a CdTe-PDDA LbL film as used in this project is shown in figure 6.1. This LbL film had 5 CdTe-PDDA bilayers, and was deposited directly onto the TEM grid. The lattice pattern of the CdTe can just be resolved, and the particles appear to be $\sim$3 nm in diameter, which is consistent with previous absorption measurements carried out by Dr Gallardo, as mentioned in Ref. [5]. The random packing of the nanoparticles can also been seen from the image, and the average inter-particle spacing of 2–3 Å was found to be consistent with packing models obtained from X-ray reflectivity data [5].

It can be seen from figure 6.2 that the CdTe-PDDA film coated the ZnO nanorods conformally when using the LbL process. This conformal coating results from the electrostatic bonding that allows the layers to build up in this process; each monolayer bonds to the surface regardless of the shape, as long as the nanoparticles/molecules can reach the surface, and the washing process ensures that an even coating is left on the surface by removing excess, poorly-bonded material. The subsequent layers then bond to the previous, leaving an even coating across the surface. The presence of CdTe and PDDA in the coating was confirmed by EDX measurements. These showed

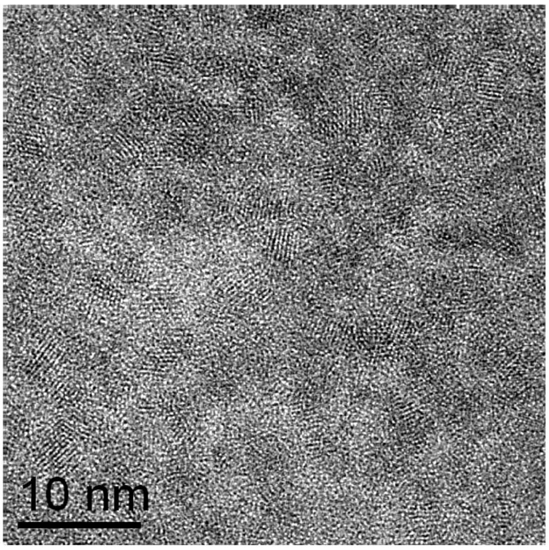

Figure 6.1: **HR-TEM image of a 5-layer CdTe-PDDA LbL film.** Deposited directly onto a TEM grid. Image obtained by Dr Gallardo, and taken from Ref. [5].

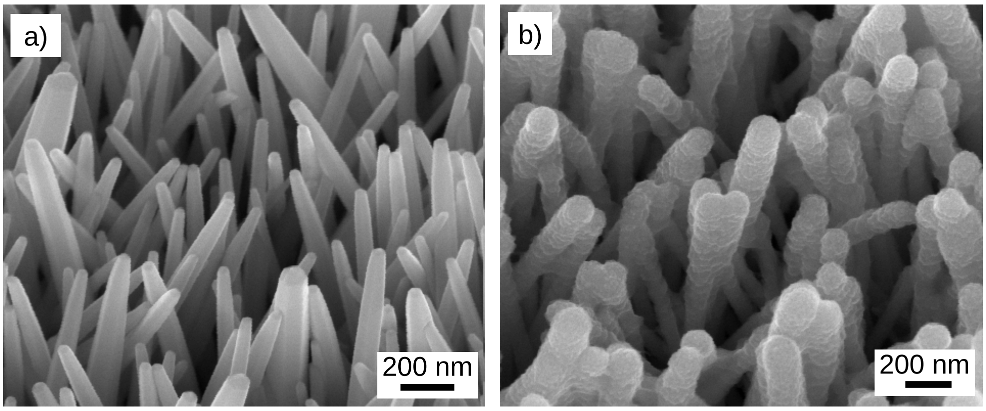

Figure 6.2: **SEM images of ZnO nanorods uncoated (a) and coated with 30 layers of CdTe-PDDA using the LbL process (b).** Nanorods were grown in 0.025 M solutions of zinc nitrate and HMT in a closed jar at 90 °C for a total of 15 hours.

Cd, Te and S from the thiol-capped CdTe, and C from the PDDA, as well as Zn and O from the nanorods (figure 6.3).

It was noted that the success of the process relied on the solutions being refreshed at reasonably regular intervals (after approximately every 100 layers coated), especially the nanoparticle solution. If the solution was not completely replaced but instead topped-up with extra nanoparticles the film produced was much less even and penetrated poorly between the nanorods (figure 6.4 a). This poor coating likely resulted from a degradation of the precursor solution(s) (PDDA and/or CdTe nanoparticles) after repeated dip cycles. This degradation caused an agglomeration of the nanoparticles in solution: agglomerated lumps were observed at the bottom of the solution after the run.

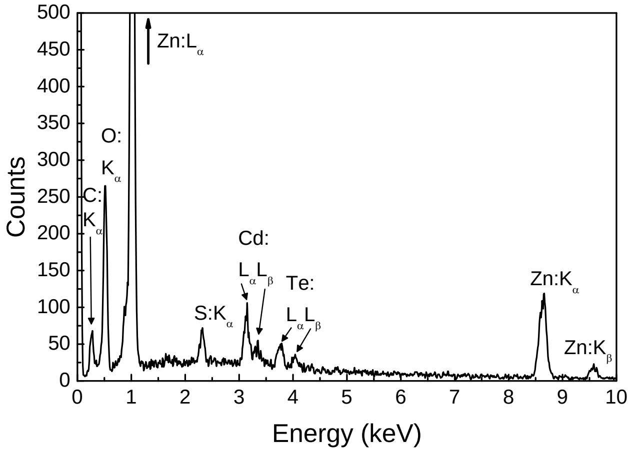

Figure 6.3: **EDX spectrum of ZnO nanorods coated with 30 layers of CdTe-PDDA using the LbL process as seen in figure 6.2 b.**Cd and Te are detected from the nanoparticles, C and S from the capping molecules, C from the PDDA and Zn and O from the nanorods.

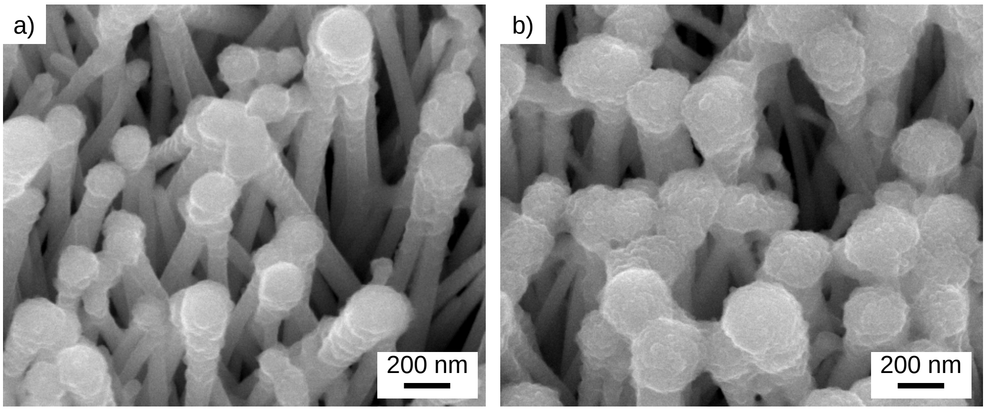

Figure 6.4: **SEM images of ZnO nanorods coated with 30 (a) and 50 (b) layers of CdTe-PDDA using a recycled nanoparticle solution.** Nanorods were grown in 0.025 M solutions of zinc nitrate and HMT in a closed jar at 90 °C for a total of 15 hours.

The degradation could be due to a transfer of PDDA into the nanoparticle solution or a degradation of the capping molecule due to a change of pH in the nanoparticle solution, both of which would cause the observed agglomeration. It is most likely that a transfer of PDDA led to the agglomeration, as small quantities of PDDA could detach from the previous layer when the substrate was dipped into the CdTe. The degradation in capping molecule due to a change in solution condition such as pH is less likely because any soluble ions likely to alter the pH in the CdTe solution would be washed off by the washing step. If PDDA was transferred to the CdTe solution, despite the washing, it would create clumps of nanoparticle-PDDA bonded together within the solution. The larger clumps would drop to the bottom of the solution, as observed, but smaller clusters could bond to the surface in subsequent dip steps, creating a less even surface, and would not penetrate as deeply between the rods leading to the clumps at the tips. This uneven coating is not desired for the solar cells as it would lead to a greater local thickness of CdTe-PDDA at the tips with little CdTe at the base of the rods. This would degrade performance as electrical charge would be less likely to reach the nanorods or hole-collector through this thicker layer at the tip, and the enhanced surface area of the rods would not be fully utilised if the whole length of the rods were not coated. The problem was even more pronounced with 50 layers of CdTe-PDDA on the rods as the coating almost completely joined at the tips of the rods (figure 6.4 b). This could cause even greater problems for the solar cells as it means that the hole collecting layer may not penetrate between all of the rods, so some areas of the cell will become inactive as the photogenerated holes are not extracted.

6.2 Optical properties

6.2.1 Absorption

The advantage of the LbL coating method for enhancing light absorption in nanoparticles films for solar cells is demonstrated in figure 6.5 a. Absorption measurements were performed on nanorods grown on seeded FTO substrates for 7.5 hours, which were shorter than the nanorods shown in figures 6.2 and 6.4. The shorter nanorods scatter less light and therefore produce clearer absorption measurements. It can be seen that increasing the number of layers of CdTe from 10 to 30 increases the intensity of absorption: at 590 nm the absorption intensity of the 30 layer sample is approximately four times larger than the 10 layer sample. The increased absorption is a consequence of the higher optical density of the thicker CdTe-PDDA layers achieved by coating a larger number of layers. To try and isolate the absorption of the CdTe layers, the spectrum for the uncoated ZnO nanorods was subtracted from the spectra

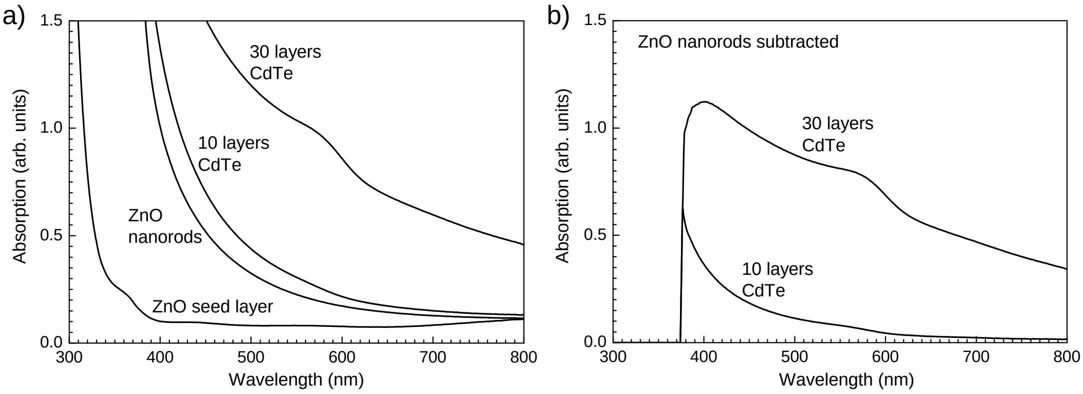

Figure 6.5: **a) Absorption spectra of ZnO seed layer, ZnO nanorods and nanorods coated with 10 and 30 layers of CdTe-PDDA. b) Absorption spectra of 10 and 30 layers of CdTe-PDDA on ZnO nanorods with the spectrum for uncoated ZnO nanorods subtracted.** Nanorods were grown in 0.025 M solutions of zinc nitrate and HMT in a closed jar at 90 °C for a total of 7.5 hours.

for 10 and 30-layer coated rods, giving the spectra shown in figure 6.5 b. The effect of the ZnO nanorods cannot be completely separated as demonstrated by the rapid drop in absorption below around 390 nm, which corresponds to the saturation of the absorption in the ZnO sample being subtracted from the data. However, this does show more clearly the absorption peaks for the CdTe nanoparticles around 590 nm for both 10 and 30 layers, which could not be resolved previously in the 10 layer sample.

In order to determine the actual level of light absorption in the nanorod-nanoparticle composite absorption measurements were carried out using an integrating sphere attachment, as described in section 3.7.4. This allows all transmitted light to be captured, including that scattered by the nanorods. Scattering therefore did not have to be minimised, so ZnO nanorods grown for a total of 15 hours and coated with 50 layers of CdTe nanoparticles by the LbL process were used. Absorption and transmission plots from these measurements are shown in figures 6.6 a and b respectively. The nanoparticles show a characteristic absorption peak at around 560–600 nm, corresponding to absorption at an energy range of 2.21–2.01 eV. This is blue shifted from the bulk band gap of CdTe of ∼1.5 eV due to quantum confinement. At the onset of absorption (∼650 nm) the 50 layer-coated nanorods transmit ∼30 % of the incident light, which reduces to ∼10 % at the onset of absorption by ZnO at around 400 nm (figure 6.6 b).

The light-harvesting efficiency (LHE) of the nanorod-nanoparticle composite at 590 nm is around 80 %. This is significantly higher than 30 % achieved at the absorption peak of approximately a monolayer of CdSe nanoparticles adsorbed onto ZnO nanorods in a previous study [67] (discussed in section 2.2.5). This confirms the advantage of using the LbL process to achieve a higher LHE by allowing the deposition of a much thicker coating of nanoparticles. However, it is noted that a monolayer in the literature example absorbs around 30 % of the incident light at the absorption peak, whereas 50 layers in the current work absorbs around 80 %. If the layers were equivalent in the two situations it would be expected that 100 % of the light would be absorbed after depositing around 3–4 layers. There are two main reasons for this

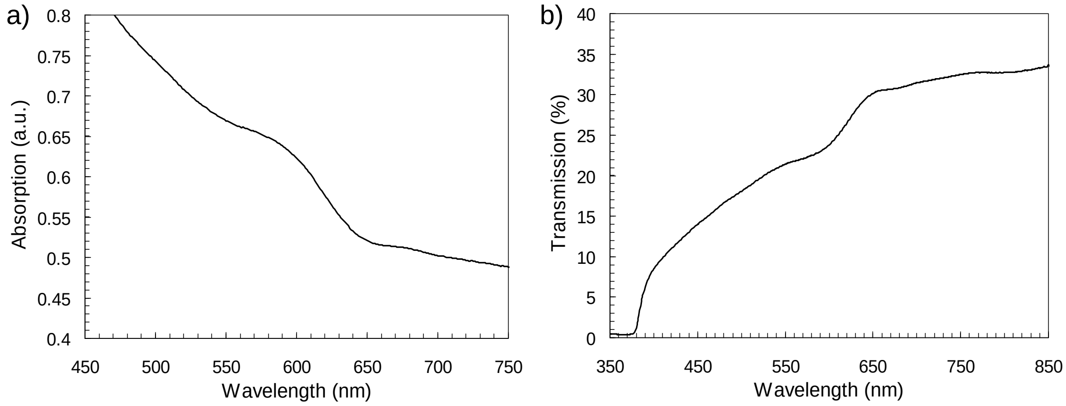

Figure 6.6: **Absorption (a) and transmission (b) spectra of ZnO nanorods coated with 50 layers of CdTe-PDDA.** Nanorods were grown in 0.025 M solutions of zinc nitrate and HMT in a closed jar at 90 °C for a total of 15 hours.

disparity between the current work and the literature example. The first factor is the length of the nanorods: the nanorods in the literature example were much longer than the nanorods in the current work (up to 12 μm long [67] compared to $\sim$3 μm in the current work). Therefore a larger optical density of nanoparticles were deposited per layer in the literature example because of the increased surface area enhancement of the nanorods. The second factor is the density of nanoparticles per layer. Because only a monolayer was used in the literature example efforts were made to maximise the packing density of this layer by treating the surface of the rods and optimising the deposition [67]. In the current work a single layer of the LbL process does not fully cover the surface, and only after a few layers does the packing lead to complete coverage of the surface, as shown by previous analysis of the LbL films [148]. Therefore a single layer of the LbL process cannot be considered equivalent to the layer that was coated in the literature example. It should also be considered that the absorption per particle is unlikely to be equivalent between the literature example and the current work, but without further data the difference cannot be quantified.

6.2.2 Photoluminescence

Photoluminescence (PL) measurements were performed on CdTe-PDDA LbL films coated onto ZnO nanorods on both Ag and FTO substrates to study the change in spectrum from both the rods and the CdTe when in direct contact with each other. The results of the PL measurements are presented in figures 6.7 and 6.8 for Ag and FTO substrates respectively. The spectra obtained for the ZnO-CdTe composite are shown as well as the spectra for uncoated ZnO (as discussed in section 4.2.2) and CdTe deposited directly on the substrate for comparison. The spectra containing ZnO are normalised to the exciton maximum, with the CdTe spectrum scaled by the same factor as the composite for comparison. As in the ZnO-only spectra in section 4.2.2, the 532 nm harmonic of the 266 nm laser excitation is present in the LbL-coated nanorod emission, and here overlaps exactly with the 532 nm peak in the ZnO only spectrum. This peak is not present in the CdTe-only spectrum.

In figure 6.7 a the spectrum of CdTe on Ag (dot-dashed line) shows an emission centred at 600$\pm$10 nm, corresponding to a band gap of $\sim$2.0–2.1eV. This is in agreement with the value of the band gap obtained from the absorption measurements above. For ten layers of CdTe on ZnO nanorods (solid line), the spectrum is not merely a superposition of the separate spectra of ZnO and CdTe. The emission around 600 nm from the CdTe is largely suppressed in the composite (slight interference features between 550 nm and 650 nm are visible instead). This would not be expected if the CdTe were emitting at the same intensity as when deposited directly onto the Ag substrate as the same amount or more CdTe should be present in the 10 layer-coated ZnO. Another difference in the composite is that the shoulder of the ZnO exciton emission is enhanced with contributions at $\sim$400 nm and $\sim$420 nm apparent, as indicated in figure 6.7 a. These shoulders were discussed in sections 2.3.2 and 4.2.2, and are often linked to surface zinc vacancies in ZnO [106, 112].

The samples prepared on FTO show similar spectra to those on Ag, but with some

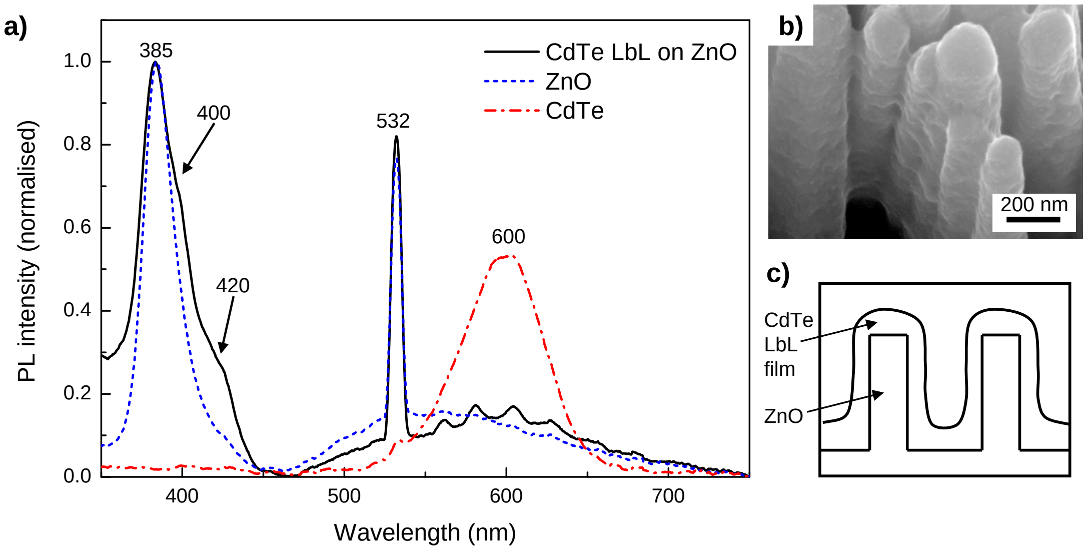

Figure 6.7: **Photoluminescence spectra of bare ZnO nanorods and 10 layer CdTe-PDDA LbL films coated directly onto the substrate or on ZnO nanorods.** a) PL spectra. b) SEM image of coated nanorods that were measured. c) Schematic of CdTe coating on the nanorods. On Ag-coated glass substrates.

differences. In the composite samples on FTO (figure 6.8 a, solid line), the 600 nm CdTe emission is not suppressed to the same degree as the composite on the Ag substrate. It can be seen by comparing figures 6.7 b and 6.8 b that the CdTe-PDDA LbL film is much less homogeneous on the rods on FTO than the rods on Ag. The difference in LbL coating on rods grown on seeded FTO compared to rods grown on Ag is due to the FTO rods being smaller, closer together and more randomly oriented than those grown on Ag. This difference in morphology and alignment of the rods is a result of the different seed size on the two substrates and the increased roughness of the FTO surface, which was discussed in section 4.1. The closer spacing and more random orientation has led to a large portion of the LbL film joining and filling between the ZnO nanorods grown on FTO, as represented in the schematic in figure 6.8 c. The LbL film has coated the rods grown on Ag more intimately, as represented in figure 6.7 c. It is suggested that in the LbL coated rods grown on FTO it is this ‘in-fill’ of the LbL film that is responsible for the emission at around 600 nm: the separation between the nanorods and the nanoparticles in this ‘in-fill’ portion of the film (shaded grey in figure 6.8 c) is greater than in any portion of the film coated on the rods grown on Ag, and this separation is too large for the photoexcited carriers to be transferred to the ZnO. Instead they recombine in the film radiatively, producing the 600 nm emission that was observed. Another feature in the composite on FTO that is different to that on Ag is that the shoulder at ∼400 nm is enhanced so much that it can be seen as a separate peak at 400±1 nm. This may be due to the fact that the 400 and 420 nm shoulders are more pronounced even before the addition of CdTe due to the higher surface-to-volume ratio of the rods on FTO, which increases the relative intensity of emission from surface states, as discussed in section 4.2.2. The energy

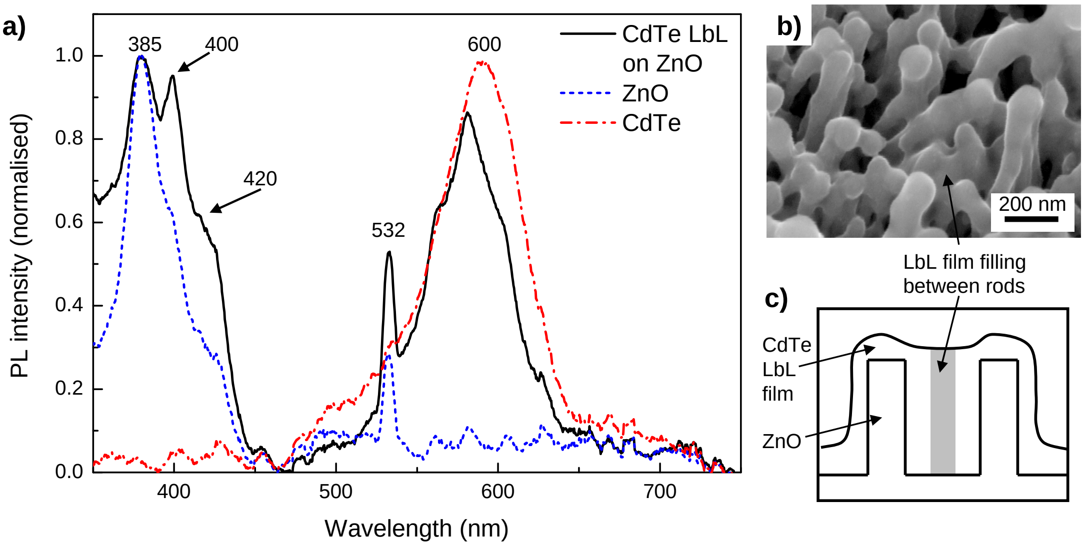

Figure 6.8: **Photoluminescence spectra of bare ZnO nanorods and 10 layer CdTe-PDDA LbL films coated directly onto the substrate or on ZnO nanorods.** a) PL spectra. b) SEM image of coated nanorods that were measured. c) Schematic of CdTe coating and filling between the nanorods. On seeded FTO-coated glass substrates.

difference of 120±20 meV between the main exciton emission and the 400 nm peak corresponds with the energy difference between the zinc vacancy (V_{Zn}) and the valence band as calculated by Lin et al., although the absolute values of each emission are shifted slightly [110].

The quenching of the CdTe luminescence combined with an enhancement of emission from surface states in the ZnO when CdTe is coated onto ZnO suggests a possible photoexcited charge transfer process from the nanoparticles to the nanorods. The process for this transfer and the energy levels of the states involved are shown in figure 6.9. The proposed process is as follows: electrons are first photo-excited in the CdTe nanoparticles from the valence to the conduction band (figure 6.9, arrow A). These are then transferred into the ZnO (figure 6.9, arrow B). For this to occur, the rate of electron transfer from the CdTe to ZnO must be faster than the exciton recombination in the CdTe nanoparticles. Some of the electrons injected into the nanorods recombine in the surface trap states (figure 6.9, arrow C), leading to emission at 400 nm from the ZnO. It is therefore the recombination of injected carriers in the surface states of ZnO that leads to the observed increase in the 400 nm emission. Electrons excited in the bulk of ZnO recombine to give the 385 nm exciton emission. This fast charge transfer between nanoparticles and nanorods is exactly that required for the operation of the ZnO-CdTe solar cells.

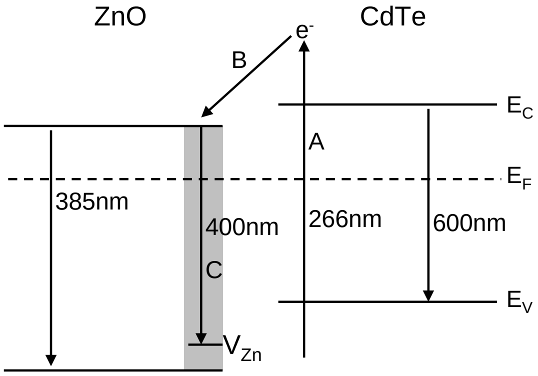

Figure 6.9: **Band alignment and charge transfer at the ZnO-CdTe interface.** Alignment of the conduction and valence bands of ZnO and CdTe based on electron affinities and expected fermi levels of the two materials. The excitonic emission of 385 nm in ZnO and near band-edge emission at 600 nm in CdTe when excited at 266 nm are shown. The process of excitation and charge transfer between CdTe and ZnO is also show with: A. excitation of electron from CdTe valence band by laser; B. transfer into surface of ZnO (shaded); C. trapping of electron in surface zinc vacancy (V_{Zn}) of ZnO, leading to emission at 400 nm.

6.3 Annealed films

As described, the LbL process deposits a films of CdTe nanoparticles embedded in a PDDA matrix. It has been shown that this process is able to strongly enhance the light absorption of the film of nanoparticles by allowing thicker layers to be deposited than when not using the LbL process. However, it is only the CdTe component of the LbL films that is desired for photovoltaic applications. PDDA is a dielectric polymer, and therefore will inhibit charge transfer between the CdTe nanoparticles, essentially introducing added series resistance to the solar cell. This section therefore describes attempts to remove the PDDA component of the film by thermal annealing to leave only the CdTe.

6.3.1 Compositional effects

To first ascertain which procedure was most appropriate for the annealing of CdTe LbL films, annealing was performed both in air and under a vacuum of 10^{-7} mbar. When heating films above 200 °C in air their appearance changed from red to brown. XPS analysis performed by Dr D. E. Gallardo (figure 6.10) revealed large secondary peaks shifted by +3.7 eV from the Te-Cd peaks. The shifted peaks correspond to oxidised tellurium (Te-O) [149], indicating that some of the original CdTe has been oxidised during the annealing stage in air. This is consistent with reported spectra of complex oxides of the form $CdTeO_x$ [149]. The XPS spectrum for vacuum-annealed samples almost overlaps with that of the unannealed samples, indicating that oxidation had not occurred in this case. It was therefore necessary to anneal the films in vacuum to avoid any oxidation of the CdTe nanoparticles, and subsequent analysis was performed

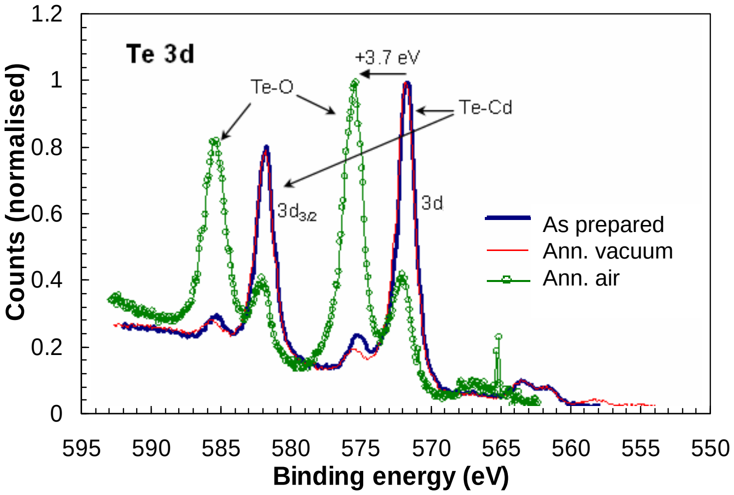

Figure 6.10: **X-ray photoelectron spectrum of LbL films of CdTe nanoparticles on ITO-coated glass.** Films were either unannealed or annealed in air or vacuum for 1 hour.

on films annealed in vacuum. All of the annealing studies here were performed on samples annealed for 1 hour. The time was kept constant in order to isolate the effect of temperature on the films.

EDX measurements were performed on all of the LbL CdTe films before and after annealing. For more in-depth analysis of the composition EDX surveys were performed on LbL films deposited on ZnO nanorods. This led to stronger signals being detected from the CdTe films as a larger volume of CdTe-PDDA was in the path of the beam. It also allowed the Cd and Te peaks to be resolved more clearly, as they overlapped with the In signal from the substrate when deposited directly onto ITO. For annealing studies, the carbon content of the films was used as an indication of PDDA content and degradation (although some carbon may be detected from the capping molecule, the majority is present in the PDDA).

The trend of carbon content at different annealing temperatures is shown in figure 6.11. The 25 °C point refers to the unannealed sample. Up to 250 °C the carbon-content remained almost unchanged within the error of the measurements. This implies that there was no loss of PDDA at this temperature, consistent with previous thermo-gravimetric analysis (TGA) of PDDA [150], i.e. the PDDA is thermally stable up to this temperature. When annealed in the range 250–350 °C, the C-content was reduced compared to unannealed films. No carbon was detected when annealing at 450 °C. These results are also consistent with TGA analysis of PDDA, which found that around 30 % of the weight of PDDA was lost when annealed at 350 °C and the full mass was lost around 450 °C [150]. The weight loss occurring around 350 °C in PDDA was attributed to the loss of a methyl group from each monomer unit with the Cl^- ion in the form CH_3Cl [150]. This would register as a loss in the C-content of the film, as found in these EDX measurements. The TGA study suggested that above around 450 °C the film decomposed into a number of smaller volatile molecules through a

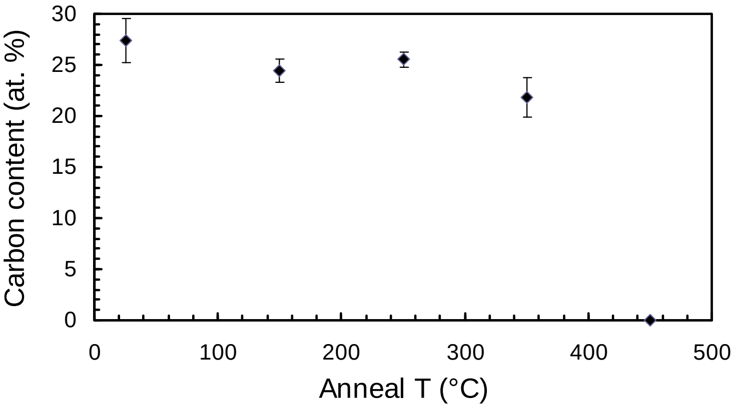

Figure 6.11: **Carbon content of 30 layer CdTe-PDDA films on ZnO nanorods annealed at 150–450 °C obtained from EDX spectra.** Films were annealed in a vacuum of 10^{-7} mbar for 1 hour. Errors obtained by repeating EDX measurements in different areas of the sample.

variety of mechanisms. However, to identify these decomposition products they indicated that further analysis such as mass spectroscopy or Fourier transform infra-red spectroscopy would be required [150].

It should be noted that the TGA analysis in Ref. 150 was performed in an inert nitrogen atmosphere. This would prevent oxidation of the PDDA similarly to annealing performed in vacuum. However, there may be a slight difference in the temperature ranges at which the decomposition would occur due to a difference in pressure between the nitrogen atmosphere and vacuum. But because only a small number of temperature points were used in the current study (5 for compositional studies, 6 for optical studies) it could not be seen whether there was a slight shift in the decomposition temperatures. Further TGA studies of PDDA in vacuum, rather than nitrogen, or annealing of LbL films in nitrogen would ascertain whether there was a large shift in the decomposition temperatures between these two atmospheres. As long as the shift is not large ($>$50 °C), then the behaviour established in the TGA study [150] can still be applied to the observations of the annealed LbL films.

Quantitatively, the carbon content after annealing at 350 °C was 80±6 % of the carbon content before annealing, corresponding to a 14–26 % loss of carbon. This equates to a loss of between one and two of the eight carbon atoms per monomer of PDDA. This could be consistent with the loss of one or both of the methyl side groups of PDDA, as suggested in Ref. 150. Further confirmation of this hypothesis would be obtained from repeated EDX measurements so that statistically significant measurements of the carbon content could be obtained, and spectroscopic analysis of the resulting material such as mass or infra-red spectroscopy to ascertain the structure of the materials present. The loss of the remainder of the PDDA mass, i.e. the remaining component of the polymer, occurred completely in the TGA study at 467 °C [150]. Therefore it can be assumed that in the samples measured here the lack of carbon detected when annealed at 450 °C indicates that all of the PDDA had been removed.

6.3.2 Optical changes

Figure 6.12 shows the trend in the optical gap of 20 layer LbL films deposited onto glass and annealed in vacuum at 150–450 °C. Factors that may have caused the change in optical gap are discussed below, and are annotated on figure 6.12 for clarity. The optical gap was calculated using a Tauc plot [144], which allowed comparison between samples despite slightly different forms of the absorption peak. Films deposited onto glass were used to study the change in optical gap of the nanoparticles because the absorption peak was more clear than for films deposited onto ZnO nanorods.

In the film annealed at 150 °C there was a slight reduction in the optical gap compared to the unannealed film. This small reduction in the optical gap of the nanoparticles may result from increased interaction between the NPs as they rearrange and come slightly closer within the PDDA matrix, possibly due to a loss of water from the PDDA, which was found to occur over 100 °C in TGA analysis [150]. There was a slight reduction in the oxygen content of the surveyed area ($\sim$2 at.%) when annealed at 150 °C, which could be due to loss of water molecules from the film. This accounts for the slight increase in C-content at 150 °C seen in figure 6.11 as with less oxygen the carbon comprises a slightly larger percentage of the sample. A red-shift resulting from closer packing has been observed previously in photoluminescence (PL) studies of LbL films of CdTe [148]. PL was not studied for annealed films as the PL intensity has been shown previously to drop dramatically with even moderate heating (<100 °C) [151].

Between 210 and 280 °C the optical gap of the NPs reduced slightly more (figure 6.12). This implies a greater interaction between the wavefunctions of the nanoparticles, leading to a slight reduction in the strength of quantum confinement. This temperature range is above the glass transition temperature (T_g) of PDDA as determined

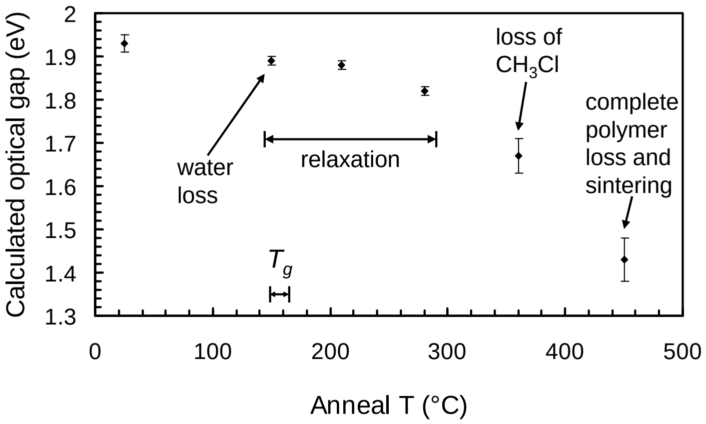

Figure 6.12: **Optical band gap of 20 layer CdTe-PDDA films deposited on glass substrates annealed at 150–450 °C in vacuum for 1 hour.** Optical gaps were calculated using a Tauc plot [144] and error bars reflect the error in fitting to these plots. Suggested origin of observed band gap changes and glass transition temperature (T_g) of PDDA [150] are annotated.

by the TGA study (T_g =150–165 °C [150]) but below the range where mass is lost from the polymer (see below). At temperatures above T_g stresses in the polymer remaining after drying at room temperature would relax. This could have allowed a more ordered arrangement of the polymer chains, reducing the separation between the nanoparticles. This reduced separation would lead to the observed increase in particle-particle interaction. The higher the temperature was raised above T_g (280 as apposed to 210 °C) the greater the extent of the relaxation and therefore the greater the increase in interaction.

At 350 °C the band gap was reduced further, but quantum confinement was not completely lost, as the optical gap was still above the bulk (band gap ~1.5 eV [72]). It is possible that the loss of CH_3Cl from the PDDA discussed above would lead to the PDDA shrinking slightly, reducing the separation between nanoparticles compared to annealing at 280 °C. This would account for the further reduction in the optical gap of the nanoparticles as the wavefunctions could interact more when in closer contact due to the narrowing and possible lowering of the potential barrier between the nanoparticles. This closer contact and narrower barrier would also be expected to increase the probability of charge transfer between the nanoparticles, reducing the resistivity of the film and allowing greater extraction of photogenerated charges in solar cells using films annealed at this temperature. The optical gap of the film annealed at 450 °C was close to the bulk band gap of CdTe, indicating that quantum confinement was lost. It is possible that when all of the PDDA was removed, as indicated by the EDX measurements and previous TGA studies [150], the nanoparticles could then easily sinter together as there was no longer any material separating the neighbouring nanoparticles and thermal energy would be sufficient to allow atomic migration. Sintering would lead to loss of quantum confinement and the CdTe would act as a bulk material.

Annealing at 350 °C was the only temperature studied where some of the PDDA was removed while some quantum confinement was also retained. Further study of the absorption spectrum of samples annealed at 350 °C indicates that the absorption peak has broadened compared to unannealed samples, with the centre of the peak red-shifted by approximately 80 nm (figure 6.13). This broadening of the absorption peak suggests a wider size distribution of nanoparticles, or a reduction in quantum confinement in some of the particles more than others. The combination of a slight red-shift and broadening of the absorption peak could be explained by a slight joining, or intimate contact of some of the nanoparticles, or possibly by an Ostwald ripening type process whereby some particles grow at the expense of others. These processes are illustrated in figure 6.14. In figure 6.14 a the particle-particle separation is reduced, which leads to an increase in the interaction between the wavefunctions and therefore a reduction in quantum confinement which would give the observed red-shift in absorption. If this occurred to some particles more than others, as expected if the film randomly rearranged, then it would also lead to a broadening of the band gap range as some particles would lose more quantum confinement than others. Alternatively, as shown in figure 6.14 b, the broadening of the peak could occur due to an Ostwald ripening type process. In the initial films the size distribution is narrow giving the sharp absorption peak. If the slightly smaller particles on average transferred material

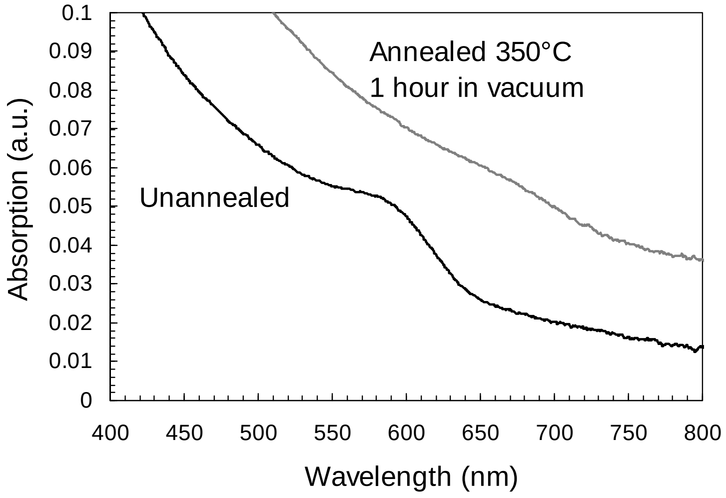

Figure 6.13: **Absorption plots of 20 layer CdTe-PDDA film deposited on glass before and after annealing at 350 °C for 1 hour in vacuum.**

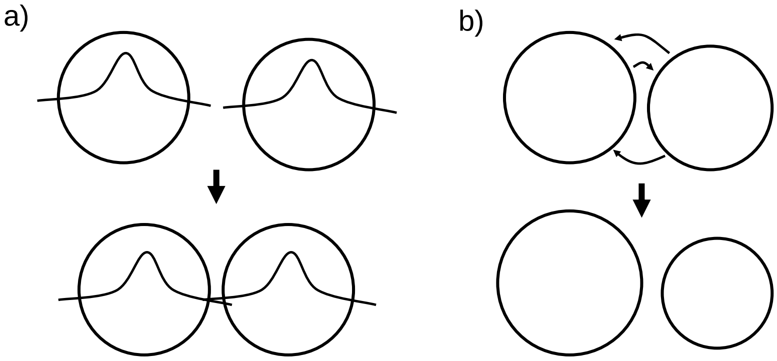

Figure 6.14: **Schematic of two possible mechanisms for a shift in the absorption spectrum of nanoparticles after annealing.** a) Reduction in separation between nanoparticles leads to increased interaction between the carrier wavefunctions and a reduction in quantum confinement. b) Ostwald ripening-type process whereby slightly larger particles grow at the expense of slightly smaller ones, increasing the size disparity between the particles.

to the larger particles then the size distribution, and therefore band gap distribution, would be broadened giving the observed broadening in absorption peak. However, the average particle size would remain unchanged, so the center of the absorption peak would not move, rather than red-shifting as observed. Additionally, for such a process to occur there would have to be mass transfer between the particles. It is likely that this would only occur once quantum confinement had been completely lost, as the polymer and capping molecule would hinder such a transfer.

Referring to other studies gives support for the first explanation of the red shift after annealing given above — that the particle separation decreased leading to increased particle-particle interaction; such a red shift has been observed previously in the LbL films due to their close packing [148]. In this study it was shown that the packing of the first few CdTe-PDDA layers in the LbL film led to a red-shift in the photoluminescence peak of the nanoparticles compared to nanoparticles in suspension due to greater particle-particle interactions. Then, as more layers were added and some particle in-fill occurred, packing particles closer together, this red shift increased due to even greater interaction, shifting by approximately 15–20 nm from one to ten CdTe-PDDA layers [148]. It is therefore suggested that as the LbL film was annealed up to 350 °C in the current work the particle separation reduced, leading to the observed red shift of approximately 80 nm. Additionally, the TGA study discussed above [150] also supports the first explanation for the observed changes in the absorption peak (represented in figure 6.14 a). The TGA analysis suggested that at 350 °C some of the side chains of the polymer were lost, but that the rest of the polymer was still present. This would lead to a slight reduction in the inter-particle separation as the loss of side chains would allow the polymer to pack more tightly, but the presence of polymer would restrict mass exchange between particles.

The observed broadening of the absorption peak is useful for photovoltaic applications, as it allows a larger portion of the solar spectrum to be absorbed by such a coating. If the increased interaction between particles also leads to enhanced charge transfer, this should also lead to improved photovoltaic performance. The final observation of the difference between the spectra before and after annealing is that after annealing the magnitude of the absorption is slightly increased. The absorption could have increased if annealing created more scattering centers in the film: more scattering would lead to a higher optical path through the CdTe, leading to more absorption. Higher scattering in the film could be caused by increased disorder as the particles rearrange, or by the changes in the molecular structure of the polymer. A less ordered film also correlates with the increased interaction suggested above for the annealed film: in a less ordered film particles would occupy any spaces in the structure thus packing more tightly. TEM studies of the LbL films after annealing would help to clarify whether the suggested changes in inter-particle separation and disorder are responsible for the observed shifts in band gap and scattering. This would also help to identify the point at which sintering does occur in the film.

When 30 layers of CdTe-PDDA were deposited onto ZnO nanorods and then annealed in vacuum at 150–350 °C a similar shift and broadening of the nanoparticle absorption peaks was observed. It can be seen from figure 6.15 a that as the annealing temperature was increased the absorption peak shifted from around 590 nm to $\sim$670 nm, and broadened slightly as in the LbL films deposited on glass. Overall the absorption also increased with annealing across the whole range shown, but especially above 600 nm, which is also useful for photovoltaic applications.

The spectra of the bare ZnO nanorod samples before CdTe-PDDA LbL coating were subtracted from those taken after coating (figure 6.15 a) to give the spectra shown in figure 6.15 b. Although the absorption amplitude from the samples is more scattered, rather than the clear trend in figure 6.15 a, the shifting absorption peaks can be see more clearly. The absorption peaks lie at approximately 595, 600, 620 and 645 nm

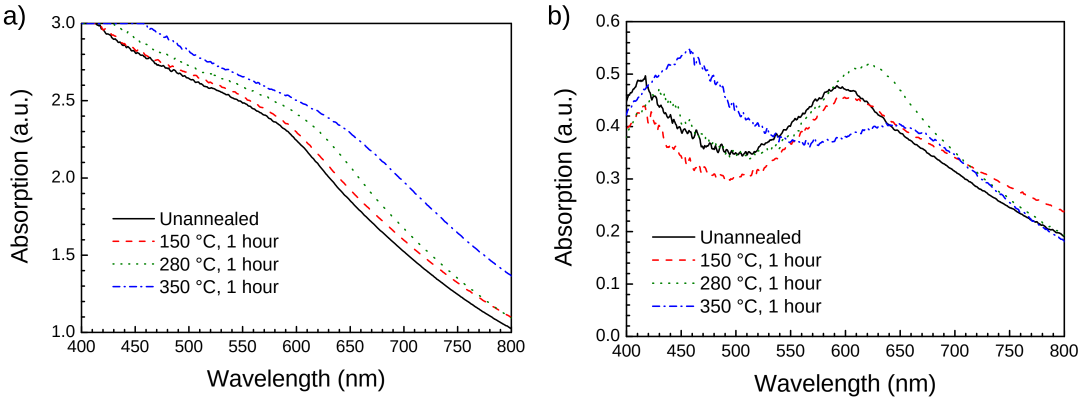

Figure 6.15: **Absorption spectra of 30 layer CdTe-PDDA film deposited on ZnO nanorods unannealed, and annealed at 150–350 °C for 1 hour in vacuum showing the region of the CdTe absorption peak.** a) Recorded spectra. b) Spectra with uncoated ZnO nanorod spectra subtracted. Nanorods were grown in 0.025 M solutions of zinc nitrate and HMT in a closed jar at 90 °C for a total of 15 hours.

for unannealed and 150, 280 and 350 °C annealed samples respectively. These wavelengths correspond to band gaps of 2.09, 2.07, 2.01 and 1.93 eV respectively. For comparison these peak positions and the visible peak position for LbL films annealed on glass are plotted in figure 6.16. The visible peak positions were used rather than Tauc gaps because the Tauc plots for LbL films on ZnO nanorods were unreliable due to scattering from the nanorods. The visible peaks for annealed 20 layer films on glass follows the same trend to the optical gaps (figure 6.12), but with all points shifted to higher energies. The trend in films annealed up to 280 °C is almost identical for films deposited on glass and ZnO nanorods, but when annealed at 350 ° the absorption peak of the film deposited on ZnO nanorods does not drop as much as the equivalent film on glass (figure 6.16). The difference in trend could imply that the presence of the ZnO nanorods reduces the effect of the annealing at higher temperatures. It is possible that the presence of the nanorods restricts the long-range order of the LbL film, reducing the ability of the film to relax above the glass transition temperature. The main inconsistency between films deposited on glass and on ZnO nanorods is observed when annealed at 350 °C. At this temperature the change in optical gap was attributed to the loss of the CH_3Cl side-group (section 6.3.2). The mass loss observed in the LbL films was measured in those deposited on ZnO nanorods and was consistent with the loss of the CH_3Cl side-groups. Therefore it is possible that these side-groups were lost both in films deposited on glass and on ZnO nanorods annealed at 350 °C, but in films deposited on ZnO nanorods the resulting film relaxation was limited by the lack of long-range order. More in-depth comparison of both the optical and compositional properties of LbL films deposited on glass and ZnO nanorods would help to clarify whether rearrangement of the films with annealing does differ between the two situations.

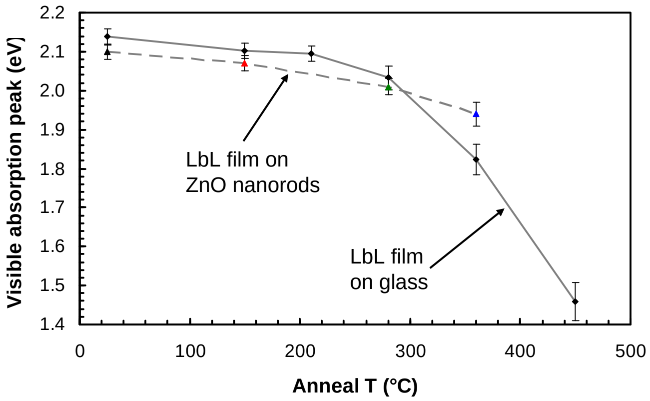

Figure 6.16: **Observed absorption peak of 20 layer CdTe-PDDA films deposited on glass substrates (solid line) and 30 layer CdTe-PDDA films deposited on ZnO nanorods (dashed line) annealed at 150–450 °C in vacuum for 1 hour.** Colour of points of LbL films on ZnO nanorods corresponds to line colour in figure 6.15. Error bars derived from uncertainty in judging the peak positions.

6.4 Summary

It has been shown that the LbL process can successfully be used to coat ZnO nanorods with conformal films of CdTe nanoparticles in a PDDA matrix, with 10, 30 or 50 layers coated onto the rods. The presence of both CdTe and PDDA were confirmed in the coating by EDX measurements. Although the rods were coated with a very uniform thickness in some cases, the uniformity of this coating did vary. It was shown that the coating was slightly thicker on the tips than the base of longer rods, possibly due to the layer components not penetrating to the base of these longer rods. This clustering at the tip of the rods was very extreme when re-using CdTe nanoparticle solutions for more than ~100 layers, even for shorter rods, indicating that fresh CdTe should always be used where possible.

Absorption measurements of CdTe-PDDA-coated rods demonstrated a distinctive absorption peak of the quantum-confined nanoparticles centred at around 2.11 eV, which is blue-shifted from the bulk band gap of CdTe of ~1.5 eV. It was shown that using the LbL process to increase the thickness of CdTe-PDDA coating clearly increased the optical absorption by the nanoparticles, with 30 layers on ZnO nanorods absorbing approximately four times as much light at the CdTe absorption peak (590 nm) as 10 layers on the same rods. Quantitative measurements of the absorption using an integrating sphere to capture all of the transmitted light showed that 50 layers of CdTe-PDDA on ZnO nanorods absorbs ~80 % of the incident light at the nanoparticle absorption peak. This is more than 2.5 times higher absorption than previous nanoparticle-coated ZnO nanorods which did not use the LbL process. This therefore confirms that the LbL process allows a much greater level of light absorption by nanoparticles on ZnO nanorods than soaking the rods in a nanoparticle solution to adsorb the nanoparticles onto the surface. When coated onto ZnO nanorods by the

LbL process, CdTe nanoparticles and the nanorods demonstrated a photoluminescence (PL) spectrum that implied a photoexcited charge transfer from the nanoparticles to the nanorods. This was suggested by the quenching of the CdTe exciton emission when coated onto the nanorods coupled with enhanced surface emissions from the nanorods. Such a carrier transfer is desirable for the use of this CdTe-ZnO system in solar cells.

Annealing of the CdTe-PDDA-coated ZnO nanorods was performed to try and remove the PDDA component from the CdTe-PDDA film. Initially it was shown that annealing must be performed in vacuum to avoid oxidation of the nanoparticles, which occurred when annealing in air above 200 °C. Annealing in vacuum up to 450 °C was performed, which displayed behaviour that agreed with previous thermo-gravimetric analysis (TGA) studies of PDDA; analysis of the carbon content of the films suggested a partial decomposition of the PDDA at 350 °C (loss of methyl side-group(s)), and full loss of PDDA at 450 °C. This behaviour was coupled with a gradual decrease in optical gap of the nanoparticles annealed up to 280 °C — likely due to a slightly increased inter-particle interaction as the particles re-arrange in the film — with greater reduction in the optical gap of 350 °C-annealed particles due to even greater interaction between particles resulting from the partial PDDA decomposition. At 450 °C the quantum confinement appeared to have been completely destroyed as the optical gap was close to the bulk band gap of CdTe. This indicated that the nanoparticles had most likely sintered to some extent once the PDDA had been fully removed.

These results show that the LbL process does have potential for depositing CdTe nanoparticle films onto ZnO nanorods to act as absorber layers in eta-style solar cells. The conformal coating of the nanorods is desirable both for optimum charge transfer into the nanorods, and for penetration of a hole-collecting material between the coated nanorods. Existence of the required charge interaction was suggested by PL measurements. The absorption measurements show that absorption of incident light can be enhanced by increasing the thickness of the CdTe coating on the nanorods so that levels approaching 100 % of the incident light can be absorbed. Attempts to remove the PDDA component of the films have also been successful, although for quantum confinement to be retained only partial decomposition of the PDDA can be preformed. Measurement of the performance of completed solar cells with a variety of these LbL coating will show whether the increased light absorption of the LbL films can be coupled with charge extraction of the resulting photoexcited carriers, and which of the adaptations of absorber thickness and annealing treatments produce the best results. These investigations are explored in the following chapter.

Chapter 7

Solar cells

Chapters 4 and 6 described the development of the methods for growing ZnO nanorods and coating them with layer-by-layer (LbL) films of CdTe nanoparticles. The properties of these components were studied and explored with reference to a variety of characterisation techniques. This chapter focuses on these materials as components of solar cells and the additional materials that are required to complete the solar cells. In this project, three sets of solar cells were made, which shall be referred to as SC1, SC2 and SC3. The cells in each set share certain synthesis methods that reflect the stage of the project at which they were produced, hence the labelling of the cells in this way. In this chapter, the ZnO nanorods and CdTe coating that were used in the solar cells are first described so that they can be easily compared to the photovoltaic performance of the final devices. Details of the p-type materials copper thiocyanate (CuSCN) and poly(styrenesulfonate)-doped poly(3,4- ethylenedioxythiophene) (PEDOT:PSS) are given, including both the development of these materials early in the project and the details of the specific films used in the solar cells. The main focus of the chapter is how the components of the solar cells influence their photovoltaic performance; differences in the ZnO nanorods, CdTe films, and p-type layers are all related to the photovoltaic performance of the solar cells. The analysis attempts to gain understanding of how the properties of the components influence the cell performance and use this understanding to improve the efficiency of the solar cells.

7.1 ZnO nanorods for solar cells

Nanorods for solar cells were always grown on FTO-coated glass substrates with a seed layer derived from a solution of zinc acetate in ethanol by the method described in section 3.1.1. Nanorods were grown in a sealed jar, with reactants mixed and substrates added while cold and placed in an oven for 2.5 hours at 90 °C. The concentration of zinc nitrate and HMT in the reaction was always 0.025 M. For devices SC1, the solution also contained ∼6 mM PEI, and the reaction was repeated 20 times using fresh solutions each time. Nanorods grown in this way are shown in figure 7.1 a. These rods grew quite large in the repeated syntheses: up to 5 μm of the largest nanorods

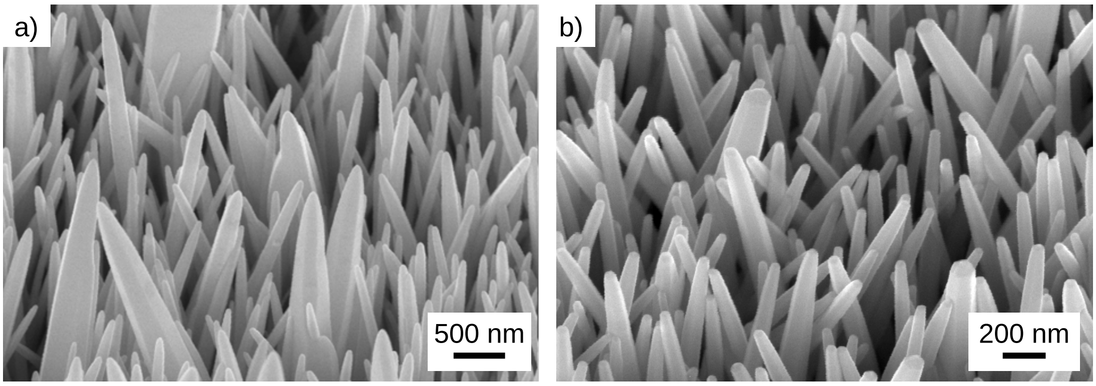

Figure 7.1: **SEM images of ZnO nanorods grown on seeded FTO substrates in aqueous 0.025 M solution of zinc nitrate and HMT for devices SC1 (a) and SC2 and SC3 (b).** a) Rods grown with ∼6 mM PEI added to reaction in a closed jar at 90 °C for a total of 50 hours. b) Nanorods grown without PEI in a closed jar at 90 °C for a total of 15 hours. In both reactions substrates were placed in consecutive syntheses of 2.5 hours in a sealed vessel with fresh solutions each time. Images taken at 45°.

were visible above the array, which were 500 nm in diameter. However, this size was not consistent across all nanorods. Many rods were only 100 nm in diameter, and around 1–2 μm could be seen above the array. The large rods can be seen extending above the majority of smaller rods in figure 7.1 a. The enhanced growth of a minority of rods compared to the rest was not expected, but could be due to inhomogeneities in the seed layer. If some of the ZnO seeds were slightly larger the rods that grew from them would both be wider and start taller than the surrounding rods. By being taller than the surrounding rods these few rods would have access to a region of solution that was less depleted of reactants than that immediately above the rest of the rods. These rods that started taller would then grow at a greater rate, accentuating the size disparity and producing the extra-large rods that were observed. This uneven morphology should not adversely affect the performance of the solar cells, as long as the hole-conducting layer fully covers all of the rods.

Later, for devices SC2 and SC3 PEI was no longer used, and the reaction was repeated only 6 times in fresh solutions. Nanorods grown in this way are shown in figure 7.1 b. These nanorods are much more consistent in size than those grown over 20 syntheses with PEI, although some slightly larger rods are also visible. It is possible that with further syntheses these size differences could become more marked, as discussed above. Around 1 μm of these rods is visible above the array, and they are ∼90 nm wide. The aspect ratio therefore differs little from nanorods grown using PEI, as discussed above. The majority of the rods were also only slightly smaller than those grown in more than three times as many syntheses using PEI. This indicates that using PEI slows the growth of the nanorods, suggesting that it is more efficient not to use PEI in the reaction.

7.2 LbL-coated nanorods for solar cells

The CdTe-PDDA films used in the solar cells were produced by the same layer-by-layer process as discussed in chapter 6. This section briefly details the morphology of the specific LbL films used in the solar cells so that the properties of the complete cells can be related to these morphologies.

In the first two sets of devices, SC1 and SC2, fresh solutions of nanoparticles were used in the LbL process and 30 bi-layers of CdTe-PDDA were deposited on the nanorods. In the final set of devices, SC3, recycled solutions of nanoparticles were used, as the detrimental effect of this was not known (see section 6.1), and there was insufficient time and remaining nanoparticles to re-grow the nanorods and coat them with fresh solution. In devices SC3 either 30 or 50 bi-layers of CdTe-PDDA were coated onto the nanorods. Some devices were also made without CdTe-PDDA coatings to compare the behaviour. Full discussion of the devices is made in section 7.5. Figure 7.2 shows 30 layer CdTe-PDDA-coated nanorods used in devices SC1, and coated nanorods from SC2 and SC3 are shown in figures 7.3 and 7.4 respectively.

The coating on cells SC2 (figure 7.3) was the most uniform of the three sets of devices, with a similar thickness of coating along the visible length of the rods, although the film is possibly slightly less thick below around 500 nm from the tip. Devices SC3 had the least uniform coating (figure 7.4), which was attributed to the use of recycled CdTe nanoparticle solutions. Devices SC1 (figure 7.2) have a slightly less uniform coating than SC2, with some clustering of CdTe around the tips of the rods. It is possible that this was a results of the slightly greater length of these rods, the presence of the especially long rods discussed in section 7.1 (seen in figure 7.2 a), or slight differences in spacing between the rods resulting from the different growth times. The longer rods may make it more difficult for the aqueous solutions of either

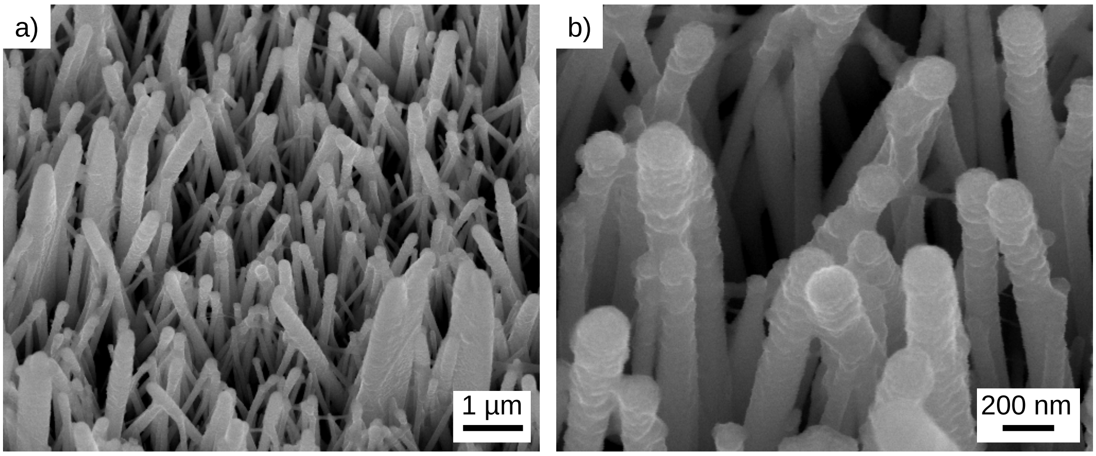

Figure 7.2: **SEM images of ZnO nanorods coated with 30 layers of CdTe-PDDA using the LbL process for solar cells SC1.** a) Wide view. b) Close-up. Nanorods were grown in 0.025 M solutions of zinc nitrate and HMT with 6 mM PEI in a closed jar at 90 °C for a total of 50 hours. Images taken at 45°.

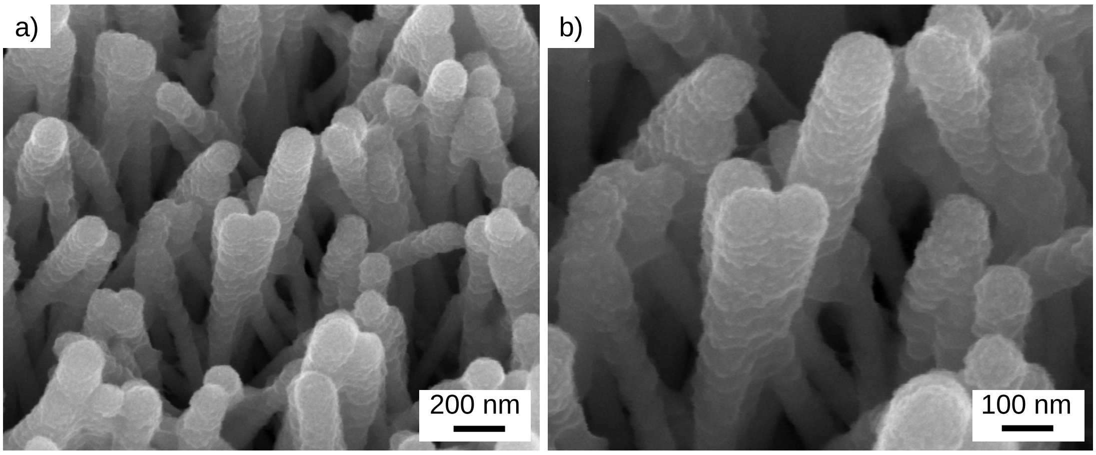

Figure 7.3: **SEM images of ZnO nanorods coated with 30 layers of CdTe-PDDA using the LbL process for solar cells SC2.** a) Wide view. b) Close-up. Nanorods were grown in 0.025 M solutions of zinc nitrate and HMT in a closed jar at 90 °C for a total of 15 hours. Images taken at 45°.

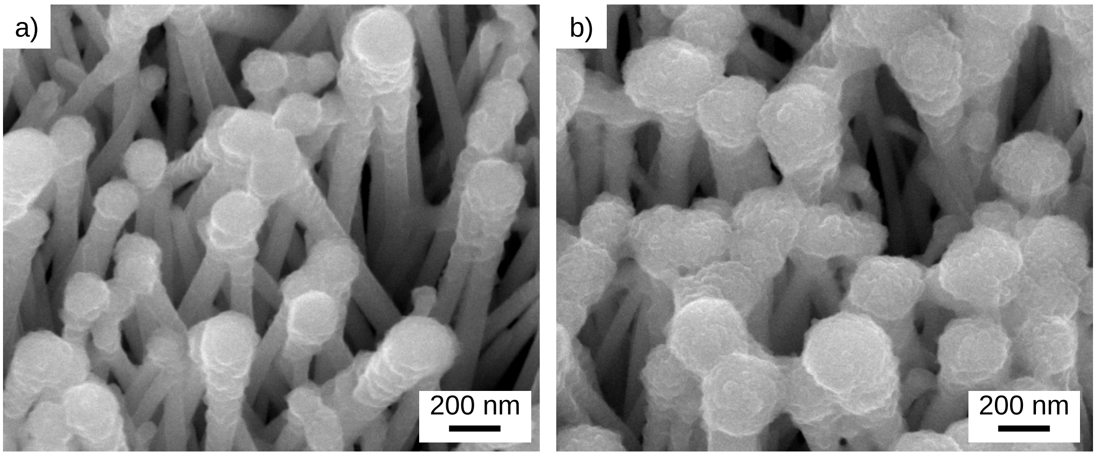

Figure 7.4: **SEM images of ZnO nanorods coated with 30 (a) and 50 (b) layers of CdTe-PDDA using the LbL process with a recycled nanoparticle solution for devices SC3.** Nanorods were grown in 0.025 M solutions of zinc nitrate and HMT in a closed jar at 90 °C for a total of 15 hours. Images taken at 45°.

CdTe, PDDA or both to penetrate between the rods, leading to the preferential deposition of CdTe-PDDA films on the tips of the rods. Alternatively, either narrower or wider spacing between the rods may lead to poorer penetration of the CdTe or PDDA solutions: if the surface tension of the solutions limited the penetration a wider spacing would improve penetration, but if the penetration was aided by capillary action a narrower spacing may draw the solutions to the base of the rods more effectively. The optimum spacing for LbL penetration could be investigated by producing a number of nanorod samples of the same length but with different aspect ratios and measuring the extent of LbL coating along the rods.

Because of the tendency for preferential deposition of the LbL films at the tip of the rods, the majority of the CdTe-PDDA was deposited on approximately the top 600 nm of the rods in all devices, the only exception being the extra-long rods in SC1, which were coated approximately 2 μm down from the tip. As there were not many of these extra-long rods, and the rest of the rods are only coated by approximately the same amount of CdTe as the other devices, the longer growth time used for cells SC1 may not have led to a significantly greater quantity of CdTe being present in cells SC1 compared to the shorter rods in SC2 and SC3. This suggests that the LbL process may need to be adjusted for future work so that longer nanorods can be coated to the bottom of the rods without agglomeration at the tips.

7.3 Copper thiocyanate

7.3.1 Spin-coating trials with ethyl sulphide

Attempts to deposit films of CuSCN by spin-coating were made using solutions of CuSCN in ethyl sulphide. Ethyl sulphide was used because the CuSCN dissolved easily in the solvent, and it was not known at that time that CuSCN forms complexes with ethyl sulphide that make the solvent difficult to fully remove, as mentioned in section 3.4. CuSCN solutions were spun onto ITO-coated, FTO-coated and uncoated glass and nanorod-coated substrates at speeds of 1000–2000 rpm for up to one minute. Methods were also trialled where the substrate was first spun for 20 seconds at 250 rpm to gently spread to solution over the substrate allowing the solvent to evaporate slightly and viscosity increase, before spinning briefly at 1000 rpm to remove any excess solution. Coatings were repeated between 10 and 50 times.

On planar substrates (ITO, FTO, glass) almost no material was deposited; on SEM analysis, the majority of areas consisted only of the bare substrate, with some small islands that may have been isolated patches of CuSCN or a CuSCN-solvent complex, but were too thin to register on EDX analysis. On ZnO nanorod-coated substrates material was deposited, almost completely covering the nanorods (figure 7.5). However, it was not possible to reliably coat a film of CuSCN over the top of the nanorods to form a micron-thick layer, however many layers were spun on. The coating shown in figure 7.5 was achieved by coating 10 layers using a 0.1 M solution of CuSCN in ethyl sulphide, followed by 15 layers using a 0.4 M solution. The spinning was performed for 20 seconds at 250 rpm, then 30 seconds at 1000 rpm. The roughness of the nanorods may cause a larger volume of solution to be left after the spinning, leading to deposition of sufficient CuSCN to build up between the rods. However, once the rods were filled the surface was essentially planar and, as with the planar substrates discussed above, no more CuSCN was deposited. It is possible that because of the high solubility of CuSCN in ethyl sulphide, subsequent coatings re-dissolved as much CuSCN as was deposited, leading to a steady-state of film thickness.

It may be possible to deposit a CuSCN film above the nanorods or on planar substrates by using CuSCN solutions in propyl sulphide: CuSCN is less soluble in propyl

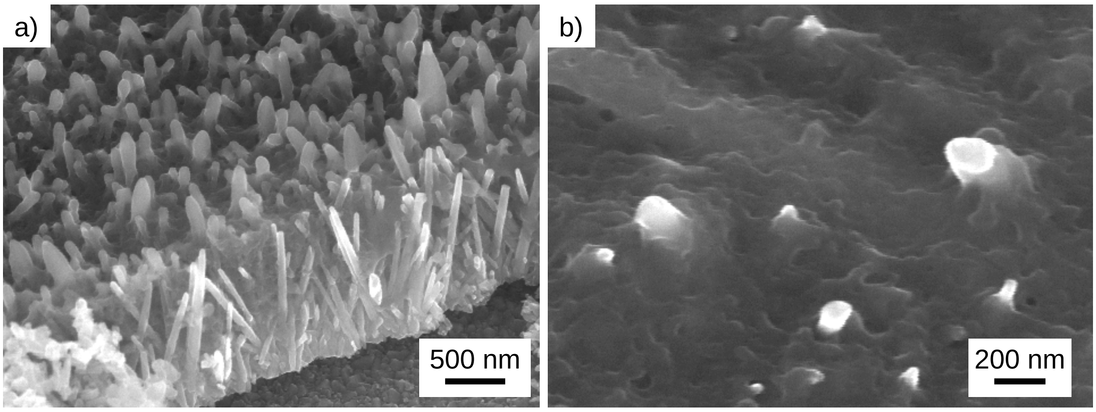

Figure 7.5: **SEM images of ZnO nanorods filled with CuSCN by spin-coating ethyl sulphide solution.** a) Cross-section showing CuSCN filled between rods almost to the tips. Rods ~1.25 μm long. b) Image of surface showing ZnO tips just protruding through CuSCN film. This was the highest above the rods that the CuSCN could be coated. Images taken at 45°.

sulphide than ethyl sulphide [30], and therefore it would be less likely for the solution to re-dissolve previous layers. This process may also be aided by heating the substrate to ~80 °C using a heat lamp during the spin-coating process to speed up the evaporation of the solvent and deposit more material per layer. Further trials using such methods would ascertain whether CuSCN could be deposited by spin-coating. These trials were not performed during this project, and subsequent deposition of CuSCN was performed by methods similar to those in the literature, where CuSCN was dribbled from a solution in propyl sulphide onto the substrate surface and allowed to dry (see section 3.4) [14, 30].

7.3.2 Early trials using propyl sulphide

In early trials of depositing CuSCN onto ZnO nanorods by spreading on the surface as in the literature (section 3.4) [14, 30], 0.1 M solutions of CuSCN in propyl sulphide were used. This solution was slowly delivered from a narrow glass pipette and spread across the surface as in figure 3.5 a. As little as possible of the solution was delivered at a time so that only a very thin layer of solution was left on the surface. If too much solution was released the CuSCN left a thick white deposit at the edge of the drop on drying, which was very cracked and easily peeled off. In the early trials the solution was spread onto the substrate at room temperature and the substrate was then placed onto a hotplate at 70 °C once the surface was covered. The solvent visibly dried after a few seconds and the substrate was then taken off and the coating repeated. This was repeated 20–50 times to build up a thicker film. After every 10 layers the substrate was left on the hotplate for 15 minutes to allow more of the solvent to evaporate. Even when attempting to deposit the solution very evenly inhomogeneities in the thickness on the surface still occurred, leading to an uneven coating across the substrate.

Figure 7.6 shows four images of CuSCN coating produced by this method. Fig-

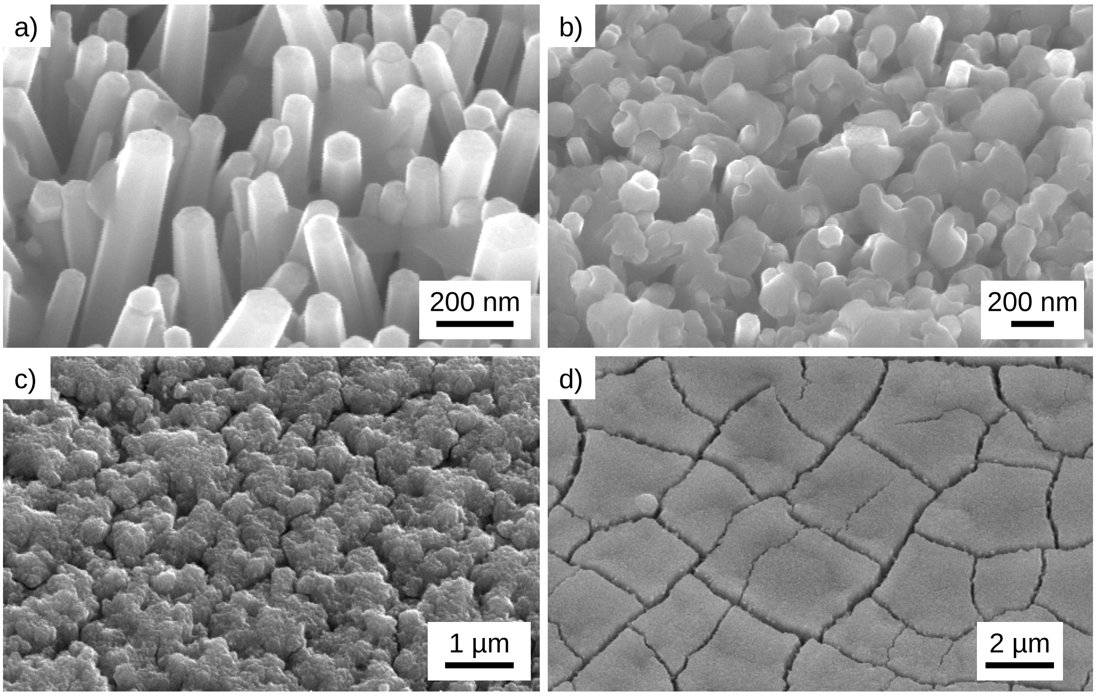

Figure 7.6: **SEM images of ZnO nanorods filled with CuSCN by repeated spreading of propyl sulphide solution over surface.** Progression of filling of rods is shown as more CuSCN was deposited from a)–d). Images taken at 45°.

ures a)–d) represent the different stages of the build-up of CuSCN between and on the ZnO nanorods. This approximately equates to the build-up as more layers were added. However, due to the irregular thickness of CuSCN deposited across the substrate, different regions of one substrate could display multiple examples of the coatings shown in a)–d) after the same number of layers had been deposited. In figure 7.6 a it can be seen that the CuSCN initially forms small clumps between the nanorods. These then join as more CuSCN solution is added, almost completely filling between the nanorods (figure 7.6 b). The film then covers the nanorods, with a number of small, regular cracks that appear to follow larger gaps between nanorods, and a textured surface that conforms to the surface of the nanorods (figure 7.6 c). As more CuSCN solution was added a more planar film built up above the nanorods, which displayed a regular 'mud-cracking' effect, with cracks as wide as 500 nm (figure 7.6 d). This method can therefore be used to fill between ZnO nanorods with CuSCN and form a continuous layer on top. However, depositing the CuSCN by this method led to a large number of very large cracks in the CuSCN film which could lead to short-circuits in the photovoltaic devices.

7.3.3 SC1 and SC2 devices

Following the above trials of CuSCN deposition by spreading a solution in propyl sulphide over the substrate surface slight modifications were made to the method to produce the CuSCN films that were used in solar cells SC1 and SC2. These modifications were made in an attempt to reduce the mud-cracking that occurred when using the method above. The main differences in the process to previous trials was that the substrates were kept at 70 °C while the solution was spread on the surface, and even more effort was made to deposit the minimum quantity of solution possible at any one time. Depositing at 70 °C made it easier to spread the solution out across the surface, possibly because of reduced viscosity at this temperature. In order to produce an even base CuSCN layer any excess solution that did not immediately dry was wicked away by brushing the surface with a cleanroom wipe for the first 10 layers. It was found that creating this even base helped to allow further layers to be coated smoothly. As previously, each layer was allowed to visibly dry before depositing the next and the substrate was left for longer after every 10 layers. However, for these devices the substrates were left for 1–2 hours on the hotplate every 10 layers, rather than 15 minutes. This was an attempt to prevent excess solvent being left in the CuSCN layer as subsequent layers were deposited.

For SC1 devices, 60 layers were deposited in total. Images of the surface after 45 and 60 layers can be seen in figure 7.7. It can be seen that after 45 layers were deposited the nanorods were almost completely covered, but some of the tips of the particularly long rods in these devices (figure 7.1 a) still protruded. The clustering of the CuSCN appears particularly marked here, and when the full 60 layers were deposited the surface appears less flat than in figure 7.6 d. There are still cracks present in the CuSCN film, but smaller than when using the earlier method: the cracks were up to ~250 nm across.

Cross sections of the CuSCN-coated nanorods used in cells SC1 are shown in figure 7.8. These films were separated from the substrate for imaging by scratching along the surface so that the ZnO seed layer came away from the FTO surface. The nanorods can be seen growing from the seed layer, which was around 400–500 nm thick. The longest nanorods, identified in section 7.1, were up to 6 μm long from the base to the tip, but the majority of rods were 3–4 μm long. These correspond to

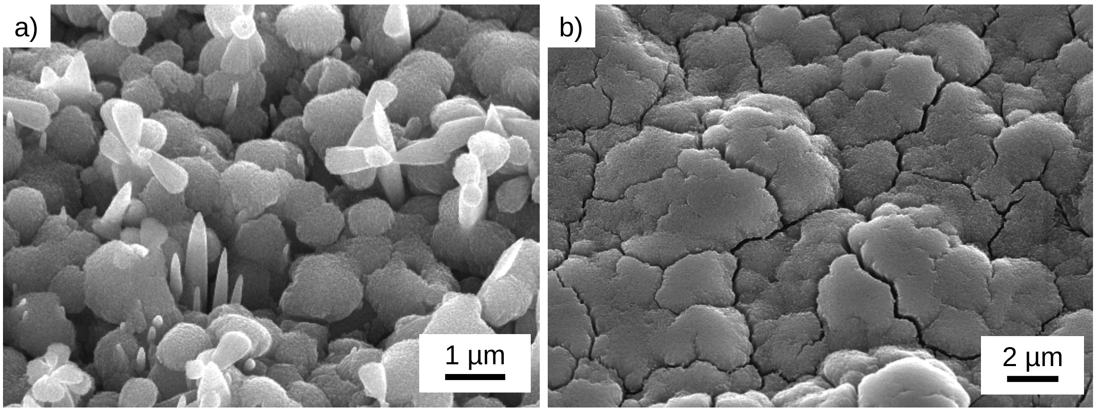

Figure 7.7: **SEM images of 30 layer CdTe-PDDA-coated ZnO nanorods filled with CuSCN from device SC1-E.** a) After 45 layers. b) After 60 layers. Images taken at 45°.

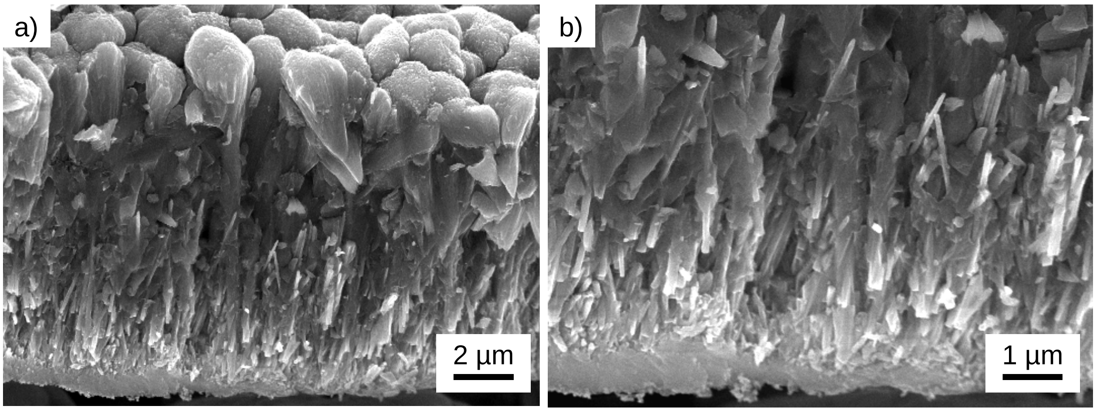

Figure 7.8: **Cross-section SEM images of 30 layer CdTe-PDDA-coated ZnO nanorods filled with CuSCN from device SC1-E.** a) Wide view showing filled nanorods and full coating of CuSCN on top. b) Close-up of nanorods. Tips of longest nanorods (∼6 μm) can be seen at the top of the picture.

the larger and shorter rods seen in the 45° images where around 5 and 1–2 μm were visible, respectively. The rods were intimately filled with CuSCN, and the CuSCN also formed a continuous films around 4–5 μm thick above the longest rods. The textured nature of the CuSCN surface can also be seen.

For SC2 devices the final surface of the CuSCN film was much flatter, but the cracks were larger than in SC1 — generally around 100–500 nm wide (figure 7.9). Although not consistently as large as the cracks in the preliminary films of CuSCN, these cracks could still produce short-circuits through the devices. EDX measurements of the CuSCN films were also performed, which detected only Cu, S, C and N when scanned on the surface (figure 7.10 a), indicating that the film was CuSCN, and was thick enough that the beam did not generate x-rays from the underlying CdTe-coated ZnO nanorods. XRD results of CuSCN deposited on ZnO nanorods are shown in figure 7.10 b. Reflections from the (003) plane and multiples thereof for β-CuSCN (ICDD 29-0581) can be seen, indicating that this phase of CuSCN was present as expected [16, 152]. The absence of peaks from other planes that are seen in the powder pattern such as the (101), (104) and (110) peaks indicate that the CuSCN in this device was oriented with the (003) plane parallel to the substrate surface. The (002) peak for wurzite ZnO (ICDD 36-1451) as discussed previously (section 5.1) can also be seen, indicating the presence of the ZnO nanorods beneath the CuSCN layer, aligned along the c-axis.

Example cross-sections of the CuSCN-filled ZnO nanorods film from device SC2-C are shown in figure 7.11. It can be seen again that the seed layer was 400–500 nm thick. The nanorods were 2–3 μm long, where 1 μm was visibly protruding in images taken of the array at 45° (section 7.1). In figure 7.11 a the CuSCN can be seen intimately filling between the rods and partially obscuring the top 1 μm of the rods. However, little CuSCN can be seen above the rods: it was found that when these films were separated from the substrate, the top section of the CuSCN separated from the

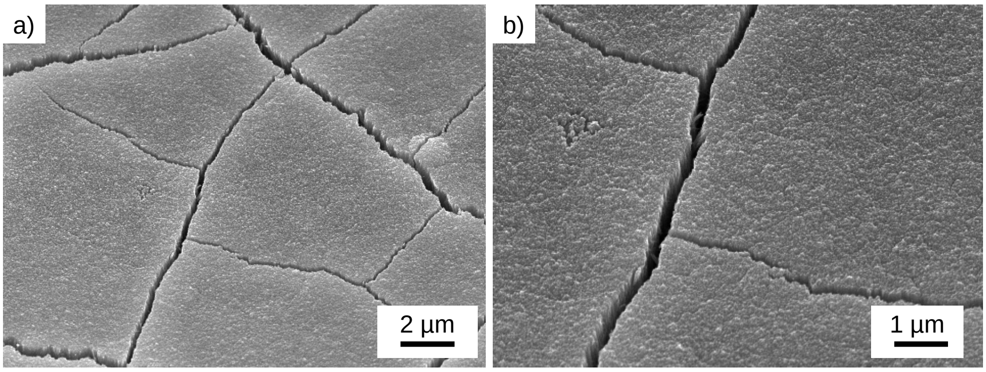

Figure 7.9: **SEM images of 30 layer CdTe-PDDA-coated ZnO nanorods filled and covered with CuSCN from device SC2-C.** a) Wide view. b) Close-up. 60 layers of CuSCN deposited. Images taken at 45°.

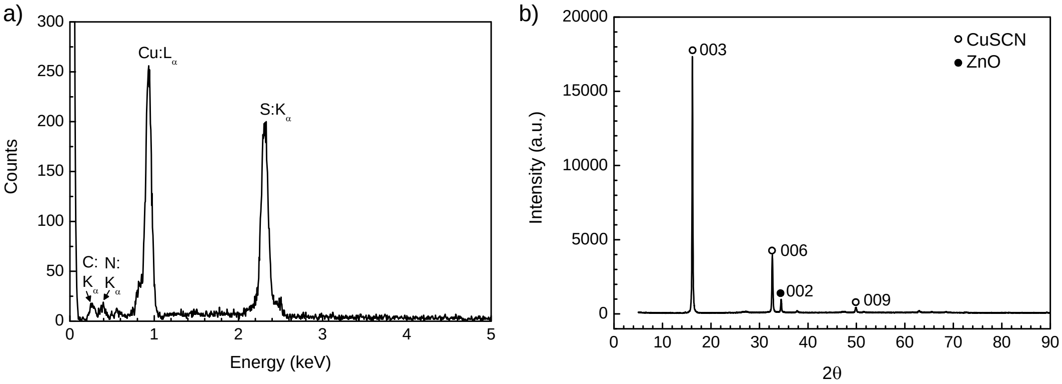

Figure 7.10: **EDX (a) and XRD (b) plots for ZnO nanorods filled and covered with CuSCN by repeated spreading of propyl sulphide solution over surface.** Only Cu, S, C and N from CuSCN are detected in EDX measurement. XRD shows the (003), (006) and (009) peaks for CuSCN, and (002) peak for ZnO.

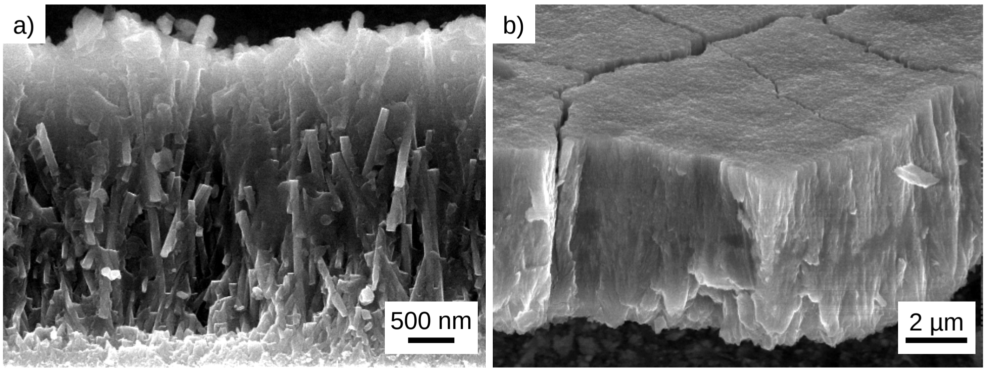

Figure 7.11: **Cross-section SEM images of 30 layer CdTe-PDDA-coated ZnO nanorods from device SC2-C.** a) Section containing ZnO nanorods filled with CuSCN. b) Separate section of CuSCN that had broken from above the nanorods, slightly tilted from the imaging angle. Cracks in surface of CuSCN can be seen.

nanorod array, and was observed as isolated pieces. Such a piece of the CuSCN film is shown in figure 7.11 b. The planar top of the CuSCN film can be seen, including the cracks and the jagged bottom where it separated from above the ZnO nanorods. The crack can be seen propagating right the way through the film, which has implications for the operation of the solar cells and are discussed in section 7.5. These separate CuSCN pieces were between 6 and 8 μm thick, indicating that the CuSCN film covered the nanorods by up to 8 μm — much thicker than the covering over the nanorods in cells SC1. This implies that a similar overall thickness of CuSCN was deposited onto cells SC1 and SC2: the rods in SC1 were filled up to a height of 6 μm (though most rods were around 3 μm), and a further 4 μm of CuSCN was coated over the top. In devices SC2 the 2 μm long rods were filled by CuSCN, and up to a further 8 μm was coated on top. Therefore, in both cases the total thickness of the CuSCN-filled ZnO nanorods and CuSCN film was 10 μm. This is consistent with the same method and the same number of layers of CuSCN being used in each case, assuming that the volume of the ZnO nanorods does not alter the thickness of the film greatly (i.e. make a difference of >1 μm). Comparison of the cross-sectional images from devices SC1 and SC2 also confirms that the extra long synthesis and use of PEI did not produce a great benefit: the longest rods in SC1 were no more than twice as long as those in SC2 despite over three times the growth time, and most were almost the same length with almost identical aspect ratios.

A thin layer of CuSCN deposited in the same way as for devices SC1 and SC2 was also deposited onto a glass substrate for optical analysis. The absorption spectrum and corresponding Tauc plot are shown in figure 7.12. The absorption increases rapidly below ~330 nm, corresponding to an optical band gap of 3.66±0.02 eV as calculated using the Tauc plot [144].

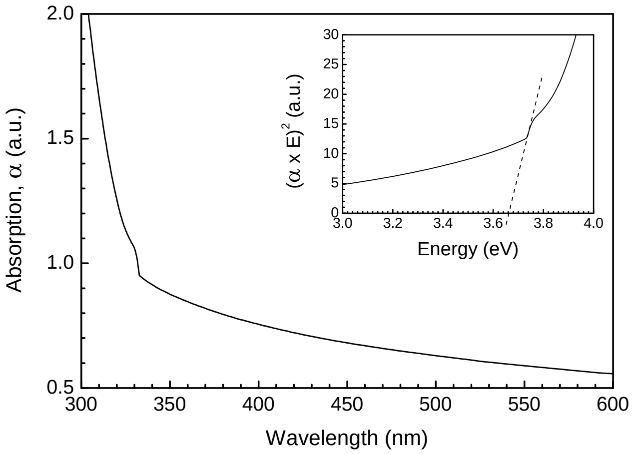

Figure 7.12: **Absorption spectrum and Tauc plot (inset) of CuSCN deposited onto glass from a propyl sulphide solution.** Tangent is taken on Tauc plot at the absorption onset, shown by a dashed line. Intercept gives the optical band gap of CuSCN as 3.66±0.02 eV.

7.3.4 SC3 devices

For CuSCN layers used in solar cells SC3 the deposition process was further modified to try and reduce the inhomogeneities and cracking of the film. The method for spreading the CuSCN in propyl sulphide solution on the surface was adapted slightly, as described in section 3.4: instead of delivering a drop of solution from the end of the pipette and spreading this drop across the surface the drop was run down the side of the pipette which was then placed above the substrate so that the drop formed a meniscus between the side of the pipette and the surface. This had two advantages: it reduced the risk of scratching the surface with the tip of the pipette and it reduced the quantity of solution deposited on the surface, as when the pipette was passed across the surface only a very small quantity of the solution was left in its wake. The other modifications to the method were in the temperatures used: the deposition temperature was increased slightly to 80 °C, and every ten layers the substrates were heated for 5 minutes at 150 °C, rather than left at 80 °C, with the aim of removing all of the residual solvent (see section 3.4). This extra heating was used because even after the surface had visibly dried and the sample had been left at 70 °C overnight a residual smell of the solvent could still be detected on the substrate, suggesting that some was still present. After heating at 150 °C no smell could be detected. The removal of this excess solvent every 10 layers was believed to help in reducing the likelihood of cracking in the film; if the solvent was removed at regular intervals the film would fully dry and solidify at these stages and the strains in the film would stabilise. However, if some of the solvent remained as the layers were built up and then gradually dried over time as suggested in the literature [14], the entire thickness of the film (1–8 μm) would dry in one go, which will increase the likelihood of cracks as the film contracts upon drying.

These modifications to the deposition method appeared to be successful, as no cracks were visible in the film upon SEM analysis (figure 7.13 a). Additionally, the macroscopic evenness of the film was improved using this method, as no pools with

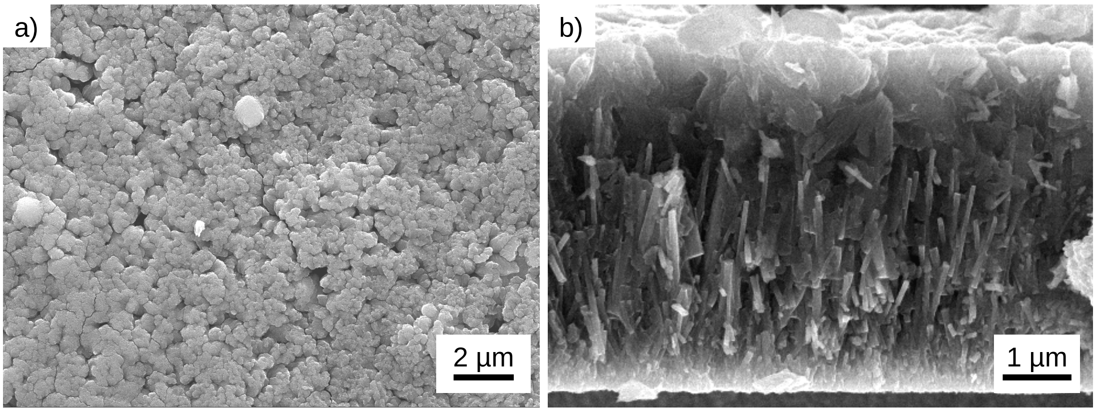

Figure 7.13: **SEM images of CuSCN film coated on top of 30 layer CdTe-PDDA-coated ZnO nanorods from device SC3-A.** a) Surface of film. b) Cross-section of film. CuSCN can be seen filling between rods and covering them by approximately 2 μm.

greater quantities of CuSCN solution formed when depositing the layers due to the quantity of solution being equal along the side of the pipette. Microscopically, the SEM images show that the surface of the film is granular with some pores, although the majority of the grains appear well joined. Cross-sections of the film show that the rods were 2–3 μm long, as with the rods in SC2 cells, which is consistent with the same growth method and time being used. They also show that the film is quite compact and that the pores were only visible on the surface. Also, in SC3 cells the CuSCN film above the rods was only $\sim$2 μm thick (figure 7.13 b). This is much thinner than the film over the rods in SC2 cells. This implies that using the modified method for depositing CuSCN deposits much less material per layer — approximately half as much as the total thickness of the CuSCN from the base of the rods was $\sim$5 μm in SC3 cells compared to 10 μm in SC2 cells.

7.4 PEDOT:PSS

Initial trials to spin-coat PEDOT:PSS between ZnO nanorods followed the literature method, which stated that the as-supplied solution (1.3 wt.% in water) was used for spin-coating [153]. Two layers were deposited at 2000 rpm by the method described in section 3.5. Using the PEDOT:PSS solution undiluted in this way led to poor penetration between the nanorods: figure 7.14 shows a section of the PEDOT:PSS coating that had been lifted off the nanorods by scratching the surface. It can be seen that the PEDOT:PSS layer was mostly deposited above the nanorods, penetrating only 100–200 nm below the tips. After the coating of two layers at this concentration the film was approximately 1.5 μm thick.

To improve the penetration of the solution between the nanorods to provide more intimate contact between the ZnO and PEDOT:PSS, the solution was diluted to 25 % of the supplied concentration by adding three parts absolute ethanol to one part PEDOT:PSS solution. Absolute ethanol was used as it has a lower surface tension than

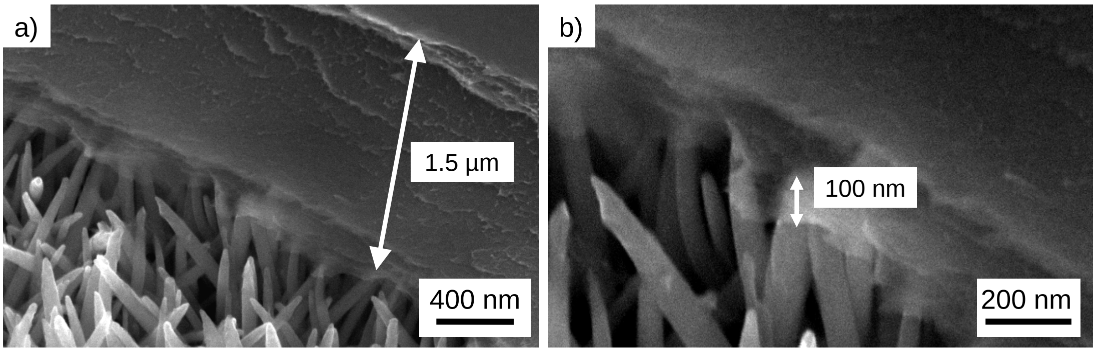

Figure 7.14: **SEM images of PEDOT:PSS film coated on top of ZnO nanorods by spin-coating undiluted PEDOT:PSS solution in water.** a) Wide-view showing $\sim$1.5 μm-thick PEDOT:PSS film covering nanorods. b) Close-up showing that PEDOT:PSS film only penetrates $\sim$100 nm below tips of nanorods. Images taken at 45°.

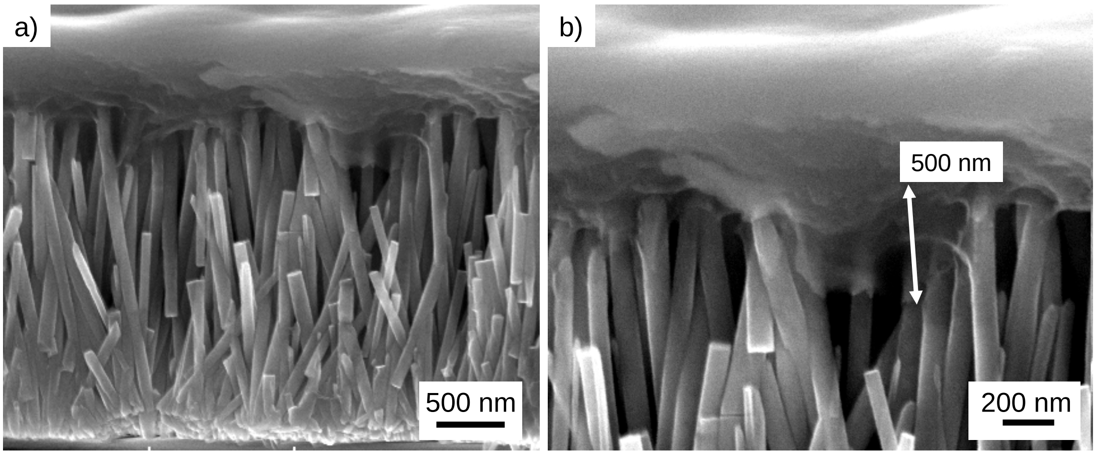

Figure 7.15: **Cross-section SEM images of PEDOT:PSS film coated on top of ZnO nanorods by spin-coating two layers of PEDOT:PSS solution diluted to 25 % in ethanol.** a) Wide-view showing ∼1.5 μm nanorods coated with PEDOT:PSS. b) Close-up showing PEDOT:PSS penetrating ∼500 nm below tips of rods.

water, so was hoped would penetrate further between the rods. This was successful, leading to approximately half the exposed length of the nanorods (∼500 nm) being coated with PEDOT:PSS (figure 7.15). Although the solution did not coat all the way to the bottom of the nanorods, the deeper coating allows at least some of the surface area enhancement of the ZnO nanorods to be utilised.

For the final method, as used in solar cells SC3, two layers of 25 % PEDOT:PSS in ethanol were coated first, followed by two layers of undiluted PEDOT:PSS solution, as the diluted solution was not needed once the film had coated above the nanorods. This led to a coating that protruded 3.5 μm above the nanorods in these solar cells (figure 7.16 a). Figure 7.16 b shows clearly the cross-section of the nanorods and the PEDOT:PSS coating. The 30 layer CdTe-PDDA LbL film can be seen coating approximately 1 μm down the length of the 2–3 μm-long nanorods, i.e. approximately half to a third of the length of the rods was coated in absorber. The CdTe-PDDA coating on these nanorods was annealed for 1 hour at 350 °C, hence the uneven morphology. Unfortunately, only about the top 200 nm of the nanorods are in contact with the PEDOT:PSS — similar to the original trials without ethanol dilution. The PEDOT:PSS solution may not have penetrated as well between the rods because the CdTe LbL coating left smaller pores between the rods. This will have been exacerbated in these cells by the agglomerated lumps of CdTe-PDDA at the tips of the rods, leaving very small pores for PEDOT:PSS penetration (see figure 7.4). These ‘lumps’ are not visible, as they are likely covered by the PEDOT:PSS. Further trials with PEDOT:PSS spin-coating on CdTe-PDDA LbL-coated nanorods are necessary to ascertain the best conditions for filling between these rods. The failure of the PEDOT:PSS film to penetrate between the rods means that although the CdTe-PDDA film coated around 1 μm down the length of the rods, it is unlikely that holes generated along the full extent of the CdTe-PDDA film will be extracted to the external circuit, unless they are able to

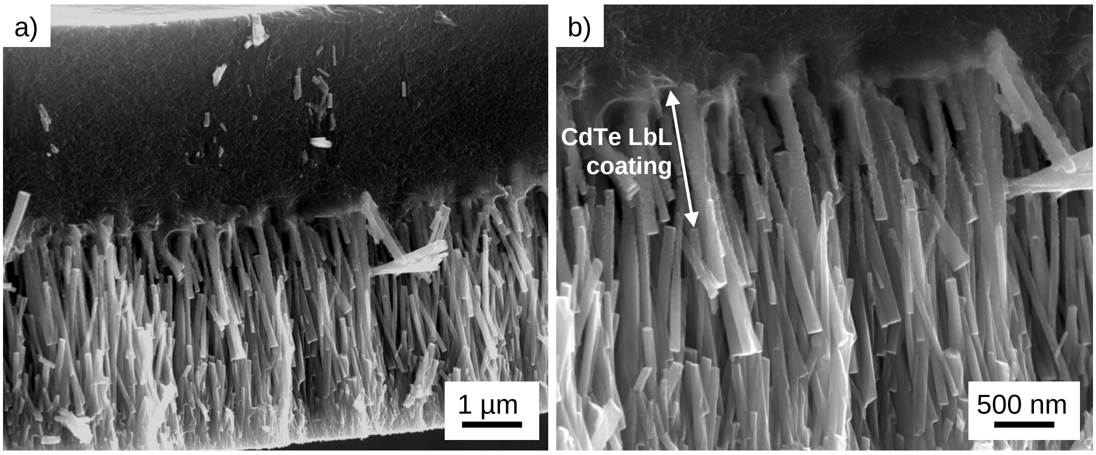

Figure 7.16: **SEM images of PEDOT:PSS film coated on top of 30 layer CdTe-PDDA-coated ZnO nanorods by spin-coating two layers of PEDOT:PSS solution diluted to 25 % in ethanol, followed by two layers of undiluted PEDOT:PSS.** a) Wide view showing full cross-section of PEDOT:PSS coating on ZnO nanorods. b) Close-up showing the CdTe-PDDA LbL coating approximately half way down the length of the nanorods, as indicated.

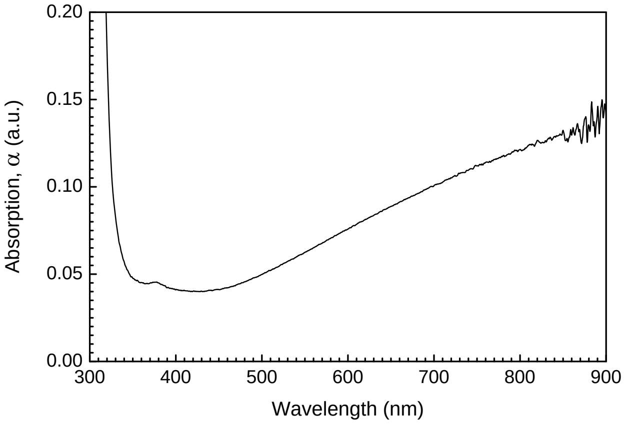

Figure 7.17: **Absorption spectrum of PEDOT:PSS film coated onto glass by spin-coating an undiluted PEDOT:PSS solution at 2000 rpm.**

travel up to 1 μm through the LbL film to reach the PEDOT:PSS layer.

Absorption measurements were performed on a PEDOT:PSS films deposited on glass by spin coating one layer of undiluted solution at 2000 rpm. The spectrum is shown in figure 7.17. There is a small absorption peak around 380 nm, indicating a band gap of around 3.3 eV. Slightly below around 350 nm the absorption increases rapidly. There is also a gradual increase in absorption from ∼450 nm to the end of the scanned range at 900 nm to around three times the level at the small peak at ∼380 nm. This increased absorption at the red end of the spectrum is responsible for the blue colour of the PEDOT:PSS films. A Tauc plot could not be used to ascertain the optical gap of PEDOT:PSS due to this increasing absorption at higher wavelengths.

7.5 Photovoltaic properties

Before looking in detail at the results of the photovoltaic characterisation of the solar cells produced in the project the effect of using an AM 1.5 filter when illuminating the cell should be considered briefly. It was stated in section 3.7.6 that unfiltered 1 sun illumination and 1 sun illumination with an AM 1.5 filter were both used. To ascertain how large an effect the use of the filter had on the results the same cell was illuminated with 1 sun both with and without the filter. The results of this test can be seen in figure 7.18. It can be seen that the *J*–*V* characteristics are very similar in the range shown, with slightly higher short-circuit current density (J_{sc}) ($\Delta J_{sc} = 0.02\,\mathrm{mAcm}^{-2}$) and lower open-circuit voltage (V_{oc}) ($\Delta V_{oc} = 5\,\mathrm{mV}$) when using the filter. The unfiltered light source available at Cranfield was therefore used for collection of all PV data, rather than the AM 1.5 source available at another laboratory. The disparity in results between filtered and unfiltered light were small enough that comparison can be made between the data reported in this chapter and data from the literature obtained using either filtered or unfiltered light. All PV results in this section were obtained using unfiltered light from a Xe arc lamp, calibrated using a Newport reference cell to give 1 sun ($100\,\mathrm{mWcm}^{-2}$) output. The results from these tests are discussed in this section and the components of each cell are shown in table 7.1 and the characteristic parameters of the cells resulting from the tests are shown in table 7.2 for easy comparison.

Figure 7.18 also shows the *J*-*V* characteristics of the same device in the dark. It

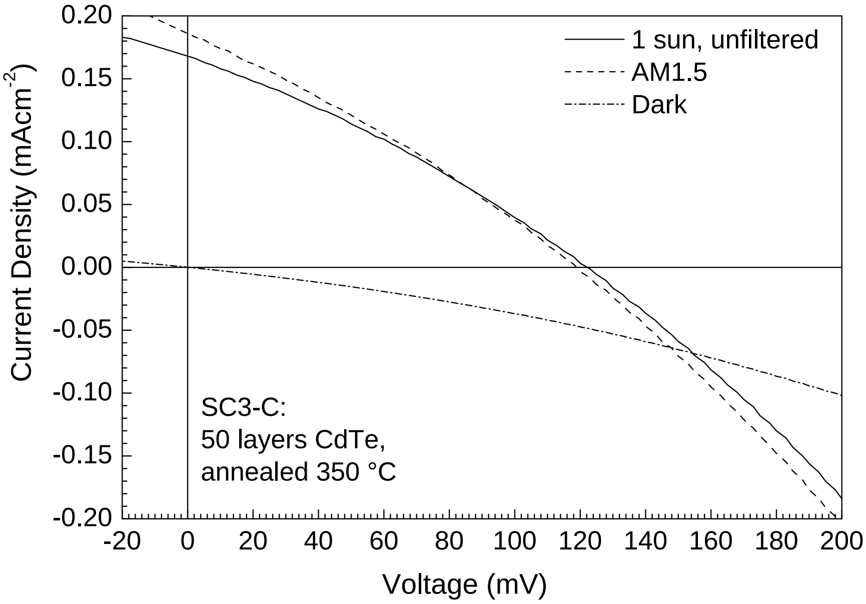

Figure 7.18: **Current density-voltage characteristics of solar cell SC3-C in the dark and illuminated by a Xe lamp at 1 sun illumination with and without an AM 1.5 filter.** Full details of cell components and treatment are in table 7.1.

Table 7.1: **Solar cell components and treatments for all devices produced in the project.** Full details of synthesis methods are given in chapter 3.

Name	ZnO [a]	Anneal [b]	CdTe [c]	Anneal [d]	P-type [e]	Anneal [f]
SC1-A	Seed only		None		CuSCN, 70 °C	70 °C
SC1-B	Seed only		30		CuSCN, 70 °C	70 °C
SC1-C	Seed only		30	350 °C, air	CuSCN, 70 °C	70 °C
SC1-D	50 h, PEI		None		CuSCN, 70 °C	70 °C
SC1-E	50 h, PEI		30		CuSCN, 70 °C	70 °C
SC1-F	50 h, PEI		30	350 °C, air	CuSCN, 70 °C	70 °C
SC2-A	15 h		None		CuSCN, 70 °C	70 °C
SC2-B	15 h		30		CuSCN, 70 °C	70 °C
SC2-C	15 h	400 °C	30		CuSCN, 70 °C	70 °C
SC2-D	15 h	400 °C	30	150 °C, air	CuSCN, 70 °C	70 °C
SC2-E	15 h	400 °C	30	280 °C, vac	CuSCN, 70 °C	70 °C
SC2-F	15 h	400 °C	30	350 °C, vac	CuSCN, 70 °C	70 °C
SC3-A	15 h	400 °C	30	450 °C, vac	CuSCN, 80 °C	150 °C
SC3-B	15 h	400 °C	50		CuSCN, 80 °C	150 °C
SC3-C	15 h	400 °C	50	350 °C, vac	CuSCN, 80 °C	150 °C
SC3-D	15 h	400 °C	30	350 °C, vac	PEDOT:PSS	120 °C
SC3-E	15 h	400 °C	50		PEDOT:PSS	120 °C
SC3-F	15 h	400 °C	50	350 °C, vac	PEDOT:PSS	120 °C

[a] Details of ZnO nanorods used in device. ‘Seed only’ indicates the seed layer was deposited on the substrate but no nanorods were grown. Time, e.g. 15 h, indicates that the nanorods were synthesised for a total of 15 hours in 0.025 M zinc nitrate and HMT solution at 90 °C, replacing the solution every 2.5 hours. ‘PEI’ indicates that ~6 mM PEI was also added to the reaction.

[b] Details of the annealing of the ZnO nanorods. Annealing temperature is given, which was held for 1 hour and performed in air.

[c] Number of layers of CdTe-PDDA LbL film, if any, that were deposited onto the ZnO.

[d] Temperature and atmosphere of the annealing of the LbL film. All annealing was performed for 1 hour.

[e] Type of hole-collecting film used in the solar cell. For CuSCN 60 layers were deposited, and the temperature at which they were deposited is given. All PEDOT:PSS films were deposited by spin-coating a 25 % dilution of as supplied PEDOT:PSS in ethanol two times at 2000 rpm, followed by undiluted PEDOT:PSS two times also at 2000 rpm.

[f] This is the temperature that the substrates were held at for 1–2 hours after every 10 layers for CuSCN, and 2 minutes after every layer for PEDOT:PSS.

Table 7.2: **Solar cell parameters for all devices produced in the project when tested under 1 sun illumination (100 mAcm^{-2}).**

Name	J_{sc} (mAcm^{-2})	V_{oc} (mV)	FF	Efficiency (%)
SC1-A	0.0056±0.0005	0.1±0.1	n/a	∼0
SC1-B	$(5.0\pm0.4)\times10^{-5}$	2.2±0.1	0.27±0.02	$(2.9\pm0.3)\times10^{-8}$
SC1-C	0.0044±0.0001	8.8±0.1	0.26±0.01	$(1.00\pm0.03)\times10^{-5}$
SC1-D	0.073±0.002	7.4±0.1	0.26±0.01	$(1.38\pm0.04)\times10^{-4}$
SC1-E	0.0240±0.0005	27±0.1	0.28±0.01	$(1.80\pm0.04)\times10^{-4}$
SC1-F	0.208±0.001	4.8±0.1	0.25±0.01	$(2.48\pm0.05)\times10^{-4}$
SC2-A	0.013±0.002	6.0±0.5	0.25±0.04	$(2.0\pm0.3)\times10^{-5}$
SC2-B	0.015±0.002	7.0±0.5	0.24±0.04	$(2.5\pm0.4)\times10^{-5}$
SC2-C	0.011±0.001	15±0.5	0.26±0.02	$(4.1\pm0.4)\times10^{-5}$
SC2-D	0.0150±0.0005	29±0.5	0.27±0.01	$(1.18\pm0.04)\times10^{-4}$
SC2-E	0.044±0.001	33±0.5	0.28±0.01	$(4.1\pm0.1)\times10^{-4}$
SC2-F	0.147±0.002	51±0.5	0.28±0.01	$(2.12\pm0.04)\times10^{-3}$
SC3-A	0.053±0.005	13±1	0.25±0.03	$(1.7\pm0.2)\times10^{-4}$
SC3-B	0.0011±0.0002	13±1	0.24±0.05	$(3.2\pm0.6)\times10^{-6}$
SC3-C	0.168±0.002	120±1	0.31±0.01	$(6.17\pm0.09)\times10^{-3}$
SC3-D	0.067±0.005	28±1	0.27±0.02	$(4.9\pm0.4)\times10^{-4}$
SC3-E	0.010±0.001	18±1	0.27±0.03	$(4.5\pm0.5)\times10^{-5}$
SC3-F	0.131±0.003	80±1	0.26±0.01	$(2.73\pm0.07)\times10^{-3}$

can be seen that the line intersects zero, as expected, and that the current density increases at a slower rate than when illuminated so that the dark and light lines cross over just above J_{sc}. All of the devices discussed in this section display similar dark *J*-*V* characteristics that cross the light curves at some point shortly above J_{sc}. These curves are not displayed on the graphs so that the light curves of a number of devices can be compared more easily without confusion.

7.5.1 Role of ZnO in the solar cells

Figures 7.19 and 7.20 show the PV characteristics of SC1 cells without and with ZnO nanorods respectively, and the characteristic parameters are shown in table 7.2. Each graph shows the data for cells with only ZnO and CuSCN, with ZnO, CuSCN and a LbL film, and with that film annealed in air at 350 °C for 1 hour. Excluding annealed cells, these devices can also be compared to cells SC2-A (ZnO nanorods and CuSCN, no CdTe) and SC2-B (ZnO and CuSCN, 30 layers CdTe-PDDA) (figure 7.21). There was a non-zero photocurrent in all cells that did not contain a LbL film (SC1-A, SC1-

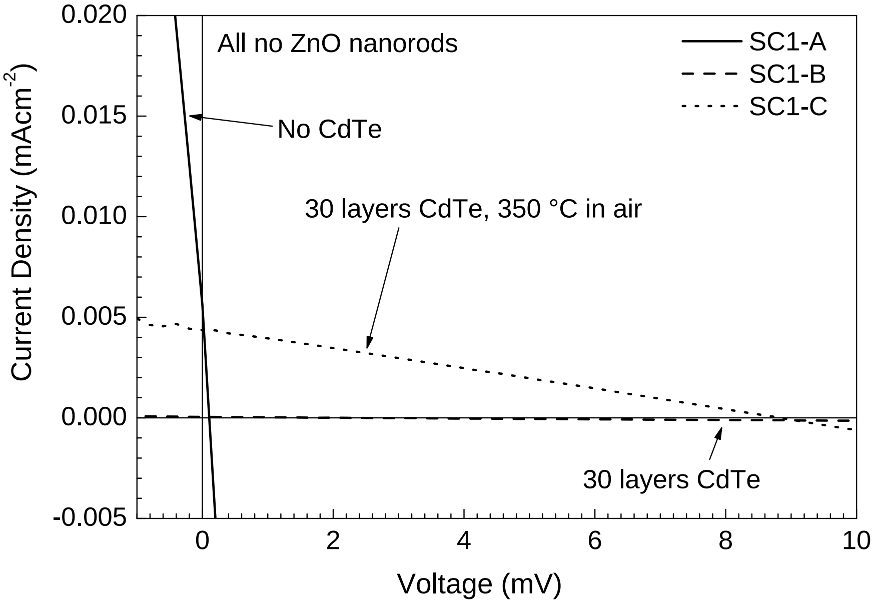

Figure 7.19: **Current density-voltage characteristics of solar cells SC1-A, B and C under illumination with a Xe arc lamp at 1 sun.** Plots are labelled with the differences between the cells for comparison. Full details of cell components and treatment are in table 7.1.

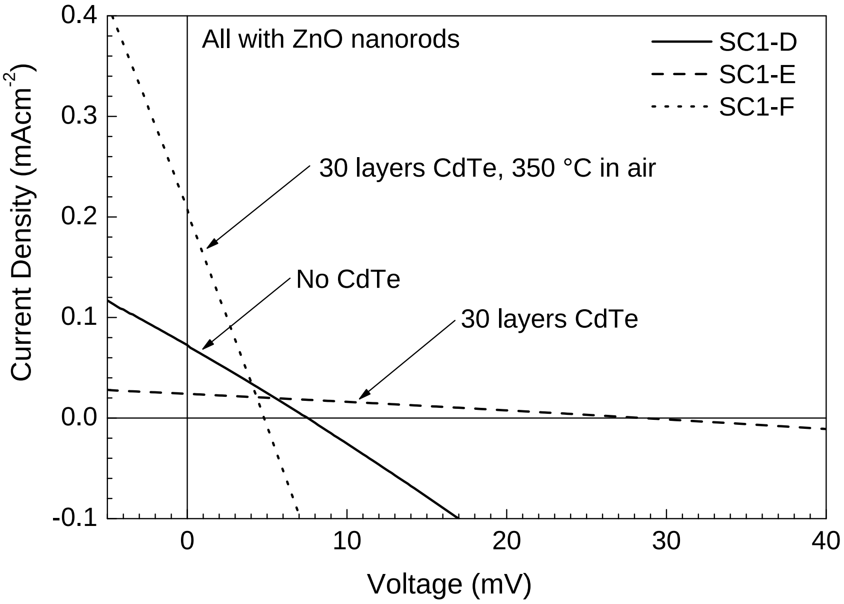

Figure 7.20: **Current density-voltage characteristics of solar cells SC1-D, E and F under illumination with a Xe arc lamp at 1 sun.** Plots are labelled with the differences between the cells for comparison. Full details of cell components and treatments are in table 7.1.

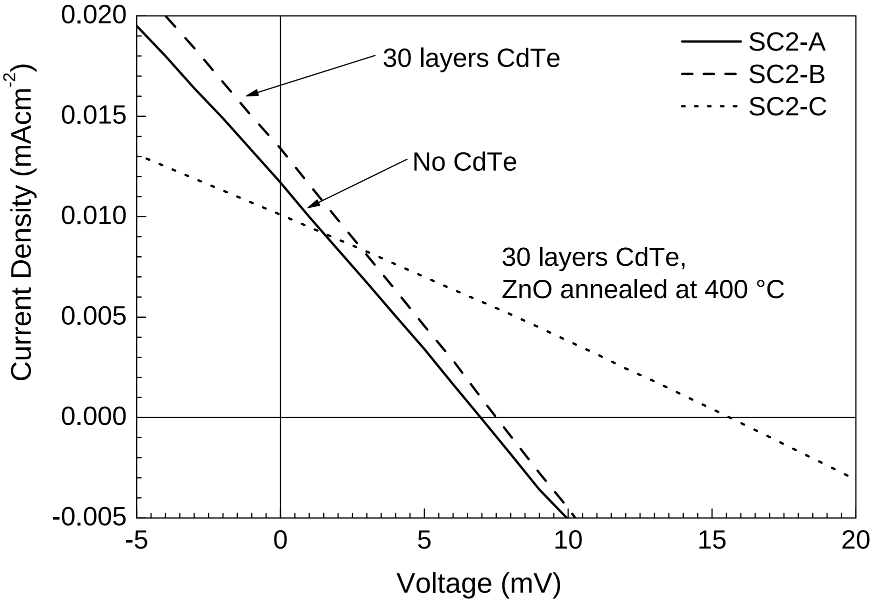

Figure 7.21: **Current density-voltage characteristics of solar cells SC2-A, B and C under illumination with a Xe arc lamp at 1 sun.** Plots are labelled with the differences between the cells for comparison. Full details of cell components and treatment are in table 7.1.

D and SC2-A). The photocurrent here must either have been generated by the ZnO or the CuSCN, as these were the only components present. In all three devices the CuSCN was deposited in exactly the same way, and therefore should be approximately the same optical density (OD). However, SC1-A, SC1-D and SC2-A all had different values of J_{sc}, with SC1-D having the largest and SC1-A the smallest (table 7.2). SC1-D contained ZnO nanorods grown for 50 hours with PEI, SC2-A contained ZnO nanorods grown for 15 hours without PEI, and SC1-A contained no nanorods, only a seed layer. It is therefore expected that SC1-D had the largest OD of ZnO, followed by SC2-A, with the OD of SC1-A being the lowest: figure 6.5 a in chapter 6 showed that the OD of the seed layer was considerably lower than nanorods grown for 7.5 hours. Therefore, it is proposed that in the cells without CdTe-PDDA LbL films it was the ZnO that generated the photocurrent, as the trend in J_{sc} between SC1-A, SC1-D and SC2-A correlates with the trend in OD of ZnO in these cells. However, further experiments would be required to prove more strongly that the ZnO was the source of the photocurrent in these cells. Construction of a number of ZnO-CuSCN only devices with varying quantities of ZnO, followed by quantitative measurement of the OD of the ZnO in each device and comparison to the photocurrent would determine whether J_{sc} is correlated with the OD of ZnO. The absorption measurements would have to be performed using an integrating sphere to remove the effect of scattering by the nanorods.

The suggestion that ZnO was the source of the photocurrent in ZnO-CuSCN only devices is supported when comparing the band gaps of ZnO and CuSCN with the

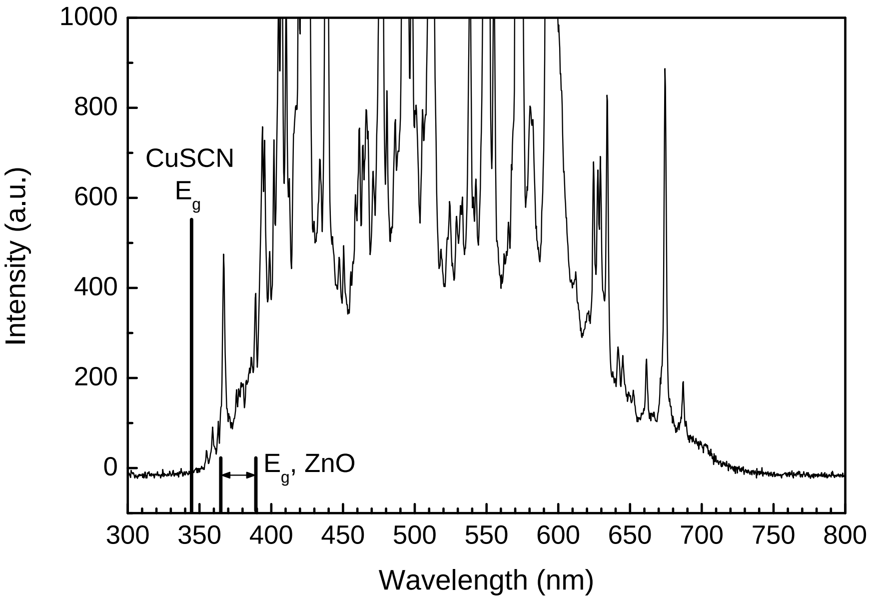

Figure 7.22: **Spectrum of Xe lamp used to test solar cells.** Band gap of CuSCN and band gap range of ZnO are indicated. Spectrum recorded using an Ocean Optics SD2000 spectrometer.

spectrum of the lamp used for testing; the reported band gap of ZnO (3.2–3.4 eV [73–75]) is slightly lower than that of CuSCN (3.6 eV [16]). The band gap of CuSCN is slightly outside of the range of wavelengths emitted by the Xe lamp used to test the solar cells, whereas all of the reported range of band gaps for ZnO are within the wavelengths emitted by the lamp (figure 7.22). The absorption measurements of CuSCN and ZnO in this thesis also agree with this explanation: the absorption onset of CuSCN is around 330 nm (figure 7.12) — outside of the emitted range of the lamps — whereas the absorption onset of ZnO is around 385 nm (figure 6.5), which is well within the range emitted by the lamp. This explanation supports the hypothesis that the ZnO generates the majority of the photocurrent in the cells without a CdTe-PDDA LbL film, as CuSCN would be able to absorb almost no light emitted by the lamp, but ZnO would be able to absorb some of the light.

Considering V_{oc}, in SC1-A (Seed layer and CuSCN only) V_{oc} was almost zero, and the gradient of the *J*–*V* plot is very high, demonstrating a very low resistance in the cell. In SC1-D (long ZnO nanorods and CuSCN only) V_{oc} was much higher, and the resistance of the cell was also higher. V_{oc} for SC2-A (short ZnO nanorods and CuSCN only) was slightly smaller than SC1-D, and still much larger than SC1-A (table 7.2). This suggests that the thin ZnO seed layer in SC1-A allowed a large number of short-circuits from the top Au contact to the bottom FTO contact, reducing V_{oc}. These short-circuits probably also passed through the CuSCN film due to the large cracks, as discussed in section 7.3.3. The use of nanorods in SC2-A blocked some of these short-circuits, increasing the resistance of the cell and increasing V_{oc}. The longer nanorods in SC1-D did not block any more of these short circuits than the shorter nanorods in SC2-A, as V_{oc} was only slightly larger in SC1-D than SC2-A.

7.5.2 Role of LbL CdTe-PDDA films in the solar cells

In cells SC1-B (no nanorods) and SC1-E (long nanorods) with 30 layers of CdTe-PDDA J_{sc} was lower and V_{oc} higher than the equivalent cells without LbL films (SC1-A and SC1-C respectively, see figures 7.19 and 7.20 and table 7.2). In cell SC1-B (no nanorods) J_{sc} was almost zero indicating almost no current reached the external circuit in this cell. In device SC2-B (short ZnO nanorods) the use of the 30 layer CdTe-PDDA LbL film led to only a slight difference in cell performance compared to the cell without CdTe-PDDA (SC2-A) (figure 7.21), unlike devices SC1-B (no nanorods) and SC1-E (long nanorods). In this case there was a very slight increase in both J_{sc} and V_{oc} when using the 30 layer LbL film with the ZnO nanorod-CuSCN structure. If the LbL was generating a photocurrent in these cells, adding to that generated by ZnO, it would be expected that all devices with LbL films would have values of J_{sc} higher than equivalent cells without LbL films. As this was not the case with the cells mentioned above, an alternative explanation is necessary.

To explain these results, it is suggested that the 30 layer CdTe-PDDA LbL film generates a photocurrent itself when coated onto ZnO nanorods and simultaneously blocks the photocurrent that is generated by the ZnO. If this is the case, then J_{sc} in cells SC1-B (no nanorods), SC1-E (long nanorods) and SC2-B (short nanorods) should be related to the OD of the CdTe only, and not the ZnO. However, the OD of the CdTe is not independent of the morphology of the ZnO: a larger surface area of ZnO leads to a larger quantity, and therefore OD, of CdTe. This explains why J_{sc} of cells SC1-E (long nanorods) and SC2-B (short nanorods) are much more similar after LbL coating than before (table 7.2): despite the ZnO nanorods being longer in SC1 cells than SC2 cells the CdTe-PDDA coating only covers a similar length of the rods (section 7.2), therefore there will be a similar OD of CdTe in the two devices. Hence J_{sc} for cell SC1-E ($0.0240 \pm 0.0005\,\mathrm{mAcm^{-2}}$) was only slightly higher than SC2-B ($0.015 \pm 0.002\,\mathrm{mAcm^{-2}}$), as the OD of CdTe was itself only slightly higher. In cell SC1-B, however, the OD of CdTe was much lower as there were no nanorods at all, leading to a J_{sc} of only $5 \times 10^{-5}\,\mathrm{mAcm^{-2}}$. If this explanation is correct, it implies that the nanorods do provide the benefit of increasing the surface area available for CdTe-PDDA coating, but making the nanorods longer only helps if the LbL coating covers further down the rods. To test this hypothesis it would be necessary to construct a series of cells in which the OD of the ZnO and the CdTe were varied independently, with some cells containing only ZnO. It is suggested that in ZnO/CuSCN cells only ZnO contributes to the photocurrent and in ZnO/CdTe-PDDA/CuSCN cells only the CdTe contributes to the photocurrent. This would be proven if J_{sc} depended only on the OD of ZnO in ZnO/CuSCN cells, and only on the OD of CdTe in the ZnO/CdTe-PDDA/CuSCN cells.

An explanation of *why* photocurrent from ZnO may be blocked in the cell when the LbL film is present can be proposed with reference to the PL results of CdTe-PDDA films coated onto ZnO nanorods discussed in section 6.2.2. Those results suggested that 10 layers of CdTe-PDDA intimately coated onto ZnO nanorods could transfer the majority of photogenerated carriers before they recombined. However, when the films were thicker, e.g. where they had filled between rods, the carriers could not reach the interface with ZnO before radiatively recombining in the film. Therefore, in the solar cells discussed here with 30 layers of CdTe-PDDA the excited carriers in approximately the first 10 layers are able to travel to the interface where they are transferred into ZnO (a slight difference in collection depth of carriers may occur due to the presence of the in-built field in the device). This may also occur with the layers nearest the CuSCN interface, but further PL studies of LbL films coated onto CuSCN would be needed to ascertain whether charge transfer occurred at this interface. The carriers that are generated in the CdTe and travel to the interface are collected in the external circuit and contribute to the photocurrent. However, once the 30 layer LbL film is coated onto the ZnO nanorods, the carriers generated in the ZnO cannot pass through the film to the interface with CuSCN before recombining, as they must travel through the full thickness of the film. Thus, once the LbL film is coated on the nanorods, carriers generated in ZnO do not contribute to the photocurrent, and the OD of ZnO has no effect on J_{sc}.

Based on this explanation a band model of the system is proposed, which is shown in figure 7.23. The model is based on the photoexcitation of excitons in the nanoparticles and the transfer of those excitons through the LbL film. It has been predicted that nanoparticle/quantum dot solar cells would be excitonic in nature [154] as quantum dots (QDs) contain very stable excitons due to the quantum confinement increasing their binding energy. The transfer of a photoexcited electron from a QD to the ZnO

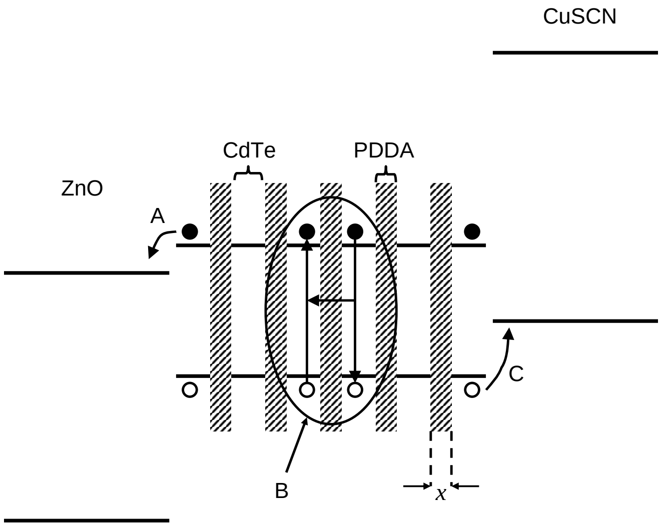

Figure 7.23: **Schematic of a simplified band model of the ZnO/CdTe-PDDA/CuSCN system.** A: Excited electron transfer from CdTe nanoparticle to ZnO. B: Förster resonant energy transfer (FRET) of exciton between adjacent nanparticles. C: Excited hole transfer from CdTe nanoparticle to CuSCN. x: PDDA thickness, approximately equivalent to nanoparticle separation.

is represented by arrow A. Although the mechanism for this transfer is not known the PL results discussed in section 6.2.2 suggest that such a transfer does take place. The equivalent process whereby a hole is transferred into the valence band of CuSCN is represented by arrow C. There is no direct evidence that this process does occur in the solar cells. A possible mechanism for charge transfer between QDs is represented by the process circled and labelled B. This process represents Förster resonant energy transfer (FRET) [155]. In this process the excitation is transferred from one particle to a neighbouring particle through non-radiative dipole-dipole coupling. For this to occur the particles must be separated by less than around 10 nm [156]. The QDs in the LbL film have been shown in a previous study to have a mean interparticle distance (approximately equivalent to PDDA thickness: x in figure 7.23) of 2–3 Å, showing that they are well within the range for FRET to occur. The absorption and emission spectra of the interacting particles must also overlap strongly, which is the case for the CdTe QDs (section 6.2). Additionally, FRET has been shown previously to occur between TGA-capped CdTe nanoparticles with a mean separation of 5 Å [156]. As the requirements for FRET are met in the LbL film and it has been observed previously in a similar if not identical situation it is quite possible that excitons travel between QDs in the LbL film through FRET, although there is no direct evidence for this. This would require no transfer of carriers between particles, only the transfer of the excited state. Essentially no carrier would have to physically cross the PDDA barrier between nanoparticles.

A potential issue in the cell arising from this model is that at the interfaces exciton separation would lead to transfer of only one carrier out of the LbL film (A or C), leaving the other in the film. This isolated carrier would either recombine with carriers at the interface or have to travel through the whole LbL film to be transferred into the layer where they are majority carriers (ZnO for electrons and CuSCN for holes) to be extracted from the cell. Unlike excitons, which can be transferred without the carriers having to physically travel between QDs, these isolated carriers would have to be transferred across a number of PDDA barriers. This makes it very likely that the carrier would recombine at interfaces or in trap states and not be able to travel through the LbL film, as discussed above for carriers generated by the ZnO. This could partly account for the low efficiencies of the cells, as this process would almost guarentee a large portion of the photoexcited carriers in the LbL film would not reach the external circuit and contribute to the photocurrent.

The ability of the PDDA component of the LbL film to block free carriers would also account for the higher V_{oc} in cells using a LbL film than in ZnO/CuSCN only cells; as discussed above the low V_{oc} in the ZnO/CuSCN cells probably results from short-circuits leading to a lower shunt resistance (R_{sh}, see section 2.1.1), lowering the photovoltage generated by the cell. As well as blocking the photocurrent generated by ZnO, the PDDA in the LbL films would also block short-circuit currents, increasing R_{sh}. The use of the LbL film may also reduce recombination at the interface, which has been reduced previously by adding insulating blocking layers [13] (section 2.2.2) and would also lead to an increase in V_{oc}.

It is therefore proposed that in the ZnO/CdTe-PDDA/CuSCN solar cell excitons are generated in the CdTe nanoparticles upon light absorption. At least at the CdTe-ZnO interface (A), and possibly also at the CdTe-CuSCN interface (C) these excitons are separated and excited carriers are transferred. At least some of the nanoparticles would be in direct contact with the ZnO or CuSCN surface without an intermediate PDDA layer, allowing this process to occur more readily. This would create a concentration gradient of excitons, with less at the interface(s). The excitons from within the LbL film would then be transferred along this concentration gradient, possibly by FRET, until they reached the interface, and were themselves separated. The further from the interface the excitons are generated the more likely that they will decay or be separated by trap states before they reach the interface with the ZnO or CuSCN. This explains why only the excitons from the first $\sim$10 layers appeared to be transferred into the ZnO before decaying in the PL study (section 6.2.2), although excitons decaying by non-radiative means would not be detected in PL measurements.

There is no direct evidence to support the proposed model of excitonic charge transfer in the LbL film. The nature of the charge transport properties of the film would have to be studied in order to elucidate the charge transfer mechanisms and try and test the proposed model. However, as stated, nanoparticles are known to have stable excitons due to quantum-confinement induced increase in binding energy, therefore it is quite possible that stable excitons exist in the CdTe nanoparticles. Analysis of the particles to establish whether FRET does occur would be highly interesting, and would shed light on the mechanisms occurring in the film.

Regardless of the mechanism of charge transfer in the LbL film, if J_{sc} is no higher and sometimes lower in cells with the LbL film than cells without the LbL film was therefore not effective as a sensitiser in the solar cells — it would be simpler to make a device with longer ZnO nanorods and no LbL film which would give a higher J_{sc}. For this reason strategies to improve the performance of the device and alter the LbL film were sought for the LbL method to be useful in the construction of a photovoltaic device. The performance of resulting solar cells are details below.

7.5.3 Annealing LbL films in air

Figures 7.19 and 7.20 show cells that had 30 layers of CdTe-PDDA added to the ZnO which were then annealed at 350 °C in air. Both without and with ZnO nanorods there was a large increase in J_{sc} after annealing in air (SC1-C and SC1-F respectively). With the nanorods, the annealed cell (SC1-F) also had a lower V_{oc} than the unannealed (SC1-E). Without ZnO nanorods, the photocurrent was so low in the unannealed cell (SC1-B) that it was hard to tell how V_{oc} changed with annealing. If the annealing removes or oxidises the PDDA component of the LbL film the increase in J_{sc} and decrease in V_{oc} could both be explained by a reduction of the resistance of the layer due to the annealing. The lower resistance of the film would significantly reduce the series resistance (R_s), which would lead to the observed increase in J_{sc}. If the annealing in air also created conductive channels or pinholes through the film it may allow more short-circuit pathways than with the unannealed film. This would reduce R_{sh}, decreasing V_{oc} as observed. This may also allow some of the photocurrent from

ZnO to be collected, further increasing J_{sc}. This implies that the annealing in air of the LbL film reduces the detrimental effect of the PDDA component of the film by reducing R_s, but also increases the number of pinholes in the film, thus decreasing R_{sh}. It would be advantageous to find a method to alter or anneal the LbL film that produced the benefit of reducing R_s, but without inducing pinholes or conductive pathways in the film that reduced R_{sh}.

7.5.4 Annealing of ZnO

Another route explored to improve the devices was to anneal the ZnO before adding the LbL film (see section 3.1.3). The effect of annealing the ZnO nanorods in the devices can be seen by comparing SC2-B and SC2-C in figure 7.24. When the ZnO was annealed, the cell produced a V_{oc} approximately twice as high as without ZnO annealing. When ZnO is annealed in air, oxygen is lost and defects are induced due to increasing non-stoichiometry, which has been linked to the n-type nature of ZnO [77]. Therefore after the annealing the Fermi level will be nearer to the conduction band in the ZnO and the built-in bias in the cell higher. This leads to a lower reverse saturation current (J_0), which reduces the leakage current across the junction and increases V_{oc}, as observed (see equation 2.6: $V_{oc} \propto \ln(1/J_0)$). The significant reduction in J_0 after annealing of the ZnO nanorods can be seen when comparing the dark *J*–*V* characteristics, which can be seen in figure 7.24. The much lower current

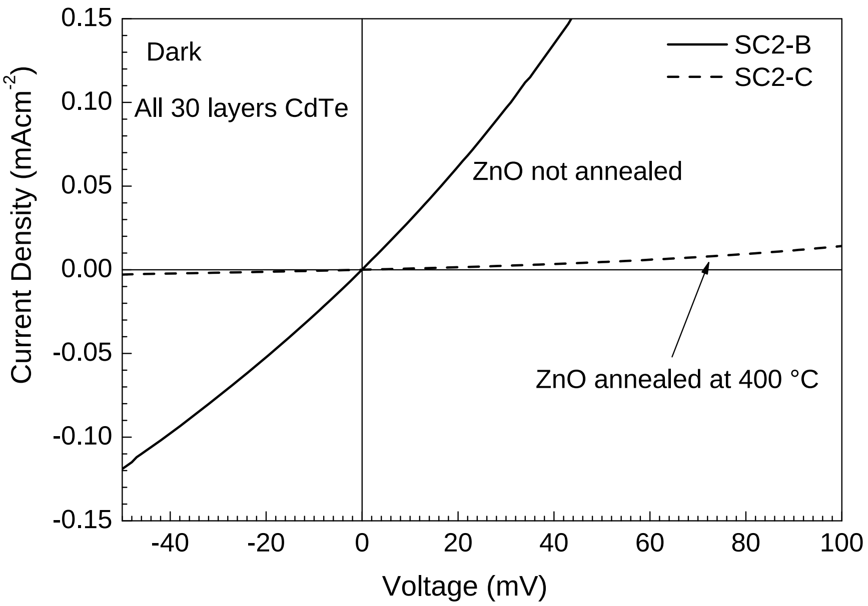

Figure 7.24: **Current density (J)-voltage (V) characteristics of solar cells SC2-B and C in the dark.** Polarity of current density is reversed compared to other *J*-*V* graphs. Plots are labelled with the differences between the cells for comparison. Full details of cell components and treatment are in table 7.1.

in the negative voltage region indicates a much lower J_0. There was also a slightly lower J_{sc} in the cell that contained annealed ZnO nanorods. This can be explained by considering equation 2.5, which shows that $J_{sc} \propto J_0$. However, with such a large decrease in J_0, it would be expected that the decrease in J_{sc} when using annealed ZnO would be much greater. This can be explained by the fact that increasing the density of intrinsic defects in ZnO through annealing would increase the conductivity as well as shift the Fermi level (in fact these two effects are intrinsically linked by the increase in carrier density). Therefore the ZnO nanorods, which are the main route for extracting photogenerated electrons from the cell, would be more conductive and the series resistance (R_s) of the cell would decrease. This would increase J_{sc} (for a large change in R_s), counteracting the decrease caused by the decrease of J_0. Therefore, overall, annealing the ZnO nanorods in the cell improves the performance (almost doubling the efficiency) by increasing V_{oc} and was therefore performed for all subsequent cells.

7.5.5 Annealing LbL films in vacuum

Further annealing of the LbL films in the solar cells was performed in vacuum as detailed studies showed that this was necessary to retain the composition of the nanoparticles (section 6.3.1). In section 6.3 it was stated that annealing of the film up to 280 °C led to a reduction in the nanoparticle separation, indicated by increased interaction lowering the band gap. At 350 °C a portion of the PDDA was lost, possibly in the form of methyl side groups, leading to further increased interaction. All of these factors suggest that annealing the LbL films in vacuum would lead to a lower R_s in the cells due to the reduction in the barrier between particles caused by the PDDA. If the nanoparticles do come into closer contact with heating it may also mean that R_{sh} may not be reduced by an increase in pinholes or conductive channels through the film as occurred when annealing in air. A decrease in R_s without associated increase in R_{sh} would be expected to increase J_{sc} in the cells without also decreasing V_{oc}. Relating this explanation to the model proposed above of charge transfer through the LbL film (represented in figure 7.23) the annealing of the film can be thought of as reducing the mean inter-particle distance, x, by rearrangement of the film and partial decomposition of the PDDA. If charge transfer in the film does occur through FRET, then reducing the particle separation would increase the efficiency of excited transfer [155]. Alternatively, if charge transfer occurred through tunneling of free carriers through the insulating barrier a reduction in the thickness of the barrier would increase the probability that the charge would tunnel through the barrier. For either mechanism, a greater number of carriers would reach the interface with both ZnO and CuSCN and these carriers would come from a greater thickness of the film. This would increase the IQE of the cell increasing J_{sc} based on equations 2.2 and 2.3.

The PV characteristics of solar cells containing 30 layer films annealed at 150–350 °C are shown in figure 7.25. Additionally, graphs comparing cells with unannealed 50 layer films to equivalent cells with annealed films are shown in figures 7.26 and 7.27 for cells with improved CuSCN films and PEDOT:PSS films respectively. It can be seen from figure 7.25 that annealing the LbL films in vacuum up to 350 °C did

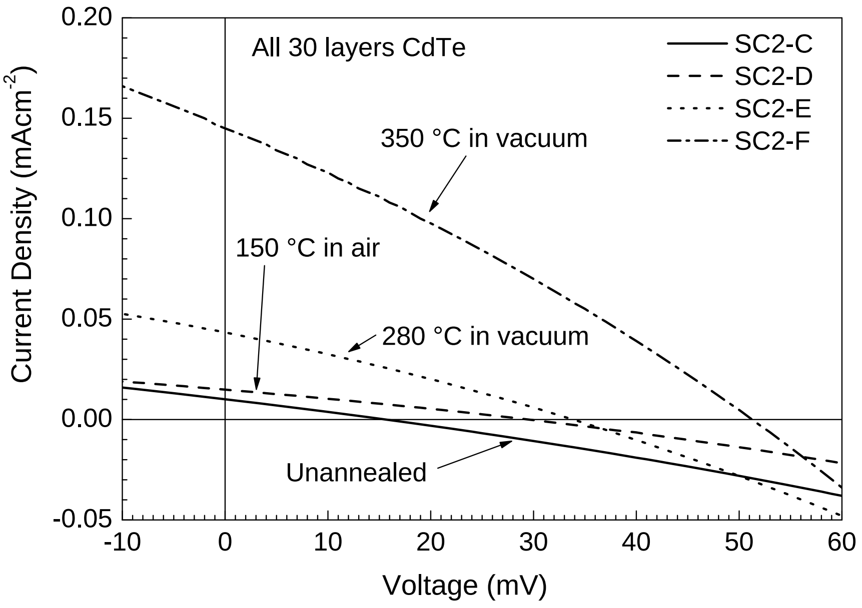

Figure 7.25: **Current density-voltage characteristics of solar cells SC2-C, D, E and F under illumination with a Xe arc lamp at 1 sun.** Plots are labelled with the differences between the cells for comparison. Full details of cell components and treatments are in table 7.1.

lead to a significant increase in J_{sc}. Annealing in vacuum also led to a slight increase in V_{oc} rather than a decrease as seen when films were annealed in air. Also, table 7.2 shows that the fill factor (FF) also increased slightly when annealing the cells. Cells with 350 °C annealed 50 layer CdTe-PDDA films and both improved CuSCN and PEDOT:PSS (SC3-C and SC3-F respectively) also demonstrated a similar increase in J_{sc} and V_{oc} compared to equivalent unannealed cells (SC3-B and SC3-E). In the cells annealed at 350 °C V_{oc} was much higher with 50 layers CdTe-PDDA and improved CuSCN (SC3-C) than with 30 layers and the earlier CuSCN (SC2-F), which is discussed below when considering the CuSCN layers.

Annealing at 150 °C mainly led to an increase in V_{oc} with little change in J_{sc} compared to the unannealed cell, whereas annealing at higher temperatures increased both J_{sc} and V_{oc}. 150 °C annealing was performed in air because it was found that the oxidation only occurred when annealing above ~200 °C. The improvement in V_{oc} at this temperature was most likely related to the loss of water from the LbL film, which was discussed in section 6.3. The loss of water could have increased the resistance of the short-circuit routes thorough the cell, which would have increased V_{oc}. At higher annealing temperatures changes in the LbL films were observed that are consistent with a decrease in separation between the nanoparticles in the LbL film and therefore an increase in interaction between those particles (section 6.3). A reduction in separation between nanoparticles would lead to greater efficiency of charge transfer through the LbL film which would produce the observed increase in J_{sc}. Such a significant change in J_{sc} (over 10 times greater in SC2-F (annealed 350 °C) compared to

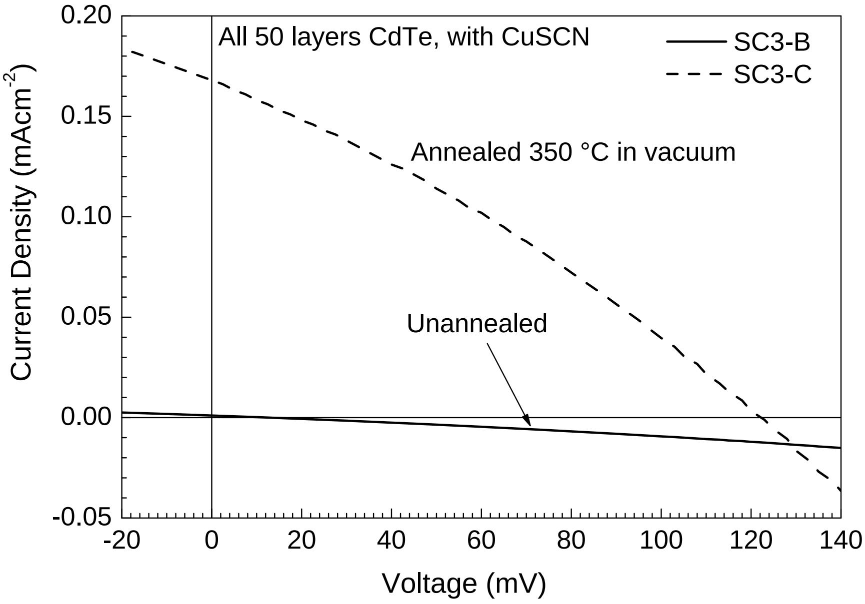

Figure 7.26: **Current density-voltage characteristics of solar cells SC3-B and C under illumination with a Xe arc lamp at 1 sun.** Plots are labelled with the differences between the cells for comparison. Full details of cell components and treatment are in table 7.1.

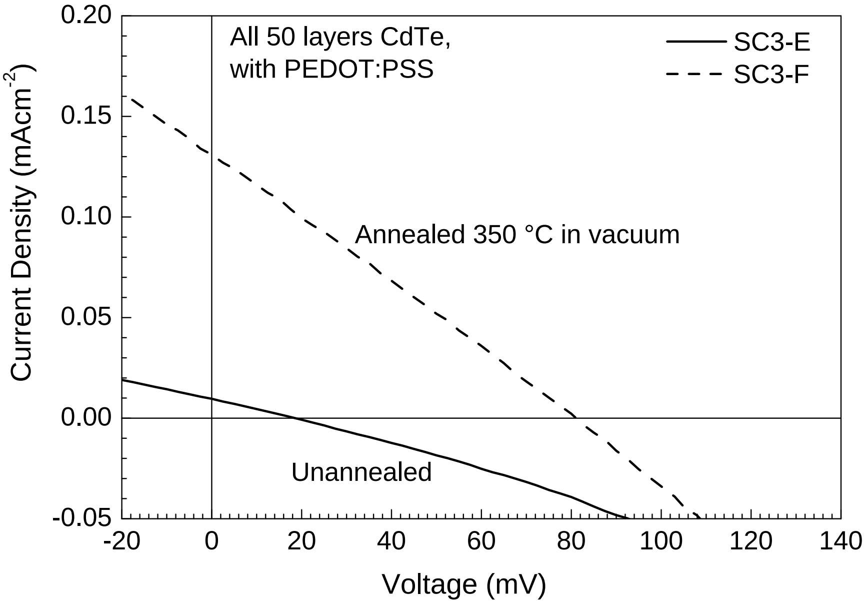

Figure 7.27: **Current density-voltage characteristics of solar cells SC3-E and F under illumination with a Xe arc lamp at 1 sun.** Plots are labelled with the differences between the cells for comparison. Full details of cell components and treatment are in table 7.1.

SC2-C (unannealed)) implies a large change in R_s and/or large change in IQE in the cell. Current-voltage measurements of the LbL films before and after annealing, such as 4-point probe measurements, would ascertain the change in film conductivity with annealing. However, if the charge transfer does occur through FRET such measurements may not fully reflect the change in carrier collection efficiency. Additionally, although V_{oc} is largely independent of R_s for low values of R_s, for such large change in R_s and J_{sc}, V_{oc} will increase slightly in the cell as observed, since $V_{oc} \propto \ln(J_{sc})$ as stated above and shown in equation 2.6. The slight increase in *FF* in the cells after annealing is also consistent with a decrease in R_s; a series resistance in the cell will reduce the current flow in the active region, $J_{sc} \leq J < V_{oc}$, 'smoothing' the turn-on, and decreasing *FF*.

Cell SC3-A contained 30 layers of CdTe-PDDA that were annealed at 450 °C for 1 hour in vacuum and an improved CuSCN layer. The *J–V* curve for this device has not been plotted, but the parameters are shown in table 7.2. Despite having an improved CuSCN layer, this device had lower J_{sc} than device SC2-F (30 layers annealed at 350 °C, original CuSCN), and lower V_{oc} than devices SC2-C, -D, -E and -F (30 layers, unannealed, and annealed at 150, 280 and 350 °C respectively, original CuSCN). It is possible that annealing at 450 °C led to not only the loss of the PDDA component of the LbL film but some of the CdTe as well so that little photocurrent was generated and short-circuits or interfacial recombination also occurred in the device. It is clear that annealing the LbL film at temperatures as high as 450 °C is not beneficial for the performance of the solar cells.

Overall, it can be seen that annealing the LbL films up to 350 °C in vacuum gives a large benefit to the performance of the solar cells: annealing at 350 °C led to an increase in efficiency of cells with 30 layers of CdTe-PDDA and CuSCN hole collectors (SC2-F) by a factor of 50 compared to the equivalent unannealed cell (SC2-C). The use of vacuum annealing of the LbL films may allow the LbL process to be successfully used to coat nanoparticle sensitisers onto ZnO nanorods. This is a significant improvement on unannealed LbL films which, as stated above, gave no greater photocurrent than uncoated nanorods. Although the largest efficiency of all cells produced was only $(6.17\pm0.09)\times10^{-3}$ %, vacuum annealed LbL films do show the potential as sensitisers for ZnO nanorods, and with further improvements of the cell components higher efficiencies may be obtainable.

7.5.6 Comparison of solar cells containing CuSCN and PEDOT:PSS

In cells SC3-D, E and F PEDOT:PSS was investigated as an alternative to CuSCN as a hole collecting layer. Figures 7.28 and 7.29 compare cells using CuSCN and PEDOT:PSS containing 50 layers of CdTe-PDDA unannealed, and annealed at 350 °C in vacuum respectively. As explained above, J_{sc} and V_{oc} were much lower for the cells containing unannealed LbL films (figure 7.28) than in cells containing annealed LbL films (figure 7.29). For cells containing unannealed films J_{sc} and V_{oc} were both lower in the cell using CuSCN than the cell using PEDOT:PSS, whereas when annealed LbL films were used the situation was reversed, with J_{sc} and V_{oc} both higher for cells

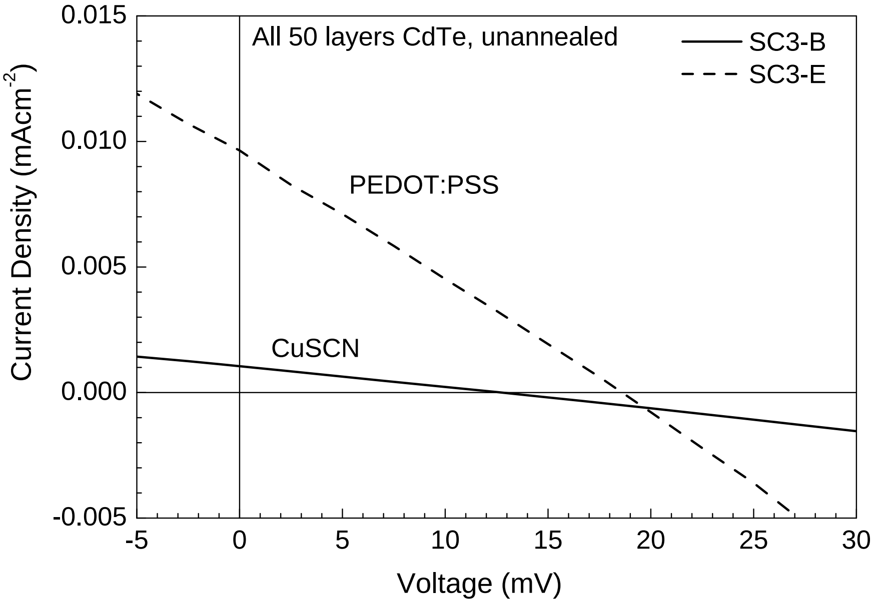

Figure 7.28: **Current density-voltage characteristics of solar cells SC3-B and E under illumination with a Xe arc lamp at 1 sun.** Plots are labelled with the differences between the cells for comparison. Full details of cell components and treatment are in table 7.1.

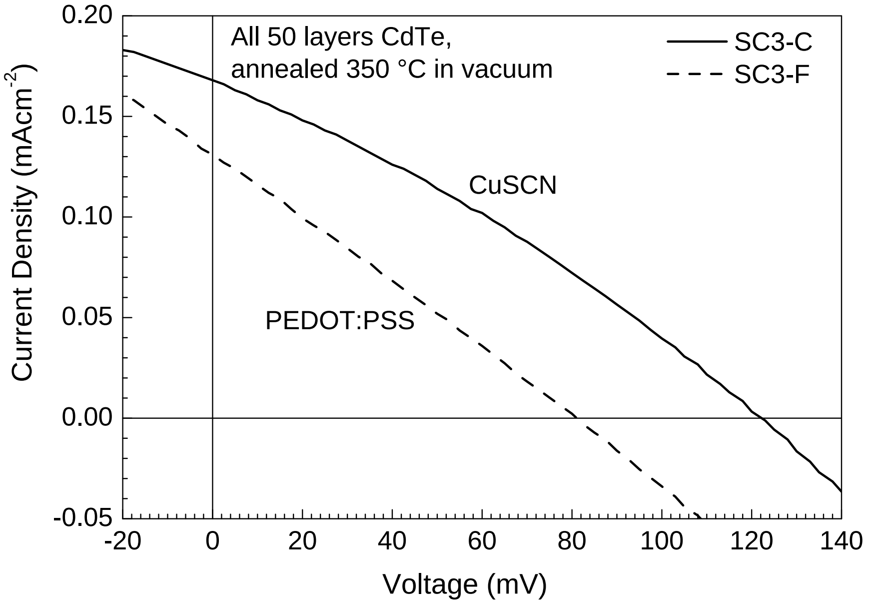

Figure 7.29: **Current density-voltage characteristics of solar cells SC3-C and F under illumination with a Xe arc lamp at 1 sun.** Plots are labelled with the differences between the cells for comparison. Full details of cell components and treatment are in table 7.1.

using CuSCN. This situation can be explained in a similar way to the explanation proposed above when comparing cells without LbL films to those with LbL films, in that the *source* of the photocurrent must be considered in each case. It is proposed that although CuSCN does not generate a photocurrent in the cells, as discussed above, the PEDOT:PSS does generate a photocurrent; CuSCN absorbs almost no light in the range emitted by the lamp, but the PEDOT:PSS absorbtion does increase at the red end of the spectrum (figure 7.17). If the PEDOT:PSS did generate a photocurrent of a similar magnitude to the photocurrent generated by the unannealed LbL film and these photocurrents added together it would be sufficient to increase J_{sc} and V_{oc} in cell SC3-E (PEDOT:PSS) over those in cell SC3-B (CuSCN). However, in cells SC3-C and SC3-F the annealed LbL films generated a photocurrent that was much larger than that generated by the PEDOT:PSS. In this case J_{sc} and V_{oc} in the cell with CuSCN (SC3-C) were larger than in the cell with PEDOT:PSS (SC3-F) because there was a much more intimate contact between the CuSCN and the LbL film. Therefore more of the photocurrent from the LbL film was collected in the cell.

For the above explanation to be valid the photocurrent generated by the PEDOT:PSS film would have to be able to travel through the unannealed LbL film in order to contribute to J_{sc}. This would require different behaviour than for the photocurrent generated by the ZnO, which it was suggested was blocked by the LbL film. Alternatively, it is possible that the PEDOT:PSS film could contribute to the photocurrent by the generation of excitons in the cell; polymer solar cells are known to operate via exciton transfer [154] and excitons may be generated in PEDOT:PSS and separate at the Au contact, which would contribute to the photocurrent. However, it must be confirmed that the PEDOT:PSS could contribute to the photocurrent. This could be achieved similarly to the test for ZnO, by constructing a series of ZnO/PEDOT:PSS only cells and ZnO/CdTe-PDDA/PEDOT:PSS films where the OD of CdTe and PEDOT:PSS were independently varied. Alternatively, PEDOT:PSS-only devices could be constructed using a FTO/PEDOT:PSS/Au structure. Such single-layer polymer devices have been shown to produce a photocurrent through exciton generation [154], and the polarity of the device would show at which interface the excitons were being separated.

7.5.7 Improvement in CuSCN

It is also useful to consider the impact the improvements of the CuSCN film in SC3 cells had compared to SC1 and SC2 cells which had more cracked and thicker CuSCN films (see section 7.3). Figure 7.30 shows the PV characteristics of two devices to explore the impact of the changes in the CuSCN film. These two devices have been chosen because they contained nanorods grown in the same way and both had CdTe-PDDA LbL films annealed at 350 °C. Unfortunately device SC2-F had 30 layers CdTe-PDDA and device SC3-C had 50 layers; devices with the same number of layers CdTe-PDDA but different CuSCN films were not produced. J_{sc} for the two devices is quite similar, with the 50 layer device with improved CuSCN (SC3-C) having J_{sc} 14 % higher than the device with 30 layers and cracked CuSCN (SC2-F). The difference in V_{oc} between the cells is much more marked: V_{oc} for SC3-C is 2.5 times that for SC2-F.

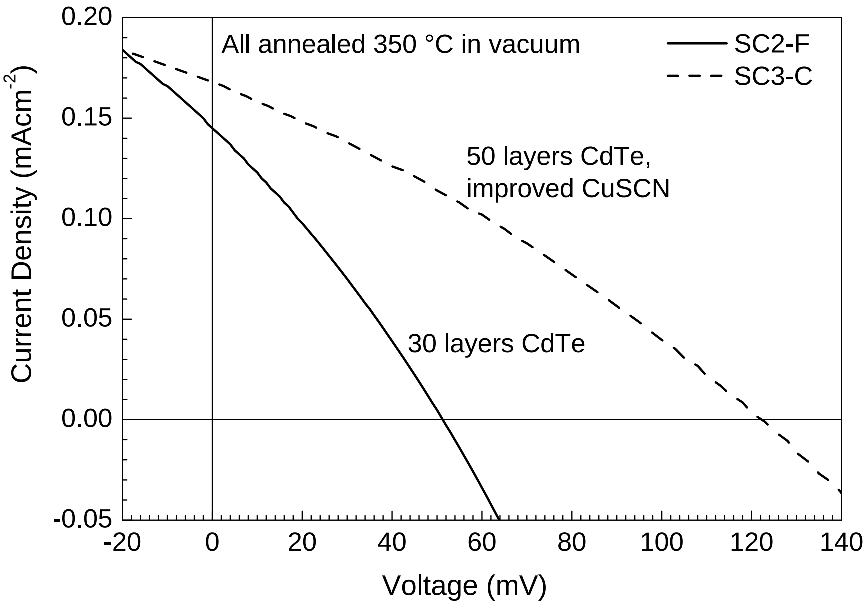

Figure 7.30: **Current density-voltage characteristics of solar cells SC2-F and SC3-C under illumination with a Xe arc lamp at 1 sun.** Plots are labelled with the differences between the cells for comparison. Full details of cell components and treatment are in table 7.1.

The increase in V_{oc} could result from an increase in R_{sh} due to reduction in cracks in the CuSCN layer in SC3-C. However, the increase in thickness of the LbL film in SC3-C could also lead to a reduction in R_{sh}. Further tests are required to ascertain the benefit of the improved CuSCN method. These would require cells to be constructed with identical nanorods and LbL films, but where CuSCN was deposited to the same thickness by the old and new methods. The effect of changing the thickness of the CuSCN film could also be studied by using identical nanorods, LbL film and CuSCN deposition method, but depositing a different number of layers of CuSCN.

7.5.8 Increasing layers in cells with annealed LbL films

Finally, it is possible to compare the effect of increasing the number of layers in annealed cells. It was shown above that cells containing 30 layers of unannealed CdTe-PDDA did not generate a higher photocurrent than equivalent ZnO/CuSCN-only cells, but with an annealed 30-layer film the photocurrent did improve. In figure 7.31 two cells with 30 and 50 CdTe-PDDA layers that were annealed at 350 °C in vacuum and use PEDOT:PSS are compared. It can be seen that using 50 rather than 30 layers of annealed CdTe-PDDA produces approximately double both J_{sc} and V_{oc} and increases the efficiency by a factor of 5.5. This increase indicates that when using annealed LbL films increasing the number of layers of CdTe-PDDA from 30 to 50 does increase the external quantum efficiency (EQE) of the cell (leading to the increase in J_{sc} observed — equation 2.2 — which also increases V_{oc} due to equation 2.6). As

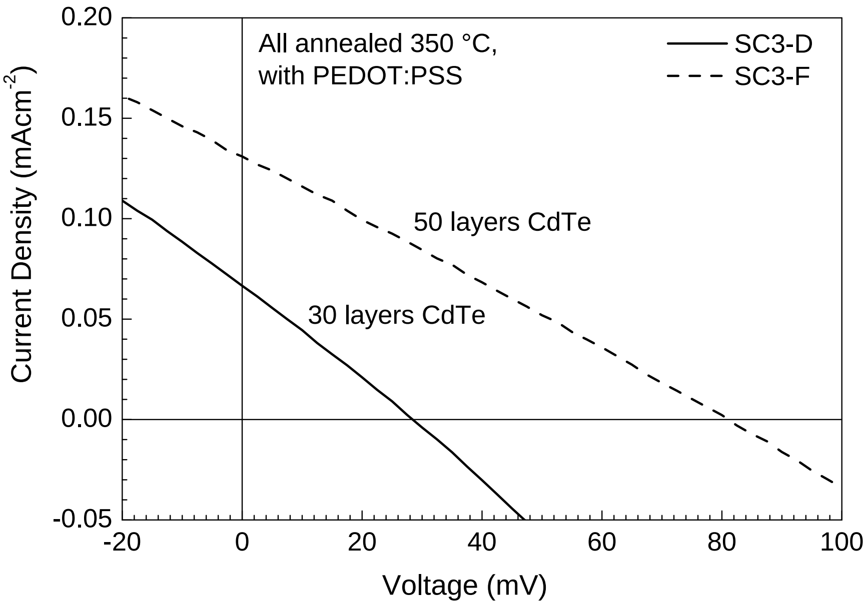

Figure 7.31: **Current density-voltage characteristics of solar cells SC3-D and F under illumination with a Xe arc lamp at 1 sun.** Plots are labelled with the differences between the cells for comparison. Full details of cell components and treatment are in table 7.1.

more light is being absorbed, the increase in EQE is most likely due to an increased light-harvesting efficiency (LHE). The fact that J_{sc} and V_{oc} do increase with increased LHE indicates that the thicker LbL film does not reduce IQE (by introducing added series resistance) by a factor greater than the increase in LHE. Referring to the exciton model above this suggests that in the annealed LbL films the excitons generated in the CdTe nanoparticles must be collected through at least 15 layers, otherwise increasing the number of layers beyond 30 would give no benefit. Therefore, when annealing at 350 °C, increasing the number of layers of CdTe-PDDA improves the performance, at least up to 50 layers, due to increased generation and collection of carriers. This again confirms the benefit of using the LbL process with post-deposition annealing to coat ZnO nanorods with a film of CdTe nanoparticles as a light-absorbing layer in a solar cell. Further experiments with even more layers would ascertain whether there would be a point where increased recombination in the LbL film would outweigh the benefit of increased light absorption.

7.6 Summary

In this chapter the components that make up the solar cells have been described and compared, i.e. the ZnO nanorods, CdTe-PDDA LbL films and CuSCN or PEDOT:PSS layers. The photovoltaic performance of the complete devices has been presented and analysed based on the properties of these components and their annealing treatments.

The effect on the solar cell parameters such as J_{sc}, V_{oc} and FF have been related to these components and their properties and a model has been proposed based on the photo-generation and transfer of excitons in the LbL film. The solar cells were produced in three different batches, labelled SC1, SC2 and SC3. Within each of these batches the ZnO nanorods, if used, were grown in the same way, and the CuSCN or PEDOT:PSS films were also deposited in the same way. However, within each batch the LbL films and annealing treatments of ZnO nanorods of LbL films were varied so that their properties could be compared.

The main characteristics of the components of the cells cells in each batch were as follows. In SC1 cells some cells did not use any ZnO nanorods and where used the nanorods were grown for 50 hours using PEI. These were therefore larger than the nanorods used in SC2 and SC3 cells, which were grown for 15 hours without PEI. The majority of nanorods in SC1 cells were 3–4 μm long and 100 nm wide, with a few extra-long rods $\sim$6 μm long and 500 nm across. In SC2 and SC3 cells the rods were 2–3 μm long and $\sim$90 nm wide. For all devices the same method for Lbl coating was used, which was described in section 3.2. However, for devices SC3 recycled solutions of CdTe nanoparticles were used, which led to an agglomeration of the LbL films at the tips of the ZnO nanorods. On all rods the majority of CdTe-PDDA coated approximately the top 500 nm of the rods, with some of the coating visible up to 1 μm from the tip, but none below that. It was suggested that the surface tension of the CdTe and/or PDDA solutions prevented the film from coating further down the rods. The LbL films for some devices were annealed at 150–450 °C in air or vacuum after coating onto the nanorods.

In devices SC1 and SC2 the common literature method was used to deposit CuSCN using a solution of CuSCN in propyl sulphide, which is spread on the surface of the substrate and allowed to dry at 70–80 °C. This method was adapted by leaving the substrates at this temperature for 1–2 hours every 10 layers to allow more of the solvent to evaporate. There were some cracks in the films, but these were smaller than when not adding the extra drying stages. 60 layers were deposited on both devices SC1 and SC2, which led to an overall film thickness from the bottom of the nanorods of $\sim$10 μm. For devices SC3 the method for depositing the CuSCN was altered slightly. The heat was increased to 150 °C every 10 layers to try and remove more of the solvent and the method for spreading the solution was also altered: the side of the pipette rather than the tip was used to spread the solution. This allowed much smaller and more controlled quantities of solution to be deposited. Films were deposited with no cracks that covered the nanorods by $\sim$2 μm, giving an overall thickness of $\sim$5 μm. The altered method was therefore successful in removing the cracks and also deposited less material. Some SC3 cells used PEDOT:PSS as a hole-collecting layer instead of CuSCN. These films were deposited by spin-coating at 2000 rpm two layers of a 25 % dilution of the supplied solution in ethanol followed by two undiluted layers. However, probably due to the large ‘blobs’ of CdTe on the tips of the rods, the film penetrated no more than 200 nm below the tips of the rods. This meant that a large amount of the CdTe-PDDA film was not in contact with the PEDOT:PSS layer.

XRD and EDX measurments were performed on the CuSCN films in the devices.

These showed peaks corresponding to the β-CuSCN crystal phase oriented with the (003) plane parallel to the surface and the elements C, N, Cu and S were detected in the film. Additionally, absorption measurements were performed on a CuSCN film deposited onto glass, which showed a sharp absorption onset below ~330 nm, and a Tauc plot gave the optical gap as 3.66 ± 0.02 eV. Absorption measurements were performed on a PEDOT:PSS film on glass, which showed a small peak at ~380 nm, sharp increase in absorption below ~350 nm and a gradual increase in absorption from ~450 nm to the end of the measurements at 900 nm. Trials were also performed to spin-coat CuSCN solutions in ethyl sulphide. However, no material could be deposited on planar substrates or to cover above ZnO nanorods, though it did successfully fill between the nanorods.

In the complete solar cells a number of components were varied to understand their role in the cell and how the cells could be improved. In ZnO/CuSCN-only cells it was suggested that ZnO produced a photocurrent, as the absorption of ZnO overlaps with the emission of the lamp whereas the absorption of CuSCN did not. Additionally the photocurrent was higher in ZnO/CuSCN-only cells with a higher optical density (OD) of ZnO. When LbL CdTe-PDDA films were used it was shown that the nanorods did provide a benefit; cells with ZnO nanorods produced J_{sc} at least 10 times higher than cells without nanorods, and V_{oc} was generally higher in cells with nanorods as well. This was attributed to the higher surface area of the nanorods allowing more CdTe to be deposited in the cell, thus having a higher OD. However, it was noted that the presence of the LbL film appeared to block the photocurrent generated by the ZnO nanorods. This could have been because free photoexcited carriers generated in the ZnO could not travel through the LbL film, whereas excitons generated within the film could, as explained below when discussing a model of charge transfer in the LbL film. The photocurrent generated by the as-deposited LbL film was not as large as that generated by the ZnO/CuSCN cells with higher OD of ZnO, therefore improvements were sought to increase the efficiency of the cells.

The improvements that were attempted in the solar cells were: annealing of the ZnO before LbL deposition; annealing the LbL film in air; annealing the LbL film in vacuum; using PEDOT:PSS as a hole collector; improving the CuSCN layer; and increasing the number of CdTe-PDDA layers used in the device. Annealing the ZnO in air at 400 °C improved the performance of the cells by almost doubling V_{oc}: annealing the ZnO significantly reduced the reverse saturation current in the device (J_0) which implies a reduced leakage current. Annealing the LbL films in air gave an increase in J_{sc}, but also a decrease in V_{oc}. It is possible that the annealing led to an increase in the conductivity in the film, increasing the current collected, but also increasing the short-circuits. Annealing the LbL films up to 350 °C in vacuum did produce improvements in the devices: devices with a 30-layer LbL film annealed at 350 °C had an efficiency 50 times greater than an equivalent cell with an unannealed film. The cell with PEDOT:PSS and unannealed LbL films had higher J_{sc} and V_{oc} than the equivalent cell with CuSCN, possibly due to the PEDOT:PSS generating a photocurrent. However, in the cells containing an annealed LbL film the CuSCN-containing device had higher J_{sc} and V_{oc}, probably due to the better penetration of the CuSCN. Using the altered method for depositing CuSCN led to much higher V_{oc} in the cells due to a reduction in cracks in the film. Increasing the number of layers in cells annealed at 350 °C improved the performance by increasing both J_{sc} and V_{oc}, which implies that in the annealed LbL film photogenerated carriers were collected from at least 15 layers.

A model of the charge generation and collection in the device was suggested to explain the above behaviour. In this model, excitons are generated in the nanoparticles on the absorption of incident photons. These excitons are transferred through the film by Förster resonant energy transfer (FRET). In this process an exciton is excited in a particle by the relaxation of an exciton in a neighbouring particle, thereby transferring the exciton without the physical transfer of a particle. This process has been known to occur in nanoparticles, which have a stable exciton. It is therefore possible that it is taking place in the particles in the LbL film, although there is no direct evidence for this. Charge transfer by this process explains many changes in performance of the solar cells described above by either blocking or increasing the charge transfer of excitons through the LbL film. For example the LbL film may block transfer of photogenerated free carriers from ZnO to CuSCN, and annealing of the LbL film may increase the efficiency of FRET in the film by reducing the nanoparticle separation. Much more in-depth analysis of the behaviour of the solar cells and the LbL films would have to be undertaken to provide more evidence of the charge generation and transfer mechanisms.

Overall, it has been shown that a solar cell can be produced from ZnO nanorods coated with CdTe nanoparticles using the LbL process, and completed with a layer of either CuSCN or PEDOT:PSS. It was shown that the as-deposited LbL films do not make very good sensitisers for the ZnO nanorods as insufficient photocurrent was generated by the film. It may be possible to modify the device by using much longer nanorods and thinner LbL films — perhaps under 10 layers — but this would require improvements in the penetration of the solutions during the LbL process between the ZnO nanorods. However, a number of modifications were made to the components of the cells to increase the efficiency. The most effective of these was the annealing of the LbL film in vacuum, with 350 °C being found to be the most effective annealing temperature. This annealing increased the charge transfer efficiency between nanoparticles, possibly by increasing the efficiency of FRET. Although the efficiency of the best device still remained below 0.01 %, the devices have a large potential for optimisation to improve this figure. Some optimisation by improvement of the components was achieved, such as annealing the ZnO nanorods, and reducing the cracks in the CuSCN films. However, the potential future work to further improve and understand these cells is discussed in the next chapter.

Chapter 8

Conclusions and Future Work

8.1 Conclusions

8.1.1 Background and aims

Prior to the research reported in this thesis nanostructured TiO_2 and ZnO had both been widely used in research into solar cell designs. The high surface area of nanostructured TiO_2 electrodes had allowed dye-sensitised solar cells (DSSCs) to achieve efficiencies of around 10 %, where they were limited to less than a tenth of that amount previously. However, the stability of such cells was poorer than inorganic cells due to degradation of both the dye layer and the liquid electrolyte (section 2.2.1). It is for this reason that researchers have investigated ways to replace these components with solid-state semiconductor alternatives. CuSCN is the most common material used to replace the liquid electrolyte as a hole collecting layer (section 2.2.2), though some organic hole-collectors have also been used. To date the highest efficiency all-solid-state nanostrucured cells (known as extra-thin absorber, or eta solar cells — section 2.2) have used CuSCN hole collectors. To replace the dye-based absorbers inorganic semiconductor thin films are generally used, and efficiencies of up to 3.4 % have been achieved in both ZnO and TiO_2-based cells. More recently nanoparticles, or quantum dots (QDs), have been used as absorber layers. These often use liquid electrolytes as in DSSCs, but some cells have been produced with both inorganic and organic solid-state hole collectors. The advantage of using QDs in solar cells is that their absorption range can be tuned by varying the size of the particles without changing their composition. This gives a greater choice of materials when selecting an absorber, as the absorption maximum is no longer fixed by the bulk band gap of the material. In TiO_2 cells reasonable success has been achieved with QD absorbers. For example, in 2009 a TiO_2/PbS QD/spiro-OMeTAD solar cell was reported with an efficiency of 1.46 % [20]. This efficiency was achievable because the very high surface area of the TiO_2 film (up to 1000 times greater than the equivalent planar area) allowed a large quantity of QDs to be adsorbed onto the surface and thus absorbed a large quantity of incident light — the same advantage that allowed DSSCs to absorb sufficient light with only a monolayer of dye.

ZnO nanorods/wires are attractive as alternatives to porous TiO_2 electrodes as they have a superior charge-collection efficiency due to the direct current path to the contact. Hence attempts have been made to replace TiO_2 in nanostructured cells with ZnO. This has led to success in some areas, such as eta cells, which have achieved the same efficiency as TiO_2-based eta cells. This is possible because the inorganic absorber layers used in eta cells can be deposited to any thickness as long as the photogenerated carriers can travel though this film. This allows sufficient light to be absorbed even in ZnO nanorod cells where the surface area enhancement may only be a factor of 10. However, using ZnO in either DSSCs or QD-sensitised cells has not been as successful since the monolayer of absorber materials that are used in these types of cell cannot absorb sufficient light due to the low surface area enhancement provided by ZnO nanorods.

Thus, the aim of the research reported in this thesis was to use the layer-by-layer (LbL) process to coat thicker layers of CdTe QDs onto ZnO nanorods to enhance the light-harvesting efficiency (LHE) of the device. It was hoped that increasing the LHE would increase the cell efficiency compared to devices that use only a monolayer of QDs. CdTe QDs were used here to test this process as they were readily available. Although CdTe does not require quantum confinement to have an optimum band gap for a photovoltaic cell, it was thought that if the LbL process is proven successful using CdTe then QDs of other materials could be investigated. CuSCN was chosen as a hole collector as it is the most common and most successful, though PEDOT:PSS was also used for comparative purposes (section 7.4). Solid-state hole collectors were used rather than a liquid electrolyte because of the stability issues mentioned above. The design of this solar cell aimed to combine the stability and enhanced light absorption achieved in eta solar cells with the tunability of QD absorbers by using all solid-state components and thickness controlled QD absorber layers. ZnO nanorod were used as a basis for the cell because of their superior charge-collecting capabilities and because their more open morphology compared to TiO_2 was more likely to be successful with the LbL process. For such a cell to be successful the following objectives had to be achieved:

- Enhance LHE through the LbL process.
- Create working devices from the ZnO nanorod/CdTe LbL film/CuSCN structure.
- Develop and improve the devices to compete with the efficiency of other QD-sensitised ZnO nanorod solar cells.

8.1.2 Stages of work

For the device to be produced, a number of stages of processing had to be achieved. These were:

- Grow ZnO nanorods on transparent substrates with a surface area enhancement of at least 10.

- Demonstrate that the LbL process could coat ZnO nanorods with a conformal coating of CdTe QDs.
- Fill this structure with CuSCN.
- Complete the devices and demonstrate a photovoltaic effect.

Growth of ZnO nanorods

For solar cells nanorods must be grown on transparent conducting glass such as ITO or FTO-coated glass. This was achieved by depositing a seed layer onto the coated glass to assist nucleation on the substrate during the chemical synthesis of ZnO nanorods. The seed layer did not adhere to the ITO-coated glass substrates, but did adhere to FTO-coated glass, possibly because the surface of the FTO was much more textured than the ITO. A reproducible synthesis method was found by varying a number of factors that affected the rod growth such as whether the vessel was covered, when the reactants were added and whether they were pre-heated. This demonstrated that careful control of the reaction conditions and substrates used was required to reproducibly grow ZnO nanorods suitable for solar cells.

Sb-doping of ZnO nanorods

Sb doping was attempted in a one-step process whereby Sb acetate was added to the synthesis of ZnO nanorods with the aim of producing p-type nanorods. These nanorods could then be used in a solar cell so that an n-type top layer could be used instead of CuSCN or PEDOT:PSS. When the Sb acetate was added directly to the reaction it had an adverse effect on the nanorod morphology, but when it was first dissolved in ethylene glycol (EG) the nanorod morphology was not strongly affected, possibly due to the chelating effect of EG. Sb was detected in the ZnO nanorods after the growth, and both the optical and electrical properties were affected by Sb-doping. However, p-type behaviour could not be proved conclusively and therefore the doped nanorods were not used in solar cells.

LbL coating of nanorods

The LbL processing parameters had been developed previously by Dr Gallardo and these produced a conformal coating of CdTe QDs on ZnO nanorods without variation (chapter 6). It was found that re-using the nanoparticle solutions too many times led to agglomeration of the LbL film at the nanorod tips (section 7.2). It was therefore established that the LbL process could be used to coat ZnO nanorods with layers of CdTe QDs for use in solar cells providing the QD solution was replaced regularly.

CuSCN filling

The method described in the literature for CuSCN deposition was used, where CuSCN is dissolved in propyl sulphide and repeatedly spread on the surface and allowed to dry.

This method was very hard to control and easily led to large quantities of CuSCN solution being deposited at one time that caused cracking and delamination (section 7.3.2). A spin-coating method was investigated as an alternative to the literature method aiming to control the deposited quantity of solution more carefully, but it was found that this was not suitable for depositing CuSCN for use in this solar cell without further modification (section 7.3.1) as too much of the deposited CuSCN re-dissolved when subsequent layers were spin-coated. Many of the problems with the literature method were overcome by changing the deposition method to use the side of the pipette rather than the end to spread the solution, slightly increasing the deposition temperature and increasing the temperature above the solvent boiling point every 10 layers (section 7.3.4). It was therefore found that this method was suitable for producing largely crack-free CuSCN films for use in these solar cells, but only with careful control of the quantity of solution deposited (by using the side of the pipette) and the extent of evaporation of the solvent (by increasing the temperature).

Completion of devices

Devices were completed by evaporating gold contacts onto the surface. However, many devices displayed behaviour consistent with short-circuits. These could have occurred through the cracks in the CuSCN films, indicating that these cracks had to be completely eliminated to improve the solar cell operation, or at the edge of the device areas. Therefore improved CuSCN layers and device layout or wider use of insulting barriers around the edges of the cells made with e.g. epoxy or PMMA may help to reduce these problems in future devices.

8.1.3 Completion of objectives

The extent to which the objectives of the project (listed in section 8.1.1) were met are discussed below.

Enhancement of LHE

As would be expected, increasing the number of layer of QDs deposited on the ZnO nanorods using the LbL process did enhance the LHE of the structure, as a greater quantity of CdTe was present in the light path; increasing the number of layers of CdTe up to 50 led to around 80 % of the incident light being absorbed at the QD absorption peak (section 6.2.1). Therefore the use of the LbL process for depositing QDs was a successful method for enhancing the LHE of a QD-sensitised solar cell. As the LbL films were close to joining between the nanorods after 50 layers, it was deemed that this would be the extent of film thickness used in cells in this research. For cells with more layers to be produced nanorods would have to be grown with greater spacing between them.

Creation of working devices

It was shown that the ZnO nanorod/CdTe LbL film/CuSCN structure did act as a solar cell in that it generated a current upon illumination. The analysis of the solar cell properties implied that the LbL QD films did act as sensitisers for the ZnO nanorods, in that photoexcited carriers were produced in the QD, some of which were transferred to the ZnO and/or CuSCN to contribute to the photocurrent.

Produce cells with competitive efficiency

Despite operating successfully as a solar cell, early devices had very low short-circuit current density (J_{sc}), open-circuit voltage (V_{oc}) and fill factor (FF), leading to an efficiency that was many orders of magnitude less than other reported devices. It was apparent that there were a number of issues with the devices that had to be rectified to improve their light-to-energy conversion performance in order to meet the final objective of the project. Some of these improvements were made by addressing the structural issues that were described above: the CuSCN layer was significantly improved and the device construction was performed with greater control to reduce the number of short-circuits.

The other main area for improvement was the LbL film itself. It was believed that the dielectric polymer component of the LbL film acted as a barrier for charge collection, restricting the devices' ability to collect the photogenerated charges. As such, the LbL films were annealed at a temperature that broke down this polymer to some extent, but still retained the quantum confinement of the nanoparticles (section 6.3). This did lead to improvement in the cells' performance (section 7.5): annealing the LbL film at 350 °C led to an efficiency improvement of a factor of 50 in 30 layer devices, and a factor of 2000 in 50 layer devices. This confirmed that a large amount of losses in the cells were caused by the polymer component of the LbL film, and the inefficiency of charge collection from the LbL film.

The best efficiency of all of the cells that were produced was $(6.17 \pm 0.09) \times 10^{-3}$ %. This is still well below the efficiency of QD-sensitised ZnO nanorod solar cells in the literature, and therefore this objective was not met in the project. For the devices to compete with those in the literature V_{oc} must be improved by up to a factor of 5, and J_{sc} by a factor of 10–50. As well as QD-sensitised solar cells, the cell structure produced in this work can also be compared to ZnO/In_2S_3/CuSCN cells with In_2S_3 layers produced by ILGAR, which have the highest efficiency of eta solar cells ($\sim$3.4 %) along with TiO_2/In_2S_3/Sb_2O_3/CuSCN cells with absorber layers produced by SILAR (section 2.2). Both these cells use thin-film absorber layers are produced by either gas-phase (ILGAR) or solution-phase (SILAR) LbL processes whereby precursors, rather than QDs, are deposited in the LbL process, and both use solution-deposited CuSCN films. These cells produce efficiencies over 500 times greater than the best cell in this project. The main difference between the ZnO/In_2S_3/CuSCN cell and the ZnO/CdTe-PDDA/CuSCN cells produced in this project is the absorber layer, as well as potentially having an improved CuSCN layer (fewer cracks and optimised thickness) and device construction (less short-circuits). The thin-films produced by SILAR and ILGAR are expected to have better charge transfer properties than a QD film as they are formed from well-connected grains without capping molecules and polymer binders between particles. Although this may suggest that the LbL-QD film would be better replaced by SILAR or ILGAR thin-films, it is still desirable to incorporate QDs into the solar cell structure for reasons outlined at the beginning of this chapter. Compared to SILAR or ILGAR thin-films QD absorbers have the potential to utilise a much wider range of materials (SILAR and ILGAR films have thus far been largely confined to metal-sulphides), including those with smaller than optimum bulk band gaps. As demonstrated, the LbL process allows the thickness of QD films to be increased to increase the light absorption. Therefore it would be of interest to investigate further possible improvements of the charge transport of the LbL-QD film as well as those of the other cell components. Studies that could be undertaken to achieve these improvements as well as a number of areas of investigation that have been suggested throughout this thesis are detailed in the section below.

8.2 Future Work

In the following section a number of suggestions for future areas of investigation that continue the work described in this thesis are given. As with the other parts of the thesis these are divided by the different components of the solar cells (ZnO nanorods, CdTe LbL film, hole-collecting layer) in addition to variations that can be made to the complete cells.

ZnO nanorods

As well as variations to the size and aspect ratio of the rods (explained in terms of the complete solar cell below) there is also the possibility of investigating different methods for growing ZnO nanorods. These include minor changes such as changing the growth temperature, time or reactant concentrations. The concentrations could be varied together, or separately as in Ref. 67 so that the reactants are no longer equimolar. Nanorod growth using zinc nitrate and ammonia could be investigated, as in section 2.3.1 and Refs. 101–103. The aims of investigating variations of the growth of the ZnO nanorods would be to try and grow more elongated nanorods with greater spacing between them. This could allow the LbL process to coat further down the nanorods, which would likely be beneficial to solar cell performance (section 7.5). Additionally it would be advantageous to grow the nanorods to the required size more rapidly or using a smaller number of reactions as this would reduce the time required to produce the solar cells, allowing a greater number of cells to be made.

QDs and LbL

The quantum dots (QDs) used in the solar cells could themselves be varied. The size of the CdTe QDs could be varied and the resulting change in interactions between the

QDs and the ZnO nanorods could be studied using photoluminescence (section 6.2.2) to better understand the interaction between the materials and the impact of quantum confinement on this. The photovoltaic performance of cells produced using a variety of QD sizes could also be investigated. This would help to understand how the band alignments between the QDs and ZnO influence the cell performance. Additionally, QDs of materials other than CdTe could also be used in the solar cells, as discussed in section 1.2. These could include commonly used QDs such as CdSe, PbS or PbSe as well as less commonly used narrow or medium band gap materials such as a number of sulphides or oxides of common metals such as FeS_2, $CuFeS_2$, Fe_2O_3 etc. which are normally not suitable for solar cells due to their band gaps being too small or having poor transport characteristics, but which may function well as QD sensitisers. If these materials could be found to function well as QD sensitisers it would be very useful as they would be much less expensive or toxic than commonly used materials such as CdTe, GaAs and $CuInSe_2$.

There may also be a number of areas of investigation related to the LbL process. An important improvement would be to increase the penetration of the LbL film between the nanorods so that more of the surface area enhancement is utilised. This may be achieved by varying the concentration of the QDs or polymer in the process or by using a different polymer to reduce the viscosity of the solutions and improve penetration.

The other areas of investigation are related to methods for reducing the resistance of the LbL film and increasing the efficiency of charge extraction from the QDs in the film. It is possible that a different polymer could be used in the LbL process with properties that could: lower the resistance of the film itself (i.e. reduce the insulating barrier between QDs); reduce the separation between the QDs, possibly by using a shorter chain polymer; be more easily removed by annealing; or possibly be able to be removed chemically while leaving the QDs in-situ. Alternately it may be possible to use a conducting polymer in the LbL process that would enable carriers to be extracted more efficiently. For example, PEDOT:PSS films have been produced previously by a LbL process [157] and it may be possible to incorporate QDs into this method.

Another area of investigation would be to try and use alternate layers of oppositely charged QDs, instead of QDs and a polymer. The QDs would adhere to each other, and without a polymer the resistance of the film should be much lower. This has been investigated previously for CdTe QDs [139] and more than a single bilayer could not be deposited as the oppositely charged QDs did not adhere to each other strongly enough and the charges in the film did not balance. It is possible that by investigating different QDs with a range of sizes and capping molecules a combination could be found that led to strongly bound multi-layer QD-only LbL films.

Finally, the annealing of the LbL films has a great deal of scope for more in-depth investigation. It would be useful to investigate the effect of temperature on the LbL films with a greater precision, i.e. investigate more temperatures in the range 150–450 °C. This would be supplemented by investigating the effect of annealing time on the LbL films including very rapid annealing and cooling at higher temperatures. Also the use of a gas flow, such as argon, in the annealing process may help to remove the polymer from the LbL film. By varying these parameters a set of conditions may be found that lead to a more efficient solar cell.

Hole collector

As mentioned in the above section the CuSCN film in the solar cells still requires optimisation. The complete removal of cracks from the CuSCN film would most likely increase V_{oc} in the devices. Also, investigation into the optimum thickness of the CuSCN film is required: the film must be as thin as possible to minimise the series resistance, while being thick enough for there to be no short-circuits through the film. The resistance of the CuSCN film could possibly be reduced further by treatment with KSCN or LiSCN as in Refs. 9, 17, 18 and 29 (sections 2.2.2 and 2.2.4), which would potentially increase J_{sc} in the devices. Construction of a series of ZnO-CuSCN diodes with varied CuSCN layers would be able to find the CuSCN type with the optimum properties. Additionally, alternative methods for producing CuSCN could be further attempted that are more reproducable than the solution-spreading method, and more likely to produce smooth, crack-free films. Such improvements may be achieved if spin-coating could be used to produce films, possibly by using CuSCN in propyl sulphide instead of ethyl sulphide to reduce the re-dissolving rate, or by heating using a heat lamp to increase the evaporation rate of the solvent. PEDOT:PSS would also benefit from further variation in the deposition method. It would be useful to find a way to fill it effectively between the pores of the LbL-coated ZnO nanorods. Additionally, alternative hole-conducting polymers such as MEH:PPV and spiro-OMeTAD could be investigated, as used in previous extra-thin absorber solar cells (section 2.2) as they may penetrate better between the nanorods, or produce more efficient devices.

Solar cell designs and variations

The final aspect of the project that could be further investigated is the solar cells themselves. A number of suggestions for further investigation were mentioned in section 7.5 and these are brought together and summarised here. In order to better understand the roles of the different components in the solar cells and test the hypotheses of the charge transport processes and limitations of the solar cells it would be beneficial to construct a number of cells that systematically study variations in each component. Testing more ZnO nanorod/CuSCN cells would allow the optical density (OD) of the ZnO to be varied and correlated with the cell performance. This would also allow the CuSCN layer to be varied as above and the impact on the photovoltaic performance to be studied. In the ZnO nanorod/CdTe LbL film/CuSCN devices it would be useful to vary the number of layers of CdTe-PDDA (e.g. 10, 30 and 50) both with unannealed and annealed LbL films to determine if there is a maximum thickness through which photogenerated carriers can be extracted, and whether this varies depending on annealing temperature. It would also be useful to vary the length of the ZnO nanorods in these cells while keeping the OD of CdTe constant if the penetration of the LbL films could be improved. This could potentially improve the efficiency of the devices by reducing the thickness of the LbL films while keeping the light-harvesting efficiency constant. It would also be useful to construct a number of devices to study the role of PEDOT:PSS in the solar cells. PEDOT:PSS-only cells, i.e. FTO/PEDOT:PSS/Au, could be studied to find if a photovoltage is generated, and the polarity of the devices would help to clarify where the excitons are being separated [154]. It would also be useful to construct ZnO nanorod/PEDOT:PSS cells to discover whether they generate a photocurrent. These could be compared to ZnO nanorod/LbL CdTe/PEDOT:PSS cells with varying thicknesses of CdTe to see whether the presence of CdTe LbL films increases or decreases the photocurrent compared to ZnO nanorod/PEDOT:PSS-only devices. For all of the cells produced it would be useful to measure incident photon-to-electron conversion efficiency (IPCE) spectra, which can be compared to LHE to ascertain at what wavelengths the photocurrent is being generated. This would help to elucidate the source of the photocurrent in various cells.

The further investigation suggested above should lead to improved understanding of ZnO nanorod/LbL CdTe QD solar cells, building on that developed in this thesis. It is hoped that with this understanding this new type of solar cell could be developed and improved so that it may operate at efficiencies that are competitive with other nanostructured solar cells under investigation at this time.

References

[1] *Renewables 2011: Global Status Report*. REN21, (2011).

[2] *Solar Generation 6*. European Photovoltaic Industry Association — Greenpeace, (2011).

[3] *Global Market Outlook For Photovoltaics Until 2015*. European Photovoltaic Industry Association, (2011).

[4] Green, M. A., Emery, K., Hishikawa, Y., and Warta, W. *Progress in Photovoltaics: Research and Applications* **19**(1), 84–92 (2011).

[5] Bertoni, C., Gallardo, D., Dunn, S., Gaponik, N., and Eychmüller, A. *Applied Physics Letters* **90**(3), 034107 (2007).

[6] Nelson, J. *The Physics of Solar Cells*. Imperial College Press, London, (2003).

[7] Belaidi, A., Dittrich, T., Kieven, D., Tornow, J., Schwarzburg, K., and Lux-Steiner, M. *physica status solidi - Rapid Research Letters* **2**(4), 172–174 (2008).

[8] Taretto, K. and Rau, U. *Progress in Photovoltaics: Research and Applications* **12**(8), 573–591 (2004).

[9] Larramona, G., Chone, C., Jacob, A., Sakakura, D., Delatouche, B., Pere, D., Cieren, X., Nagino, M., and Bayon, R. *Chemistry of Materials* **18**(6), 1688–1696 (2006).

[10] Herzog, C., Belaidi, A., Ogacho, A., and Dittrich, T. *Energy & Environmental Science* **2**(9), 962–964 (2009).

[11] O'Regan, B. and Grätzel, M. *Nature* **353**(6346), 737–740 (1991).

[12] Tennakone, K., Kumara, G. R. R. A., Kottegoda, I. R. M., Perera, V. P. S., and Weerasundara, P. S. R. S. *Journal of Photochemistry and Photobiology A: Chemistry* **117**(2), 137–142 (1998).

[13] Taguchi, T., Zhang, X. T., Sutanto, I., Tokuhiro, K., Rao, T. N., Watanabe, H., Nakamori, T., Uragami, M., and Fujishima, A. *Chemical Communications* (19), 2480–2481 (2003).

[14] O'Regan, B., Lenzmann, F., Muis, R., and Wienke, J. *Chemistry of Materials* **14**(12), 5023–5029 (2002).

[15] Vogel, R., Pohl, K., and Weller, H. *Chemical Physics Letters* **174**(3-4), 241–246 (1990).

[16] Tennakone, K., Kumara, G. R. R. A., Kottegoda, I. R. M., Perera, V. P. S., and Aponsu, G. M. L. P. *Journal of Physics D: Applied Physics* **31**(18), 2326–2330 (1998).

[17] Itzhaik, Y., Niitsoo, O., Page, M., and Hodes, G. *The Journal of Physical Chemistry C* **113**(11), 4254–4256 (2009).

[18] Page, M., Niitsoo, O., Itzhaik, Y., Cahen, D., and Hodes, G. *Energy & Environmental Science* **2**(2), 220–223 (2009).

[19] Bayón, R., Musembi, R., Belaidi, A., Bär, M., Guminskaya, T., Fischer, C. H., Lux-Steiner, M. C., and Dittrich, T. *Comptes Rendus Chimie* **9**(5-6), 730–734 (2006).

[20] Lee, H., Leventis, H. C., Moon, S.-J., Chen, P., Ito, S., Haque, S. A., Torres, T., Nesch, F., Geiger, T., Zakeeruddin, S. M., Grätzel, M., and Nazeeruddin, M. K. *Advanced Functional Materials* **19**(17), 2735–2742 (2009).

[21] Tena-Zaera, R., Katty, A., Bastide, S., Lévy-Clément, C., O'Regan, B., and Muñoz-Sanjosé, V. *Thin Solid Films* **483**(1-2), 372–377 (2005).

[22] Tena-Zaera, R., Ryan, M. A., Katty, A., Hodes, G., Bastide, S., and Lévy-Clément, C. *Comptes Rendus Chimie* **9**(5-6), 717–729 (2006).

[23] Nadarajah, A., Word, R. C., VanSant, K., and Könenkamp, R. *physica status solidi (b)* **245**(9), 1834–1837 (2008).

[24] Deckman, H. W., Wronski, C. R., Witzke, H., and Yablonovitch, E. *Applied Physics Letters* **42**(11), 968–970 (1983).

[25] Hagfeldt, A., Didriksson, B., Palmqvist, T., Lindström, H., Södergren, S., Rensmo, H., and Lindquist, S.-E. *Solar Energy Materials and Solar Cells* **31**(4), 481 – 488 (1994).

[26] O'Regan, B. and Schwartz, D. T. *Chemistry of Materials* **7**(7), 1349–1354 (1995).

[27] Tennakone, K., Kumara, G., Kumarasinghe, A., Wijayantha, K., and Sirimanne, P. *Semiconductor Science and Technology* **10**, 1689–1693 (1995).

[28] Rost, C., Sieber, I., Siebentritt, S., Lux-Steiner, M. C., and Konenkamp, R. *Appl. Phys. Lett.* **75**(5), 692–694 (1999).

[29] O'Regan, B. and Schwartz, D. *Chemistry of Materials* **10**(6), 1501–1509 (1998).

[30] Kumara, G. R. R. A., Konno, A., Senadeera, G. K. R., Jayaweera, P. V. V., Silva, D. B. R. A. D., and Tennakone, K. *Solar Energy Materials and Solar Cells* **69**(2), 195–199 (2001).

[31] Sankapal, B. R., Goncalves, E., Ennaoui, A., and Lux-Steiner, M. C. *Thin Solid Films* **451–452**, 128–132 (2004).

[32] Nicolau, Y. F., Dupuy, M., and Brunel, M. *Journal of The Electrochemical Society* **137**(9), 2915–2924 (1990).

[33] O'Regan, B., Schwartz, D. T., Zakeeruddin, S. M., and Grätzel, M. *Advanced Materials* **12**(17), 1263–1267 (2000).

[34] O'Regan, B. C. and Lenzmann, F. *The Journal of Physical Chemistry B* **108**(14), 4342–4350 (2004).

[35] Zhang, X.-T., Liu, H.-W., Taguchi, T., Meng, Q.-B., Sato, O., and Fujishima, A. *Solar Energy Materials and Solar Cells* **81**(2), 197–203 (2004).

[36] O'Regan, B. C., Scully, S., Mayer, A. C., Palomares, E., and Durrant, J. *The Journal of Physical Chemistry B* **109**(10), 4616–4623 (2005).

[37] Kohtani, S., Kudo, A., and Sakata, T. *Chemical Physics Letters* **206**(1-4), 166–170 (1993).

[38] Zhang, Y., Xie, T., Jiang, T., Wei, X., Pang, S., Wang, X., and Wang, D. *Nanotechnology* **20**(15), 155707 (2009).

[39] Hoyer, P. and Könenkamp, R. *Applied Physics Letters* **66**(3), 349–351 (1995).

[40] Vogel, R., Hoyer, P., and Weller, H. *The Journal of Physical Chemistry* **98**(12), 3183–3188 (1994).

[41] Liu, D. and Kamat, P. V. *Journal of Physical Chemistry* **97**(41), 10769–10773 (1993).

[42] Zaban, A., Micic, O., Gregg, B., and Nozik, A. *Langmuir* **14**(12), 3153–3156 (1998).

[43] Niitsoo, O., Sarkar, S. K., Pejoux, C., Rühle, S., Cahen, D., and Hodes, G. *Journal of Photochemistry and Photobiology A: Chemistry* **181**(2-3), 306–313 (2006).

[44] Yu, P., Zhu, K., Norman, A. G., Ferrere, S., Frank, A. J., and Nozik, A. J. *The Journal of Physical Chemistry B* **110**(50), 25451–25454 (2006).

[45] Chang, C.-H. and Lee, Y.-L. *Applied Physics Letters* **91**(5), 053503–3 (2007).

[46] Lee, H. J., Yum, J.-H., Leventis, H. C., Zakeeruddin, S. M., Haque, S. A., Chen, P., Seok, S. I., Grätzel, M., and Nazeeruddin, M. K. *The Journal of Physical Chemistry C* **112**(30), 11600–11608 (2008).

[47] Sun, W.-T., Yu, Y., Pan, H.-Y., Gao, X.-F., Chen, Q., and Peng, L.-M. *Journal of the American Chemical Society* **130**(4), 1124–1125 (2008).

[48] Lan, G.-Y., Yang, Z., Lin, Y.-W., Lin, Z.-H., Liao, H.-Y., and Chang, H.-T. *Journal of Materials Chemistry* **19**, 2349–2355 (2009).

[49] Lee, H. J., Chen, P., Moon, S.-J., Sauvage, F., Sivula, K., Bessho, T., Gamelin, D. R., Comte, P., Zakeeruddin, S. M., Seok, S. I., Grätzel, M., and Nazeeruddin, M. K. *Langmuir* **25**(13), 7602–7608 (2009).

[50] Möller, J., Fischer, C. H., Muffler, H. J., Könenkamp, R., Kaiser, I., Kelch, C., and Lux-Steiner, M. C. *Thin Solid Films* **361–362**, 113–117 (2000).

[51] Ernst, K., Sieber, I., Neumann-Spallart, M., Lux-Steiner, M., and Konenkamp, R. *Thin Solid Films* **361**, 213–217 (2000).

[52] Könenkamp, R., Ernst, K., Fischer, C. H., Lux-Steiner, M. C., and Rost, C. *physica status solidi (a)* **182**(1), 151–155 (2000).

[53] Kaiser, I., Ernst, K., Fischer, C. H., Könenkamp, R., Rost, C., Sieber, I., and Lux-Steiner, M. C. *Solar Energy Materials and Solar Cells* **67**(1-4), 89–96 (2001).

[54] Musembi, R. J., Rusu, M., Mwabora, J. M., Aduda, B. O., Fostiropoulos, K., and Lux-Steiner, M. C. *physica status solidi (a)* **205**(7), 1713–1718 (2008).

[55] Oja, I., Belaidi, A., Dloczik, L., Lux-Steiner, M.-C., and Dittrich, T. *Semiconductor Science and Technology* **21**(4), 520–526 (2006).

[56] Plass, R., Pelet, S., Krueger, J., Grätzel, M., and Bach, U. *Journal of Physical Chemistry B* **106**(31), 7578–7580 (2002).

[57] Könenkamp, R., Boedecker, K., Lux-Steiner, M. C., Poschenrieder, M., Zenia, F., Levy-Clement, C., and Wagner, S. *Applied Physics Letters* **77**(16), 2575–2577 (2000).

[58] Kieven, D., Dittrich, T., Belaidi, A., Tornow, J., Schwarzburg, K., Allsop, N., and Lux-Steiner, M. *Applied Physics Letters* **92**(15), 153107 (2008).

[59] Tena-Zaera, R., Elias, J., and Levy-Clement, C. *Applied Physics Letters* **93**(23), 233119–3 (2008).

[60] Baxter, J. B. and Aydil, E. S. *Applied Physics Letters* **86**(5), 1–3 (2005).

[61] Bauer, C., Boschloo, G., Mukhtar, E., and Hagfeldt, A. *Journal of Physical Chemistry B* **105**(24), 5585–5588 (2001).

[62] Law, M., Greene, L. E., Johnson, J. C., Saykally, R., and Yang, P. *Nature Materials* **4**(6), 455–459 (2005).

[63] Lévy-Clément, C., Tena-Zaera, R., Ryan, M. A., Katty, A., and Hodes, G. *Advanced Materials* **17**(12), 1512–1515 (2005).

[64] Dittrich, T., Kieven, D., Rusu, M., Belaidi, A., Tornow, J., Schwarzburg, K., and Lux-Steiner, M. *Applied Physics Letters* **93**(5), 053113–3 (2008).

[65] Belaidi, A., Dittrich, T., Kieven, D., Tornow, J., Schwarzburg, K., Kunst, M., Allsop, N., Lux-Steiner, M.-C., and Gavrilov, S. *Solar Energy Materials and Solar Cells* **93**(6-7), 1033–1036 (2009).

[66] Dittrich, T., Kieven, D., Belaidi, A., Rusu, M., Tornow, J., Schwarzburg, K., and Lux-Steiner, M. C. *Journal of Applied Physics* **105**(3), 034509 (2009).

[67] Leschkies, K. S., Divakar, R., Basu, J., Enache-Pommer, E., Boercker, J. E., Carter, C. B., Kortshagen, U. R., Norris, D. J., and Aydil, E. S. *Nano Letters* **7**(6), 1793–1798 (2007).

[68] Tang, Y., Hu, X., Chen, M., Luo, L., Li, B., and Zhang, L. *Electrochimica Acta* **54**(10), 2742–2747 (2009).

[69] Cao, X., Chen, P., and Guo, Y. *The Journal of Physical Chemistry C* **112**(51), 20560–20566 (2008).

[70] Tak, Y., Kim, H., Lee, D., and Yong, K. *Chemical Communications* **2008**, 4585–4587 (2008).

[71] Kuo, K. T., Liu, D. M., Chen, S. Y., and Lin, C. C. *Journal of Materials Chemistry* **19**(37), 6780–6788 (2009).

[72] Birkmire, R. W. and Eser, E. *Annual Review of Materials Science* **27**(1), 625 – 653 (1997).

[73] Grätzel, M. *Nature* **414**(6861), 338–344 (2001).

[74] Schmidt-Mende, L. and MacManus-Driscoll, J. L. *Materials Today* **10**(5), 40–48 (2007).

[75] Look, D. C. *Materials Science and Engineering B* **80**(1-3), 383–387 (2001).

[76] Wang, Z. L. *Journal of Physics: Condensed Matter* **16**(25), R829–R858 (2004).

[77] Aoki, T., Shimizu, Y., Miyake, A., Nakamura, A., Nakanishi, Y., and Hatanaka, Y. *Physica Status Solidi (B) Basic Research* **229**(2), 911–914 (2002).

[78] Chopra, K. L., Major, S., and Pandya, D. K. *Thin Solid Films* **102**(1), 1–46 (1983).

[79] Vayssieres, L. *Advanced Materials* **15**(5), 464–466 (2003).

[80] Law, M., Goldberger, J., and Yang, P. *Annual Review of Materials Research* **34**, 83–122 (2004).

[81] Yi, G. C., Wang, C., and Park, W. I. *Semiconductor Science and Technology* **20**(4), S22–S34 (2005).

[82] Jie, J., Wang, G., Chen, Y., Han, X., Wang, Q., Xu, B., and Hou, J. G. *Applied Physics Letters* **86**(3), 1–3 (2005).

[83] Conley Jr., J. F., Stecker, L., and Ono, Y. *Nanotechnology* **16**(2), 292–296 (2005).

[84] Li, C., Fang, G., Fu, Q., Su, F., Li, G., Wu, X., and Zhao, X. *Journal of Crystal Growth* **292**(1), 19–25 (2006).

[85] Xiang, B., Wang, P., Zhang, X., Dayeh, S. A., Aplin, D. P. R., Soci, C., Yu, D., and Wang, D. *Nano Letters* **7**(2), 323–328 (2007).

[86] Jie, J., Wang, G., Wang, Q., Chen, Y., Han, X., Wang, X., and Hou, J. G. *Journal of Physical Chemistry B* **108**(32), 11976–11980 (2004).

[87] Wang, L., Zhang, X., Zhao, S., Zhou, G., Zhou, Y., and Qi, J. *Applied Physics Letters* **86**(2), 024108 (2005).

[88] Lin, S., Tang, H., Ye, Z., He, H., Zeng, Y., Zhao, B., and Zhu, L. *Materials Letters* **62**(4-5), 603–606 (2008).

[89] Lévy-Clément, C., Katty, A., Bastide, S., Zenia, F., Mora, I., and Munoz-Sanjose, V. *Physica E: Low-Dimensional Systems and Nanostructures* **14**(1-2), 229–232 (2002).

[90] Könenkamp, R., Word, R. C., and Schlegel, C. *Applied Physics Letters* **85**(24), 6004–6006 (2004).

[91] Greene, L. E., Law, M., Goldberger, J., Kim, F., Johnson, J. C., Zhang, Y., Saykally, R. J., and Yang, P. *Angewandte Chemie International Edition* **42**, 3031–3034 (2003).

[92] Greene, L., Law, M., Tan, D., Montano, M., Goldberger, J., Somorjai, G., and Yang, P. *Nano Letters* **5**(7), 1231–1236 (2005).

[93] Vergés, M. A., Mifsud, A., and Serna, C. J. *Journal of the Chemical Society and Faraday Transactions* **86**(6), 959–963 (1990).

[94] Vayssieres, L., Keis, K., Lindquist, S. E., and Hagfeldt, A. *Journal of Physical Chemistry B* **105**(17), 3350–3352 (2001).

[95] Govender, K., Boyle, D. S., Kenway, P. B., and O'Brien, P. *Journal of Materials Chemistry* **14**(16), 2575–2591 (2004).

[96] Chen, Z. and Gao, L. *Journal of Crystal Growth* **293**(2), 522–527 (2006).

[97] Hung, C. H. and Whang, W. T. *Materials Chemistry and Physics* **82**(3), 705–710 (2003).

[98] Li, Q., Kumar, V., Li, Y., Zhang, H., Marks, T. J., and Chang, R. P. H. *Chemistry of Materials* **17**(5), 1001–1006 (2005).

[99] Lin, C. C., Chen, H. P., and Chen, S. Y. *Chemical Physics Letters* **404**(1-3), 30–34 (2005).

[100] Wang, D., Chu, X., and Gong, M. *Nanotechnology* **18**(18), 185601 (2007).

[101] Tak, Y. and Yong, K. *The Journal of Physical Chemistry B* **109**(41), 19263–19269 (2005).

[102] Tak, Y. and Yong, K. *The Journal of Physical Chemistry C* **112**(1), 74–79 (2008).

[103] Tak, Y., Hong, S. J., Lee, J. S., and Yong, K. *Journal of Materials Chemistry* **19**, 5945–5951 (2009).

[104] Reynolds, D. C., Litton, C. W., and Collins, T. C. *Phys. Rev.* **140**(5A), A1726–A1734 (1965).

[105] Vanheusden, K., Warren, W. L., Seager, C. H., Tallant, D. R., Voigt, J. A., and Gnade, B. E. *J. Appl. Phys.* **79**(10), 7983–7990 (1996).

[106] Wu, X. L., Siu, G. G., Fu, C. L., and Ong, H. C. *Applied Physics Letters* **78**(16), 2285–2287 (2001).

[107] Li, C., Fang, G., Su, F., Li, G., Wu, X., and Zhao, X. *Nanotechnology* **17**(15), 3740–3744 (2006).

[108] Djurišić, A. B., Leung, Y. H., Tam, K. H., Hsu, Y. F., Ding, L., Ge, W. K., Zhong, Y. C., Wong, K. S., Chan, W. K., Tam, H. L., Cheah, K. W., Kwok, W. M., and Phillips, D. L. *Nanotechnology* **18**(9), 095702 (2007).

[109] Sun, H., Zhang, Q. F., and Wu, J. L. *Nanotechnology* **17**(9), 2271–2274 (2006).

[110] Lin, B., Fu, Z., and Jia, Y. *Applied Physics Letters* **79**(7), 943–945 (2001).

[111] Gong, Y., Andelman, T., Neumark, G. F., O'Brien, S., and Kuskovsky, I. L. *Nanoscale Research Letters* **2**(6), 297–302 (2007).

[112] Wang, Z., Huang, B., Liu, X., Qin, X., Zhang, X., Wei, J., Wang, P., Yao, S., Zhang, Q., and Jing, X. *Mater. Lett.* **62**(17-18), 2637–2639 (2008).

[113] Limpijumnong, S., Zhang, S. B., Wei, S. H., and Park, C. H. *Physical Review Letters* **92**(15), 155504–1 (2004).

[114] Cao, Y., Miao, L., Tanemura, S., Tanemura, M., Kuno, Y., and Hayashi, Y. *Applied Physics Letters* **88**(25), 251116 (2006).

[115] Look, D. C., Reynolds, D. C., Litton, C. W., Jones, R. L., Eason, D. B., and Cantwell, G. *Applied Physics Letters* **81**(10), 1830 (2002).

[116] Wei, Z. P., Lu, Y. M., Shen, D. Z., Zhang, Z. Z., Yao, B., Li, B. H., Zhang, J. Y., Zhao, D. X., Fan, X. W., and Tang, Z. K. *Applied Physics Letters* **90**(4), 042113 (2007).

[117] Ryu, Y. R., Lee, T. S., Leem, J. H., and White, H. W. *Applied Physics Letters* **83**(19), 4032–4034 (2003).

[118] Xiu, F. X., Yang, Z., Mandalapu, L. J., Zhao, D. T., Liu, J. L., and Beyermann, W. P. *Applied Physics Letters* **87**(15), 152101 (2005).

[119] Kang, H. S., Kim, G. H., Kim, D. L., Chang, H. W., Ahn, B. D., and Lee, S. Y. *Applied Physics Letters* **89**(18), 181103 (2006).

[120] Liu, J. L., Xiu, F. X., Mandalapu, L. J., and Yang, Z. *Zinc Oxide Materials and Devices* **6122**(1), 61220H (2006).

[121] Lopatiuk-Tirpak, O., Chernyak, L., Xiu, F. X., Liu, J. L., Jang, S., Ren, F., Pearton, S. J., Gartsman, K., Feldman, Y., Osinsky, A., and Chow, P. *Journal of Applied Physics* **100**(8), 086101 (2006).

[122] Mandalapu, L. J., Xiu, F. X., Yang, Z., Zhao, D. T., and Liu, J. L. *Applied Physics Letters* **88**(11), 112108 (2006).

[123] Guo, W., Allenic, A., Chen, Y. B., Pan, X. Q., Che, Y., Hu, Z. D., and Liu, B. *Applied Physics Letters* **90**(24), 242108 (2007).

[124] Pan, X., Ye, Z., Li, J., Gu, X., Zeng, Y., He, H., Zhu, L., and Che, Y. *Applied Surface Science* **253**(11), 5067–5069 (2007).

[125] Ilican, S., Caglar, Y., Caglar, M., Yakuphanoglu, F., and Cui, J. *Physica E: Low-dimensional Systems and Nanostructures* **41**(1), 96 – 100 (2008).

[126] Kim, D. H., Cho, N. G., Kim, K. S., Han, S., and Kim, H. G. *Journal of Electroceramics* **22**(1-3), 82–86 (2009).

[127] Yang, Y., Qi, J., Liao, Q., Zhang, Y., Tang, L., and Qin, Z. *The Journal of Physical Chemistry C* **112**(46), 17916–17919 (2008).

[128] Zang, C. H., Zhao, D. X., Tang, Y., Guo, Z., Zhang, J. Y., Shen, D. Z., and Liu, Y. C. *Chemical Physics Letters* **452**(1-3), 148–151 (2008).

[129] Lee, W., Jeong, M. C., Joo, S. W., and Myoung, J. M. *Nanotechnology* **16**(6), 764–768 (2005).

[130] Sun, M., Zhang, Q. F., and Wu, J. L. *Journal of Physics D: Applied Physics* **40**(12), 3798–3802 (2007).

[131] Lalitha, S., Karazhanov, S. Z., Ravindran, P., Senthilarasu, S., Sathyamoorthy, R., and Janabergenov, J. *Physica B: Condensed Matter* **387**(1-2), 227–238 (2007).

[132] Zhang, L., Wett, D., Nagel, M., Peisert, H., Szargan, R., and Chassé, T. *Journal of Electron Spectroscopy and Related Phenomena* **154**(3), 48–52 (2007).

[133] Cao, G. *Nanostructures and Nanomaterials - Synthesis, Properties and Applications*. Imperial College Press, London, (2004).

[134] Berg, T. W. and Hvarn, J. M. In *Optics of semiconductors and their applications,* Kalt, H. and Hetterich, M., editors, 249–273. Springer-Verlag, Berlin (2004).

[135] Shavel, A., Gaponik, N., and Eychmüller, A. *Journal of Physical Chemistry B* **110**(39), 19280–19284 (2006).

[136] Talapin, D. V., Haubold, S., Rogach, A. L., Kornowski, A., Haase, M., and Weller, H. *The Journal of Physical Chemistry B* **105**(12), 2260–2263 (2001).

[137] Wuister, S. F., Swart, I., van Driel, F., Hickey, S. G., and de Mello Donegá, C. *Nano Letters* **3**(4), 503–507 (2003).

[138] Gaponik, N., Talapin, D., Rogach, A., Hoppe, K., Shevchenko, E., Kornowski, A., Eychmüller, A., and Weller, H. *Journal of Physical Chemistry B* **106**(29), 7177–7185 (2002).

[139] Shavel, A., Gaponik, N., and Eychmüller, A. *European Journal of Inorganic Chemistry* **2005**(18), 3613–3623 (2005).

[140] Varahramyan, K. and Lvov, Y. *Proceedings of the Institution of Mechanical Engineers, Part N (Journal of Nanoengineering and Nanosystems)* **220**(N1), 29–37 (2006).

[141] Cassagneau, T. P. and Fendler, J. H. In *Electrochemistry of nanomaterials,* Hodes, G., editor, 247–286. Wiley-VCH, Weinheim (2001).

[142] Gallardo, D. E., Bertoni, C., and Dunn, S. *Proc. SPIE* **5840**(1), 516–522 (2005).

[143] Pettersson, L. A. A., Ghosh, S., and Inganäs, O. *Organic Electronics* **3**, 143–148 (2002).

[144] Wood, D. L. and Tauc, J. *Phys. Rev. B* **5**, 3144–3151 (1972).

[145] Solé, J., Bausa, L., and Jaque, D. *An Introduction to the Optical Spectroscopy of Inorganic Solids*. Wiley, (2005).

[146] Christian, P. and O'Brien, P. *Journal of Materials Chemistry* **15**(46), 4949–4954 (2005).

[147] Mandalapu, L. J., Xiu, F. X., Yang, Z., and Liu, J. L. *Journal of Applied Physics* **102**(2), 023716 (2007).

[148] Gardner, H., Gallardo, D., Dunn, S., Gaponik, N., and Eychmuller, A. *Journal of Nanoscience and Nanotechnology* **8**, 2578–2581 (2008).

[149] Castro-Rodríguez, R., Iribarren, A., Bartolo-Pérez, P., and Peña, J. *Thin Solid Films* **484**(1-2), 100–103 (2005).

[150] Francis, S., Varshney, L., and Sabharwal, S. *European Polymer Journal* **43**, 2525–2531 (2007).

[151] Dunn, S., Gardner, H., Bertoni, C., Gallardo, D., Gaponik, N., and Eychmuller, A. *Journal of Nanoscience and Nanotechnology* **8**, 2544–2548 (2008).

[152] Tennakone, K., Jayatissa, A. H., Fernando, C. A. N., Wickramanayake, S., Punchihewa, S., Weerasena, L. K., and Premasiri, W. D. R. *Physica Status Solidi (a)* **103**(2), 491–497 (1987).

[153] Bayon, R., Musembi, R., Belaidi, A., Br, M., Guminskaya, T., Lux-Steiner, M.-C., and Dittrich, T. *Solar Energy Materials and Solar Cells* **89**(1), 13 – 25 (2005).

[154] Gregg, B. A. *The Journal of Physical Chemistry B* **107**(20), 4688–4698 (2003).

[155] Förster, T. *Annalen der Physik* **437**, 55–75 (1948).

[156] Tang, Z., Ozturk, B., Wang, Y., and Kotov, N. A. *The Journal of Physical Chemistry B* **108**(22), 6927–6931 (2004).

[157] Wakizaka, D., Fushimi, T., Ohkita, H., and Ito, S. *Polymer* **45**(25), 8561–8565 (2004).